CROSS and CUPID-Mo : future strategies and new results in bolometric search for $0\nu\beta\beta$

Hawraa Khalife

université
PARIS-SACLAY

CROSS and CUPID-Mo: future strategies and new results in bolometric search for $0\nu\beta\beta$

Thèse de doctorat de l'université Paris-Saclay

École doctorale n° 576, Particules, Hadrons, Energie, Noyau, Instrumentation, Imagerie, Cosmos et Simulation (PHENIICS)
Spécialité de doctorat: astroparticules et cosmologie
Unité de recherche: Université Paris-Saclay, CNRS, IJCLab, 91405, Orsay, France
Référent: : Faculté des Sciences d'Orsay

Thèse présentée et soutenue en visioconférence totale, le 21/01/2021, par

Hawraa KHALIFE

Composition du jury:

Nathalie BESSON Directrice du DPhP et Directrice de recherche, CEA-IRFU	Présidente
Michel SOREL Directeur de recherche, HDR, IFIC	Rapporteur et Examinateur
Christine MARQUET Directrice de recherche, HDR, CENBG	Rapportrice et Examinatrice
Carlos Peña GARAY Directeur du LSC et Directeur de recherche, CSIC	Examinateur
Stefano PIRRO Directeur de recherche, INFN	Examinateur
Andrea Giuliani Directeur de Recherche, IJCLab	Directeur de thèse

Thèse de doctorat

NNT: 2021UPASP002

To my family
my everything

Résumé entendu en français

Cette thèse introduit une nouvelle technologie dans la recherche bolométrique de la double désintégration bêta sans neutrinos ($0\nu\beta\beta$) développée dans le cadre du projet CROSS dans le but de discriminer les événements α et β générés par une contamination radioactive de surface. Cette source de fond limite actuellement la sensibilité sur la demi-vie de la double désintégration bêta sans neutrinos dans les expériences bolométriques. En outre, la thèse couvre l'expérience CUPID-Mo, un démonstrateur de CUPID, une expérience bolométrique de nouvelle génération $0\nu\beta\beta$ à l'échelle de la tonne. CUPID-Mo a récemment atteint une nouvelle limite sur la demi-vie de ^{100}Mo, démontrant avec succès la technologie de double lecture chaleur-lumière.

Les neutrinos, ces particules fondamentales les plus insaisissables du modèle standard (SM), sont encore mystérieux et mal compris. On pensait qu'ils n'avaient pas de masse dans le modèle standard, mais la découverte de l'oscillation des neutrinos a prouvé que les neutrinos ont une masse finie. On ne sait toujours pas comment les neutrinos obtiennent leur masse ni combien ils pèsent. Une autre question ouverte concernant les neutrinos est de savoir s'ils sont des particules de Dirac (les neutrinos et les anti-neutrinos sont distincts) ou de Majorana (les neutrinos et les anti-neutrinos sont identiques). La seule façon pratique d'étudier expérimentalement cette question est de rechercher la double désintégration bêta sans neutrinos. Ce processus peut également donner des contraintes sur l'échelle de masse absolue des neutrinos.

La $0\nu\beta\beta$ est une transition nucléaire hypothétique avec des demi-vies de l'ordre de $T_{1/2}>10^26$ ans. Elle peut se produire dans certains noyaux qui ont un nombre pair de protons et de neutrons, et consiste en la transformation d'un noyau (A, Z) en un isobar plus léger (A, Z+2) accompagné de l'émission de deux électrons et d'aucune autre particule. Sa découverte prouverait que le nombre de leptons n'est pas une symétrie de la nature, ce qui conduirait à une physique au-delà du SM. En outre, elle implique que les neutrinos coïncident avec leurs antiparticules, ce qui permettra de déterminer qu'il s'agit de fermions de Majorque. Le processus $0\nu\beta\beta$ est énergétiquement autorisé pour 35 noyaux (^{76}Ge, ^{82}Se, ^{100}Mo, ^{116}Cd, ^{130}Te, ^{136}Xe...). Sa signature est un pic monochromatique à la valeur Q ($Q_{\beta\beta}$) de la transition correspondant à la somme des énergies cinétiques portées par les deux électrons émis. Les isotopes les plus prometteurs et les plus souhaitables à étudier sont ceux dont la valeur de $Q_{\beta\beta}$ est supérieure à la

limite d'énergie de la majeure partie de la radioactivité gamma naturelle (^{208}Tl, 2615 keV), car cela implique moins de bruit de fond dans la région d'intérêt (ROI). Un $Q_{\beta\beta}$ élevé implique également une probabilité de décroissance plus élevée. Une mesure de la demi-vie de $0\nu\beta\beta$, dans l'interprétation la plus simple de ce processus, donnerait une indication de la masse effective des neutrinos, une combinaison linéaire des trois masses de neutrinos. En fait, le taux de $0\nu\beta\beta$ est inversement proportionnel au carré de la masse effective des neutrinos. Le lien entre la demi-vie et la masse des neutrinos est connu avec quelques incertitudes liées au choix des modèles nucléaires. Cependant, la mesure de la demi-vie de $0\nu\beta\beta$ reste l'une des méthodes les plus prometteuses pour fixer l'échelle de masse absolue des neutrinos.

Comme la demi-vie du processus est extrêmement longue, la recherche de cette rare décomposition est une tâche extrêmement difficile. Une expérience doit être réalisée avec des détecteurs radio-purs, de grande masse et de haute résolution énergétique et une radioactivité négligeable provenant de tout autre élément que le noyau étudié, car sinon le signal sera enterré dans le fond.

L'une des techniques les plus prometteuses pour rechercher la double désintégration bêta sans neutrinos sont les bolomètres. Les bolomètres sont des détecteurs à basse température constitués d'un cristal dans lequel est incorporé l'isotope candidat à la double désintégration bêta et d'un capteur thermique couplé au cristal (généralement collé à celui-ci). Lorsqu'une particule libère de l'énergie dans l'absorbeur bolométrique (le cristal), elle produit des vibrations du réseau qui génèrent une augmentation de la température du cristal mesurée par le capteur qui fait office de thermomètre. Les bolomètres présentent de nombreux avantages, dont voici quelques-uns : haute résolution énergétique, rendement élevé, possibilité d'amélioration pour obtenir une identification des particules (PID) ou une discrimination de la forme des impulsions (PSD) pour rejeter les événements de fond difficiles. Deux types de bolomètres sont considérés dans notre travail, basés sur des cristaux de Li_2MoO_4 et de TeO_2, intégrant les candidats double bêta prometteurs ^{100}Mo et ^{130}Te respectivement.

Une partie de cette thèse est consacrée au CUPID-Mo, précurseur du CUPID, et basée sur des bolomètres à scintillation Li_2MoO_4. Un bolomètre à scintillation est un bolomètre basé sur un cristal qui émet une lumière scintillante lorsqu'une particule interagit en son sein. La technique du CUPID-Mo est basée sur une mise à jour du bolomètre simple de base, qui est la technologie de lecture à double chaleur-lumière. Le bolomètre à scintillation principal, qui intègre l'isotope de désintégration double bêta, est couplé à un

détecteur de lumière (un bolomètre également) pour enregistrer le signal lumineux. Cette technique peut être exploitée pour se débarrasser des α's de surface, un fond important dans la région d'intérêt (ROI) autour de $Q\beta\beta$. En fait, les rendements lumineux des particules α et des particules β/γ sont différents pour la même énergie déposée, ce qui donne la possibilité de rejeter α en lisant simultanément la chaleur et la lumière pour chaque événement. L'expérience CUPID-Mo a démontré avec succès cette technologie. Elle a permis d'atteindre une nouvelle limite de la demi-vie de $0\nu\beta\beta$ de la désintégration du ^{100}Mo de $T_{1/2} > 1.5\times10^{24}$ ans à 90% C.I., la meilleure jamais obtenue au niveau mondial sur cet isotope.

L'autre partie majeure de cette thèse est consacrée au développement d'une nouvelle technologie bolométrique pour se débarrasser non seulement des α de surface, mais aussi des β de surface . Cela nous permettra d'atteindre un niveau de bruit de fond encore plus bas dans le retour sur investissement, ce qui augmentera la sensibilité de $0\nu\beta\beta$. La technologie CROSS est basée sur le revêtement de la surface du cristal avec un matériau approprié pour fournir au cristal une DSP pour les événements de surface par rapport aux événements de masse. Le matériau de revêtement fonctionne comme un modificateur de forme d'impulsion pour les événements de surface, de sorte qu'il est possible de les distinguer des dépôts d'énergie se produisant dans le volume.

L'idée originale de CROSS était de recouvrir le cristal d'une pellicule d'aluminium supraconductrice. Nous commençons à tester cette approche avec une configuration simplifiée consistant en un revêtement d'un côté de cristaux de Li_2MoO_4 et de TeO_2 de $2\times2\times1$ cm. Le capteur utilisé est un Ge-NTD (thermistance au germanium dopée par transmutation de neutrons) qui a une réponse assez lente et qui est sensible principalement aux phonons thermiques. Les résultats ont montré une excellente séparation entre les α de surface (provenant d'une source α placée face au film d'Al) et les événements de masse (événements loin de la surface revêtue) avec peu d'épaisseur du film d'Al µm. Ceci a été observé pour le Li_2MoO_4 et le TeO_2. En fait, les phonons à haute énergie qui sont produits après une interaction de particules dans le cristal sont efficacement piégés dans le film d'Al lorsqu'ils proviennent d'événements de surface. Cela conduit à une dégradation plus rapide de l'énergie des phonons, accélérant ainsi la thermalisation des phonons induits en surface par rapport aux phonons induits en masse qui sont moins efficacement piégés dans le film d'Al. Le fait de recouvrir entièrement les cristaux d'un film d'aluminium a entraîné la perte de la bonne discrimination entre les événements de α surface et ceux de la masse.

Comme la discrimination des β de surface n'a pas été obtenue avec un revêtement de film d'aluminium, il a été décidé d'essayer un autre matériau de revêtement : le Pd métallique normal. Un métal normal a été envisagé car il est censé conduire à une meilleure thermalisation par rapport à un supraconducteur qui piège les phonons sous forme de quasi-particules, introduisant un effet qui concurrence la thermisation plus rapide obtenue en émettant des phonons de plus faible énergie. Le seul inconvénient du métal normal est sa grande capacité thermique qui peut affecter la sensibilité du bolomètre. Un film de Pd de quelques nm a été déposé sur une face des cristaux de Li_2MoO_4 et TeO_2. Un résultat très encourageant a été obtenu en réalisant l'objectif du CROSS consistant à discriminer les particules de surface α et β. Ce résultat n'a clairement été obtenu que pour le Li_2MoO_4. Cependant, le revêtement complet du cristal avec du Pd a détruit la sensibilité du bolomètre, comme prévu par les estimations de la capacité calorifique.

Pour résoudre le problème de la capacité calorifique élevée du Pd, l'effet de proximité a été exploité. En effet, le dépôt d'une couche de film d'Al supraconducteur sur le Pd induira la supraconductivité de ce dernier, diminuant ainsi la capacité thermique globale du film bicouche (Al-Pd). Les résultats ont été probants en termes de séparation et de diminution de la capacité thermique des β et α de surface pour le Li_2MoO_4 et il a été moins apprécié pour le TeO_2. Pour éviter d'avoir une grande fraction de la surface revêtue lorsque le cristal est entièrement recouvert, on a pensé à essayer des grilles Pd-Al au lieu d'un film. Cela s'est avéré parfaitement efficace pour obtenir une discrimination de la surface et du volume lorsqu'il est revêtu sur une surface.

La thèse est divisée en 6 chapitres : les trois premiers (1, 2 & 3) sont des chapitres d'introduction, suivis de deux chapitres (4 & 5) présentant les résultats expérimentaux obtenus au cours de la thèse. Le chapitre 6 est réservé aux conclusions

Le premier chapitre contient un bref historique des neutrinos et présente les questions de la masse et de la nature des neutrinos par la description de l'origine des masses de neutrinos, le mélange des neutrinos et les différentes mesures de la masse des neutrinos. Ce chapitre fournit les apports théoriques et expérimentaux nécessaires pour apprécier la pertinence de la recherche sur le double bêta sans neutrinos, qui est détaillée dans le chapitre suivant.

Le deuxième chapitre donne une description détaillée de la double désintégration bêta sans neutrinos et des défis associés pour sa détection. Les nombreuses techniques expérimentales développées pour cette recherche sont également décrites.

Le troisième chapitre est consacré à la technologie bolométrique. Le principe général de cette technique est donné, en présentant tous les composants utilisés dans de tels détecteurs. Ensuite, les bolomètres à scintillation et leurs avantages pour la recherche en double bêta sans neutralité sont présentés, donnant une description générale de la technologie CUPID. Ensuite, ce chapitre est complété par une brève description des principes de la physique des phonons qui permettent de comprendre la technologie CROSS et les objectifs basés sur la discrimination de la forme des impulsions. Enfin, les paramètres PSD utilisés pour discriminer les événements de surface des événements de masse sont présentés.

Le quatrième chapitre présente les résultats obtenus sur les prototypes CROSS. Deux types de cristaux, Li_2MoO_4 et TeO_2, ont été testés avec différentes épaisseurs de revêtements supraconducteurs en Al et en Pd métallique normal. Ces travaux ont démontré pour la première fois la capacité à discriminer les interactions α et β sur les surfaces des cristaux, au moyen de revêtements bi-couches en Al et Pd.

Le dernier chapitre présente les conclusions et les perspectives liées aux travaux décrits dans les chapitres précédents. Le démonstrateur CROSS est décrit : cette expérience pilote sera bientôt installée dans le laboratoire souterrain de Canfranc, visant à démontrer l'efficacité du revêtement de grille Pd-Al pour la discrimination des événement de surfaces α et β. Ce chapitre présente les résultats possibles à venir sur les niveaux de fond pouvant être atteints avec la technologie CROSS et l'impact sur la sensibilité d'une future expansion possible du CUPID (CUPID-1T) en utilisant cette technologie de discrimination d'événements de surface.

La technologie CROSS est une percée dans la technologie bolométrique de la double désintégration bêta qui peut aider à atteindre un indice de bruit de fond dans la gamme de 10^{-5} comptes/(keV kg an), à comparer avec celui prévu dans le CUPID qui est un ordre de grandeur plus élevé. La sensibilité de CUPID en termes de masse effective des neutrinos s'arrête à environ 0,02 eV (l'une des meilleures pour les expériences de la prochaine génération), tandis qu'une expérience basée sur la technologie CROSS pourrait s'améliorer d'un autre factor ~ 3, augmentant le potentiel de découverte même en cas de la hiérarchie normale des masses de neutrinos.

Acknowledgements

I am grateful to many people, professionally and personally, for their continuous support during my thesis. This work would not have been possible to complete without them.

First I would like to thank my thesis jury: Nathalie Besson, Michel Sorel, Christine Marquet, Carlos Peña Garay and Stefano Pirro for accepting to evaluate my thesis. Thank you for the interest you brought to my work and for the useful remarks and advice you have provided me.

I would like to express my immense gratitude to my supervisor Andrea Giuliani for his constant support. I appreciated your words of encouragement, guidance and advice. It has been an amazing journey to work under his supervision.

I would also like to thank all my colleagues at IJCLab. In particular I am grateful to Denys Poda for his continuous help and support. Thanks to Emiliano Olivieri, Anastasiia Zolotarova, Louis Dumoulin, Riham Mariam, Pierre de Marcillac, Claire Marrache-Kikuchi and all the group who had a hand in this work. I would like to thank also Dounia Helis and Beatrice Mauri for the good times we spent at the lab together.

A friend in a foreign land is a homeland. I would like to thank all my friends here in France, that share the same ambitions as mine. We spent an amazing time together. I thank specially Nour for being such a good companion in the hard times of quarantine.

I thank my sister Hanine, for being always there for me, my supporter and my backbone. We dove together through all the ups and the downs, traveled, had adventures, and shared all the moments together.

Finally, my deepest gratitude to my parents for their many years of support and a lot of encouragement. I appreciate all the sacrifices they gave, nothing in this world can pay them back.

Contents

Chapter 1

Introduction to Neutrino Physics

This chapter will present a summary on neutrino physics, including the history and the current knowledge of this particle, with the purpose to open the way for the next chapter that will introduce neutrinoless double-beta decay ($0\nu\beta\beta$), the main subject of this thesis.

1.1 A brief history of neutrino

Up-to-date, neutrino's picture is still incomplete. This elusive particle, that has been postulated by Pauli in 1930 [1], is pushing physicists to perform sophisticated experiments to fully understand it.

A hint for the existence of neutrino was proposed after having no explanation for the energy deficit and non-conservation of the angular momentum in nuclear β-decay. The emitted electron shows a continuum energy spectrum with a maximum value at around 1/3 of the Q-value — representing the total kinetic energy available in the final state — and not a single narrow peak as one would expect if only electrons were emitted from the decay. This means that part of the energy is carried away by a weakly interacting particle with zero charge and spin $\frac{1}{2}$ for quantum number conservation (charge and angular momentum respectively). E. Fermi developed Pauli's suggestion in a theory for β decay [2] that incorporated the neutrino in a coherent theoretical framework describing the interaction of this particle with electrons and nucleons, following the successful scheme developed for electrodynamics.

More than 20 years later, F. Reines and C.L. Cowan [3] were the first to confirm neutrino existence in 1956. It took so much time and efforts to detect the neutrino because of its low cross-section which leads to a very low interaction probability. F. Reines and C.L. Cowan placed three cadmium chloride ($CdCl_2$) inorganic liquid scintillator tanks — facing the Savannah River reactor's core in the USA — which were equipped with photo-multipliers to detect the anti-neutrinos via the inverse beta decay:

$$\overline{\nu}_e + p \rightarrow e^+ + n. \tag{1.1}$$

The hint for neutrino's interactions with protons (hydrogen in water molecule) comes from the detected gamma rays that are promptly released after the positron-electron annihilation and are followed by the delayed ones related to neutron capture in cadmium.

Neutrinos exist in three flavors, ν_e, ν_μ and ν_τ. The ν_μ was discovered in 1962 with the first accelerator neutrino beam at Brookhaven National Laboratory [4] in the USA. The third type of neutrino, ν_τ, was observed recently in 2000 at Fermi National Laboratory

(USA) by the DONUT experiment [5]. These three types of neutrinos are distinguished according to how they interact with matter, meaning that a ν_α will produce the charged lepton α by charged current interactions.

In the late 1960's, R. Davis conducted the first experiment [6] to measure the flux of neutrinos coming from the sun, which used the reaction:

$$\nu_e + {}^{37}Cl \rightarrow e^- + {}^{37}Ar. \tag{1.2}$$

The experiment has been running for more than 2 decades between 1970 and 1994. It was successful to detect the solar neutrinos, but only one third of the expected electron neutrinos flux calculated by his colleague J.N. Bahcall were measured [7]. This became known as "The Solar Neutrino Problem". Possible explanations started to arise to solve this problem. Three types of solutions were proposed: incorrect theoretical calculation of the solar neutrino flux, unexplained detection inefficiency in the experiment itself, or something not understood about how neutrinos behave when they travel. The reason of the discrepancy was found not to be theoretical in terms of solar model nor experimental, after checking and refining the calculations and increasing the experimental efficiency.

In 1969, B. Pontecorvo and V. Gribov had an idea [8] (Pontecorvo already considered this idea in 1957). They proposed that neutrinos might oscillate, changing from one flavour to another, and since the experiment is sensitive only to one flavour type, it is showing deficit. Initially, this explanation was not fully accepted within the community, because it meant that neutrinos have a mass, which contradicts what is assumed in the Standard Model (SM) of elementary particles. The first evidence for neutrino oscillations came from SuperKamiokande in 1998 [9]. The experiment, located in a mine in Japan, was detecting atmospheric muon neutrinos which showed a different proportions for down-going neutrinos and upward-going neutrinos, coming from the opposite side of the Earth. The results were perfectly consistent with a change of a fraction of upward-going muon neutrinos to tau neutrinos due to flavor oscillations. The conclusive evidence for solar neutrino oscillations was found by the Sudbury Neutrino Observatory (SNO) experiment [10]. The experiment was sensitive to all the three neutrino types, allowing it to measure the total flux of solar neutrinos, which agrees with the value predicted theoretically. In addition, the experiment was able also to measure separately ν_e's, which resulted to be about $1/3$ of the total neutrino flux, proving that about $2/3$ of the ν_e's emitted by the sun changed to a different flavour before reaching a terrestrial detector.

Neutrinos are massless in the SM: discovering neutrino oscillation meant that conversely neutrinos are massive. However, the absolute mass scale of neutrino is still unknown, because oscillation experiments measure only the mass-squared difference between the three mass states of neutrino (ν_1, ν_2 and ν_3). The three neutrino flavors are quantum-mechanical combinations of the three neutrino mass states. For flavour changing to occur, the three neutrino masses have to be different. The mass ordering is also an unknown: if m_1 is the lightest, we speak of normal hierarchy (or ordering), while if m_3 is the lightest we speak of inverted hierarchy. Notice that $m_1 < m_2$ is well established by the study of solar neutrino oscillations.

Since neutrinos are uncharged, there is a possibility that they are their own anti-particles. This was proposed by E. Majorana in 1937 in a theory of massive fermions [11]. Neutrinos and anti-neutrinos can only be distinguished by their lepton number. If lepton

number conservation is broken, a neutrino and an anti-neutrino can't be distinguished, i.e. they are Majorana particles. Current experiments aim to answer the following big unknowns about neutrino:

- Their fundamental nature: Dirac or Majorana
- The mass hierarchy
- The absolute mass scale
- CP violation in the lepton sector
- Sterile neutrino

1.2 The origin of neutrino masses

A neutrino mass term can be introduced in the Lagrangian of the electroweak interaction in two distinct ways: a Dirac mass term and a Majorana mass term. The combination of these two forms predicts that a heavy massive neutrino must exist along side the known light massive neutrino according to the so-called see-saw mechanism, which will be briefly summarized below in a simplified approach.

The Standard Model includes three left-handed neutrinos. In order to generate a Dirac mass term for neutrinos by the Higgs mechanism, a right-handed neutrino, which will be sterile with respect to weak interaction, must be introduced. The Dirac mass term is written as follows:

$$\mathcal{L}^{D}_{mass} = -m_D(\overline{\nu}_R\nu_L - \overline{\nu}_L\nu_R) \tag{1.3}$$

where ν_R and ν_L are the left-handed and the right-handed chiral neutrino fields expressed as

$$\nu_R = \begin{pmatrix} \nu_{eR} \\ \nu_{\mu R} \\ \nu_{\tau R} \end{pmatrix}, \quad \nu_L = \begin{pmatrix} \nu_{eL} \\ \nu_{\mu L} \\ \nu_{\tau L} \end{pmatrix}. \tag{1.4}$$

and m_D is a complex non diagonal mass matrix.

In addition, the Lagrangian can contain a Majorana mass term because of neutrino neutrality:

$$\mathcal{L}^{M}_{mass} = -\frac{m_L}{2}(\overline{\nu}_L{\nu_L}^c + \overline{\nu_L}^c\nu_L) - \frac{m_R}{2}(\overline{\nu}_R{\nu_R}^c + \overline{\nu_R}^c\nu_R). \tag{1.5}$$

In this case the neutrino fields ν_R and ν_L, according to the Majorana condition, are linked via this relation:

$$\nu_R = {\nu_L}^c. \tag{1.6}$$

The first term in Eq. 1.3 destroys a left-handed neutrino and creates a right-handed neutrino, which means that lepton number is conserved in the Dirac mass term. Conversely,

the first term in Eq. 1.5 creates two left-handed neutrinos out of vacuum, so the lepton number is violated by two units by the Majorana mass term. If the lepton number is violated, there is no quantum number to distinguish the neutrinos from anti-neutrino, and thus the neutrino is a Majorana particle.

Combining Eq. 1.3 and Eq. 1.5 to have Dirac-Majorana mass terms, one obtains:

$$\mathcal{L}_{D+M} = -\frac{m_L}{2}(\overline{\nu}_L\nu_L^c + \overline{\nu}_L^c\nu_L) - \frac{m_R}{2}(\overline{\nu}_R\nu_R^c + \overline{\nu}_R^c\nu_R) - m_D(\overline{\nu}_R\nu_L - \overline{\nu}_L\nu_R). \tag{1.7}$$

that can be simplified to

$$\mathcal{L}_{D+M} = -\frac{1}{2}\overline{N_L}^c\mathcal{M}N_L + h.c., \tag{1.8}$$

where $\mathcal{M}$ is the symmetric mass matrix

$$\mathcal{M} = \begin{pmatrix} m_L & m_D \\ m_D & m_R \end{pmatrix} \tag{1.9}$$

and N_L is the column matrix of the left-chiral neutrino

$$N_L = \begin{pmatrix} \nu_L \\ \nu_R^c \end{pmatrix} \tag{1.10}$$

Diagonalizing the matrix $\mathcal{M}$ by a unitary matrix $\mathcal{U}$ will give us the fields ν and N with definite masses:

$$\mathcal{U}^T\mathcal{M}\mathcal{U} = \tilde{\mathcal{M}} = \begin{pmatrix} m_1 & 0 \\ 0 & M_1 \end{pmatrix} \tag{1.11}$$

and

$$\begin{pmatrix} \nu_L \\ \nu_R^c \end{pmatrix} = \mathcal{U}\begin{pmatrix} \nu \\ N \end{pmatrix} \tag{1.12}$$

The Lagrangian will look like

$$\mathcal{L}_{D+M} = -\frac{1}{2}\begin{pmatrix} \overline{\nu} & \overline{N} \end{pmatrix}\tilde{\mathcal{M}}\begin{pmatrix} \nu \\ N \end{pmatrix} + h.c., \tag{1.13}$$

The see-saw mechanism, introduced by Yanagida and Gell-mann, provides an explanation to why neutrinos have such a small mass compared to the other elementary particles. In this case:

$$m_D << m_R, \quad m_L = 0 \tag{1.14}$$

and we obtain

$$m_1 \simeq \frac{m_D^2}{m_R} \tag{1.15}$$

$$m_2 \simeq m_R \tag{1.16}$$

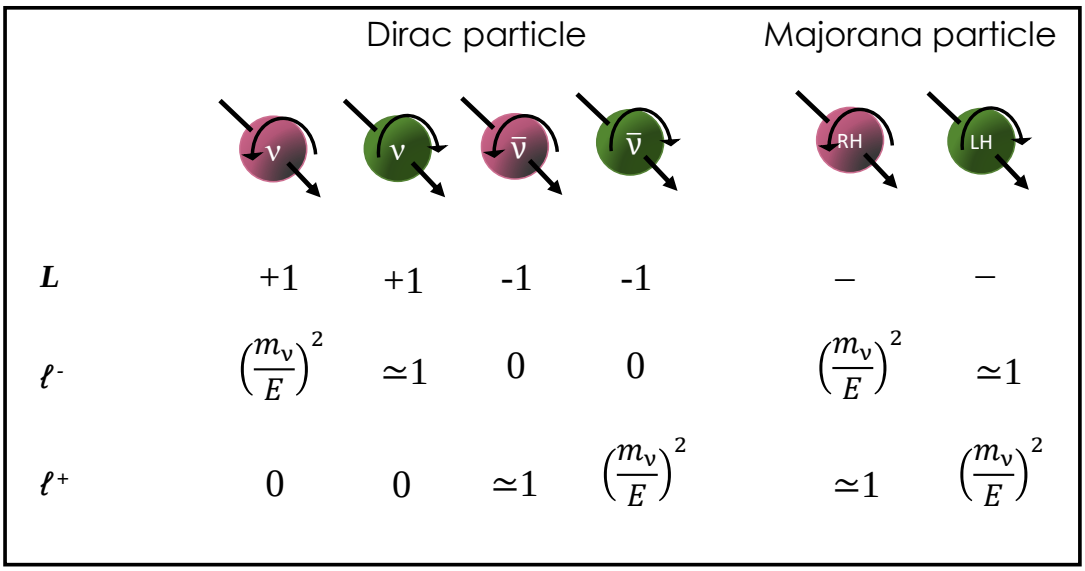

Figure 1.1 – Dirac and Majorana neutrino states. There are four Dirac neutrino states: right and left-handed neutrino, right and left-handed anti-neutrino. There are only two neutrino states for a Majorana particle, a left and a right-handed particle. L corresponds to the lepton number and ℓ to the charged leptons.

so there is a heavy neutrino state N with a mass m_R connected to a very light neutrino state ν with a mass $\frac{m_D^2}{m_R}$.

Dirac and Majorana neutrino states

The massive neutrinos can be described and differentiated by their helicity. A given helicity state is a superposition of the negative and positive chirality states. The Dirac neutrino consists of four different states. The Dirac neutrino produces only negatively-charged leptons and the Dirac anti-neutrino produces only positively-charged leptons, conserving the lepton number. The left-handed neutrino and the right-handed anti-neutrino contribute the most in producing charged leptons, as indicated in Fig. 1.1. There are only two neutrino states for Majorana particles, since states with equal helicities are indistinguishable because of lepton number violation, i.e. left-handed Majorana neutrinos and left-handed Majorana anti-neutrinos are indistinguishable (neutrino identical to anti-neutrino). In contrast to Dirac neutrinos, Majorana neutrino can generate both positively and negatively-charged leptons, with a higher production rate for the same-sign lepton ($\simeq 1$).

It is a very challenging task to investigate whether neutrinos are Majorana or Dirac particle. Most of the observed neutrinos are ultra-relativistic ($m/E << 1$), and in this case there is no distinction between a Dirac and a Majorana neutrino [12]. Neutrinoless double-beta decay is considered, at the present time, the only viable approach to answer this question (Chapter 2).

1.3 Neutrino mixing

Neutrino flavour oscillations were confirmed by several experiments, and in particular for the first time by Super-Kamiokande for atmospheric neutrinos, SNO for solar neutrinos (explaining coherently the results previously observed by other searches in terms of flavour oscillations), KamLAND for reactor neutrinos [13] and K2K for accelerator neutrinos [14]. After these pioneering investigations, many other experiments observed and studied deeply this phenomenon from these neutrino sources. As they propagate, neutrinos can change from one flavour to another. This showed that neutrinos have a non-zero mass and are mixed particles. Neutrino mixing implies that flavour eigenstates ν_l are a superposition of the mass eigenstates ν_i and are expressed as:

$$\nu_l = \sum_{i=1}^{3} U_{li}\nu_i \qquad l = e, \nu, \tau \tag{1.17}$$

where U is Pontecorvo-Maki-Nkagawa-Sakata (PMNS) lepton-mixing matrix:

$$U = \begin{pmatrix} c_{12}c_{13} & s_{12}c_{13} & s_{13}e^{-i\delta} \\ -s_{12}c_{23} - c_{12}s_{23}s_{13}e^{i\delta} & c_{12}c_{23} - s_{12}s_{23}s_{13}e^{i\delta} & s_{23}c_{13} \\ s_{12}s_{23} - c_{12}c_{23}s_{13}e^{i\delta} & -c_{12}s_{23} - s_{12}c_{23}s_{13}e^{i\delta} & c_{23}c_{13} \end{pmatrix} \cdot \begin{pmatrix} 1 & 0 & 0 \\ 0 & e^{i\alpha_2/2} & 0 \\ 0 & 0 & e^{i\alpha_3/2} \end{pmatrix} \tag{1.18}$$

where, $c_{ij} = \cos\theta_{ij}$, $s_{ij} = \sin\theta_{ij}$. θ_{12}, θ_{23} and θ_{13} the three mixing angles. δ is the Dirac CP-violating phase and α_i are the Majorana phases.

Neutrino oscillation experiments provide the squared-mass differences of the three ν_i mass eigenstates. The probability of neutrino oscillation from a flavour α to another β is given by:

$$\begin{aligned} P(\nu_\alpha \to \nu_\beta) = \delta_{\alpha\beta} &- 4\sum_{i>j} Re(U^*_{\alpha i}U_{\beta i}U_{\alpha j}U^*_{\beta i})\sin^2\Phi_{ij} \\ &+ 2\sum_{i>j} Im(U^*_{\alpha i}U_{\beta i}U_{\alpha j}U^*_{\beta i})\sin^2 2\Phi_{ij} \end{aligned} \tag{1.19}$$

where

$$\delta_{\alpha\beta} = \begin{cases} 1, & \alpha = \beta \\ 0, & \alpha \neq \beta, \end{cases}$$
$$\Phi_{ij} = \frac{\Delta m^2_{ij} L}{4E_\nu} \tag{1.20}$$

E is the energy of the neutrino, L is the distance between the neutrino source and the detector and $\Delta m^2_{ij} = m^2_j - m^2_i$.

A good approximation for many actual physical situations is provided by a simplified

Parameter	Best fit	3σ range
$\Delta m^2_{12} = \Delta m^2_{sol}$ (IH or NH) [10^{-5} eV^2]	7.34	6.92-7.90
$sin^2\theta_{12}$ (IH or NH) [10^{-1}]	3.05	2.65-3.47
$\lvert\Delta m^2_{13}\rvert = \lvert\Delta m^2_{atm}\rvert$ (IH) [10^{-3} eV^2]	2.465	2.374-2.556
$\lvert\Delta m^2_{13}\rvert = \lvert\Delta m^2_{atm}\rvert$ (NH) [10^{-3} eV^2]	2.485	2.389-2.578
$sin^2\theta_{23}$ (IH) [10^{-1}]	5.51	4.39-5.96
$sin^2\theta_{23}$ (NH) [10^{-1}]	5.45	4.36-5.95
$sin^2\theta_{13}$ (IH) [10^{-2}]	2.23	2.03-2.43
$sin^2\theta_{13}$ (NH) [10^{-2}]	2.22	2.01-2.41

Table 1.1 – Oscillation parameters for the best fit and 3σ range for the 3 ν oscillation taken from [15]. IH and NH stand for inverted and normal hierarchy order (see Section 1.3.1).

case with only two neutrino flavours:

$$P(\nu_\alpha \to \nu_\beta) = \sin^2 2\theta_{ij} \sin^2 \left[1.27 \frac{\Delta m^2 L}{E}\right] \tag{1.21}$$

So, the survival probability of a certain neutrino flavour is given by:

$$P(\nu_\alpha \to \nu_\alpha) = 1 - \sin^2 2\theta_{ij} \sin^2 \left[1.27 \frac{\Delta m^2 L}{E}\right] \tag{1.22}$$

The neutrino mixing parameters, θ_{ij} and m_{ij} are obtained experimentally exploiting the aforementioned different neutrino sources: solar, atmospheric, reactor and accelerator sources. The recent (2020) measured values of the neutrino mixing parameters are shown in the Table 1.1.

1.3.1 Neutrino mass hierarchy

It is worth noting that there are only 2 independent mass splittings. The smaller one is often defined "solar mass splitting" and the larger one "atmospheric mass splitting". The solar mass splitting, Δm^2_{12}, is measured from experiments using solar and reactor neutrino, and the atmospheric mass splitting, Δm^2_{13}, is measured from experiments using atmospheric and accelerator neutrinos. The sign of Δm^2_{13} is unknown, leading to two possible neutrino mass hierarchies:

Normal Hierarchy

$$m_1 < m_2 \ll m_3 \ : \begin{cases} m_2 = \sqrt{m_1^2 + \Delta m^2_{sol}} \\ m_3 = \sqrt{m_1^2 + \Delta m^2_{atm} + \Delta m^2_{sol}/2} \\ m^2_{sol} << m^2_{atm} \Rightarrow m_3 \simeq \sqrt{\Delta m^2_{atm}} \end{cases} \tag{1.23}$$

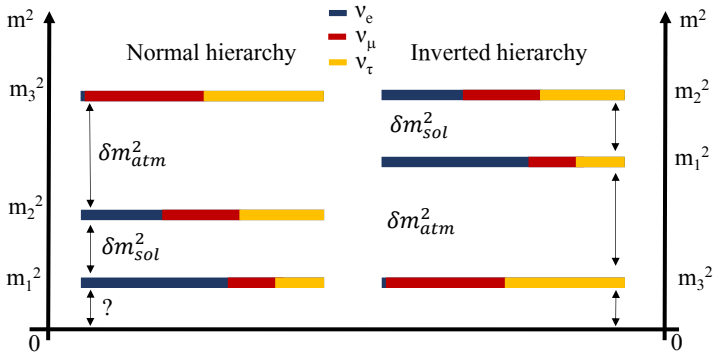

Figure 1.2 – Normal and inverted hierarchies of the mass patterns and neutrino flavor composition of the mass eigenstates.

Inverted Hierarchy

$$m_3 \ll m_1 < m_2 \ : \begin{cases} m_1 = \sqrt{m_3^2 + \Delta m^2_{atm} - \Delta m^2_{sol}} \simeq \sqrt{\Delta m^2_{atm}} \\ m_2 = \sqrt{m_3^2 + \Delta m^2_{atm}} \simeq \sqrt{\Delta m^2_{atm}} \\ m_3 =<< \sqrt{\Delta m^2_{atm}} \end{cases} \tag{1.24}$$

If the lightest neutrino mass is much larger than $\sqrt{\Delta m^2_{atm}}$, implying that $m_1 \simeq m_2 \simeq m_3$, this situation is usually referred to as **Quasi-Degenerated Hierarchy**, even if actually one of the two situations mentioned before still holds.

1.4 Neutrino mass measurement

Evidently, neutrino has a non-zero mass, however the absolute mass scale is still unknown just like the mass hierarchy. As pointed out above, neutrino oscillation experiments measure only the mass squared differences and not the absolute mass scale. There are however other ways to measure the neutrino mass.

tritium beta decay:

The kinematics of tritium beta-decay gives a way to determine the mass of the neutrino, which can be deduced from the shape of the β-spectrum close to the endpoint of Fig. 1.3. The decay equation is as follows:

$$^3_1H \rightarrow ^3_1 He^{+1} + e^- + \overline{\nu}_e \tag{1.25}$$

tritium beta decay is studied because of the following favorable features:

- A relatively short half-life (12.32 yr), which helps in getting a high enough statistics.
- A small Q_β (18.6 keV): more events fall in the high energy range because of the smaller phase space.
- Relatively simple nuclear structure for ^{3}H and molecular structure for $^3H_2$.

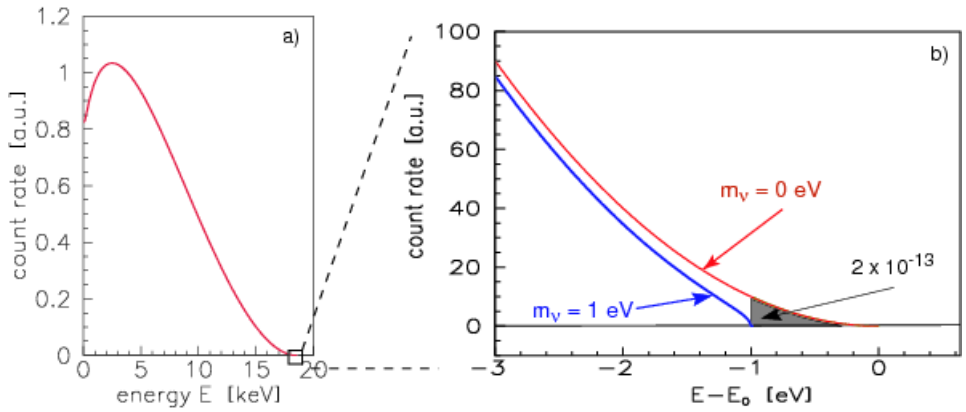

Figure 1.3 – Spectrum of the tritium beta decay. (*left*) The whole energy spectrum. (*right*) Endpoint of the spectrum. The fraction of events contained in the last 1 eV is very low (2×10^{-13}). Figure from [16].

The energy carried by the electron is equal to:

$$E_e = (E_i - E_f) - E_\nu \tag{1.26}$$

where m_i and m_f are the initial and final energy of the decaying atom respectively and E_ν is the neutrino energy. If $m_\nu = 0$, the endpoint of the β-spectrum will be at $Q_\beta = 18.6$ keV. A finite value of the neutrino mass will distort the shape of the spectrum in its final part, moving the endpoint to a lower energy with respect to Q_β, and the difference between the new endpoint and Q_β will be equal to the neutrino mass. Considering the very small mass of neutrino, the discrepancy will be very small. For example, the fraction of counts in the zero-neutrino-mass spectrum that occur in the last 1 eV interval is only 2×10^{-13}. The neutrino mass determined in this approach is a sort of effective mass, corresponding to an incoherent sum of the three neutrino masses depending on the lepton mixing matrix elements:

$$m_\beta^2 = \sum_{i=1}^{3} |U_{ei}|^2 m_i^2 \tag{1.27}$$

Very recently, the KATRIN collaboration reached the currently most stringent upper limit on the effective neutrino mass [17]:

$$m_\beta < 1.1\, eV \tag{1.28}$$

at 90% confidence level (C.L.). The KATRIN experiment aims at an ultimate limit of m_β<0.2 eV at 90% C.L., better than the results from Mainz [18] and Troistk [19] by an order of magnitude ($m_\beta \lesssim 2$ eV).

Cosmology:

Constraints on neutrino masses can also be obtained from cosmology, like the measurement of the temperature and polarization anisotropies of the Cosmic Microwave Background (CMB), or the distribution of large scale structures. The sum of the three neutrino mass states can be inferred from cosmology:

$$\sum m_\nu = m_1 + m_2 + m_3 \tag{1.29}$$

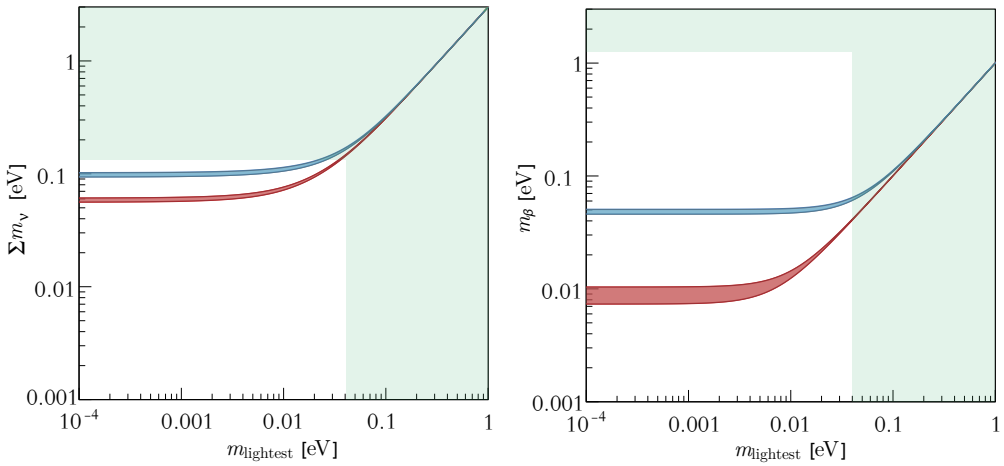

Figure 1.4 – Constraints on the lightest neutrino mass $m_{lightest}$ coming from cosmology (*left*) and tritium β-decay experiments (*right*) based on the neutrino mixing parameters in Table 1.1 (3σ ranges). Blue (red) band corresponds to the inverted (normal) ordering allowed regions. The excluded regions are highlighted with a green band.

However the bound is model dependent. The tightest bound found by PLANCK [20] is $\sum m_\nu < 0.12$ eV.

Neutrinoless double-beta decay:

Neutrinoless double-beta decay ($0\nu2\beta$), the main subject of this work, is a hypothetical nuclear transition. If the process is mediated by the so-called "mass mechanism", it provides the effective neutrino mass defined by the following equation:

$$\langle m_{\beta\beta} \rangle = \sum_{i=1}^{3} U_{ei}^2 m_i \tag{1.30}$$

Combining neutrino mass information from different sources give hints about the absolute mass scale of the neutrino and other neutrino properties. In particular, this is the only known method that, at least in principle, can determine the value of the Majorana phases.

Fig. 1.4 (*left*) shows the relationship between $\sum m_\nu$ and the lightest neutrino mass $m_{lightest}$ obtained from cosmology. The blue (red) band corresponds to the inverted (normal) ordering where m_3 (m_1) is the lightest. The upper limit on $\sum m_\nu < 0.12$ eV is given by the horizontal green band. The allowed region for the neutrino mass obtained from tritium β-decay is shown in Fig. 1.4 (*right*), where the upper limit on m_β is indicated by the horizontal green band. In the quasi-degenerate case, the upper limit on $m_{lightest} \simeq \sum m_\nu/3 \leq 0.04$ eV is given by the vertical green band in Fig. 1.4 (*left* and *right*). Fig. 1.5 shows the effective Majorana neutrino mass extracted from $0\nu\beta\beta$ as a function of the $m_{lightest}$.

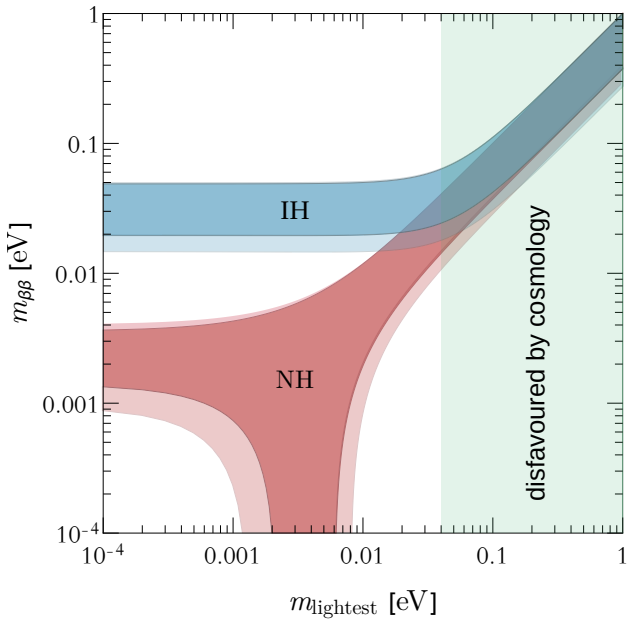

Figure 1.5 – Allowed region for the effective Majorana neutrino mass as a function of the lightest neutrino mass. The red and blue regions indicate the normal and inverted hierarchy, respectively. The green band is excluded by cosmology.

Conclusions

A variety of running experiments aim to probe the mysteries of neutrino: its nature (Dirac or Majorana), the mass hierarchy, the absolute mass scale, CP violation in the lepton sector and whether sterile neutrinos exist. Each of the experiments listed in section 1.4 depends on some of these unknowns. Only ($0\nu\beta\beta$) is sensitive to all of them. $0\nu\beta\beta$ is possible only if neutrino is a Majorana particle. The neutrino mass is associated with the half-life of this decay. The effective mass measured from the half-life has two possible regions defined by the hierarchy of the neutrino mass. That is what makes $0\nu\beta\beta$ very interesting, by letting us explore the neutrino from different perspectives. The next chapter will go through this decay in details.

Chapter 2

Neutrinoless double-beta decay

2.1 The two double-beta decay modes

Double-beta decay ($2\nu\beta\beta$), proposed by M. Goeppert-Mayer in 1935 [21], is a very rare second order nuclear transition in which a nucleus (A, Z) decays into an isobar $(A, Z+2)$ with two more protons accompanied by the emission of two electrons and 2 anti-neutrinos:

$$(A, Z) \rightarrow (A, Z + 2) + 2e^- + 2\overline{\nu}_e \tag{2.1}$$

The decaying nucleus is an even-even one, in which decaying by a single beta decay is kinematically forbidden since the final state has a higher energy than the initial state due to the nuclear pairing force. 35 nuclei in nature are capable of undergoing $2\nu\beta\beta$ and only 11 have been observed experimentally shown in Table 2.1 (there are also 3 observed double electron capture on: ^{130}Ba, ^{78}Kr and ^{124}Xe). Two double-beta decay isotopes are studied in this thesis, ^{100}Mo and ^{130}Te. The decay schemes are shown in Fig. 2.1.

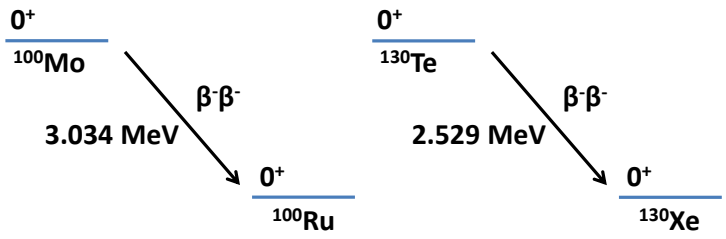

Figure 2.1 – Schematic diagram of energy levels involved in double-beta decay for Molybdenum and Tellurium.

In 1939, W. H. Furry proposed that double-beta decay could occur without neutrino emission [22], i.e. neutrinoless double-beta decay ($0\nu\beta\beta$), after E. Majorana suggested that neutrino and anti-neutrino may be identical [11]:

$$(A, Z) \rightarrow (A, Z + 2) + 2e^- \tag{2.2}$$

This decay, on the other hand, is forbidden in the Standard Model because it leads to lepton number violation by two units [23–26]. Feynman diagrams for $0\nu\beta\beta$ and $2\nu\beta\beta$ are shown in Fig. 2.2. $0\nu\beta\beta$ can be described by a virtual Majorana neutrino exchange

Isotope	Isotopic abundance (%)	$T^{2\nu}_{1/2}$ (yr)	$Q_{\beta\beta}$ (keV)
^{48}Ca	0.19	$5.3^{+1.2}_{-0.8} \times 10^{19}$	4272
^{76}Ge	7.73	$1.88 \pm 0.08 \times 10^{21}$	2039
^{82}Se	8.73	$0.87^{+0.02}_{-0.01} \times 10^{19}$	2995
^{96}Zr	2.8	$2.3 \pm 0.2 \times 10^{19}$	3350
^{100}Mo	9.82	$7.06^{+0.15}_{-0.13} \times 10^{18}$	3034
^{116}Cd	7.49	$2.69 \pm 0.09 \times 10^{19}$	2813
^{128}Te	31.74	$2.25 \pm 0.09 \times 10^{24}$	865.87
^{130}Te	34.08	$7.91 \pm 0.21 \times 10^{20}$	2527
^{136}Xe	8.86	2.18×10^{21}	2457
^{150}Nd	5.64	$9.34 \pm 0.65 \times 10^{18}$	3371
^{238}U	99	$2.0 \pm 6 \times 10^{21}$	~1100

Table 2.1 – Decaying nuclei, isotopic abundances, half-lives and Q-values for the observed two-neutrino double-beta transitions [27].

at the two vertices. The neutrino created at one vertex has a higher probability to be a right-handed than a left-handed particle. In case it is created as a right-handed neutrino, it will be absorbed in the second vertex with a flip in helicity to a left-handed neutrino. If it is created as a left-handed neutrino, it will be absorbed without a helicity flip in the second vertex. This is possible only if neutrinos are massive Majorana particles. Helicity flip is rare, which leads to a very low rate for the process.

Experiments searching for double-beta decay measure the sum of the energies of the two emitted electrons. In case of $2\nu\beta\beta$, the energy is shared between the two electrons and the two anti-neutrinos, which gives a continuous energy spectrum from 0 to the Q-value. The kinetic energy of the daughter nucleus is negligible due its heaviness in comparison to the electrons. The signal for $0\nu\beta\beta$ is a monochromatic peak (which will be widen depending on the energy resolution of the detector) at the Q-value of the transition, which equals the sum of the kinetic energy of the two emitted electrons [23, 24, 28]. Fig. 2.3 shows the energy spectrum for the two double-beta decay modes. Table 2.1 shows the Q-values, $T^{2\nu}_{1/2}$ and the isotopic abundances of the $\beta\beta$ isotopes.

There are many mechanisms that can lead to the existence of $0\nu\beta\beta$. The mechanism that is shown in Fig. 2.2 consists of an exchange of a light Majorana neutrino. This mechanism requires the least modifications of the SM by introducing a Majorana mass term that will produce light Majorana neutrinos (section 1.2). There are more exotic mechanisms which can induce $0\nu\beta\beta$: left-right symmetry; light or heavy sterile neutrinos; supersymmetry with R-parity violation; GUTs; extended technicolor or compositeness models [29]. In case of light Majorana neutrino exchange mechanism, the decay rate of $0\nu\beta\beta$, $T^{0\nu}_{1/2}$, is expressed as follows:

$$(T^{0\nu}_{1/2})^{-1} = G_{0\nu} \, |M^{0\nu}|^2 \left(\frac{m_{\beta\beta}}{m_e} \right)^2 \tag{2.3}$$

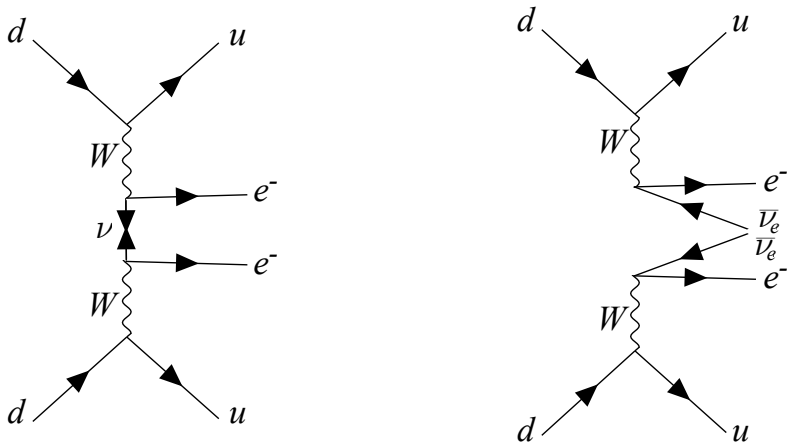

Figure 2.2 – Feynman diagrams at the quark level for ($0\nu\beta\beta$)(left) and for ($2\nu\beta\beta$) (right).

where $T^{0\nu}_{1/2}$ is the half-life, $G_{0\nu}$ is a phase space factor, $M^{0\nu}$ is the nuclear matrix elements (NME) and $m_{\beta\beta}$ is the effective Majorana neutrino mass defined as:

$$\begin{aligned} m_{\beta\beta} &= \left| \sum_{i=1}^{3} U_{1i}^2 m_{\nu_i} \right| \\ &= \left| cos^2\theta_{12} cos^2\theta_{13} m_1 + sin^2\theta_{12} cos^2\theta_{13} e^{i\alpha_2} m_2 + sin^2\theta_{13} e^{-i(2\delta-\alpha_3)} m_3 \right| \end{aligned} \tag{2.4}$$

where θ_{ij} are the mixing angles, α_i are the Majorana phases and δ is the Dirac CP-violating phase. From a $0\nu\beta\beta$ rate measurement (Eq. 2.3), the value of $m_{\beta\beta}$ can be inferred with some uncertainties from NME. In case there is no observation of $0\nu\beta\beta$, the results are interpreted in terms of an upper bound on $m_{\beta\beta}$. The relationship between $m_{\beta\beta}$ and $m_{lightest}$ is shown in Fig. 2.4. The blue (red) band corresponds to the inverted (normal) hierarchy region where the m_3 (m_1) is the lightest neutrino. The width of the bands is due to the uncertainties in the measured oscillation parameters (Table 1.1) and the unknown CP-violation phases. The vertical bars correspond to the upper excluded limits achieved by various experiments. The effective Majorana mass $m_{\beta\beta}$ can provide information about the absolute mass scale and the mass hierarchy using Eq. 2.4 and by substituting the appropriate approximation for each neutrino mass (Eq. 1.23 or Eq. 1.24) based on the right hierarchy.

2.1.1 Nuclear matrix elements

The nuclear matrix elements (NME) presents the main limiting factor for evaluating the half-life $T^{0\nu}_{1/2}$ precisely, which in turn influences the accuracy for measuring the effective Majorana mass $m_{\beta\beta}$. If $0\nu\beta\beta$ is observed and the value of $m_{\beta\beta}$ is inaccurate, then no precise conclusion can be drawn on neutrino masses, CP violation phases and the mass hierarchy. In addition, comparing the results and the sensitivities of different experiments will not be precise. The NME is obtained theoretically and it in-codes all the nuclear structure effects. It is expressed as the sum of the two terms, Gamow-Teller (GT) and Fermi (F):

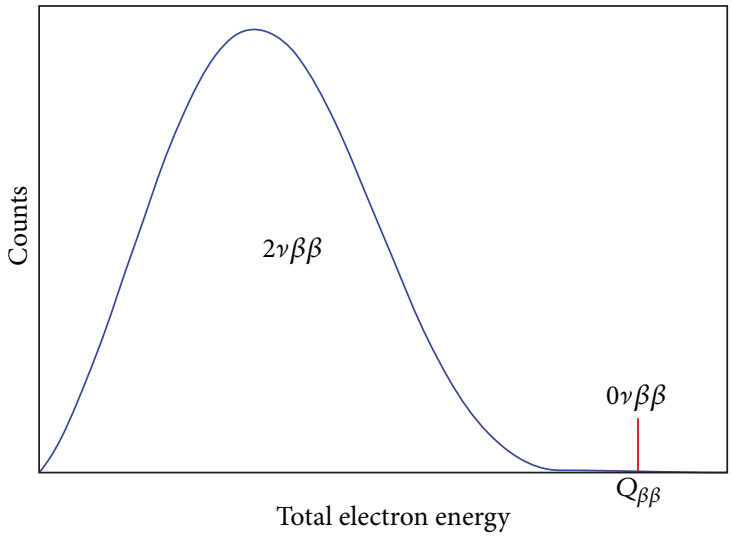

Figure 2.3 – Energy spectra of $2\nu\beta\beta$ and $0\nu\beta\beta$.

$$M^{0\nu} = M^{0\nu}_{GT} - \frac{g_V^2}{g_A^2} M^{0\nu}_F \tag{2.5}$$

where g_V and g_A are the vector and the axial coupling constants respectively. The value of g_A is usually taken equal to ~ 1.27 obtained from the free neutron decay into free proton. There is still doubts on whether g_A is quenched as in $2\nu\beta\beta$, adding further uncertainties.
Different nuclear-structure approaches are used to compute the NME:

- Quasi-particle random phase approximation (QRPA): calculations include large number of particles, but with limited number of correlations. The pairing of proton-proton and neutron-neutron are taken into account [30].
- Nuclear shell model (NSM): considers all possible correlations within its configuration space, but with very restricted single particles which are the nucleons near the Fermi level. Complications arise when considering all possible configurations for medium to heavy nuclei as double-beta decay isotopes because of the factorial growth of the possible configurations [31].
- Interacting boson model (IBM): It is based on NSM with reduced complexity by combining the nucleons in pairs. It is suitable for describing intermediate and heavy nuclei [32].

2.2 Sensitivity

Maximizing the sensitivity of the experiment is the ultimate goal to be able to explore the very rare hypothetical neutrinoless double-beta decay. Several factors must be taken into account when building a double-beta decay experiment: the mass of the double-beta decay isotope, energy resolution, duration of the experiment, background counts in the region of interest (ROI) and some other factors mentioned later. As pointed out, the

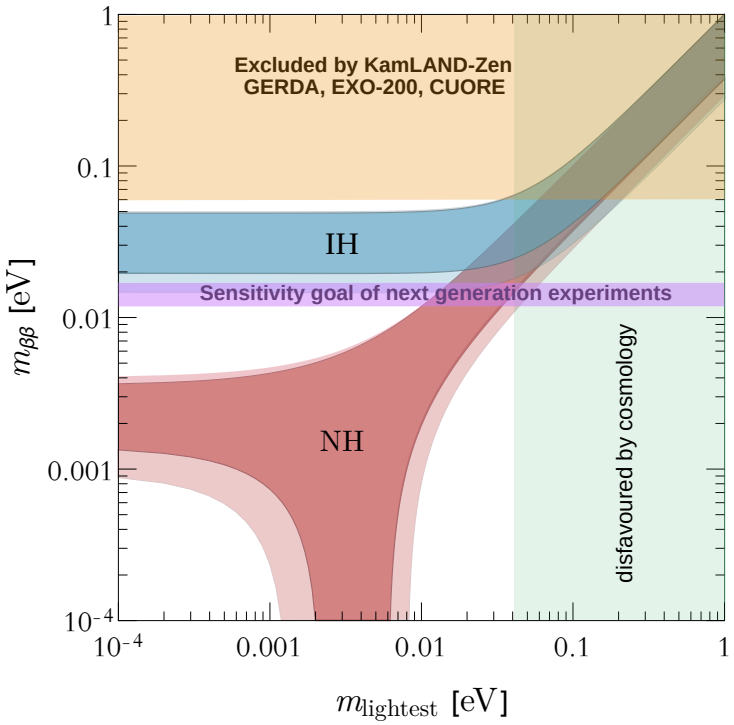

Figure 2.4 – Allowed region for the effective Majorana neutrino mass as a function of the lightest neutrino mass. The red and blue regions indicate the normal and inverted hierarchy, respectively. The green band is the region excluded by cosmology. The experimental situation for $0\nu\beta\beta$ (present and future) is shown.

experiments are searching for a peak at the $Q_{\beta\beta}$ of the process. If this feature is observed, the half-life can be evaluated as:

$$T_{1/2}^{0\nu} = \ln 2 \cdot \epsilon \cdot T \frac{N_{\beta\beta}}{N_{peak}} \tag{2.6}$$

where ϵ is the detection efficiency, T is the live-time of the measurement, $N_{\beta\beta}$ is the number of $\beta\beta$ source nuclei and N_{peak} is the number of observed $0\nu\beta\beta$ events.

Till now, no peak that accounts for the decay has been discovered. In this case, an upper limit is set on $m_{\beta\beta}$ and therefore a region from the top of Fig. 2.4 is excluded. The sensitivity is then expressed as:

$$S^{0\nu} = \ln 2 \cdot \epsilon \cdot \frac{x\eta N_A}{A} \cdot \sqrt{\frac{M \cdot T}{BI \cdot \Delta E}} \tag{2.7}$$

where x is the number of isotope atoms in the molecule, η is the isotopic abundance, N_A is Avogadro's number, A is the molecular weight, M is the $\beta\beta$ isotope mass, T is the effective duration of the physics data taking, ΔE is the energy resolution of the detector

and BI is known as the background index and is defined as:

$$BI = \frac{N_B}{\Delta E \cdot M \cdot T} \text{ counts/(keV kg yr)} \tag{2.8}$$

where N_B is the number of background events. The major goal of the experiments is to reach an extremely low background level so that the number of background events in the ROI is zero:

$$BI \cdot \Delta E \cdot M \cdot T \lesssim 1 \tag{2.9}$$

In this case, the background term in Eq. 2.7 is replaced with N_L, the number of excluded events in the ROI at a given confidence level (C.L.) when zero counts are observed, to get:

$$S^{0\nu} = \ln 2 \cdot \epsilon \cdot \frac{x\eta N_A}{A} \cdot \frac{M \cdot T}{N_L} \tag{2.10}$$

For a 90 % C.L., N_L is equal to 2.3 [33]. In the zero-background case, the sensitivity grows linearly with the increase of the $\beta\beta$ isotope mass. However in the non-zero background case, the sensitivity is proportional to the square root of the isotope mass, which means that the experiment is not fully exploiting the large (and expensive) isotope mass. From the above discussion, we deduce that a successful double-beta decay experiment must satisfy four main requirements to increase the sensitivity:

- An ultra low background
- An excellent energy resolution
- A large $\beta\beta$ isotope mass
- Very long live-time

2.3 Experimental challenges

The detector design of a double-beta decay experiment is a very challenging task. Below we list the most essential detector features:

2.3.1 Isotope choice

The candidate double-beta decay isotope to be chosen is based on some considerations to be taken into account to increase the sensitivity of the experiment:

- **$Q_{\beta\beta}$:** The most promising and desirable isotopes to study are those with a high $Q_{\beta\beta}$, at least higher than 2 MeV or, even better, above the natural γ radioactivity (^{208}Tl, 2.615 MeV), since this will imply less background in the ROI. In addition, this leads also to a higher decay probability because the phase space factor has a leading term proportional to Q^5. The most favourable candidates are: ^{48}Ca, ^{76}Ge, ^{82}Se, ^{100}Mo, ^{116}Cd, ^{124}Sn, ^{130}Te, ^{136}Xe and ^{150}Nd. The double-beta decay isotopes $Q_{\beta\beta}$ is shown in Fig. 2.5. Above 3.27 MeV, the region is also free from ^{214}Bi β spectra. However the isotopes with a Q-value above this point have difficulties for enrichment, which is on the other hand necessary because of the low isotopic abundance.

- **Nuclear matrix elements:** NME is the major source of uncertainties when computing the neutrino masses from the half-life. Isotopes with higher NME have a higher decay rate of $0\nu\beta\beta$.
- **Natural isotopic abundance:** High isotopic abundance (IA) means low cost for the experiment in terms of enrichment if needed and a more compact apparatus with a higher mass of the source (double-beta-decay isotope) with respect to the total mass. The IAs of the most interesting candidates are shown in Table 2.1.

Other factors to be taken into consideration is the possibility of enrichment and the available detector technology to study the isotope.

2.3.2 Energy resolution

A high energy resolution is a crucial condition to increase the sensitivity of the experiment. It helps reduce the source of background coming from $2\nu\beta\beta$, also it improves the signal-to-noise ratio in the ROI by narrowing the ROI which leads to a reduction in the background level.

2.3.3 Low background

A zero-background experiment is a very desirable feature for future $0\nu\beta\beta$ searches. There are different sources of background that can be controlled:

- Choosing radio-pure materials to build the detector and its surrounding is mandatory to have a low radioactive contamination that are mainly due to ^{208}Tl and ^{214}Bi from the ^{232}Th and ^{238}U decay chain.
- External natural γ radioactivity from the ^{232}Th and ^{238}U decay chain can be stopped by using a dense materiel (high Z) as a shield, such as lead.
- Radon, a decay product of thorium and uranium, is a source of background that can contaminate the detector materials. Flushing the detector with nitrogen and working in an anti-radon environment can mitigate radon contamination.
- Cosmic muons can swamp the ROI if they are not stopped. Running the experiment in underground laboratories will reduce muon flux. High-energy secondary particles can also be produced after muon interaction. Adding a veto system and active shields can eliminate background from residual muons and the secondary particles interaction.
- Cosmic neutrons can activate detector materials and produce radioactive nuclei. The activation can be reduced storing the material underground. Environmental neutrons can induce the emission of high energy γ's that can contribute to the background. Polyethylene or any hydrogenous material can shield against environmental neutrons.

2.4 Current and future experiments

There are many experiments with different technologies searching for $0\nu\beta\beta$. The current experiment are very close to reach the top of the inverted hierarchy band. In five years,

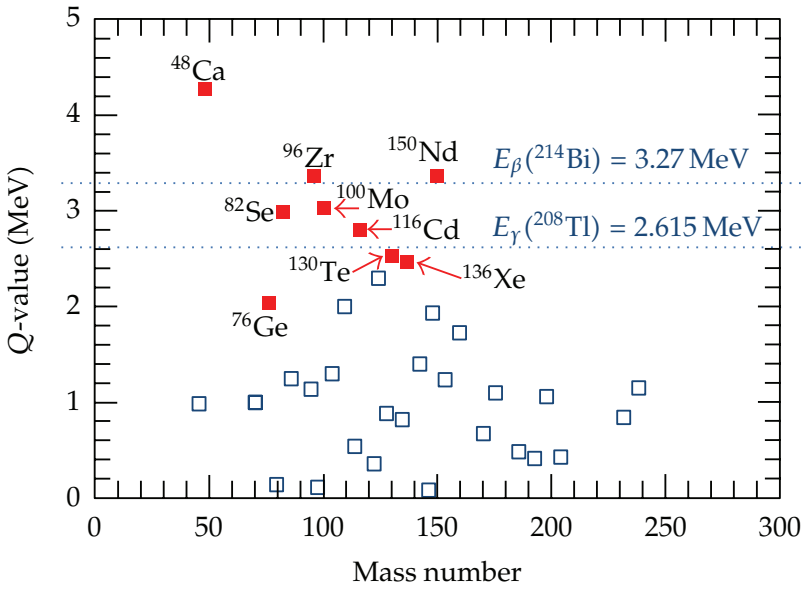

Figure 2.5 – Double-beta decay candidates and their $Q_{\beta\beta}$. Red squares indicate the most promising candidates. Two energy markers showing the upper limits of the γ environmental radioactivity (2.615 MeV) and of the ^{222}Rn-induced radioactivity (3.27 MeV) are shown.

several experiments will start to go deep inside the region. In 10 year, the goal is to fully cover it. We list the most relevant current and future experiments.

2.4.1 High purity germanium detectors (HPGe)

GERDA

GERDA (GERmanium Detector Array), located in the underground Laboratori Nazionali del Gran Sasso (LNGS) in Italy, is an experiment based on 37 enriched high purity germanium detectors (HPGe) (semi-coaxial and point-contact BeGe detectors) with a total mass of 35.6 kg enriched to 87% in ^{76}Ge. The detectors are placed in a liquid argon (LAr) cryogenic bath, which is situated in turn inside a water tank. The setup is equipped with photomultipliers (PMTs) to detect the scintillation provided by LAr after radiation interaction, and it serves as an internal active veto system to reject background radiation that deposits energy in LAr in coincidence with the Ge crystals. The purified water also shields against external radiation and neutrons. The features of HPGe detectors are the intrinsic purity of Ge, excellent energy resolution and high detection efficiency (source=detector). GERDA holds the record for the lowest background in double-beta decay experiments, with a BI= $5.6^{+3.4}_{-2.4}\cdot 10^{-4}$ counts/(keV kg yr) and an energy resolution of 3.0 keV (FWHM) at $Q_{\beta\beta}$= 2039 keV. The half-life 90% confidence level (C.L.) lower limit is derived to be $T^{0\nu}_{1/2} > 1.8 \cdot 10^{26}$ yr for a total exposure of 127.2 kg·yr [34].

MAJORANA

The MAJORANA demonstrator, located at the Sanford Underground Research Facility (SURF) in the USA, is also searching for $0\nu\beta\beta$ in ^{76}Ge using P-type point-contact (PPC) HPGe detectors (25 kg of ^{76}Ge). It is more traditional compared to GERDA, as it uses

inner copper shields, lead shield and muon veto. With a total enriched Ge exposure of 26 kg·yr, the MAJORANA demonstrator achieved a lower limit on the half-life of $0.27 \cdot 10^{26}$ yr at 90% C.L. (median sensitivity $0.48 \cdot 10^{26}$ yr at 90% C.L.) with an excellent energy resolution 2.5 keV at $Q_{\beta\beta}$ [35].

LEGEND

LEGEND (The Large Enriched Germanium Experiment for Neutrinoless Double-Beta Decay) is a next-generation $0\nu\beta\beta$ experiment based on ^{76}Ge. It builds on the two successful GERDA and MAJORANA experiments and use PPC (inverted-coaxial) detectors which have several advantages: easiness of fabrication; pulse shape discrimination (PSD) capability to reject background; and very low capacitance. The LEGEND strategy is to combine the best features of GERDA and MAJORANA aiming to increase the sensitivity to 10^{27} yr in the first phase and 10^{28} yr in the second phase by improving the radio-purity of materials close to the detector, increasing the ^{76}Ge mass and improving the LAr light scintillation efficiency. In the first phase, LEGEND-200, which envisages about 200 kg of enriched Ge detectors, will be operated in the existing GERDA infrastructure at LNGS. For a 1000 kg·yr exposure and background reduction to $< 2 \cdot 10^{-4}$ counts/(keV kg yr), the experiment will have a discovery potential corresponding to a half-life of 10^{27} yr. The second phase, LEGEND-1000, will require a new infrastructure to house 1000 kg of detectors. The total mass will be deployed in several batches at stages; each batch will contain ∼250 kg. The background index is planned to be reduced by a factor of 10 with respect to LEGEND-200. The goal is to achieved a sensitivity beyond 10^{28} yr with a total exposure of 10 t·yr [36].

2.4.2 Bolometers

CUORE

CUORE (Cryogenic Underground Observatory for Rare Events) is searching for ^{130}Te $0\nu\beta\beta$ using TeO_2 bolometers. Bolometers, which operate at very low temperatures, use single crystals as detecting medium. They react to a particle interaction with a temperature rise measured by a thermistor glued or deposited at the surface of a crystal, which converts the temperature variation into an electrical signal. In the case of CUORE, the thermistor consists of a small neutron-transmutation-doped germanium crystal (Ge-NTD). The features of bolometers are: high energy resolution; high detection efficiency (source=detector); and, sometimes, PSD capability. CUORE consists of 988 bolometers arranged in 19 towers with a total mass of 741 kg (206 kg of ^{130}Te) housed in a cryostat to cool down to mK scale. CUORE placed a lower limit on the half-life $T^{0\nu}_{1/2} > 3.2 \cdot 10^{25}$ yr (90% C.L.) [37] and sensitivity bound on $m_{\beta\beta}$ 75-350 meV for a 372.5 kg·yr exposure [38]. The energy resolution at $Q_{\beta\beta}$ is 7.7 keV FWHM. The current background index of CUORE is $1.38 \cdot 10^{-2}$ counts/(keV kg yr) mostly dominated by energy-degraded α's from surface contamination in the materials constituting the detector. In 3 yr from now, CUORE is expected to reach a sensitivity of the order of 10^{26} yr. The CUORE collaboration developed a background model using directly the data and showed that by rejecting the α's, the BI in the ROI can be improved to be around $2.5 \cdot 10^{-3}$ counts/(keV kg yr) and even better at higher energy, above 2.6 MeV, with a value down to 10^{-4} counts/(keV kg yr).

CUPID and its demonstrators

CUPID (CUORE Upgrade with Particle IDentification) is the proposed next-generation experiment following CUORE. CUPID adopts scintillating bolometers to search for $0\nu\beta\beta$. Scintillating bolometers are low temperature calorimeters based on a crystal that scintillates when particles impinge on it, providing thus both a heat and a light signal for each event. An additional bolometer is needed to register the emitted scintillation light from the crystal. The simultaneous detection of heat and light is a powerful tool for particle identification. It provides the ability to distinguish α's from β's/γ's thanks to the different light yield between them. This is of huge importance, as α's are the dominant background of CUORE, as mentioned above. CUPID will be located in LNGS using the same cryogenic facility of CUORE, which can deploy the next-generation required ton-scale $0\nu\beta\beta$ isotope mass. The results obtained by CUPID-Mo (see below) led the collaboration to choose Li_2MoO_4 for CUPID future experiment. CUPID goals are to achieve a background level of the order of 10^{-4} counts/(keV kg yr), which is possible according to the results of the background model of CUORE, and a sensitivity on $m_{\beta\beta}$ in the range 12-20 meV for a 10 yr live-time [39] and a lower limit on the half-life $T^{0\nu}_{1/2} > 1.5 \cdot 10^{27}$ yr at 90% C.L.

CUPID-0 is the first pilot demonstrator of CUPID, started in June 2017, that is based on $Zn^{82}Se$ enriched in the isotope ^{82}Se at 95% corresponding to a mass of 4.7 kg of ^{82}Se. The $Q_{\beta\beta}$ of Se is 2997 keV well beyond the endpoint of γ natural radioactivity. A germanium bolometer was used as a light detector to collect the scintillation emitted by ZnSe. The background index in the ROI is $3.5 \cdot 10^{-3}$ counts/(keV kg yr) which is the lowest background reached by a cryogenic calorimeter along with the CUPID-Mo experiment (see below). For a total exposure of 10 kg $\cdot$ yr and an obtained energy resolution of 20.05 keV, the experiment has set the most stringent half-life lower limit on ^{82}Se, corresponding to $T^{0\nu}_{1/2} > 3.5 \cdot 10^{24}$ yr at 90% C.L. [40]. However, drawbacks for ZnSe appeared: not a very good energy resolution, difficulty of crystallization and internal ^{228}Th contamination.

CUPID-Mo is another pilot experiment of CUPID that studies the isotope ^{100}Mo which has a $Q_{\beta\beta}$ at 3034 keV, also well above the endpoint of γ natural radioactivity. The isotope is embedded in Lithium Molybdate crystals (Li_2MoO_4). The experiment has been running until Summer 2020 in the Modane underground laboratory (LSM) in France, and it consists of 20 Li_2MoO_4 coupled to 20 Ge light detectors to register the scintillation light emitted by the scintillating Li_2MoO_4 elements. The crystals are enriched to 95 % in ^{100}Mo. Very promising results where achieved: very good energy resolution — 5.3 keV FWHM at the ^{208}Tl peak at 2615 keV — and clear demonstration of the capability of the double-readout to reject the dominating background due to α's. The experiment has set the most stringent half-life lower limit on ^{100}Mo, corresponding to $T^{0\nu}_{1/2} > 1.5 \cdot 10^{24}$ yr at 90% C.L. [41]. The background index in the ROI is determined with a large uncertainty due to the poor statistics, and corresponds to $3^{+7}_{-3} \cdot 10^{-3}$ counts/(keV kg yr).

AMoRE

AMoRE (The Advanced Molybdenum-based Rare process Experiment) is based on scintillating bolometers that are equipped with metallic magnetic calorimeter (MMC) phonon sensors to measure the temperature rise of the crystal. ^{100}Mo is the candidate isotope that is embedded and chosen to be tested in one of three possible crystals: $^{48dep}CaMoO_4$, Li_2MoO_4, Na_2MoO_4. The AMoRE pilot experiment, performed at Yangyang under-

ground laboratory (South Korea), was using six $^{48}CaMoO_4$ crystals (total mass 1.9 kg), reporting an upper limit on the half-life $T^{0\nu}_{1/2} > 9.5 \cdot 10^{22}$ yr with a live exposure of 111 kg day. AMoRe-I will be implemented with 12 more crystals of various types ($^{48}CaMoO_4$, Li_2MoO_4, Na_2MoO_4) to improve the detector performance opening the way to the choice of the appropriate crystal for the main phase of the project, namely AMoRE-II. AMoRE-II will consist of 200 kg of crystals mass, aiming at improving the effective Majorana neutrino mass sensitivity down to 20–50 meV [42].

2.4.3 Xenon Time-Projection Chamber (TPC)

EXO

EXO (Enriched Xenon Observatory) searched for $0\nu\beta\beta$ of the isotope ^{136}Xe using a time-projection chamber (TPC) that contains liquid Xenon (LXe). When a particle deposits energy in the LXe it ionizes and excites the Xe atoms at some location and some of the electrons are drifted towards a wired grid by an applied electric field providing a 2D information (X and Y) about their position. The de-excitation of xenon-ions and the recombination of some of electron with xenon ions will lead to the emission of scintillation light that is collected by an arrays of large area avalanche photodiodes (LAAPDs). A 3D location of the event can be reconstructed from the difference in time between the ionization signal that needs some time to be collected and the scintillation time which is registered very shortly after the interaction. This kind of technology allows to get information about the event energy, location, site multiplicity and the type of interacting particle. The EXO-200 pilot experiment was located in Waste Isolation Pilot Plant (WIPP), New Mexico in the USA. The mass of the detector is 175 kg of which 75 kg are ^{136}Xe. The ^{136}Xe were in the TPC active volume, and the enrichment factor in ^{136}Xe was 80%. For a total exposure of 234.1 kg $\cdot$ yr, the lower limit on the half-life was measured to be $3.5 \cdot 10^{25}$ yr at 90% C.L. (median half-life sensitivity is $5 \cdot 10^{25}$ yr at 90% C.L.) [43]. nEXO is the proposed next-generation follow-up to EXO-200 using 5000 kg of isotopically enriched liquid-xenon. The half-life sensitivity is predicted to be $9.2 \cdot 10^{27}$ yr (median half-life sensitivity is $9.2 \cdot 10^{27}$ yr at 90% C.L.) [29, 44].

NEXT

NEXT (Neutrino Experiment with a Xenon TPC) is another TPC experiment based on high pressure gaseous xenon (HPXe). HPXe TPCs offer two advantages: high energy resolution and possibility of track topology, which enables discriminating γ-induced electrons from the two electrons emitted in a $0\nu\beta\beta$ decay. In NEXT, the ionization signal that drifts to the anode is amplified using the electroluminescence of xenon, which is induced by an intense electric field in a region near the anode, causing a secondary scintillation light after atomic excitation. NEXT-White, running in the underground laboratory of Canfranc (LSC) in Spain, is using 5 kg of xenon enriched to 91% in ^{136}Xe. The purpose of this run is to establish the technology for the following 100 kg experiment (NEXT-100) and to measure the background and the ^{136}Xe $2\nu\beta\beta$ decay. The background index is expected to be $4 \cdot 10^{-4}$ counts/(keV kg yr), which will lead to a sensitivity of $1 \cdot 10^{26}$ yr after a total exposure of 400 kg·yr for NEXT-100 [45]. NEXT-HD is the ton scale long term prospect, with the aim to reach a sensitivity $1.5 \cdot 10^{27}$ yr for 5 yr live-time [46, 47].

2.4.4 Liquid loaded scintillators

KamLAND-Zen

KamLAND-zen 400 experiment used ^{136}Xe-loaded liquid scintillator. It consists of a 13 m outer balloon that is filled with liquid scintillator (LS) that contains a 3.08 m mini-balloon including 13 ton of xenon-loaded liquid scintillator (Xe-LS) of which Xe constitutes 750 kg, enriched to 91% in ^{136}Xe. PMTs are placed on the inner surface to detect the scintillation light caused by particle interactions. KamLAND-Zen 400 reached the most sensitive constraint on the effective Majorana neutrino mass with a lower limit on the half-life $T^{0\nu}_{1/2} > 1.07 \cdot 10^{26}$ yr (90% C.L.) corresponding to $|m_{\beta\beta}| < 61 - 165$ meV [48]. The current project, KamLAND-zen 800 with 750 kg Xe, that started in January 2019, is expected to touch the inverted hierarchy region after 3 years of data acquisition.

SNO+

The SNO+ experiment is using tellurium-loaded liquid scintillator (Te-LS). 780 tons of liquid scintillator are contained in a acrylic vessel, which have 0.5% ^{nat}Te-loading by weight, corresponding to 1330 kg of ^{130}Te. The expected sensitivity for this phase is $T^{0\nu}_{1/2} > 1.9 \cdot 10^{26}$ yr after 5 years of data taking. SNO+ future phase, called phase II, will include 1% tellurium loading, improvement in the light yield and a higher transparency LS to increase the energy resolution, and ^{130}Te enrichment. This will boost SNO+ sensitivity to effective Majorana neutrino mass with the aim to cover the inverted hierarchy region. [49].

2.4.5 Tracking detector

SuperNEMO

SuperNEMO employs a tracking-calorimetry detection technique to search for $0\nu\beta\beta$. It is built on the successful NEMO-3 experiment. In this technique, a layer of the isotope under study in the form of a thin foil is is placed in a gaseous tracker that in turn is surrounded by a calorimeter. The tracker consists of drift cells which reconstruct particles trajectories, and the calorimeter consists of optical modules based on plastic scintillators which measure particle energy. This allows for a full event-topology reconstruction. SuperNEMO studies the isotope ^{82}Se which has a $Q_{\beta\beta}$=2998 keV. The SuperNEMO demonstrator, under commissioning at Laboratoire Souterrain de Modane (LSM), contains 6.3 kg of the isotope with the aim to reach a sensitivity $T^{0\nu}_{1/2} > 5.9 \cdot 10^{24}$ yr (90% C.L.) with a 2.5 yr exposure [50]. The full SuperNEMO experiment should use 100 kg of ^{82}Se. It would require a very big underground space (20 times bigger than the demonstrator). The foreseen sensitivity for a 5 yr exposure is $T^{0\nu}_{1/2} > 10^{26}$ yr (90% C.L.) [50].

Tables 2.2 and 2.3 show a summary of the current and future experiments.

In the next chapter, the bolometric technique for the search of neutrinoless double-beta decay will be introduced. A new method for pulse shape discrimination will be described to reject the challenging background from surface contamination.

Experiment	detection technique	isotope	mass $0\nu\beta\beta$ isotope (kg)	FWHM (keV)	lim $T^{0\nu}_{1/2}$	lim $m_{\beta\beta}$ (meV)	exposure (kg yr)	Ref.
NEMO-3	tracking calorimeter	^{48}Ca	0.007	∼679	$2 \cdot 10^{22}$	6000-26000	0.037	[51]
GERDA	HPGe detector	^{76}Ge	127.2	3	$1.8 \cdot 10^{26}$	79-180	82.4	[52]
MAJORANA	HPGe detector	^{76}Ge	25	2.5	$2.7 \cdot 10^{25}$	200–433	26	[35]
NEMO-3	tracking calorimeter	^{82}Se	0.9	∼140	$2.5 \cdot 10^{23}$	1200-3000	4.9	[53]
SuperNEMO demonstrator	tracking calorimeter	^{82}Se	6.5		$5.9 \cdot 10^{24}$	260-500	2.5 yr	[54] [50]
CUPID-0	scintillating bolometers	^{82}Se	4.7	20.05	$3.5 \cdot 10^{24}$	311-638	10	[40]
NEMO-3	tracking calorimeter	^{96}Zr	0.009	∼520	$9.2 \cdot 10^{21}$	7200-19500	0.0031	[55]
AMoRE	scintillating bolometers	^{100}Mo	0.886	14.43	$9.5 \cdot 10^{22}$	1200-2100	0.3	[42]
NEMO-3	tracking calorimeter	^{100}Mo	7	∼809	$1.1 \cdot 10^{24}$	330-620	34	[56]
LUMINEU	scintillating bolometers	^{100}Mo	0.45	5-6	$0.7 \cdot 10^{23}$	1400-2400	0.1	[57]
CUPID-Mo	scintillating bolometers	^{100}Mo	2.3	7.7	$1.4 \cdot 10^{24}$	310-540	1.2	[41]
AURORA	scintillators	^{116}Cd	0.3	∼170	$2.2 \cdot 10^{23}$	1000-1700	4.7	[58]
NEMO-3	tracking calorimeter	^{116}Cd	0.4	∼722	$1 \cdot 10^{23}$	1400-2500	0.02	[59]
CUORE	bolometers	^{130}Te	206	7.7	$3.2 \cdot 10^{25}$	75-350	372.5	[38]
EXO-200	liquid TPC	^{136}Xe	75	72.38	$3.5 \cdot 10^{25}$	93-286	234.1	[43]
KamLAND-Zen 400	liquid scintillator	^{136}Xe	346	270	$1.07 \cdot 10^{26}$	61-165	504	[48]
NEMO-3	tracking calorimeter	^{150}Nd	0.04	∼535	$2 \cdot 10^{22}$	1600-5300	0.19	[60]

Table 2.2 – Previous and current experimental limits on the effective Majorana neutrino mass.

Experiment	detection technique	isotope	mass (kg)	lim $m_{\beta\beta}$	Ref.
LEGEND-200	HPGe detector	^{76}Ge	200	35-73	[29]
LEGEND-1000	HPGe detector	^{76}Ge	1000	15-50	[36]
SuperNEMO	tracking calorimeter	^{82}Se	100	50-100	[50]
CUPID	scintillating bolometers	^{100}Mo	253	12-20	[39]
AMoRE II	scintillating bolometers	^{100}Mo	200	20-50	[42]
nEXO	liquid TPC	^{136}Xe	5000	5.7-17.7	[44]
NEXT-100	gaseous TPC	^{136}Xe	100	46-170	[46] [45]
NEXT-2	gaseous TPC	^{136}Xe	∼ton	17-40	[46]
KamLAND-Zen 800	liquid scintillator	^{136}Xe	∼800	∼ 40	[46]
SNO+ (Phase I)	liquid scintillator	^{136}Xe	1330	40-90	[61]

Table 2.3 – Sensitivities of future experiments.

Chapter 3

Bolometric detectors

The detector technology used to investigate neutrinoless double-beta decay plays a major role to get a better sensitivity. Bolometers are amongst the most powerful detectors for double-beta decay searches. They have intrinsic good features and are flexible in terms of making modifications, thus allowing to design various strategies to maximize the sensitivity. Bolometers have an intrinsic high energy resolution, a high detection efficiency, a low energy threshold, possibilities of background reduction employing active rejection techniques [62]; in addition, and more importantly, they can be fabricated from a variety of materials — including the element of interest — with the possibility of enrichment in the $\beta\beta$ isotope. All these features provide a powerful detection technique. Reducing the background due the surface contamination is of particular importance, as it is shown to be the dominant background in the ROI for bolometric experiments [63]. Two main bolometric experiments are covered in this work: CUPID-Mo and CROSS.

CUPID-Mo (CUORE Upgrade with Particle IDentification) is a $0\nu\beta\beta$ experiment based on scintillating bolometers formed by Li_2MoO_4 crystals coupled to light detectors. This configuration gives the ability to reject α particles background by reading simultaneously the heat and the light signal that is typically different for α and β/γ events for the same deposited energy in the crystal (section 3.2).

The CROSS project (Cryogenic Rare-event Observatory with Surface Sensitivity) is based on surface sensitive bolometers that is achieved by coating the crystals (Li_2MoO_4 and TeO_2) with the appropriate materials, providing the detector with an active rejection technique for surface contamination events (section 3.4).

3.1 The classical bolometric technique

The use of bolometers for the search for double-beta decay was first proposed by E. Fiorini and T.O. Niinikoski [64]. Bolometers are calorimetric detectors that consist of an absorber (a crystal) with a sensor affixed to the surface of the crystal. The ensemble is in thermal link to a heat bath. When a particle releases energy in the absorber it is converted into lattice vibrations that generate eventually a temperature rise in the crystal. This temperature rise is measured by the sensor, which acts as a thermometer. It converts thermal excitations into a readable signal which typically consists of a voltage pulse as the one in Fig. 3.1 (*left*).

An essential requirement to build a bolometer is to ensure a low heat capacity C of the absorber. In fact, the temperature variation ΔT induced by an energy deposition E is given by:

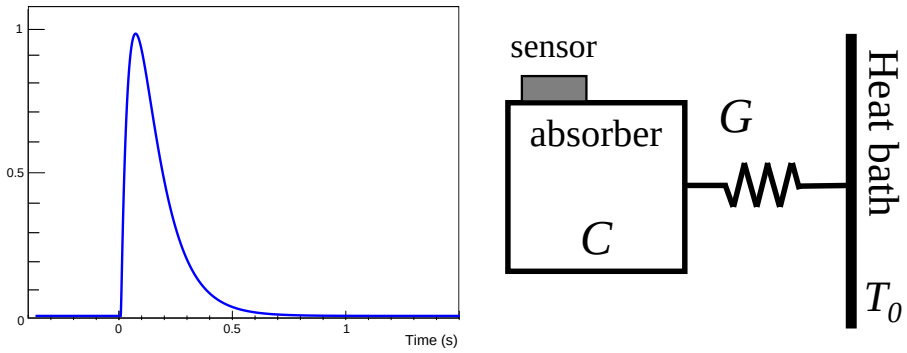

Figure 3.1 – *left*: A typical pulse shape. *right*: Simplified thermal model scheme of the bolometer which consists of an absorber with heat capacity C coupled through the thermal conductance G to a thermal bath.

$$\Delta T = \frac{E}{C} \tag{3.1}$$

which translates into an increase in temperature variation as the heat capacity decreases. The typical temperature variation of a bolometer of the types discussed in this work is a few tens or hundreds of µK per MeV.

The bolometer presents thermal connections between the absorber and the thermistor to read the deposited energy precisely and between the absorber and the heat sink to ensure keeping the bolometer at low temperature and recovering back the initial temperature after the bolometer heats up as a result of an energy deposition. Fig. 3.1 (*right*) shows a simplified bolometric thermal model.

3.1.1 The absorber

The absorber contains the $\beta\beta$ decaying isotope, implying that the source is the detector itself. It can be fabricated from a wide variety of materials, provided that they have a low heat capacity at very low temperatures as addressed above in Eq. 3.1. The heat capacity for a dielectric and a diamagnetic material, in which the contribution is only from the lattice, is given by:

$$C = \frac{12}{5}\pi^4 N_A \frac{m}{M} k_b \left(\frac{T}{\Theta_D}\right)^3 \tag{3.2}$$

where m is the mass of the crystal, M is the molar mass, N_A is Avogadro's number, k_b is Boltzmann constant (1.38×10^{-23} J/K), T is the temperature of the crystal, and Θ_D is Debye temperature. Working at very low temperature, around 10 mK, will make C sufficiently low.

The absorber with a heat capacity C is in weak thermal link through a thermal conductance G with a heat sink held at a very low and constant temperature T_0 (Fig. 3.1 (*right*)). So when the temperature of the absorber rises after a particle impinges on it, it will restore to the original temperature thanks to the connection to the heat sink. The time evolution of the temperature variation is given by:

$$\Delta T(t) = \frac{E}{C} e^{-t/\tau} \tag{3.3}$$

where $\tau = C/G$ is the time required for the absorber to return to the base temperature and it is referred to as the decay-time. It depends strongly on the material and the thermal coupling to the heat bath. The decay-time appears in the pulse as the decaying part after the maximum.

In principle, the absorber can be a conductor rather than a dielectric material. But in this case the heat capacity has a contribution coming from the electrons in which C is proportional to T:

$$C = \frac{\pi^2}{2} \frac{N_A}{E_F} k_b^2 T = \gamma_N T \tag{3.4}$$

where E_F is Fermi energy. The term in front of T in the above equation is often defined "Sommerfeld coefficient" γ_N. So conductors are not preferred because their heat capacity is much higher compared to the heat capacity of dielectric materials ($C \propto T^3$) at very low temperatures.

However, if the metal is in a superconductive state well below the critical temperature T_C , the electron specific heat is modified as follows (according to the BCS theory):

$$C = A \cdot \gamma_N \cdot T_C \cdot \exp\left(\frac{-\Delta}{k_B T}\right) \tag{3.5}$$

where A is a dimensionless constant and $\Delta = 1.764 \cdot k_B\ T_c$ is the zero temperature limit of the superconductive gap. Therefore, the electron heat capacity will vanish exponentially in superconductors as the temperature decreases and will become negligible with respect to the lattice contribution.

Two types of crystals are considered in our work, lithium molybdate (Li_2MoO_4) [65, 66] and tellurium dioxide (TeO_2) [38]. The heat capacity for a 2×2×1 cm^3 crystals is given in the table below:

Crystal	θ_D (K)	C (J/K)
Li_2MoO_4	316 [67]	$3 \cdot 10^{-5}\ T^3$
TeO_2	232 [68]	$7 \cdot 10^{-5}\ T^3$

Table 3.1 – The heat capacity for the a 2×2×1 cm^3 dielectric Li_2MoO_4 and TeO_2 crystals.

As for metals, we will deal with two types of metal coating: superconductive aluminum ($T_C = 1.2$ K) and normal palladium ($\gamma_N = 9.6 \cdot 10^{-3}$ (J/K^2/mol)).

3.1.2 The sensor

The sensor is responsible for registering the temperature rise. It collects the phonons produced in the absorber after energy deposition and converts it into an electrical signal. Often (and always in the present work) the sensor is a thermistor characterized by a function $R(T)$, providing the dependence of the resistance on the temperature. The sensor performance is characterized then by the sensitivity, which is expressed as:

$$A = \left| \frac{d \ln R(T)}{d \ln T} \right| \sim \frac{\Delta R}{R} \frac{T}{\Delta T} \tag{3.6}$$

This parameter shows the ability and efficiency of the thermistor in converting a small temperature rise into a detectable electrical signal, which is obtained by flowing a constant current in the thermistor and registering the voltage variation induced by the resistance change.

In our work we consider two types of thermistors: Neutron transmutation doped (NTD) [69] Germanium thermistors and NbSi films [70, 71].

Neutron transmutation doped (NTD) Germanium thermistor

An NTD Ge thermistor consists of a semiconductor germanium crystal doped just below the metal-insulator transition (MIT). Doping is achieved by using the NTD technique, in which a natural germanium wafer is bombarded with a high flux of thermal neutrons from a nuclear reactor, which will induce nuclear transformations in some germanium atoms giving a homogeneous dopant concentration:

$$\begin{aligned} {}^{70}Ge + n \rightarrow {}^{71}Ge \rightarrow {}^{71}Ga + \nu_e \quad & \text{(acceptor)} \\ {}^{74}Ge + n \rightarrow {}^{75}Ge \rightarrow {}^{75}As + \overline{\nu_e} \quad & \text{(donor)} \\ {}^{76}Ge + n \rightarrow {}^{77}Ge \rightarrow {}^{77}As + \nu_e & \\ \rightarrow {}^{77}Se + \nu_e \quad & \text{(double donor)} \end{aligned} \tag{3.7}$$

At low temperatures, the electrons transport in Ge-NTDs is explained by the variable range hopping (VRH) mechanism. In VRH the charge tunneling between impurities is assisted by phonons. Charges tunnel or hop between impurity sites by absorbing or emitting phonons. The resistivity of the NTD as a function of temperature according to the VRH with soft Coulomb gap [72], which well describes the thermistors used in this work, is given by:

$$\rho = \rho_0 e^{(T_0/T)^\gamma} \tag{3.8}$$

where γ is equal to 0.5 [73], while R_0 and T_0 are determined experimentally by characterizing the thermistor. In general, T_0 depends on the dopant concentration, $R_0 = \rho_0 \cdot L/S$ (L being the contact distance and S the thermistor section) depends on the geometry and weakly on the T_0 value, γ depends on the electron density of states near the Fermi level and, as stated above, is equal to 0.5 for our thermistors operating in the VRH with soft Coulomb gap regime. The mechanical stress of the sample, induced for example by differential thermal contractions with respect to the glue used to fix the thermistor, can change the $R(T)$ curve, typically increasing both T_0 and ρ_0. The doping density is critical to ensure that the conductivity goes to zero at zero temperature when it is below the MIT (Metal Insulator Transition). Doping close to the MIT is the favoured condition as this will provide a thermistor with a high sensitivity, low noise and a high reproducibility. Random and homogeneous doping, which is provided by the NTD technique, will prevent resistivity changes due to fluctuations in the local hopping probability for carriers between the dopant atoms [74].

A thermistor is characterised by gluing it either directly at a crystal in a detector configuration or at a copper holder with a thermal link to a heat sink held at a very low temperatures. The resistance of the Ge-NTD is then measured at different temperatures

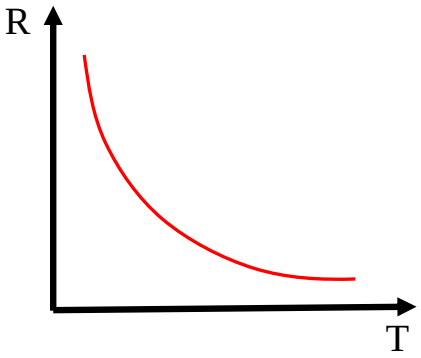

Figure 3.2 – The resistance as a function of the temperature for Ge-NTD

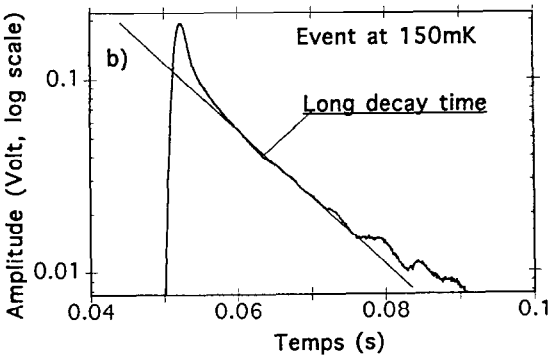

Figure 3.3 – Typical pulse shape in log scale with NbSi [76].

to get a plot similar to the one shown in Fig. 3.2. Then the curve is fitted with the equation below derived from Eq. 3.8:

$$R = R_0 e^{(T_0/T)^\gamma} \tag{3.9}$$

from which R_0 and T_0 are extracted. The gluing of the thermistor is done using Araldite® bi-component epoxy glue. Gluing can be done with a thin veil of glue or small spots arranged in array with a thickness fixed by a spacer, typically between 20 and 50 μm. The small spot option is safer, as the mechanical stress between the Ge-NTD and the absorber is weaker compared to a large veil.

The Ge-NTD being glued to the crystal and intrinsically slow in response, it shows mainly sensitivity to thermal phonons (see section 3.3).

It may be useful to evaluate the heat capacity at low temperatures of a Ge-NTD. For the devices used in this thesis, consisting of a doped Ge crystal with dimensions $3 \times 3 \times 1$ mm, the heat capacity is given by $C_{NTD} = 8.8 \times 10^{-9} \cdot T$ [J/K] [75], dominated by the electronic system of the device.

Niobium-silicon film (Anderson insulator)

Nb_xSi_{1-x} is a thermometer sensitive mainly to out-of equilibrium phonons (see section 3.3). It has an excellent coupling to the heat absorber because it is deposited on a large surface without a glue interface. For $x > 0.13$, the sensor displays superconductivity, for $0.09 < x < 0.13$ the sensor shows a non-superconducting metallic behaviour, and for

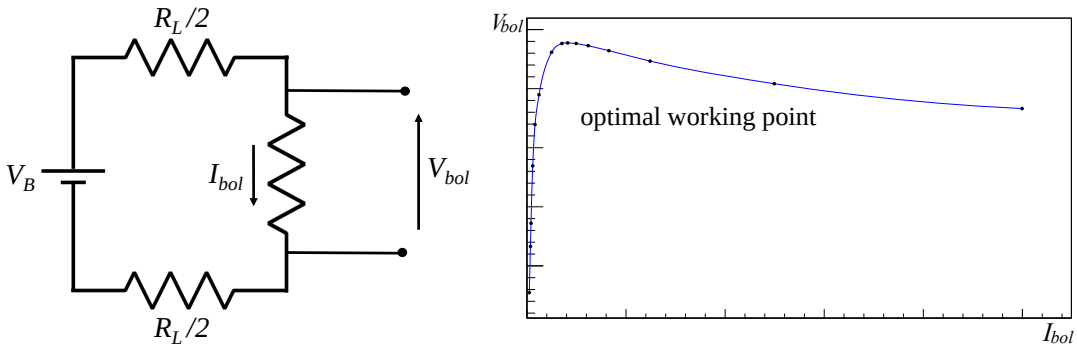

Figure 3.4 – (*left*): Bias circuit scheme for the NTD readout. (*right*): The I-V load curve.

$x < 0.09$ it behaves as an Anderson insulator [70] and it is similar to a Ge-NTD in terms of $R(T)$ curve. The latter case is the one considered in our work.

This sensor follows the law of Eq (3.9). At low temperatures, the sensor has two different behaviours in terms of resistance. For $T > 150$ mK it shows a Mott behaviour, where γ=0.25, and for $T < 150$ mK, it behaves according to Efros and Shklovskii law, where γ=0.5. The pulse shape for NbSi readout is similar to the one shown in Fig. 3.3. It has a slight difference compared to the pulse of a Ge-NTD (Fig. 3.1 (*left*)). It has a fast rise-time and often two well distinguishable decay times, a fast component and a long component. The short rise-time is due to the fact that sensor electrons absorb directly a fraction of a deposited energy in the form of out-of-equilibrium phonons. The fast decay time represents the energy relaxation to the absorber through the electron-phonon coupling of the sensor and Kapitza resistance between the sensor and the absorber. The long decay time comes from the weak thermal link between the absorber and the heat bath through the gold wires.

Detector operation and the load curve

The sensor is biased with the circuit shown in Fig. 3.4 (*left*). To read the signal by the thermistor, a constant bias current I_B is generated by a DC power supply. The thermistor is placed in series with load resistors of resistance R_L much larger than the resistance of the thermistor R_{bol}. This means that I_B is practically independent of the value of R_{bol}, since $I_B = V_B/(R_L + R_{bol}) \simeq V_B/R_L$. Measuring the voltage drop across the thermistor V_{bol} will lead to reading the resistance of the thermistor R_{bol} which is related to the temperature of the bolometer.

Before starting data taking, it is crucial to search for the optimal working point, in which the signal to noise ratio is the highest. A set of I_{bol} and V_{bol} points are measured by varying V_B to get a curve similar to Figure 3.4 (*right*). The load curve starts almost linearly, where R_{bol} is almost constant, and then it starts to deviate from linearity because of what is called the electrothermal feedback. The applied bias across the thermistor leads to a temperature rise of T_{bol} caused by the dissipated power $P = I_{bol} \cdot V_{bol}$, which in turn will lower R_{bol}. This happens until equilibrium is reached, where the power dissipated in the sensor is equal to the power being evacuated to the heat bath:

$$T_{bol} = T_0 + \frac{P}{G} \tag{3.10}$$

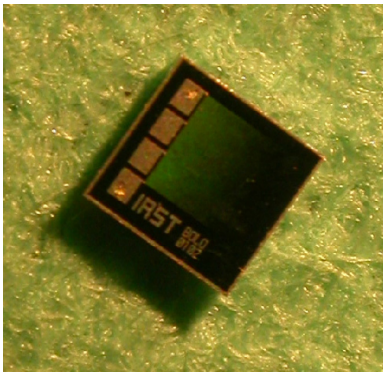

Figure 3.5 – The heater.

The voltage V_{bol} initially increases as we increase the applied current I_{bol}, until it reaches a maximum ("inversion point") where then the voltage starts to drop as the current increases. Tracking the signal-to-noise ratio at each applied bias will specify the optimal working point, which typically is just below the inversion point.

At a specific working point and at static conditions, i.e. no energy is deposited to perturb the equilibrium between the bolometer and the heat bath, the voltage of the thermistor is given by:

$$V_{bol} = V_B \frac{R_{bol}}{R_{bol} + R_L} \sim V_B \frac{R_{bol}}{R_L} \tag{3.11}$$

When energy is released in the absorber, the voltage variation in the dynamic conditions is expressed as:

$$\Delta V = V_B \frac{\Delta R}{R_L} = A V_{bol} \frac{\Delta T}{T_{bol}} = \frac{E}{C T_{bol}} A \sqrt{P R_{bol}} \tag{3.12}$$

The equation characterizes the detector performance, as it relates the signal amplitude ΔV to the energy deposited E that has generated the signal. The parameter $\Delta V/E$ (usually expressed in this work in nV/keV) is defined "sensitivity". Of course, the higher the sensitivity the better the performance of the detector for a given noise level.

3.1.3 The heater

Temperature fluctuations and instability of the cryogenics can arise and affect the quality of the data of a measurement, especially if it is running for a long period of time, spoiling as a consequence the energy resolution. To control and stabilize the thermal response of the bolometer, a pulser is used to deliver periodically a constant amount of energy (through Joule effect on a resistive element glued at the crystal and referred to as "heater" in the following) that will generate pulses very similar to pulses from particle interactions. An offline correction to the detector response for pulser events can be applied. In addition, the heater allows us to search quickly for the optimum working point. The heater that is used in our experiments is a Si semiconductor heavily doped element, shown in Fig. 3.5, and it is glued on the crystal with Araldite® epoxy glue.

Stabilization by heater is performed by establishing a relationship between the pulse amplitude of the heater-induced pulses and the DC baseline level before the pulse onset, which is an instantaneous measurement of the detector temperature. The lower the

baseline level, the lower the temperature and the higher the pulse amplitude. This relationship is fitted, typically with a polynomial of first or second degree, and the fit results can be used to correct any pulse amplitude according to the baseline level preceding the pulse.

3.1.4 Intrinsic energy resolution

Thermodynamic noise: At the fundamental level, the intrinsic energy resolution of the bolometer is limited by the fluctuations of energy transported by the phonons exchanged between the absorber and the heat bath. A crude method to evaluate the amount of these fluctuations is the following. The mean energy of the phonons is k_bT. For a total deposited energy in absorber $E = C/G$, the number of created phonons is $N = E/(k_bT)$, in case of full thermalization of the deposited energy. Considering a Poisson fluctuation in N, the mean of the energy fluctuation is given by:

$$\Delta E = \sqrt{N}\ k_bT = \sqrt{k_bC(T)T^2} \tag{3.13}$$

The intrinsic energy resolution is independent of the deposited energy. To get a feeling of how excellent is the intrinsic energy resolution of a bolometer, consider a Li_2MoO_4 crystal with a 1 kg of mass operating at 10 mk. The heat capacity in this case is around $2.5 \cdot 10^{-2}\ T^3$ J/K, so ΔE is equal to 11.6 eV ($\Delta E_{FWHM} = 2.35\ \Delta E = 23.2$ eV).

It should be noted that, if the detection takes place mainly through out-of-equilibrium phonons transmitted directly from the crystal to the sensor before full thermalization, the intrinsic energy resolution is expected to be much worse. In fact, prompt phonons created by particle interactions are in the meV range, and so their number is much smaller than in the case of thermal phonons, leading to larger relative Poisson fluctuations. This situation is analogous to that occurring in conventional nuclear and particle detectors, where the energy resolution is limited but the fluctuation in the number of out-of-equilibrium elementary excitations (electron-hole pairs, electron-ion pairs, scintillation photons) produced by the impinging particle. Here, the elementary excitations are the “high" energy prompt phonons.

Johnson noise: Since the thermistor can be considered as a resistor with resistance R, it generates a white noise with a power spectrum:

$$e_R = \sqrt{4k_bRT} \tag{3.14}$$

where T is the temperature of the resistor, R is the resistance and k_b is Boltzmann constant. This is another source of irreducible limitation of the energy resolution. It can be shown [77] that in a well optimised bolometer with resistive readout this component can be kept under control without affecting seriously the energy resolution with respect to that given by Eq. 3.13.

However, the real energy resolution is affected by the dominant extrinsic noise. The extrinsic noise includes the noise coming from the cryogenic setup and the mechanical vibrations of the bolometers (microphonic noise), the electronic noise, electromagnetic references and baseline temperature variations not fully corrected by the heater method.

3.1.5 The complete thermal model

A real bolometer is actually more complicated than what is shown in Fig. 3.1 (*right*). The heat capacity C and conductance G are actually a sum of many contributions from

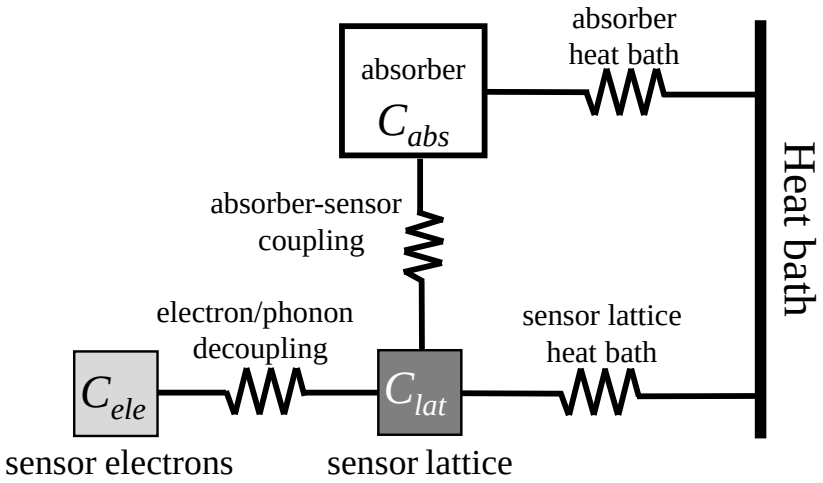

Figure 3.6 – Three-node thermal model for a bolometer, which consists of the absorber, sensor lattice and sensor electrons nodes.

different elements in the detector and not just one global contribution. Figure 3.6 illustrates a more complete bolometer scheme. The model consists of three nodes: the absorber and two nodes for the sensor, each having a certain heat capacity C. The sensor at low temperature shows a decoupling behaviour between the phonons and the electrons explained by the Hot Electron Model (HEM). The two subsystems are at different temperatures and are thermally coupled by a conductance. In this case, the resistivity (Eq. 3.8) depends on the temperature of the electrons system since the injected bias current to measure the resistance of the thermistor is deposited in the electrons node.

The nodes are thermally connected through conductance that transfers heat from the higher temperature node to the lower temperature one. The link between the absorber and the thermistor is through the glue. There are two thermal links from the bolometer to the heat sink. One is from the absorber through the PTFE (polytetrafluoroethylene) pieces, and are used to fix the crystal well in the copper holder. The other thermal connection to the heat bath is from the thermistor lattice and it is through Au bonding wires which give also the electrical connection with the thermistor. There is no direct link between the sensor electron system and the heat sink. It is crucial that the transmission time of the heat from the absorber to heat sink is longer than the time needed to reach an equilibrium between the absorber and the sensor. This is controlled by having a weak conductance between the absorber and the heat sink.

3.1.6 Pulse amplitude and comparison of two bolometers

In order to compare the performance of two bolometers, we need before to make some considerations about pulse amplitudes.

Equation 3.12 assumes implicitly that the bolometer is monolithic. Actually, the bolometer has a complicated structure described by the thermal network discussed in the previous section. In addition, the mechanism of pulse formation could be not completely thermal: a fraction of the energy deposited in the absorber could reach the sensor electrons through out-of-equilibrium phonon transmission.

Also, we have access only to the temperature of the electrons T_{el}: it is this parameter that fixes the resistance of the thermistor, whose variations provide the thermal signal.

Therefore, a more general version of equation 3.12 is:

$$\Delta V = AV_{bol} \cdot \frac{\Delta T_{el}}{T_{el}} \tag{3.15}$$

This equation is composed by two parts. The factor AV_{bol} depends on the operation point and on the thermistor properties: it is related to the efficiency of the readout in converting a (fractional) temperature change into a voltage signal. The factor $\frac{\Delta T_{el}}{T_{el}}$ is intrinsic to the bolometer and does not depend on the readout: it is related to the efficiency of the bolometer in converting a deposited energy into a fractional temperature change of the electrons. In the naive case of monolithic bolometer, $\frac{\Delta T}{T} = \frac{E}{C_{tot} \cdot T}$, where $T = T_{el}$: the only relevant parameter it the total heat capacity C_{tot}. In the most general case, $\frac{\Delta T_{el}}{T_{el}}$ is an almost linear function of the deposited energy E that depends on the thermal conductances and the heat capacities appearing in Fig. 3.6, but also on parameters related to out-of-equilibrium phonons if the bolometers has no pure thermal behaviour.

We can incorporate all the deviations from the naive monolithic bolometer by introducing a parameter C_{eff} with the dimension of a heat capacity and assuming that $\Delta T_{el} = \frac{E}{C_{eff}}$. If the bolometric response is purely thermal, we will have that $C_{eff} \geq C_{tot}$, as the thermal network of Figure 3.6 can only make the transmission of heat to the thermistor electrons less efficient with respect to the monolithic case. (The equality will hold in the monolithic case.) However, if there is an important athermal component in the pulse formation (see Section 3.3), energy can be transferred efficiently to the thermistor before thermalization in the absorber, and therefore the heat capacity of the thermistor electrons becomes the relevant parameter. In this case, it may happen that $C_{eff} < C_{tot}$.

In this thesis work, we have often to compare the intrinsic performance of two bolometers, in order to evaluate the effect of adding thin films on bolometer faces. It would be misleading to do this by comparing the respective sensitivities only, as they depend also on the operation points and thermistor properties. It is more accurate to compare two different bolometers in terms of the fractional temperatures changes. From Eq. 3.15 one can derive what we will define a “reduced sensitivity", η, which is equal to the fractional variation of the electron temperature in the thermistor and can be extracted by the signal amplitude and easily measurable parameters.

$$\eta = \frac{\Delta T_{el}}{T_{el}} = \frac{\Delta V}{AV_{bol}} \tag{3.16}$$

The thermistor logarithmic sensitivity $A{=}1/2(T_0/T)^{1/2}$ can be derived by characterizing the thermistor and so determining T_0. The parameter V_{bol} can be extracted when doing the load curve and choosing the operation point.

A bolometer is intrinsically better than another one if it has a higher η. If we want to show that the addition of a thin film does not spoil bolometric performance, we can check that η does not change after film deposition.

3.2 Scintillating bolometers

The background in the ROI, according to the CUORE background model [63, 78], is dominated by energy-degraded α's due to the contamination of the materials surrounding the detector or the surface of the bolometer itself. This represents a limiting factor on the sensitivity of the $0\nu\beta\beta$ experiments.

Surface events in the ROI

In terms of location of the sources, there are three types of contamination that can contribute to the background in bolometers: internal (bulk) contamination of the crystals, external contamination, and surface contamination (both of the crystals and of the material surrounding them).

Internal contamination can be controlled by choosing radiopure materials for the detector construction. In addition, when having ^{238}U and ^{232}Th internal contamination, a β decay may be in sequence with an α decay. Therefore, β/γ events can be rejected using delayed α-β coincidences.

The external contamination can be mitigated with a proper shielding (lead, polyethylene,...), and if necessary active vetoes.

Surface contamination on the other hand is difficult to control. Bolometers are very sensitive detectors to any decay or event happening close to it because they are detectors with a full active volume lacking a dead layer. Fig. 3.7 illustrates the origin of the surface background events, which are due to radioactive decays occurring in the detector surrounding materials. An α and a recoil nucleus can be produced from a decaying nucleus on the surface of the bolometer or the surrounding materials that will produce a signal in the detector through five different cases:

1. An α decay occurs on the surface of the crystal and the decay energy is not fully confined in it. The energy of the α and of the corresponding recoil nucleus is shared between two crystals.

2. An α decay occurs on the surface of the crystal. The α deposits all its energy E_α in the absorber. The recoil nucleus deposits some of its energy E_{recoil} in the absorber and loses the remaining fraction in the surrounding inert materials, such as copper. The signature of this case is a peak at E_α with a tail that extends up to E_α+E_{recoil}.

3. An α decay occurs on the surface of the surrounding inert material. The α loses all of its energy in this material and the recoil nucleus releases some of its energy in this material and the rest in a bolometer. A continuous distribution that end at E_{recoil} appears in the energy spectrum.

4. An α decay occurs on the surface of a surrounding material. The recoil nucleus deposits all of its energy in this material and the α particle loses some of its energy E_α in it before releasing the rest in a bolometer. A broad distribution up to E_α is produced in the energy spectrum.

5. An α decay occurs on the surface of the crystal. The recoil nucleus releases all of its energy in the crystal and the α's energy is partially deposited in the surrounding materials. A broad distribution starting from E_{recoil} and extending at higher energies (even close to E_α) appears in the spectrum.

Since the ROI for $0\nu\beta\beta$ searches is around 2.5-3 MeV, case-3 isn't dangerous. In fact, the recoil nucleus has an energy of few tens/hundreds of keV which is far below the $Q_{\beta\beta}$ of the $0\nu\beta\beta$ isotopes. Case-2, case-4 and case-5 affect the ROI, since most of the α's have an energy between 4-8 MeV and may reach the bolometer with a degraded energy close to the $Q_{\beta\beta}$. Surface events as in case-1 can be excluded by performing coincidence cut.

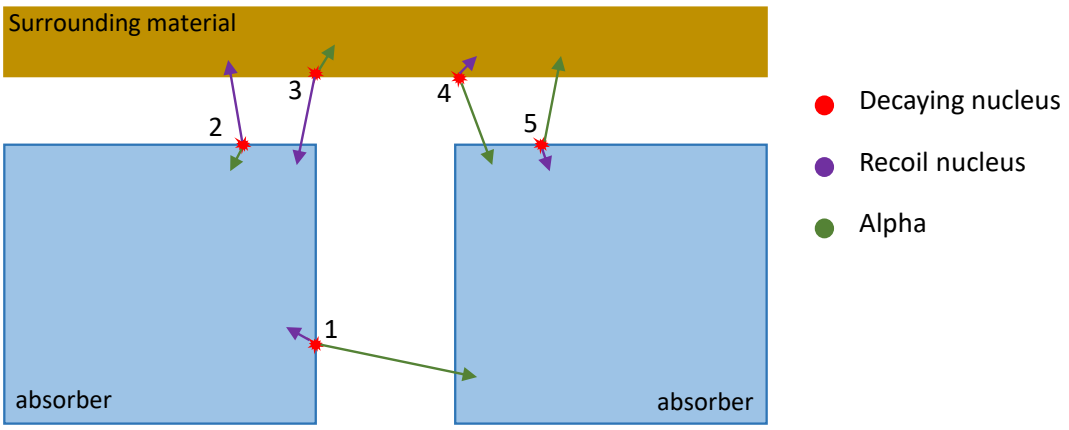

Figure 3.7 – Scheme showing the origin of surface alpha background.

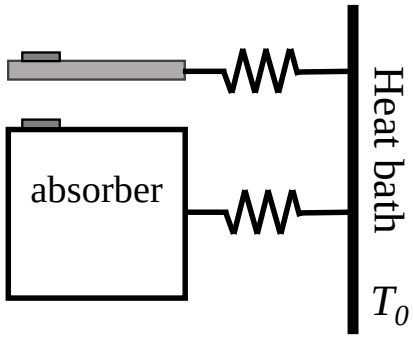

Figure 3.8 – A scheme of a scintillating bolometer in which the main crystal is coupled to another bolometer acting as a light detector.

It is necessary then to develop a technology that allows us to mitigate the background induced by surface α particles.

CUPID, which is an upgrade of CUORE with particle identification capability, adopts a method to reject the α events based on scintillating bolometers, which allow for particle identification. In a scintillating bolometer, the absorber containing the double-beta candidate emits scintillation light when a particle interacts in it. Only a small fraction of the total energy released in the absorber is converted into light. A second independent bolometer, a light detector, is placed facing the primary scintillating bolometer to collect the emitted light (Fig. 3.8). This technology of having a dual read-out of heat and light is powerful and it can be exploited to get rid of the α background. This is possible because α and β/γ events have a different light yield (LY). The light yield is defined as the fraction of the energy emitted in scintillation photons (L) to the total deposited energy in the absorber (E):

$$LY = \frac{L}{E} \tag{3.17}$$

The light yield for α's is usually quenched compared to the β/γ events of the same energy (Fig. 3.9 (*bottom left*)). This was observed in almost all of the tested scintillating crystals (Li_2MoO_4 is one of them). On the other hand, ZnSe scintillating bolometer,

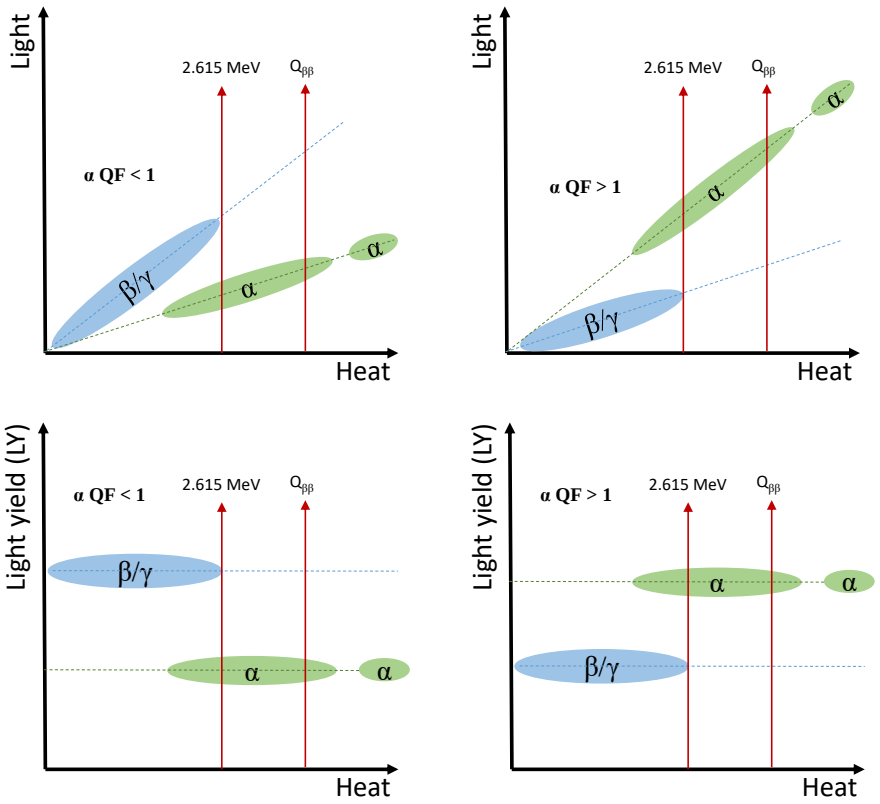

Figure 3.9 – *top left*: Light versus heat scatter plot for crystals with a quenching factor (QF) < 1. *top right*: Light versus heat scatter plot for crystals with a quenching factor (QF) > 1. *bottom left*: The light yield scatter plot for (QF) < 1. *bottom right*: The light yield scatter plot for (QF) > 1.

which was tested in the pilot project LUCIFER (evolved subsequently in the experiment CUPID-0 [79]), showed a peculiar behaviour: the α light yield is higher in this case than the β/γ light yield. So, the quenching factor (QF), which is defined as ratio between LY_α and $\mathrm{LY}_{\beta/\gamma}$, is greater than 1 for ZnSe scintillating crystals, while it is less than 1 for most of the other tested crystals. An explanation for why usually α's have a lower LY with respect to β's is given by the fact that α's have a larger stopping power. Consequently, the energy deposited for unit volume is much higher, leading to a saturation in the light centers.

The discrimination capability between α's and β/γ can be quantified in terms of the discrimination power (DP), where μ and σ are the mean and the standard deviation respectively extracted from the Gaussian fit applied to the LY distributions of α and β/γ:

$$DP = \frac{|\mu_\alpha - \mu_{\beta/\gamma}|}{\sqrt{\sigma_\alpha^2 + \sigma_{\beta/\gamma}^2}} \tag{3.18}$$

We notice that the same formula can be used for any other parameter that has a different mean value for α's and β/γ's or — this is very relevant for this thesis work — for bulk and surface events. In particular, we will use pulse-shape parameters for the discrimination, and the formula 3.18 will refer to the distributions of these parameters,

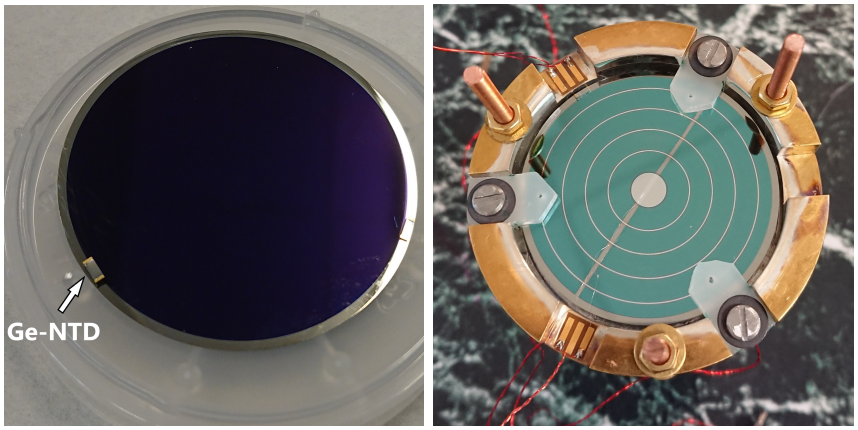

Figure 3.10 – *Left*: ordinary Ge light detector with a Ge-NTD glued on it. *Right*: Neganov-Luke light detector.

described in Section 3.5.

The light detector consists of a highly pure Ge or Si wafer coupled to a sensor for temperature rise measurement as shown in Fig. 3.10 (*left).*

Neganov-Luke light detector

The ordinary Ge light detectors shows a good performance when detecting the scintillation light [80], which enables the discrimination between α particles and β/γ's [62]. But some bolometers are poor scintillators, such as TeO_2 [81, 82]. In this case, detecting the Cherenkov light produced by the particle interaction is a viable alternative, as proposed by T. Tabarelli de Fatis [83]. The energy threshold for electrons to produce a Cherenkov radiation is 50 keV, while for α particle a very high energy threshold, around 400 MeV. Thus, the α interactions will have almost no light and would be possible to discriminate α's from β/γ's. However, the discrimination efficiency is very low because of the weak emitted Cherenkov light signal from β/γ interaction. The tiny detected Cherenkov signal in the light detector is also partially trapped in the absorber because of the high refraction index of TeO_2. The light signal in this case has to be amplified exploiting the Neganov-Luke effect [84, 85] to achieve the required particle identification. When Cherenkov photons with an energy E_0 interacts in the LD, phonons and charge carriers are produced. An applied electric field between Al electrodes (shown in Fig. 3.10 (*right*)) will drift the electron-hole pairs generating additional phonons which will amplify the thermal signal so that the total energy E is equal to:

$$E = E_0 + \xi \frac{q.V}{\epsilon} E_0 \tag{3.19}$$

where q is the charge of the electron, V is the applied voltage, ϵ is the energy needed to create an electron-hole pair, and ξ is a coefficient taking into account the energy lost due to charge recombination and trapping in the light detector. It varies between 0 and 1, and tends to 1 when conditions are perfect: high purity Ge, high electrodes bias, short drift length and neutralised germanium. The gain can be expressed as:

$$G = 1 + \xi \frac{q.V}{\epsilon} \tag{3.20}$$

Fig. 3.10 (*right*) shows a Neganov-Luke light detector.

3.3 Phonon physics

When energy is released in the absorber, the mechanism that leads to a detectable signal depends on which type of sensor we are using. Some sensors are sensitive to athermal phonons, as the case of NbSi, while others are mainly sensitive to thermal phonons, as the Ge-NTD. It is crucial to understand how phonons propagate and evolve in the crystal, and for this it is useful to provide some basic and qualitative notions of phonon physics.

3.3.1 Generalities on phonons

Phonons play an important role in various solid state phenomena, such as the thermal and electrical conductivity of the materials. The term phonon, a quantum of lattice vibrations, is used as an analogy to the photons which represent a quantum of the electromagnetic radiation. So they are described as the allowed energy levels of lattice vibrations. Even if we are working at very low temperatures, the atoms of the lattice do not stay still, they vibrate, because of the Heisenberg uncertainty principle that does not allow atoms to have a definite position and momentum at the same time, even at 0 K.

The phonon dispersion relation (shown in Fig. 3.11) expresses the relation between the wave vector k and the frequency (ω) or energy (E). It can consist of two modes: the acoustic and the optical modes. In acoustic mode the atoms coherently move together from their equilibrium position. When k is small (long wave limit) the dispersion curve is linear taking the form $\omega = vk$, where v is the phase velocity. The nature of vibrations in this region is like sound waves. By looking into the entire lattice, it is as if the whole crystal were stretched and compressed. In the optical mode, the atoms move against each other. In the long wave limit (k$\rightarrow$0), the frequency in the optical branch is constant. It corresponds to the maximum frequency of vibrations. The optical phonons can be created or annihilated by radiation, thanks to the electric field that can displace the two oppositely charged ions in different directions.

Each type of phonon modes is further divided into transverse and longitudinal phonons. In the transverse case, the direction of atomic displacement is perpendicular to the direction of propagation, while for the longitudinal it is parallel. For a three-dimensional crystal with n atoms per unit cell, there are two transversal acoustic (TA) and one longitudinal acoustic (LA) branches, and there are $3n - 3$ optical branches, where n is the number of atoms in the elementary cell. So a mono-atomic lattice ($n = 1$) can have only acoustic branches.

After this brief introduction to phonon physics, it is important for our application to see how phonons generated by a particle interaction propagate and evolve in the crystal.

3.3.2 Athermal and thermal phonons

When an ionizing particle impinges in a dielectric crystal, it loses energy to the atomic electrons in the media via Coulomb interaction. This leads to the production of a cloud of electrons and holes far from the thermal equilibrium containing most of the energy of the particle (within $\sim$0.1 ps). In turn, the cloud of electrons and holes relaxes on the edges of the conduction and valence bands respectively, producing optical phonons in the crystal (within a time scale $\sim$10 ps). On a much longer time scale (a few µs) the electrons and holes recombine releasing an energy that produces acoustic phonons around the Debye

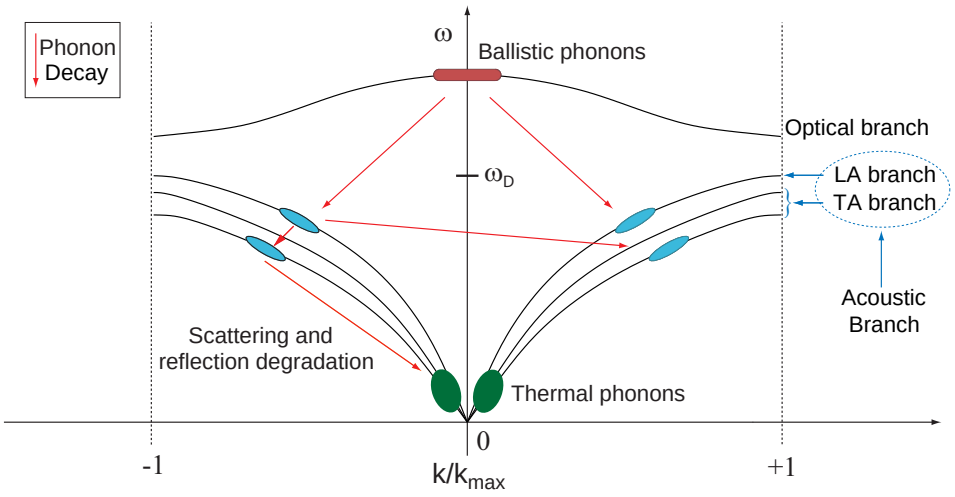

Figure 3.11 – Phonon dispersion curve.

energy (ω_D). Another possibility is that the released energy is transferred to an electron in the conduction band that then de-excites producing optical phonons. Therefore, after few μs, the particle energy released in the crystal is stored in the form of optical and Debye-energy phonons. These phonons are referred to as athermal phonons, which are phonons out of thermal equilibrium with an energy around few tens of meV. In this work, we use “athermal phonons" and “out-of-equilibrium phonons" as synonyms. The optical phonons will decay to longitudinal acoustic phonon around the Debye energy. The acoustical phonons can undergo two important scattering processes [86]:

- spontaneous anharmonic decay in which the acoustic phonon splits into two lower-energy phonons;
- elastic scattering with lattice imperfections (isotopes, impurities and point defects).

One process rate can dominate over the other depending on the phonon frequency. The relation between the rate and the frequency for each process is given by:

- Anharmonic decay: $\tau_a^{-1}=\eta\omega_D(\omega/\omega_D)^5$
- Elastic scattering: $\tau_e^{-1}=\gamma\omega_D(\omega/\omega_D)^4$

where ω_D is the Debye frequency, η and γ are the material-defined constants.

If the rate of the elastic scattering dominates ($\tau_e \ll \tau_a$), then the phonons with frequency ω during its life-time τ_a will undergo multiple elastic collisions separated by time τ_e. This results in diffusive propagation mode. In case the anharmonic decay process rate dominates (($\tau_e \gg \tau_a$), the phonons along the crystal will decay to lower energy phonons, such as LA decaying to two TA. This mode is referred to as “quasiballistic" mode [87]. Quasidiffusive transport has been defined as occurring when the rate at which acoustic phonons scatter elastically exceeds the anharmonic interaction rate. The life-time and the distance traveled by a generation of ω-frequency phonons increases as ω decreases. This will lead to long living ballistic phonons ($\sim$1-10meV) that will further thermalise to reach an energy of the order of μeV.

The excess phonons produced by the impinging particle are measured by a phonon sensor. The phonon sensor is connected to the absorber with an interface capable of

transmitting athermal and/or thermal phonons. If the sensor is mainly sensitive to thermal phonons and if its response is slow with respect to the time required for the out-of-equilibrium phonons to degrade in energy and for the thermal equilibrium to be reached among the various detector components, we return to the case of monolithic bolometer.

As already extensively discussed, there are two types of sensors that will be used in this thesis, thermal and athermal sensitive sensors. The Ge-NTD belongs to former case, it is glued to the surface of the crystal with an epoxy glue which leads to a slow transmission interface. The NbSi is athermal phonons sensitive thermistor and having a good transmission interface with absorber due to the fact it is deposited directly with a relatively large contact surface ($\sim$cm^2). The Ge-NTD will feel the temperature rise when the bolometer reaches thermal equilibrium, which translates into a excellent energy resolution (better than NbSi sensor case) since all the deposited energy is measured in the final state as heat. It is important to state however that no sensor is able to select exactly thermal or athermal phonons. All in general are sensitive to both, but with different efficiencies.

3.4 The CROSS technology

We have shown in Section 3.2 how challenging for double-beta decay experiments the surface α background is, and how it is possible to discriminate α from β/γ by using scintillating bolometers. However this method has two drawbacks: an additional device, the light detector, to collect and measure light is needed, and — much more important — surface β events are not rejected. In fact, the surface α background is not the only surface background limiting future $0\nu\beta\beta$ experiments, but also surface β contamination.

Above 2615 keV, there are two β transitions — originated from ^{214}Bi and ^{208}Tl — with Q-values greater than 3 MeV (respectively, 3270 and 4999 keV). Thus, these two isotopes produce γ's and β's that are energetic enough to give events around 2.5-3 MeV on the whole if they are absorbed together. When these processes happen in the bulk of the crystal, if the internal radioactivity is low enough (typically below a few μBq/kg) these high energy β transitions are not harmful for next-generation experiments as they are accompanied by α emissions and can be rejected by delayed coincidences, as stated above. Conversely, if the processes described above occur at the surface of the materials facing the crystal, since the β range is of the order of 1 mm while that of the α's of a few tens of μm, it may happen that the α particle does not reach the crystal, which will register a pure high-energy β event. This source is extremely challenging as it is very difficult to model, measure and control. We remark once again that scintillating bolometers cannot get rid of this contribution, as they tag α but not surface contamination of βs.

It is then crucial to develop new experimental ideas that could extend the sensitivity of future searches by rejecting all sources of background. An innovative detector technology is tested in the R&D project CROSS (Cryogenic Rare-event Observatory with Surface Sensitivity). In CROSS, the problem can be definitely solved thanks to generalised surface sensitivity (both for α and β). CROSS, in its firstly proposed version, is based on providing bolometers with surface sensitivity features by coating them with a few μm thick superconducting Al film [88]. The film coating will act as a pulse shape modifier for surface events, thus allowing to identify them. The proof of concept of CROSS was a test performed in 2010 at CSNSM lab (Orsay, France) with a TeO_2 crystal coupled to NbSi sensor [89]. In this experiment, a 10 μm Al film coating on

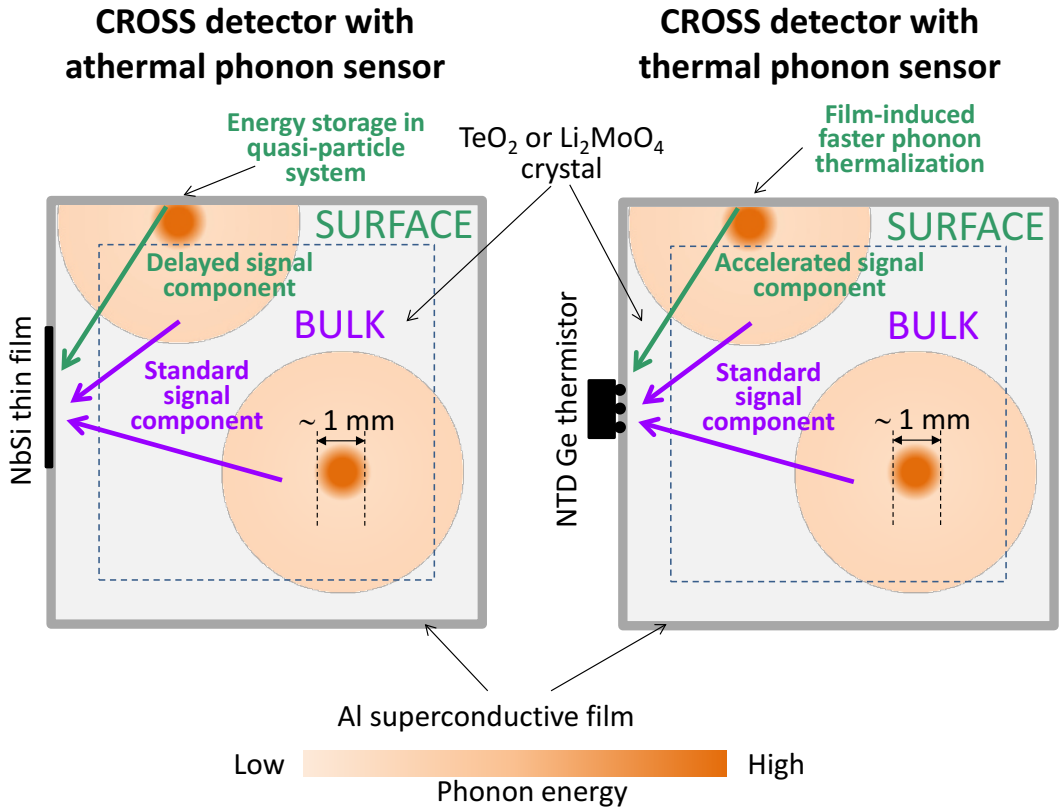

Figure 3.12 – Scheme of surface identification events in CROSS.

one surface faced by an α source showed capability of modifying pulse shapes of surface events, thus allowing their discrimination versus bulk events. The mechanism of how pulses are modified is described below. CROSS will use two types of crystals for the bolometer construction: Li_2MoO_4 and TeO_2.

3.4.1 Sensitivity to surface events

In the original CROSS proposal, which underwent some important revisions thanks to the work performed in this thesis, discriminating surface events from bulk events is obtained by depositing a few μm thick superconducting Al film on the surface of the crystal. Al film critical temperature is T_c= 1.2 K [90]. The discrimination results depend critically on the type of sensor used, especially whether the sensor is sensitive to thermal phonons or athermal phonons.

Let's first study the case in which we a have an athermal phonon sensitive thermistor (NbSi-based in our work) as shown in Fig. 3.12 (*left*). As discussed in the previous Section, when a particle deposits energy in a non-metallic absorber [91]), it produces athermal phonons that, on a time scale much shorter than μ's, form a cloud of about $\sim$ 1 mm size around the event location, with energies of about a few meV (Debye energy), corresponding to temperatures $\geq$ 30 K. If the produced high energy phonons are far from the surface (at a distance larger than about 1 mm), i.e. bulk event, the phonons from this cloud will decay spontaneously due to the quasi-diffusive mode of phonon propagation before reaching the surface, with a decay rate proportional to the fifth power of the phonon energy (or frequency) [92]. Therefore, they will reach the Al film with an

energy insufficient to break the Cooper pairs, even if they will still be far from thermal equilibrium. The binding energy of Cooper pair in Al is about 0.1 meV, corresponding to T_c= 1.2 K. Since our sensor is sensitive to high energy phonons, it will register them with a fast response due to their quick thermalization in the NbSi film itself. On the contrary, the events happening close to the surface with Al film have enough energy to break Cooper pair, since the primordial phonon cloud will intersect the film without no important degradation in the phonon energy. Breaking Cooper pair will produce quasi-particles that have a long recombination time at temperature well below the transition temperature of the superconductor. So a significant fraction of the particle energy will be trapped in the superconducting film in the form of quasi-particles for a time that can extend up to the millisecond range in ultra-pure aluminium (as it is the case for our work). Subsequently, the quasi-particles will recombine to $\sim$ 1.2 K phonons, adding a delayed component to the phonon signal read by the NbSi film [93]. By studying the pulse shape of bulk and surface events we will see that there is a difference between them. In particular, the pulse rise-time of bulk events are faster than the surface events, which have a delayed component. The rising part for surface and bulk events is shown in Fig. 3.13.

In CROSS, it was proposed initially to use the mechanism described above using NbSi films, sensitive to athermal phonons. We anticipate here that, in this thesis work, we have been able to demonstrate that pulse shape discrimination works also with Ge-NTD as a thermistor, that initially was deemed too slow to highlight pulse shape differences between surface and bulk events. This solution was chosen in all the CROSS prototypes and is now the best candidate for the future large-scale CROSS demonstrator. This choice was preferred because it will allow us to keep the present CUORE approach in terms of detector structure and construction. In addition, the manipulation of Ge-NTD thermistors is much easier than that of NbSi films. The Ge-NTDs are simply glued at the crystal, while the NbSi films must be evaporated with a rather complicated and time-consuming process. Furthermore, the use of photo-lithography for the preparation of structured NbSi films is problematic on Li_2MoO_4 because this crystal is hygroscopic.

When we adopted a Ge-NTD phonon readout, we saw an opposite behaviour in terms of the rise-time since these devices are mainly sensitive to thermal phonons. For the bulk events, it will require a long time (on the order of millisecond) for the high energy phonons to degrade to thermal phonons. Only after thermalization the NTD will feel efficiently the bulk events. However, for the surface events, a significant fraction of the energy will be absorbed by the Al film. After the quasi-particle recombination, the phonons are re-injected from the film to the crystal with a much lower energy, equal to the superconducting gap of Al $\sim$ 1.2 K (of the order of 0.1 meV). The phonons produced in the proximity of the film are energy down-graded and thermalized faster than the phonons created in the bulk, as the film converts efficiently phonon energy from the meV scale to $\sim$ 0.1 meV, in a shorter time with respect to that required for spontaneous phonon energy degradation in the bulk. Hence the surface events are faster than bulk events when read by a Ge-NTD as shown in Fig. 3.13 (*right*).

3.5 Pulse shape parameters

The analysis program used to study the bolometer readout is based on the optimal filter developed by E. Gatti and P.F. Manfredi [94], which is a powerful tool to reduce the noise contribution to a signal, leading to the best possible estimation of the signal amplitude in

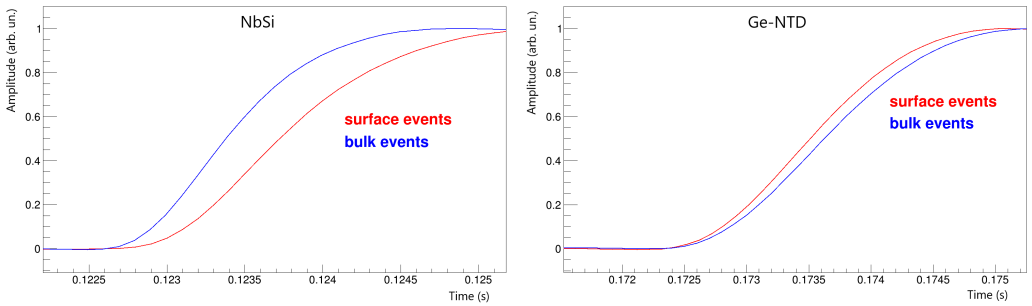

Figure 3.13 – The pulse rise-time edge for surface and bulk events. *left*: Surface events are slower than bulk events when having NbSi sensor. *right*: Surface events are faster than bulk events for Ge-NTD readout.

presence of noise whose power spectrum is known. The signal shape in absence of noise is also assumed to be known. The signal is filtered through a unique transfer function given by

$$H(\omega) = \frac{S_m(\omega)}{|N(\omega)^2|} e^{-i\omega\tau_m} \tag{3.21}$$

where $S_m(\omega)$ is Fourier transform of a mean pulse built by averaging over a large number of pulses — in order to minimize the impact of noise — and $N(\omega)$ is the noise power spectrum obtained by averaging the power spectrum of a large set of data windows not containing signals. The optimal filter does not preserve the signal shape, but the amplitude of the filtered signal provides the best estimation of the original pulse amplitude and thus of the particle energy.

Several pulse shape parameters associated to each single pulse are extracted after data processing. Some of them are computed directly from the pulse waveform in the time domain, without applying any digital filtering. Others are applied always in the time domain, but after the application of the optimum filter. All of them have been tested to check which is the best for discriminating surface from bulk events. Two parameters were chosen, the rise-time and the so-called “fitted amplitude". They are described below.

3.5.1 The rise-time

The rise-time is a very simple parameter. It is the time interval from 10% to 90% of the maximum pulse amplitude, using the waveform in the time domain without any digital filtering. This parameter is the most intuitive one and can be directly related to physical interpretations. For athermal phonon sensitive thermistor, the rise-time is in general shorter compared to the thermal phonons sensitive thermistor. As discussed above, the way the rise-time of the signal works for discrimination depends on the type of sensor and in particular on its sensitivity to athermal or thermal phonons.

3.5.2 The fitted amplitude

The parameter “fitted amplitude” has shown to be very effective in discriminating surface from bulk events. It is obtained in the following way.

Individual pulses and the average pulse are transformed using the optimum filter transfer function — built from a template of the pulse shape and from the noise power

spectrum — and considered in the time domain. The waveforms discussed below refer always to these pulses transformed according to the optimum filter.

An average pulse $A(t)$ with sampled amplitudes $A_i = A(t_i)$ at time t_i is constructed from the bulk events. The maximum amplitude is normalized to 1. Let $S_i = S(t_i)$ be the sampled amplitude of an individual pulse $S(t)$ without normalizing it. The average pulse and the individual pulses are synchronized according to their maximum. When plotting S_i vs A_i we obtain approximately a straight line. (If the individual pulse and the mean pulse are identical, the straight line will have a slope equal to the individual pulse amplitude passing through the origin.) By fitting linearly the straight line we will obtain two parameters, the y-intercept and the slope m.

The slope m is an estimator of the filtered pulse amplitude and it almost coincides with the pulse amplitude S_m estimated with the optimum filtering if $S(t)$ and $A(t)$ have the same shape. Our pulse shape parameter is m/S_m, which turns out to be a very sensitive parameter to the pulse shape, and is equal to 1 for pulses with the same shape as the average pulse. It turns out that in general bulk events have $m/S_m \sim 1$, as expected, of course with a dispersion related to noise. On the contrary, for surface events this parameter deviates considerably from 1.

Unlike the rise-time, which takes into account only the rising edge of the pulse, this parameter is sensitive to the whole pulse shape.

Conclusion

After a general introduction about bolometric detectors, where we have established all the basic notions on which the CROSS technology is based, we have discussed how superconducting Al coating can give surface sensitivity to bolometers to reject surface background.

In the next chapter, we will present the results obtained by coating several sample crystals. We will follow the path that led us to change the initial protocol in favour of a new solution, which allowed us to achieve the desired sensitivity to surface α and β events.

Chapter 4

Study of the surface sensitivity for CROSS detectors

As discussed in the previous chapters, the main limiting factor for the investigation of neutrinoless double-beta decay is the background in the region of interest. In the bolometric approach, the dominant background is due to the α surface contamination in addition to a less dominant contribution from β surface contamination. The BI is estimated to be of the order of 10^{-5} counts/(keV kg yr) after the surface background rejection. So it is crucial to develop a bolometer capable of rejecting the surface backgrounds. This can be achieved by developing a bolometer with surface sensitivity by coating the crystal with the appropriate material.

4.1 Isotope and compound choice in CROSS

Many bolometric compounds have been tested throughout the years in many projects studying neutrinoless double-beta decay: MIBETA [95], CUORICINO [96], CUORE-0 [97] and CUORE [38] with TeO_2 bolometers; LUCIFER/CUPID-0 [79] with ZnSe bolometers; LUMINEU/CUPID-Mo [98] with Li_2MoO_4 bolometers. The results obtained showed that the TeO_2 and Li_2MoO_4 are the best choices in terms of energy resolution, ease of crystallization and internal radiopurity. Two crystal samples used for CROSS prototype tests are shown in Fig. 4.1.

TeO_2 detectors exhibit an excellent energy resolution with values around 5 keV FWHM at the $Q_{\beta\beta}$ of ^{130}Te at 2527 keV and a very high internal radio-purity [99] being less than 1 μBq/kg for ^{238}U and ^{232}Th and their daughters. TeO_2 has been tested in CUORE, the first tonne scale bolometric experiment. In addition, ^{130}Te has a high natural isotopic abundance (34%) which will translate into easiness of enrichment and lower cost as well. One drawback of ^{130}Te is the position of $Q_{\beta\beta}$ just below the end point of the natural γ radioactivity at 2615 keV of ^{208}Tl belonging to ^{232}Th decay chain. This means that controlling the ^{232}Th contamination is a major issue. Another drawback of TeO_2, as mentioned in the previous chapter, is being a poor light emitter. This will lower the ability to discriminate α particles from β/γ to reject them. It is needed then to detect the tiny Cherenkov radiation emitted by β particles with a high performance light detector. This requires an intense R&D that needs some time.

The other choice, Li_2MoO_4, fulfills the major requirement of having a $Q_{\beta\beta}$ of 3034 keV above the highest-energy line of ^{208}Tl. This crystal has been tested extensively as a scintillating bolometer, coupled to a light detector, under LUMINEU and CUPID-Mo

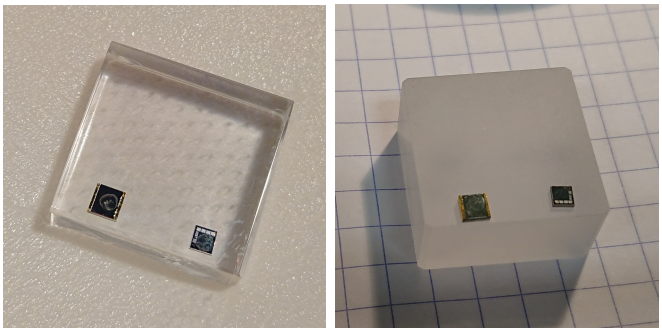

Figure 4.1 – Li_2MoO_4 (*left*) and TeO_2 (*right*) with a Ge-NTD and a heater glued on each crystal.

projects. The energy resolution of Li_2MoO_4 is excellent, 5 keV in the ROI, and its radiopurity is very high (< 1 μBq/kg for ^{238}U and ^{232}Th and their daughters). The crystallization process is simple with a negligible irrecoverable losses of ^{100}Mo ($< 4\%$). This implies low-cost crystal production and high production rate [100]. A drawback of ^{100}Mo is the relatively fast $2\nu\beta\beta$ decay with a half-life $T_{1/2} \sim 7 \cdot 10^{18}$ yr [101]. This will induce background in the ROI because of the random coincidences of the $2\nu\beta\beta$ events (two overlapping $2\nu\beta\beta$ events) due to the slow bolometric response [102].

CROSS aims to study both options, in order to guide the selection of the appropriate bolometer for future experiments or to have a multi-isotope $0\nu\beta\beta$ bolometric experiment [103]. The CROSS technology, as explained in chapter 3, provides a technique to mitigate background due do the surface contamination without relying on the light emitted by the crystals. This technology is especially convenient for the case of TeO_2 due to being a poor scintillation in addition to the difficulty to detect the tiny Cherenkov radiation. The CROSS approach can only control the surface α and β background, so the γ's in the ROI for ^{130}Te are still challenging. But what encourages employing the CROSS approach on ^{130}Te is its high natural isotopic abundance. Thus this compound would be ready for large-scale future experiment that could be hosted in an extremely radio-pure environment with low γ emission.

4.2 Detector assembly

4.2.0.1 Detectors and detector holders

We have designed a very simple holder consisting of a copper disc to fix the bolometers. The holder is capable of holding four $20 \times 20 \times 10$ mm crystals simultaneously, 2 crystals on each side of the holder (Li_2MoO_4 (small LMO) and TeO_2 (small TeO_2)). Another holder was designed to hold $\varnothing 40 \times 20$ mm cylindrical Li_2MoO_4 (big LMO). The two copper holders with crystals are shown in Fig. 4.2. The crystals are grown with materials of natural isotopic composition. Li_2MoO_4 crystals are cut from a large crystalline boule grown with the low-thermal gradient Czochralski technique at Nikolaev Institute of Inorganic Chemistry (Novosibirsk, Russia) [100]. TeO_2 crystals are produced by the company SICCAS (Shanghai, China) [104]. The Li_2MoO_4 and TeO_2 sample crystals have the same features as the crystals employed for CUPID-Mo and CUORE. Each crystal is fixed to the holder using two small PTFE pieces under the crystal and two PTFE pieces pressing from the top and affixed to the holder by copper/brass screws. Table 4.1 shows

Bolometer	Compound	Crystal size [mm]	crystal mass [g]
small LMO	Li_2MoO_4	$20 \times 20 \times 10$	12
small TeO_2	TeO_2	$20 \times 20 \times 10$	25
big LMO	Li_2MoO_4	$\varnothing 40 \times 20$	67

Table 4.1 – Crystalline samples used in the CROSS tests.

the description of the three types of crystals used for the CROSS above-ground tests here described.

Although CROSS aims to get rid of the light detector, relying on rejecting the background by coating the crystal with the appropriate material, a light detector was used in all of the CROSS prototype tests. The purpose was mainly to discriminate neutron capture events on ^{6}Li from the β/γ events. These events are generated by the reaction ^{6}Li(n,t)α, which has a high cross section of 940 barns, and the available energy for the two products is 4.78 MeV. The discrimination is possible because neutrons capture events (which produce the heavy charged particles triton and α) have a lower light yield compared β/γ events, similar to the pure α light yield. This will help in understanding the effect of the interaction point location with respect to the crystal coated-surface on the PSD (details in Section 4.7). In addition, light detection is often useful for a better interpretation of the results achieved on surface event discrimination, as in many measurements most of these events are generated by α sources, providing a useful redundancy for their identification. The light detector used is an optical bolometer consisting of a high-purity germanium wafer ($\varnothing 44 \times 0.175$ mm).

The light detector also has another role, which is to veto the high flux of cosmic muon events since we are working above-ground. It was a Neganov-Luke light detector with a purpose to enhance the device sensitivity [105]. The Neganov-Luke light that has been used is shown in Fig. 4.3.

The copper holder is covered with a reflecting foil (Vikuiti^{TM} Enhanced Specular Reflector Film) and also the crystals are enclosed inside a reflecting foil and then a copper foil. Adding the reflecting foil will increase the light collection in the light detector, which is placed facing the two crystals and fixed with copper rods. The closed assembly is shown in Fig. 4.4.

4.2.0.2 Phonon sensors

The phonon sensor used for the three bolometers is a Ge-NTD that is glued on the surface of the crystals by means of six small epoxy spots of Araldite® glue and a 25 μm thick Mylar spacer. The mass of the Ge-NTD is around 50 mg, and the size is 3×3×1 mm. Two opposite 3×1 mm faces are metallized for electrical and thermal contact through gold bonding wires. The light detector also has a Ge-NTD sensor with one third of the size of the Ge-NTD glued on the crystals. At 20 mK, the resistance of the Ge-NTD is around 1 MΩ. A heater is glued on each crystal to provide periodically thermal pulses in order to stabilize the response of the bolometers [106]. The crystals heat sink is thermalised mainly through the sensor bonding gold wires with a thickness of 25 μm, which give also the electrical connection to read the signal.

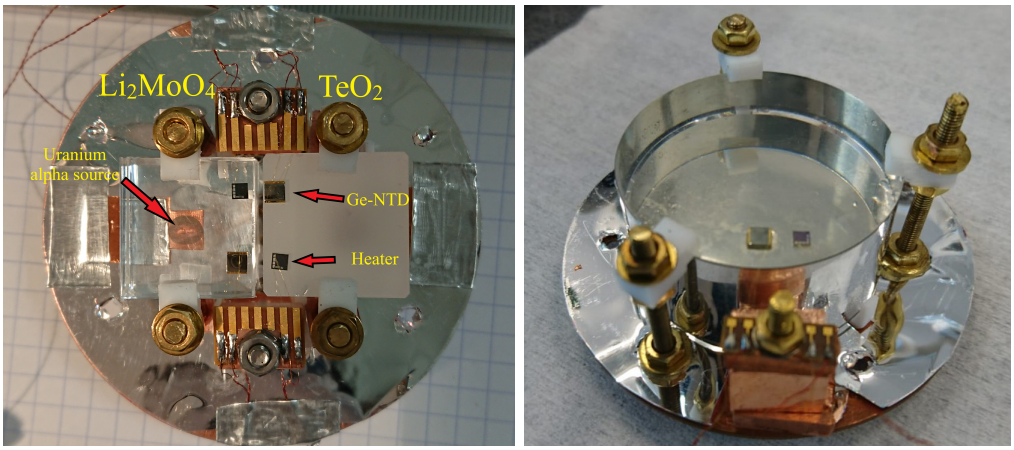

Figure 4.2 – Photographs of the assembly of the three bolometers used for CROSS prototypes. *left*: small LMO and small TeO_2 with a size of $20 \times 20 \times 10$ mm affixed on a copper holder that is covered with a reflecting foil. Two small PTFE pieces are placed under each crystal, and two other PTFE pieces are used on the top to press and fix the crystals. A Ge-NTD and a heater are glued on the top of each crystal. An uranium α source is placed below the crystals to induce surface events. This source appears clearly under small LMO crystal, as in this case no Al film is deposited on the bottom surface. Sometimes a Po α source is used and it is placed facing the upper face of the bolometers. *right*: Big LMO also assembled in the sane way. The Po α source for this detector is placed facing the lateral surface.

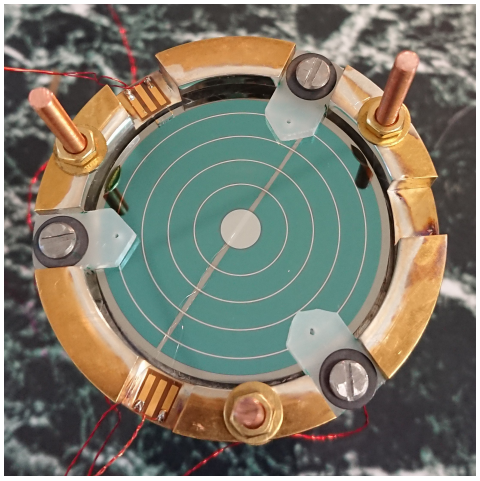

Figure 4.3 – The Neganov-Luke light detector used for CROSS prototype assembly. The light detector is facing the crystals. It consists of a Ge wafer coated with a SiO thin layer to reduce the light reflection.

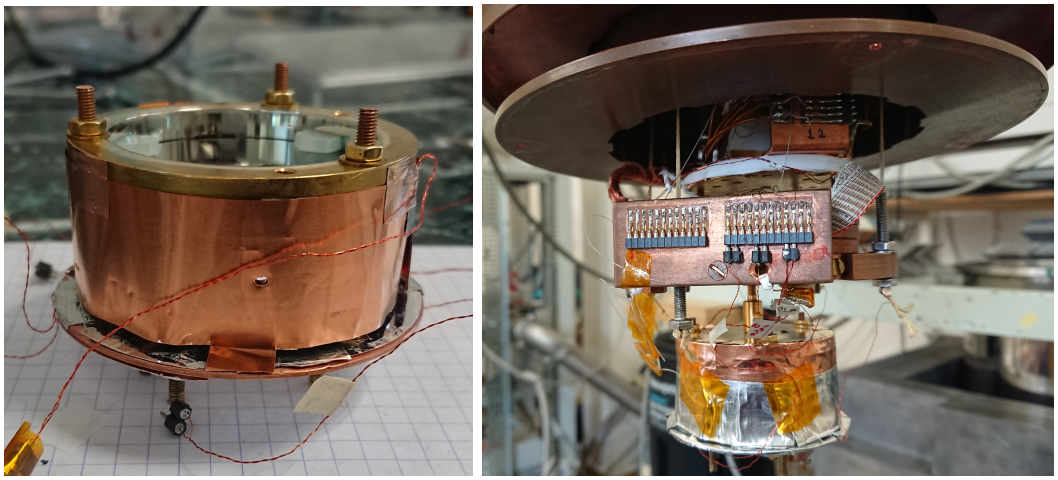

Figure 4.4 – *left*: The crystals and the light detector are surrounded by a copper foil covered with a reflector internally. *right*: The final assembly is attached to the floating plate.

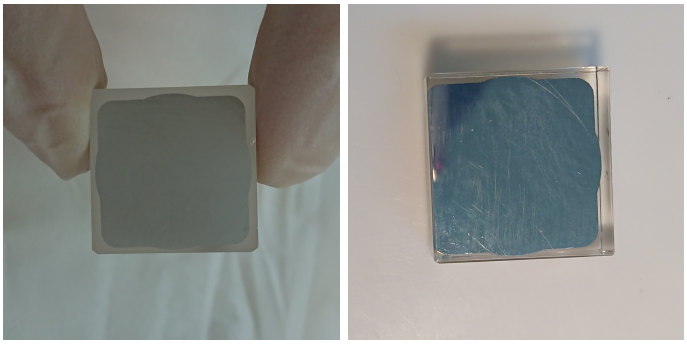

Figure 4.5 – Small TeO_2 (*left*) and small LMO (*right*) with 10 μm Al film coating on one surface.

4.2.0.3 Film evaporation on crystals

To provide the crystal with surface sensitivity, the surface is coated with a thin layer of aluminum. First the Li_2MoO_4 crystal is polished to avoid effects due to the weak hygroscopicity of Li_2MoO_4. The TeO_2 surface are roughly treated to have an opaque surfaces as for CUORE crystals. The surface of the crystals is then bombarded by 90 eV Ar ions that remove about 1 nm layer from the surface. Before depositing Al on the surface, a 25 nm thick SiO under-layer is deposited in order to improve the Al adhesion on the surface. Al coating is done by evaporation under vacuum on a side of the crystal, that is mechanically fixed, by means of an electron gun located at IJCLab. The thickness of the Al tested was between 1 and 10 μm with a deposition rate of 4 nm/s. The thickness of Al is controlled by looking at the evaporation duration with a periodic check of the rate through a piezoelectric quartz. Fig. 4.5 shows Li_2MoO_4 and TeO_2 with one surface coated with Al.

4.2.0.4 α and β sources

To induce surface events, an α source was placed facing the surface of the crystal. Two α sources were used, an uranium and a polonium sources.

The uranium α source is obtained by desiccating a drop of uranium acid solution on a copper foil. The source is 0.6 mm away from the surface of the crystal. The source has two main α lines at $\sim$ 4.2 and $\sim$ 4.7 MeV from ^{238}U and ^{234}U decays respectively. In addition, it works also as a β source with a spectrum extending up to $\sim$ 2.27 MeV from the isotope ^{234m}Pa decay. The decay chain of ^{238}U is shown in Fig. 4.6. The β rate of ^{234m}Pa is very close to the α rate of ^{238}U. Due to the fact that the solution is acid, it was concluded from the results (the α energy is degraded for a significant fraction of the events) that this source penetrates below the surface of the copper foil and exhibits significant straggling.

The polonium α source is obtained by implanting ^{218}Po atoms (produced by ^{222}Rn decay) on a copper tape which will decay quickly into ^{210}Pb. (The polonium source is in fact a ^{210}Pb source.) This nucleus has a half-life of 22.3 yrs and decays to ^{210}Po that provides a $\sim$ 5.3 MeV monochromatic α line. This source is in addition a β emitter from the isotope ^{210}Bi, direct daughter of ^{210}Pb, with a spectrum extending up to $\sim$1 MeV (see Fig. 4.6 for the ^{210}Pb sub-chain). Even in this case, the α and the β rates are very similar to each other.

The uranium α source is placed facing the coated side, thus generating identifiable surface events. The ^{210}Po is usually placed facing an uncoated side which will generate events similar to the bulk events. More seldom, it is placed facing a coated face (we will point out which is the case when this source is used). In the following, even if improperly, we will define surface events those events occurring close to the surface with a coating film, and bulk events are the ones occurring far from the surface with the film. The sensitivity to surface events with respect to the distance from the Al film is discussed in 4.7.

After completing the assembly, the detector is ready for cooling inside the cryostat located above-ground at IJCLab (Appendix A). The cryostat used is a dry high-power dilution refrigerator with a 4 K stage cooled by a pulse-tube [107]. Fig. 4.4 (*right*) shows the detector attached to the floating plate which is thermally coupled and mechanically decoupled to the mixing chamber by four springs to reduce the acoustic noise due to cryostat vibrations. The cryostat is surrounded by a lead shield to suppress the environmental γ background. The measurements are typically done at mixing-chamber base temperatures of 15.5 mK and 22 mK.

4.3 Electronic readout system

In order to read out the resistance of the thermistor, a current is injected in the thermistor using a DC bias circuit. By imposing a potential across the series of the thermistor and two load resistors with resistance $R_L >> R_{bol}$, a constant current flow across the thermistor with resistance R_{bol}. The value of the load resistor is in the range 100 MΩ-30 GΩ depending on the thermistor resistance.

The front end electronics is located at room temperature. The electronics chain is custom [108] and consists of a differential voltage-sensitive low-noise preamplifier, a programmable gain amplifier (PGA), and a Bessel low-pass filter, which is usually set with a high frequency cut-off at 675 Hz. The data acquisition is performed by a commercial 16 bit Analog-to-Digital Converter (ADC) with 5 kHz sampling frequency.

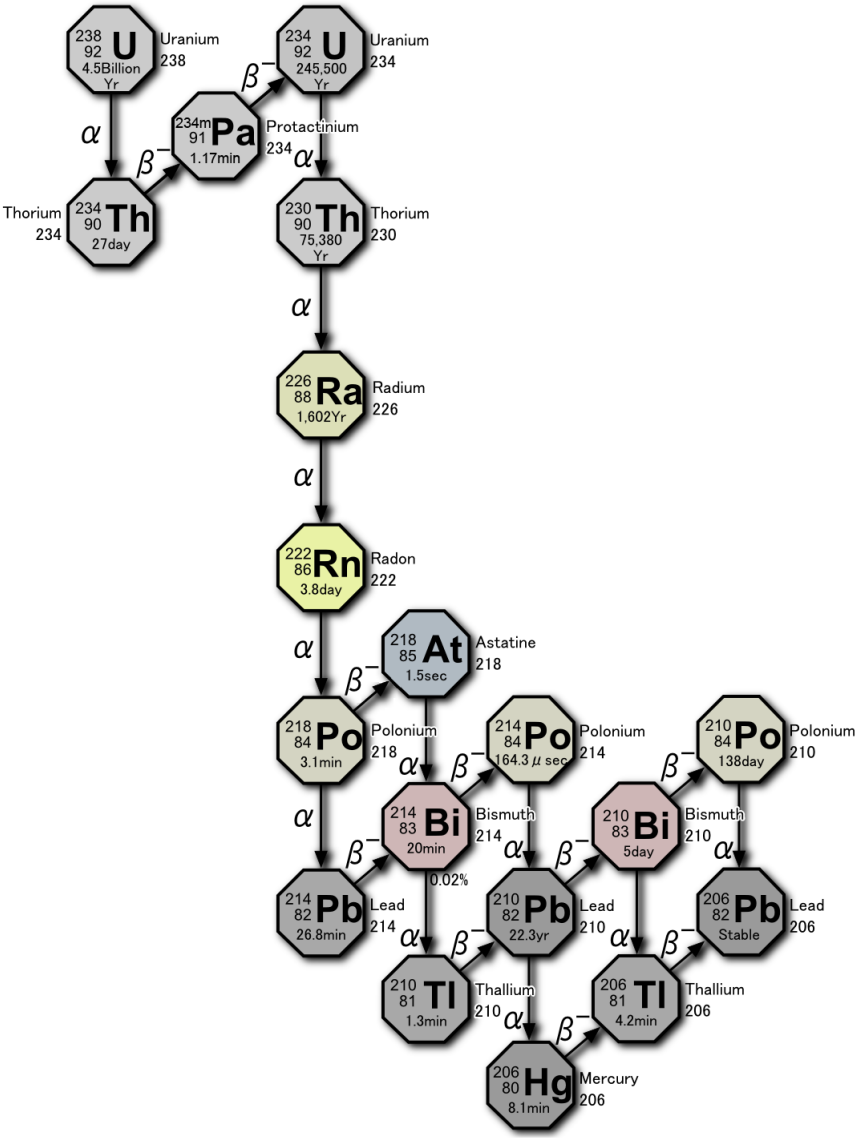

Figure 4.6 – The decay chain of ^{238}U.

4.4 Data processing and data analysis

The data of the measurements are streamed and stored continuously. Then they are treated and analyzed offline with a tool developed at IJClab (Ithaca program). The program extracts signal amplitudes according to the Gatti-Manfredi optimum filter [94], whose purpose is to maximise the signal to noise ratio, providing the best estimation of the signal amplitude under given noise conditions and with known signal shape. This filter doesn't preserve the pulse shape.

First, the data processing starts by building a template for a measurement. It consists of a mean pulse obtained by averaging over a certain number of pulses chosen manually within a specific amplitude range (they are taken from the bulk events at an amplitude much below that of the surface α's events) and a noise power spectrum. The next step is to trigger the required events. Triggering the events is based on setting two parameters: (i) the threshold, an amplitude value above which events are tagged — it is chosen to be a multiple of the standard deviation of the baseline to avoid selecting noise fluctuations; (ii) a parameter called "correlation", which quantifies how much the filtered pulse is similar to the mean pulse — it is the Pearson correlation coefficient between the individual pulse above threshold and the mean pulse (if they are identical, the correlation is equal to 1, otherwise it is < 1). To be triggered, a pulse must have a correlation above a given fixed value.

At the end of data processing, the output of the analysis is an n-tuple file that contains a set of parameters for each event, arranged in columns. Some of the parameters are: the raw amplitude, the filtered amplitude S_m, the correlation, the decay time (from 90% to 30% of the maximum amplitude), the rise-time and the slope of the fitted amplitude parameter m (the last two parameters are discussed in section 3.5).

4.5 Surface events identification with Ge-NTD sensor

Many tests of prototypes have been performed with Li_2MoO_4 and TeO_2 crystals. Each test had the aim to understand how film coating works in providing discrimination between surface and bulk events and how different variables affect discrimination. The varying parameters in the runs were the type of coating material, the thickness of the coating and the fraction of coating material covering the crystal. The description of each run is shown in Table 4.2 and 4.3.

In the following, each cryogenic run will be designed with the code "CROSS#", where # refers to the time ordering of the runs. Some numbers are skipped, as the related run did not succeed or provided no relevant results.

CROSS run number	Li_2MoO_4 (LMO) small LMO ($20 \times 20 \times 10$ mm^3) & big LMO ($\varnothing 40 \times 20$ mm)	TeO_2 ($20 \times 20 \times 10$ mm^3)
1	no Al film	no Al film
2	small LMO: 10 μm Al film on one surface	10 μm Al film on one surface
3	small LMO: 10 μm Al film on one surface	1 μm Al film on one surface
7	small LMO: 10 nm Pd film on one surface + big LMO: 10 μm on one base surface	10 nm Pd film on one surface
8	big LMO: 10 μm on one base surface + 2 μm on the lateral surface	-
9	big LMO: 10 μm on one base surface + 2 μm on the lateral surface (repetition of CROSS8)	-

Table 4.2 – A description of all of the CROSS prototype tests performed above-ground.

CROSS run number	Li_2MoO_4 (LMO) small LMO ($20 \times 20 \times 10$ mm^3) & big LMO ($\varnothing 40 \times 20$ mm)	TeO_2 ($20 \times 20 \times 10$ mm^3)
10	small LMO: 10 nm Pd film fully covered + big LMO: 10 μm on one base surface + lateral side polished	10 nm Pd film fully covered
11	small LMO: 10 nm Pd film fully covered	10 nm Pd film fully covered
12	10 nm Pd + 100 nm Al small LMO: bi-layer films on one surface U source	10 nm Pd + 100 nm Al bi-layer films on one surface U source
13	10 nm Pd + 100 nm Al small LMO: bi-layer films on one surface Po source	10 nm Pd + 100 nm Al bi-layer films on one surface U source
14	10 nm Pd + 100 nm Al small LMO: bi-layer films on one surface no source	10 nm Pd + 100 nm Al bi-layer films on one surface no source
15	10 nm Pd + 100 nm Al small LMO: bi-layer grid on one surface U source	-

Table 4.3 – A description of all of the CROSS prototype tests performed above-ground.

4.5.1 Small Li_2MoO_4 with Al coating

4.5.1.1 *Test on bare Li_2MoO_4 crystal (CROSS1)*

The first test performed on Li_2MoO_4 (small LMO in Table 4.1) was without any coating, just a bare crystal. This test is very important as it helps to understand the intrinsic discrimination power (DP) of the crystal with Al film. In addition, checking the bolometric performance in terms of energy resolution and sensitivity is essential. This will confirm later if the bolometric performance is affected by the addition of a coating material. The measurements were performed at 15.5 and 22 mK (mixing chamber temperatures).

The Ge-NTD was characterized to obtain the resistance as a function of temperature (shown in Fig. 4.7). By a variable transformation that linearizes Eq. 3.9 and fitting the points we obtain the R_0 and T_0 parameters. The load-curve and the optimum working point is obtained before starting data taking to choose the bias with best signal to noise ratio. The load-curve is shown in Fig. 4.8. The optimum working point at each temperature is shown in the table below:

Temperature	Current [nA]	V_{bol} [mV]	R_{bol} [MΩ]	Thermistor temperature [mK]
15.5 mK	1.3	5.9	4.7	19.0
22 mK	8.3	4.1	0.49	26.4

Table 4.4 – The bias current, voltage, the resistance and the temperature of the thermistor of small LMO without Al film coating.

Although the floating plate temperature is at 22 mK (or 15.5 mK), the temperature of the thermistor is in fact at a higher temperature because of the applied bias. The real temperature, when bias is applied, can be deduced from the resistance of the thermistor using the equation below derived from Eq 3.9:

$$T_{bol} = \frac{T_0}{(log\frac{R}{R_0})^2} \tag{4.1}$$

Substituting the value of R_0, T_0 and R_{bol} at the working point we get the real temperature of the thermistor which is stated in Table 4.4. This temperature is a few mK higher than the stabilised temperature on the floating plate, as the detector is heated up by the readout power.

At very low bias or at low power, the temperature of the thermistor is close to the temperature of the floating plate. Fig. 4.9 shows the temperature of the bolometer as a function of power which tends to the floating plate temperature as the power decreases.

An external thorium calibration source was placed facing the detector (external to the cryostat) in order to calibrate the energy spectrum. The ^{232}Th source provides some main γ-lines: ^{212}Pb 238.6 keV, ^{208}Tl 510.7 keV, ^{208}Tl 583.2 keV, ^{228}Ac 911.2 keV. The calibrated energy spectrum of small LMO at 15.5 mK is shown in Fig. 4.10. Some of the peaks are from ^{238}U natural γ radioactivity, such as the ^{214}Bi 609.3 keV, related to radon in the air. The energy resolution is about 3.5 keV FWHM at the ^{208}Tl 583 keV.

In Table 4.5 we report the sensitivity, defined as the pulse amplitude/deposited energy [nV/keV] and it is calculated using this formula:

$$S = \frac{DR\ A}{2^n\ G\ E} \tag{4.2}$$

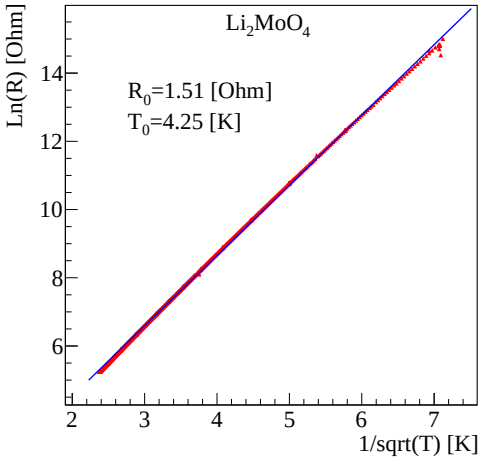

Figure 4.7 – The RT curve of small LMO, fitted to extract R_0 and T_0.

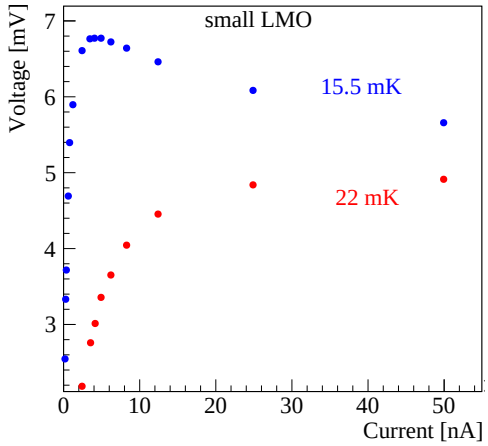

Figure 4.8 – The load curve of small LMO without Al film at 15.5 and 22 mK.

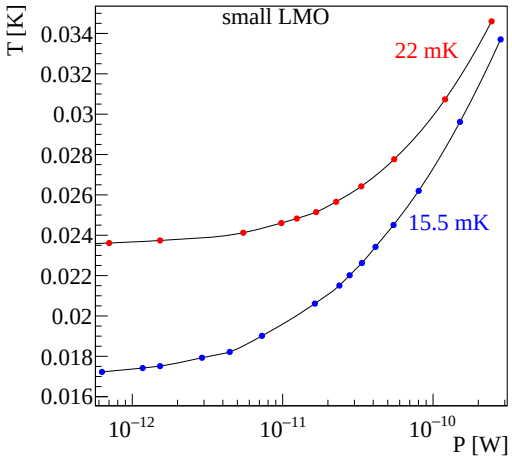

Figure 4.9 – This graph shows the temperature as a function of power for small LMO without Al film.

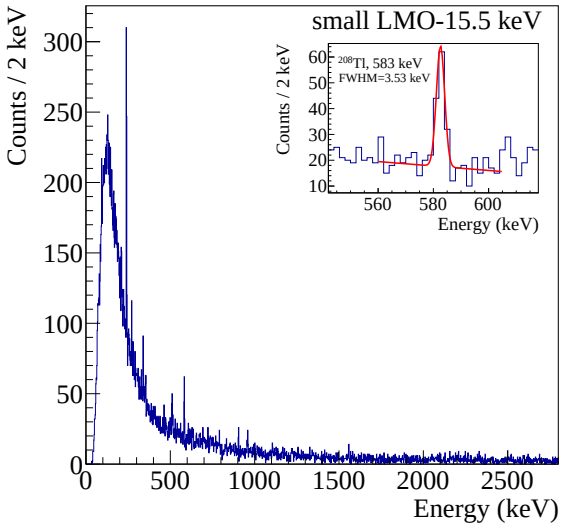

Figure 4.10 – The spectrum for small LMO without Al coating at 15.5 mK. The peaks are generated by the environmental radioactivity and by the ^{232}Th calibration source.

where DR is the dynamic range, n is the ADC digitization, G is the gain, A is the amplitude of the peak in ADU and E is the energy of the same peak in keV. In addition, the reduced sensitivity (η), the rise-time τ_r, the decay-time τ_d and the baseline resolution are reported in the table.

Temperature (mK)	Sensitivity (nV/keV)	η (MeV^{-1})	τ_r (ms)	τ_d (ms)	FWHM$_{bsln}$ (keV)	FWHM$_{bsln}$ (nV)
15.5	292	6.7 $\times 10^{-3}$	12	38	1.2	350
22	58	2.2 $\times 10^{-3}$	8.5	33	1.3	75

Table 4.5 – The sensitivity, η, rise-time (at 2.6 MeV), decay-time (at 2.6 MeV), baseline resolution in keV and nV for LMO without Al coating.

It is interesting to compare the observed sensitivity with the one expected from the considerations reported in Section 3.1.6 and using the Eq. 3.15. The thermistor logarithmic sensitivity A (related to T_0 by $A = 0.5 \cdot \sqrt{T_0/T_{ele}}$), the voltage across the thermistor V_{bol} and the thermistor-electron temperature T_{ele} are known. Assuming a monolithic bolometer, $\Delta T_{ele} = \Delta T$ is given by the deposited energy divided by the total heat capacity, which can be obtained by summing that of the LMO crystal (see Section 3.1.1) and that of the Ge-NTD (see Section 3.1.2). Using the values reported in Table 4.4 for the operation point and the value of T_0 reported in Figure 4.7, it is readily calculated that the sensitivity should be 202 nV/keV at 22 mK base temperature and 1000 nV/keV at 15.5 mK base temperature. The real sensivities (see Table 4.5) are between 3 and 4 times lower. This is not surprising when considering the brutal approximation of monolithic bolometer. A full thermal simulation — based on the actual bolometric thermal model of Section 3.1.5 — shows indeed that the temperature variation of the Ge-NTD electrons is in general a few times smaller than that obtained when considering a single thermal stage.

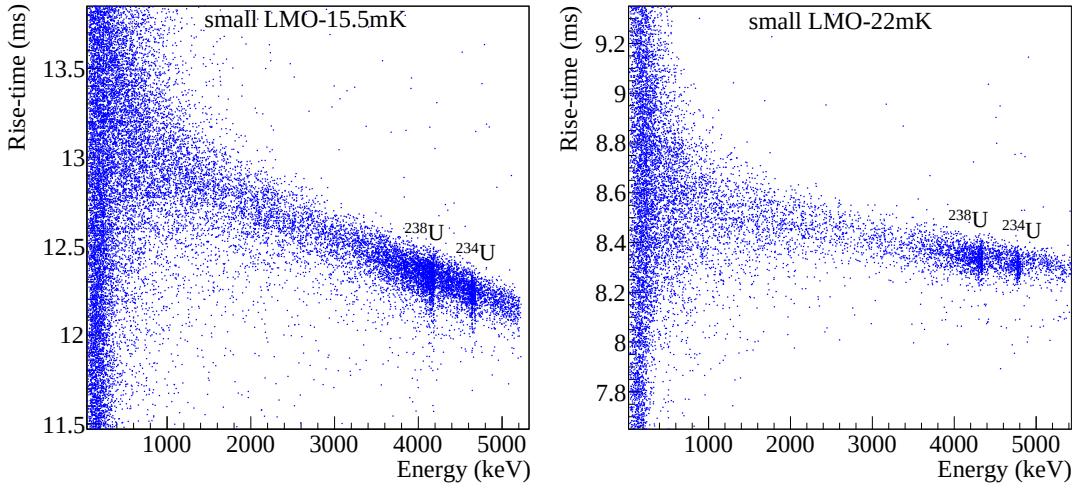

Figure 4.11 – The rise-time vs pulse-amplitude of small LMO without Al film. The amplitude is calibrated using the γ calibration. The two lines of the uranium α source are apparent in the β/γ band with a very slight deviation towards faster events.

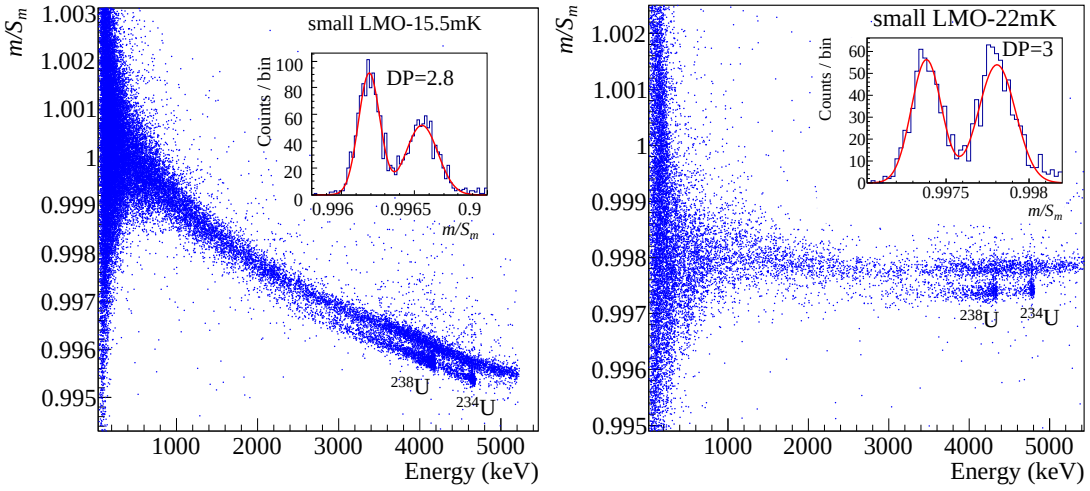

Figure 4.12 – The fitted-amplitude PSD parameter vs pulse-amplitude for small LMO without Al film coating. Discrimination between α and β/γ events is apparent that is discussed in the text.

We have tested the intrinsic pulse shape discrimination for LMO without Al film. We will report the pulse shape discrimination capability between α and β/γ using the rise-time and the fitted-amplitude pulse shape parameters (described in section 3.5). In terms of the pulse rise-time, LMO shows hints of discrimination between α and β/γ as shown in Fig. 4.11. Using the fitted-amplitude parameter (Fig. 4.12), a clear separation between α and β/γ appears, although it is not enough to reject the α's completely without losing β/γ events. The discrimination powers (as defined in Eq. 3.18) are 2.8 and 3 using rise-time and fitted amplitude respectively. (We consider discrimination acceptable when DP$>$ 3.2, which corresponds roughly to 99.9% rejection of the background events.) This discrimination is due to the fact that LMO is a scintillating bolometer, and it is a well known phenomenon especially for molybdates [109]. The light yield depends on the nature of the interacting particle in the crystal. For α's, the scintillation states along their path in the crystal are saturated because of the high ionization density. This implies a larger fraction of their energy to flow in the heat channel. This is less significant for β/γ. This will lead also to different time evolutions of the signal between α and β/γ in the heat channel. The discrimination power is computed for a range around the 4.2 MeV taking only ^{238}U α line.

4.5.1.2 *One surface 10 μm Al film coating (CROSS3)*

10 μm Al film was evaporated on one side of the small LMO crystal (20×20 mm^2) that is facing a uranium α source. The fraction of the coated surface represents 1/4 of the total crystal surface. We try to reproduce the same experimental conditions with respect to the initial test without Al film. The working points at 15.5 and 22 mK has been chosen to have a resistance of the thermistor comparable to the one of CROSS1 (as referred to in Table 4.4). The table below shows the biased current, V_{bol}, R_{bol} and the thermistor temperature:

Temperature	Current (nA)	V_{bol} (mV)	R_{bol} (MΩ)	Thermistor temperature [mK]
15.5 mK	1.3	5.1	4.08	19.4
22 mK	6.3	3.0	0.484	26.4

Table 4.6 – The bias current, voltage, the resistance and the temperature of the thermistor of small LMO with 10 μm Al film coating on one side.

The Ge-NTD in this run was not characterized, so it was assumed to have the same R_0 and T_0 as the previous measurement, since it is the same sensor and was glued in the same way. The temperature of the thermistor at the working point is comparable to the previous measurement and it is stated in Table 4.6. So the working temperature between this run and the previous run with no Al film are almost the same.

The energy spectrum of small LMO with Al film at 15.5 mK is shown Fig. 4.13. The energy resolution of the bolometer at the ^{208}Tl 583 keV peak is around 3.8 keV, which is comparable to CROSS1. The resolution of the bolometer in this run was affected by the unstable baseline that shows a lot of variations over time. The sensitivity of the measurement and also the reduced sensitivity η are similar to the corresponding CROSS1 parameters, which means that the Al film did not have an impact on the performance of the bolometer (Table 4.7). Also the baseline resolution is good and similar to small

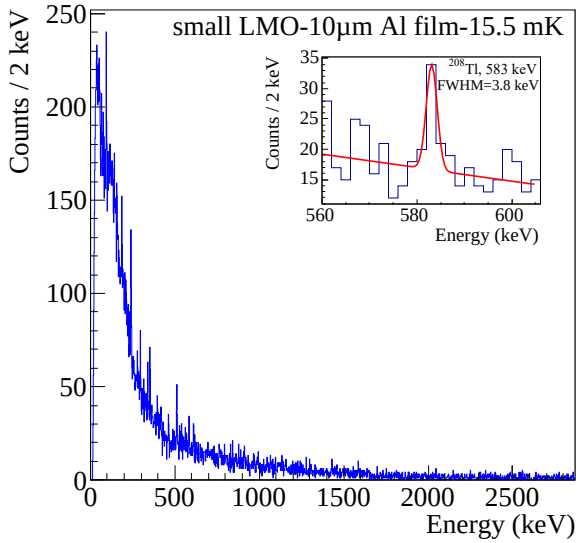

Figure 4.13 – The spectrum for small LMO with 10 μm Al coating at 15.5 mK. The peaks are generated by the environmental radioactivity and by the ^{232}Th calibration source.

Temperature (mK)	Sensitivity (nV/keV)	η (MeV^{-1})	τ_r (ms)	τ_d (ms)	FWHM$_{bsln}$ (keV)	FWHM$_{bsln}$ (nV)
15.5	192	5.5 $\times 10^{-3}$	6.7	39	1.2	230
22	53	2.8 $\times 10^{-3}$	4.1	32	1.9	101

Table 4.7 – The sensitivity, η, rise-time (at 2.6 MeV), decay-time (at 2.6 MeV), baseline resolution in keV and nV for small LMO with 10 μm Al-film-coating.

LMO without a coating material. Since the Ge-NTD was re-glued and re-bonded, it is not surprising that the rise-time and the decay-time vary to some extent with respect to the previous measurement.

The effect of the Al film appears clearly if we look at Fig. 4.14 which shows the rise-time versus the energy. The film provides a faster pulse for the surface events as it has been anticipated in section 3.4.1. So surface events are characterized by a shorter rise-time. All the surface α's can be safely rejected with a full acceptance of β/γ. No clear discrimination is visible for surface β which are emitted also from the uranium source. However, a hint of β discrimination can perhaps be appreciated in the plot of the rise-time vs energy at 15.5 mK (Fig. 4.14) where there is a faster rise-time population (merging with the bulk population) that extends up to 2 MeV. Since this population did not appear in CROSS1, it could be a hint of β's from ^{134m}Pa. Note that calibrating the spectrum by means of the γ peaks leads to the a miscalibration of surface α events: the low energy uranium α line appears at about 4.7 MeV instead of the nominal 4.2 MeV. This is consistent with the argument that close-to-film events are more effectively thermalised, in addition to that the detector response to heavy charged particles is different from that to γ's in Li_2MoO_4 (thermal quenching of alphas). We have to consider however that the application of the optimum filtering [94] may distort the amplitude evaluation for surface

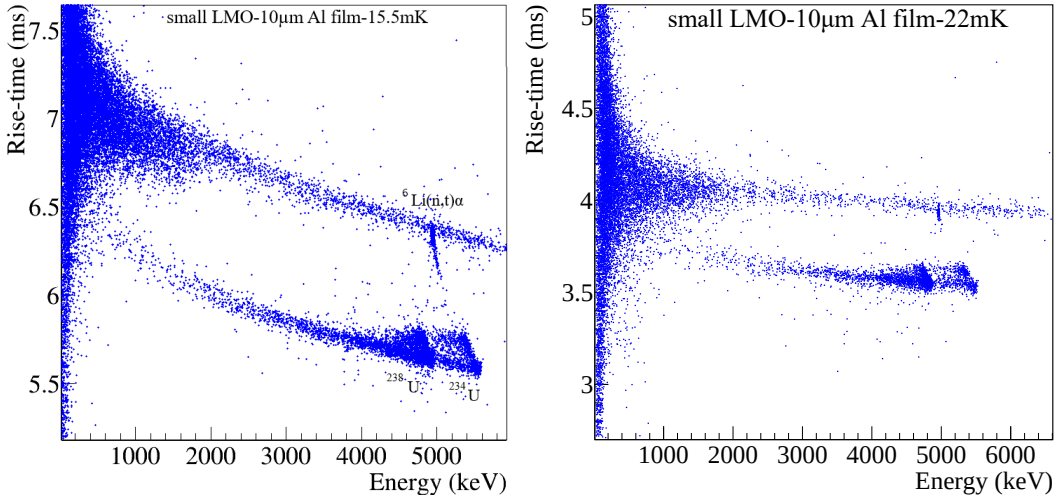

Figure 4.14 – The rise-time vs pulse-amplitude of small LMO with 10 μm Al coating. The surface α events, from the uranium source placed facing the Al film, are faster than the bulk events. The α lines shows different populations. These population are discussed in the text.

events, since the reconstruction of the amplitude by the optimal filter depends on the pulse shape. In fact, two pulses with the same amplitude but different shapes will be assigned a different amplitude after filtering, and so different energy.

In general, we use the fitted-amplitude pulse shape parameter because it shows to provide a better discrimination power between surface and bulk events. Fig. 4.15 shows the fitted-amplitude parameter versus the energy, where surface α's are completely separated from the bulk if we neglect the pile-up that affects heavily the pulse shape. The discrimination powers are shown in the insets. As discussed below, the shape of the α distributions is not simply Gaussian, because of the non-negligible thickness of the Al film. Therefore, in some cases we fit the alpha distribution with two Gaussian curves (for example in 4.15, *right*), obtaining two values for DP. The lower value will be considered to establish if the discrimination is sufficient. In this case, α's are separated well above the requirements.

As stated above, the α event region shows different populations. It is important to stress that the α range in aluminum is around 16.8 μm and 20 μm at 4.2 MeV and 4.7 MeV respectively. This means that α particles that are emitted at a small angle with the surface of the crystal are fully absorbed in the Al film since the thickness of the Al film is similar to the range of the α's in aluminum. α particles that have been emitted almost normal to the surface of the crystal, deposit partially their energy in Al film and the rest in the crystal.

Fig. 4.16 illustrates the three different α populations (regions 1,2 and 3) and the neutron capture in lithium events (region 4, section 4.7). Region 1 are the α particles that are fully absorbed in the Al film. Region 2 represents the α particles that deposited partially their energy in the Al film and the rest in the crystal. A GEANT4 based Monte Carlo simulation [110, 111] of this configuration was done to measure the ratio between α's in region 1 and region 2. It is expected that $\sim 58\%$ of the α particles are fully absorbed in Al film for the 4.2 MeV line. This showed a very good agreement with the experimental distribution of the two regions. Fig. 4.17 shows the experimental distribution of the 4.2 MeV α's. Region 3 correspond to the energy-degraded α's that

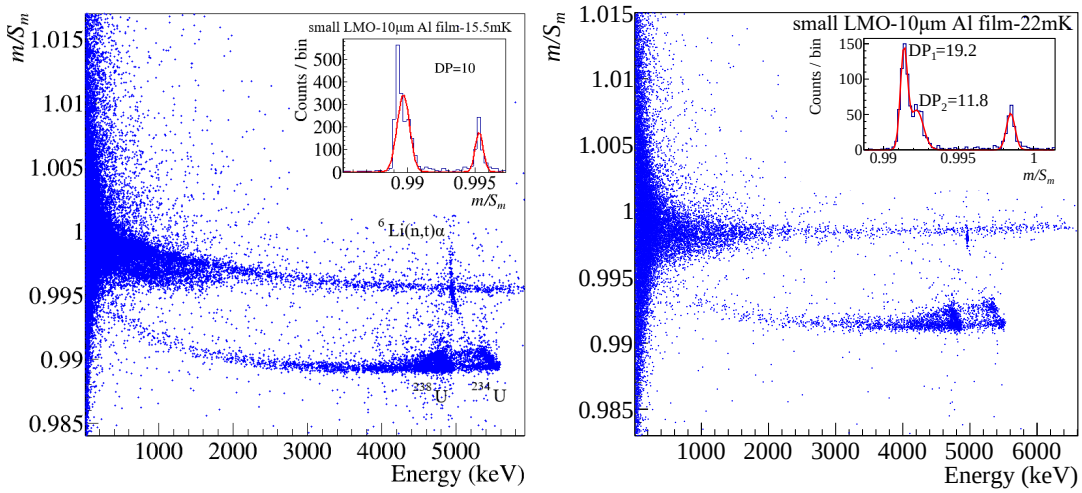

Figure 4.15 – The fitted-amplitude parameter is plotted as function of the energy for small LMO with 10 μm Al coating. The α events from the uranium source are clearly discriminated.

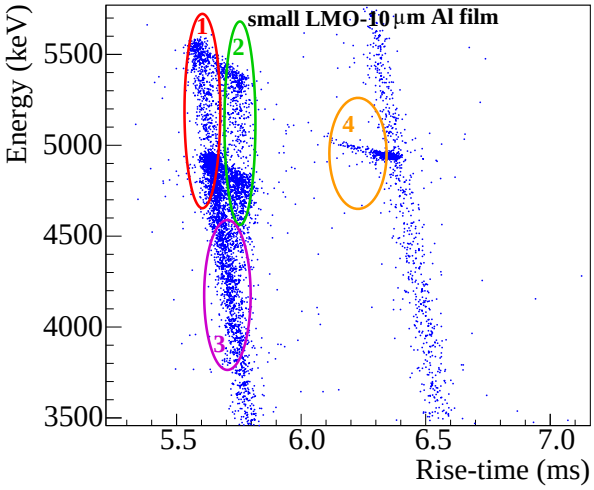

Figure 4.16 – The energy vs the rise-time for small LMO coated on one side with Al film facing an α source. The different populations are discussed in the text.

lose some of their energy in the source before reaching the Al film.

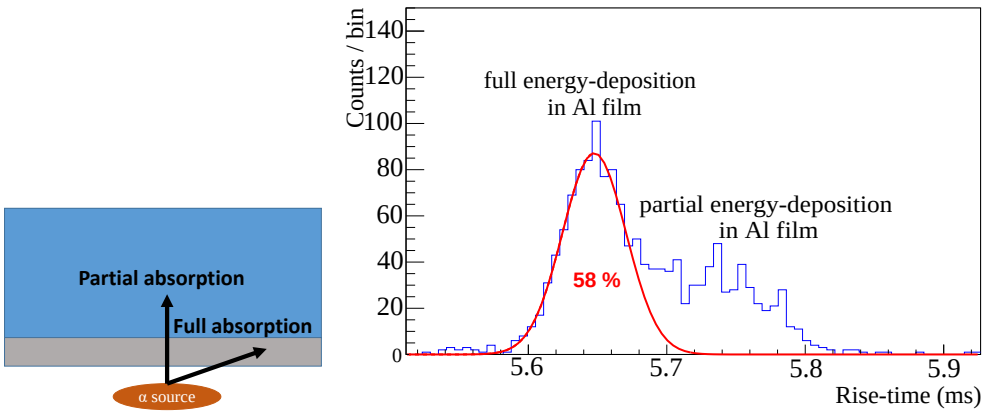

Figure 4.17 – *Left*: Schematic geometry of the α-particles absorption in the Al-film coated on a side of the crystal. *Right*: The distribution of the rise-time of the events corresponding to the ∼4.2 MeV α-particle from the uranium source.

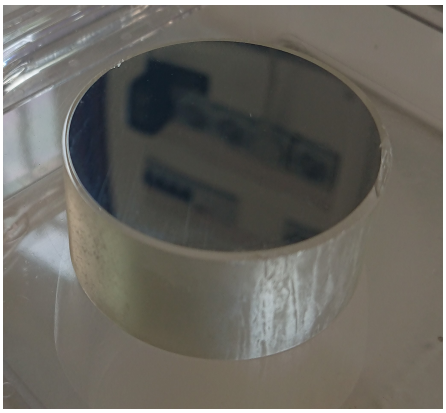

Figure 4.18 – A 10 μm Al film evaporated on one side on big LMO.

4.5.2 Large Li_2MoO_4 with Al coating

The fact that the CROSS demonstrator, that will take place in Canfranc underground laboratory, will be based on large crystals and not small ones, as demanded by double-beta decay applications, led us to move to large crystals to see if in this case the discrimination can be kept even with a large fraction of the crystal surface covered by Al film coating. A preliminary test was performed on a $\varnothing 40 \times 20$ mm cylindrical Li_2MoO_4 crystal, with a mass of about 67 g, (big LMO) to confirm first that pulse shape discrimination for surface α events also works on big crystals. The crystal is shown in Fig. 4.18.

4.5.2.1 *One surface Al film coating (CROSS7)*

A 10 μm Al film was evaporated on one base of the cylindrical crystal shown in Fig. 4.18. The Al film was faced by an uranium α source. The NTD was glued with a thin layer of glue spread all under it (not 6 small spots). A measurement was performed at 22 mK with the bias and the corresponding resistance shown in Table 4.8. The temperature of the crystal is around 26.8 mK with a floating plate temperature of 22 mK. The sensitivity for big LMO, 36 nV/keV, is lower than small LMO, as expected, due the

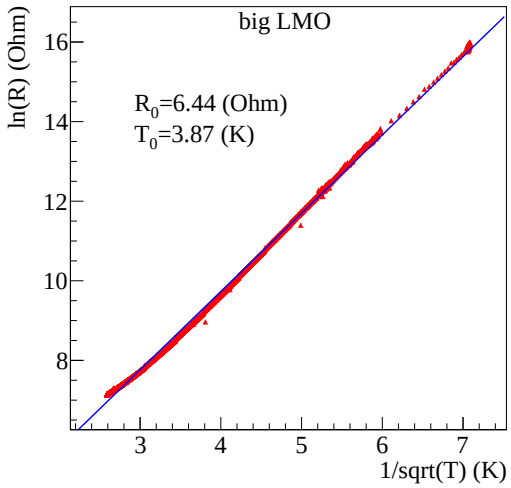

Figure 4.19 – The RT curve of big LMO, fitted to extract R_0 and T_0.

larger heat capacity. It should however be noted that the reduced sensitivity is only half that of small LMO in spite of a mass ∼6 times higher, showing the good performance of the detector. The sensitivity, reduced sensitivity, rise-time, decay-time and the baseline resolution are given in Table 4.9.

Temperature	Current [nA]	V_{bol} [mV]	R_{bol} [MΩ]	Thermistor temperature [mK]
22 mK	4.6	4.97	1.07	26.8

Table 4.8 – The bias current, voltage, the resistance and the temperature of the thermistor of big LMO with 10 μm Al film coating on one side.

Temperature (mK)	Sensitivity (nV/keV)	η (MeV^{-1})	τ_r (ms)	τ_d (ms)	FWHM$_{bsln}$ (keV)	FWHM$_{bsln}$ (nV)
22	36	1.2 $\times 10^{-3}$	3.4	90	9.3	335

Table 4.9 – The sensitivity, η, rise-time (at 2.6 MeV), decay-time (at 2.6 MeV), baseline resolution in keV and nV for big LMO with 10 μm Al film coating on one side.

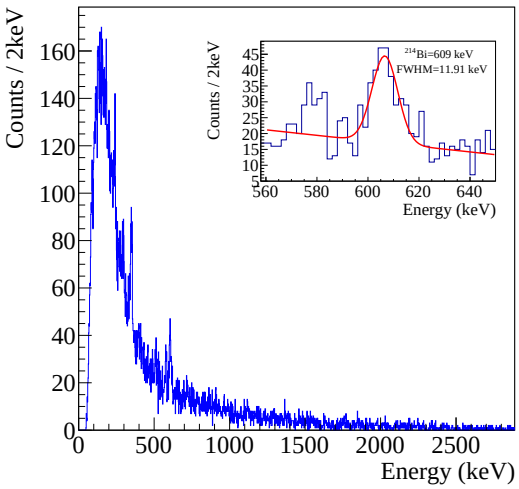

Figure 4.20 – The spectrum for big LMO with 10 μm Al film coating at 22 mK.

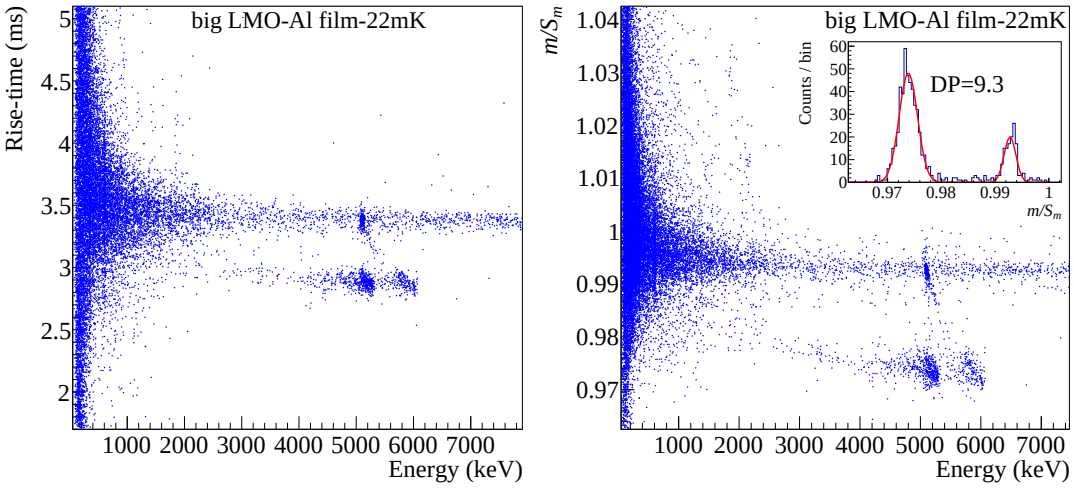

Figure 4.21 – *Left*: The rise-time vs the energy. *Right*: The fitted-amplitude vs the energy for big LMO with 10 μm Al film coating on one side.

The energy resolution in the energy spectrum is not excellent. The FWHM of the ^{214}Bi 609 keV peak is around 11.9 keV, however justified by the large baseline noise (FWHM$_{bsln}$ = 9.3 keV). Fig. 4.20 shows the energy spectrum of big LMO with one side Al coating. The discrimination capability between surface α's and the bulk is preserved for bigger crystals. Fig. 4.21 shows the rise-time and the fitted amplitude parameters vs the amplitude. The discrimination power using the fitted amplitude parameter for big LMO with one-surface-Al-coating is around 9.3. This is a very important results, as it confirms that the discrimination can work for big crystals as the CROSS demonstrator will require. However, no surface β's discrimination is appreciable, as observed in small LMO.

4.5.2.2 *Lateral surface Al-film-coated crystal (CROSS9)*

The next step was to increase the fraction of the coated surfaces for big LMO. In addition to the existing 10 μm Al film on the bottom face, a 2 μm Al film was evaporated on the lateral curved side, by rotating the crystal during the deposition. A polonium α source was placed facing the lateral side, leaving the uranium α source facing the bottom coated face. The measurement working point was chosen to achieve the same thermistor resistance as the previous measurement. It was necessary to work at a lower temperature, 20.6 mK, to have the required Ge-NTD resistance, as given in Table 4.10. This is related to the non-complete reproducibility of the assembly. The bolometric performance in terms of the sensitivity was decreased a little, but this is not surprising since the setup was reassembled (Table 4.11). What is more important is that the reduced sensitivity of this measurement is the same as the previous one.

Temperature	Current [nA]	V_{bol} [mV]	R_{bol} [MΩ]	Thermistor temperature [mK]
20.6 mK	4.0	4.2	1.1	26.8

Table 4.10 – The bias current, voltage, the resistance and the temperature of the thermistor of big LMO with 10 μm Al film coating on one side plus 2 μm-thick Al film on the lateral surface.

Temperature (mK)	Sensitivity (nV/keV)	η (MeV^{-1})	τ_r (ms)	τ_d (ms)	FWHM$_{bsln}$ (keV)	FWHM$_{bsln}$ (nV)
20.6	31	1.2 $\times 10^{-3}$	3.4	120	6.3	195

Table 4.11 – The sensitivity, η, rise-time (at 2.6 MeV), decay-time (at 2.6 MeV), baseline resolution in keV and nV for big LMO with 10 μm Al film coating on one side plus 2 μm-thick Al film on the lateral surface.

The discrimination capability for surface α's from the uranium source (facing the 10 μm Al-coated-surface) has been reduced significantly (Fig. 4.22). The α's from the polonium source (facing the 2 μm Al-coated-surface) appear to be better discriminated from the bulk events with respect the α's from the uranium. Looking at the bulk events, it seems that they are affected by the large fraction of surface Al-film-coated leading to their better thermalization as happens for the surface α's. It is not clear what could be the reason for the better separation of polonium α's compared to the uranium α's. The two possible options that first come to the mind are the Al film thickness or the quality of the Al film. The Po α's are facing a 5 times less Al film thickness compared to uranium α's. The second possibility could be that the Al film quality on the lower side was affected, since it was evaporated before the lateral surface. To clarify if the loss in discrimination is due to a deterioration of the bottom Al film coating or the increase of the coated-surface fraction, the Al film on the lateral surface was removed and the surface was polished. The next section describes this test and the results in details.

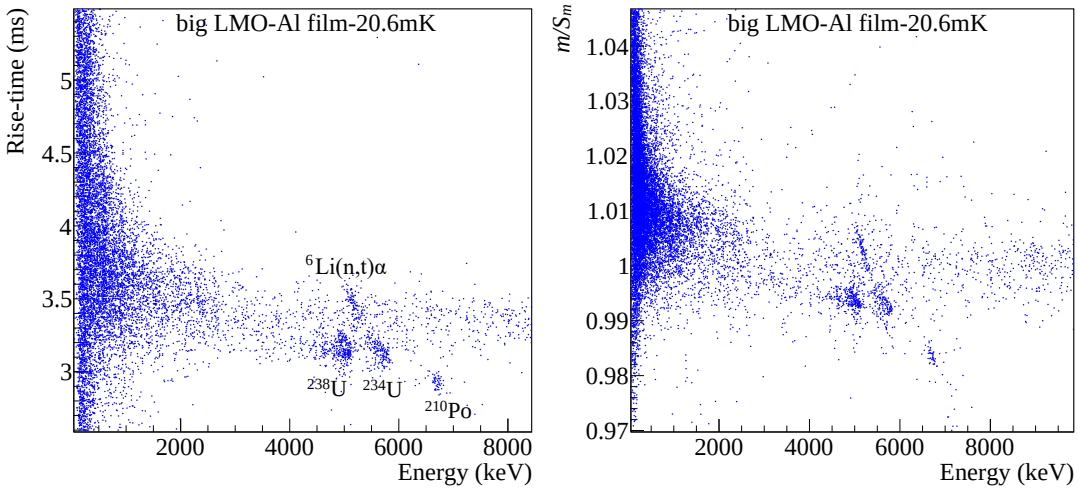

Figure 4.22 – *Left*: The rise-time vs the energy. *Right*: The fitted-amplitude vs the energy for big LMO with 10 μm Al film coating on one side plus 2 μm-thick Al film on the lateral surface.

4.5.2.3 *Polishing lateral surface (CROSS10)*

To investigate the possible reason of losing most of our discrimination capability in big LMO, it was decided to recover the initial setup of big LMO with just Al-film coating on the bottom surface. If the discrimination capability is recovered, it means that increasing the fraction of coated surfaces affects the discrimination of surface α's. If not, it means that the Al film on the bottom surface is not doing its job anymore because of possible defects appeared after the first test on big LMO. This may happen due to the hygroscopicity of LMO that can lead to an alteration of the LMO-Al interface. The same working point as the previous tests was chosen (Table 4.12). The sensitivity and the reduced sensitivity is similar to that obtained in the first measurement of the big LMO. The baseline resolution has been improved due the better measurement conditions, especially in terms of noise level. The sensitivity and the pulse-shape parameters are given in Table 4.13.

Temperature	Current [nA]	V_{bol} [mV]	R_{bol} [MΩ]	Thermistor temperature [mK]
20.6 mK	4	4.9	1.02	27

Table 4.12 – The bias current, voltage, the resistance and the temperature of the thermistor of big LMO with 10 μm Al film coating on one side after polishing the lateral side.

Temperature (mK)	Sensitivity (nV/keV)	η (MeV^{-1})	τ_r (ms)	τ_d (ms)	FWHM$_{bsln}$ (keV)	FWHM$_{bsln}$ (nV)
20.6	38	1.2 $\times 10^{-3}$	3.7	104	4.4	167

Table 4.13 – The sensitivity, η, rise-time (at 2.6 MeV), decay-time (at 2.6 MeV), baseline resolution in keV and nV for big LMO with 10 μm Al film coating on one side after polishing the lateral side.

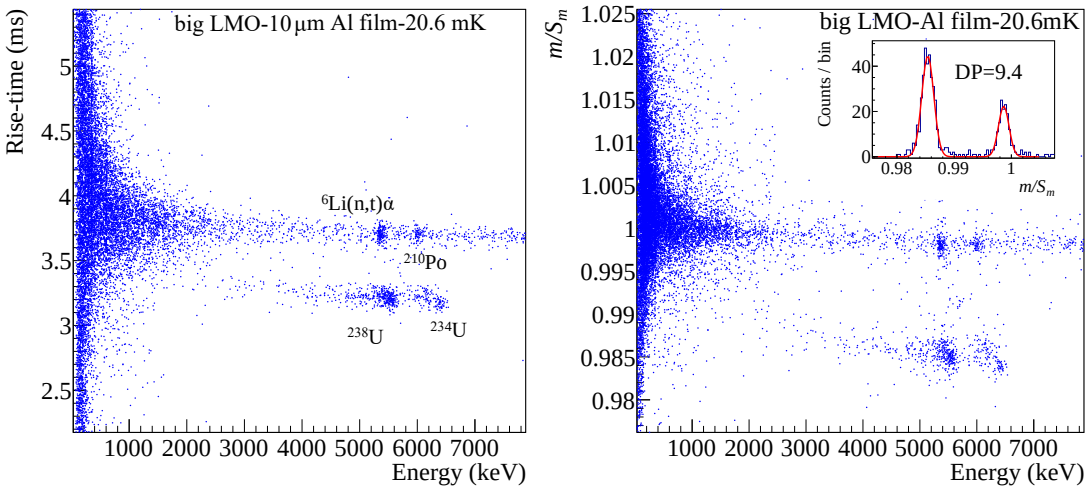

Figure 4.23 – *(Left)*: The rise-time vs the energy. *(Right)*: The fitted-amplitude vs the energy. The detector is big LMO with 10 μm Al film coating on one side after polishing the lateral side.

Fig. 4.23 shows the rise-time and fitted-amplitude vs the amplitude for big LMO with one surface coating. The discrimination power has been recovered after removing the lateral surface coating. This result leads to a primary conclusion that increasing the fraction of coated surface affects the discrimination capability, it reduces our pulse shape discrimination power. The reason is not fully understood yet, but it may be explained by the fact that the bulk events are also being affected by the Al film in terms of faster thermalization since they see a large fraction of the crystal surface coated.

4.5.3 Small TeO_2 with Al coating

4.5.3.1 *Test on bare TeO_2 crystal (CROSS1)*

As for small LMO, the first test on small TeO_2 was carried out with a crystal without any Al coating (CROSS1). This test is important to check the intrinsic performance of the crystal without any coating. The Ge-NTD was characterized to obtain R_0 and T_0 (Fig. 4.24). The load-curve and the optimum working point was obtained before starting data taking to choose the bias with best signal to noise ratio. The load-curve is shown in Fig. 4.25. The optimum working point at 22 mK is shown in the table below:

Temperature	Current [nA]	V_{bol} [mV]	R_{bol} [MΩ]	Thermistor temperature [mK]
22 mK	5.0	4.2	0.83	22.7

Table 4.14 – The bias current, voltage, the resistance and the temperature of the thermistor of small TeO_2 without coating.

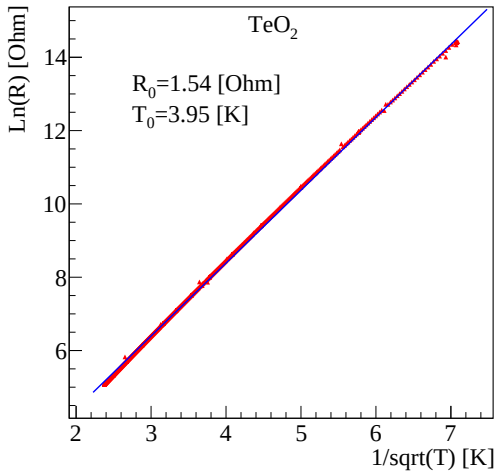

Figure 4.24 – The RT curve of small TeO_2, fitted to extract R_0 and T_0.

The thermistor temperature, derived from Eq. 4.1, is given in Table 4.14. The power versus the temperature of the thermistor at 22 mK is given in Fig. 4.26. For a low bias or power, the temperature of the thermistor is close to the temperature of the floating plate.

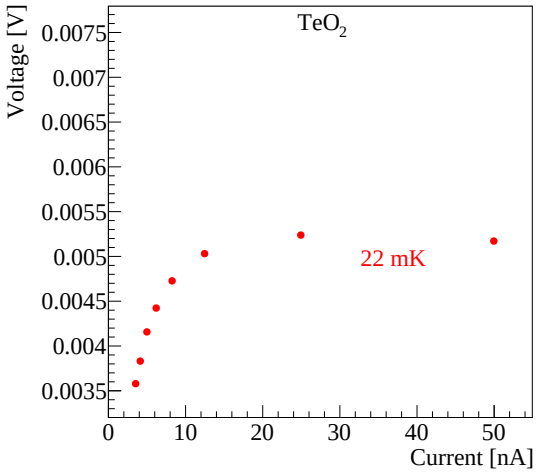

Figure 4.25 – The load curve of small TeO_2 without Al film at 22 mK.

A thorium calibration source was placed in front of the detector and outside the cryostat. The energy spectrum of small TeO_2 at 22 mK is shown in Fig. 4.27. The

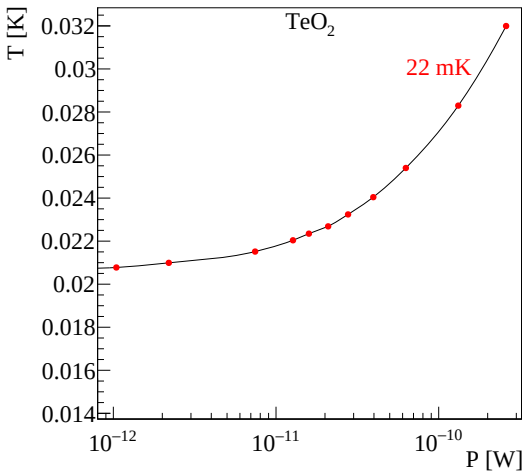

Figure 4.26 – This graph shows the temperature as a function of power for small TeO_2 without Al film.

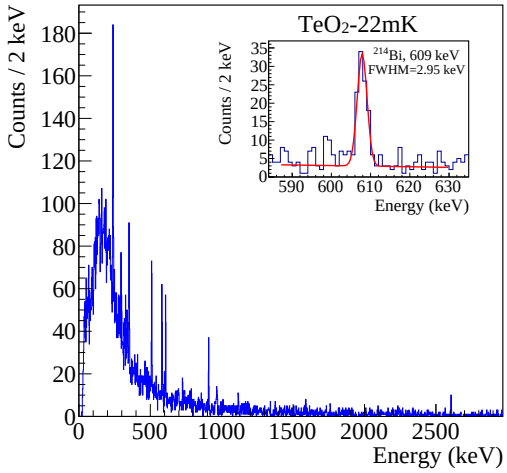

Figure 4.27 – The energy spectrum for small TeO_2 without Al coating at 15.5 mK. The peaks are generated by the environmental radioactivity and by the ^{232}Th calibration source.

peaks that appear in the spectrum are γ-lines from the ^{232}Th and ^{238}U decay chains. The energy resolution is about 3 keV FWHM at the ^{214}Bi 609 keV. More pronounced γ peaks appear in TeO_2 compared to small LMO because of its higher density and average atomic number. In Table 4.15 we report the sensitivity, the reduced sensitivity (η), the rise-time (τ_r), the decay-time (τ_d) and the baseline resolution at 22 mK for small TeO_2. The sensitivity of small TeO_2 is similar to the one of small LMO.

The test showed that there is no discrimination between α and β/γ using either pulse shape parameters, the rise-time or the fitted-amplitude. This is explained by the same but reversed argument used for LMO crystal. Since TeO_2 is a very poor scintillator, the pulses in the heat channel for α and β/γ have the same time evolution. Fig. 4.28 shows the rise-time and the fitted-amplitude versus the pulse amplitude.

Temperature (mK)	Sensitivity (nV/keV)	η (MeV^{-1})	τ_r (ms)	τ_d (ms)	FWHM$_{bsln}$ (keV)	FWHM$_{bsln}$ (nV)
22	48	1.8 $\times 10^{-3}$	8.0	69	1.5	72

Table 4.15 – The sensitivity, η, rise-time (at 2.6 MeV), decay-time (at 2.6 MeV), baseline resolution in keV and nV for small TeO_2 without Al film coating.

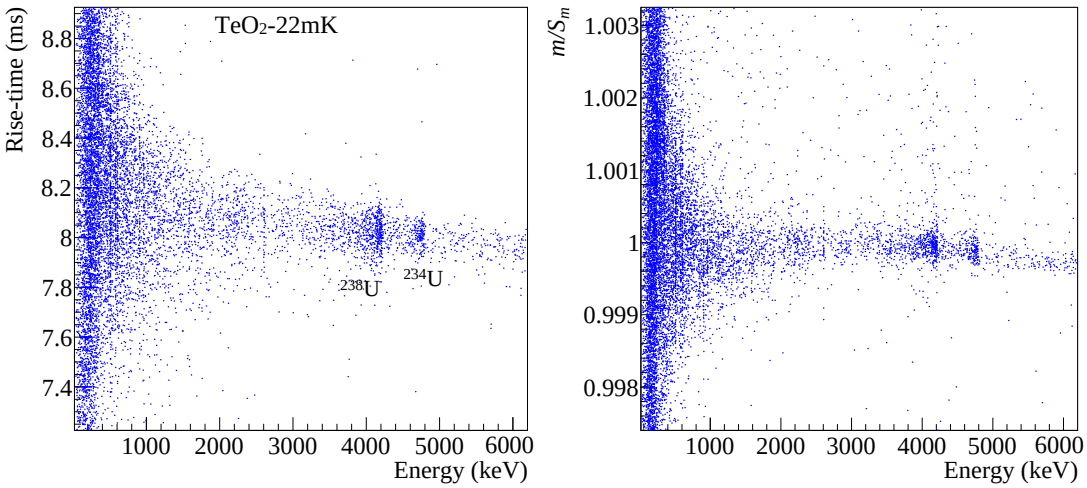

Figure 4.28 – *Left*: The rise-time vs the energy . *Right*: The fitted-amplitude vs the energy for the same crystal for small TeO_2 without Al film coating.

4.5.3.2 *One surface 10 μm Al film coating (CROSS2)*

A 10 μm thick Al film was evaporated on one surface of small TeO_2 (20×20 mm side). An uranium α source is facing the Al film to induce surface α's. A polonium α source was placed facing a non-coated surface, the surface opposite to the coated one. 1/4 of the total crystal surface is coated. The working point of the experiment is close to the one of the previous measurement. The bias current, V_{bol} and R_{bol} at 22 mK are given in Table 4.16. The temperature of the thermistor at the working point is 22.2 mK (Table 4.16). The working temperature of the thermistor between this run and the previous one are close.

Temperature	Current [nA]	V_{bol} [mV]	R_{bol} [MΩ]	Thermistor temperature [mK]
22 mK	5	4.7	0.95	22.2

Table 4.16 – The bias current, voltage, the resistance and the temperature of the thermistor of small TeO_2 with 10 μm-Al-film-coating on one side.

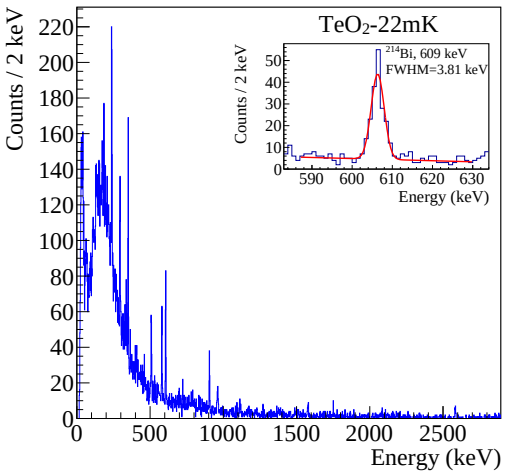

Figure 4.29 – The γ spectrum for small TeO_2 with 10 μm-thick Al film coating on one side. The peaks are generated by the environmental radioactivity and by the ^{232}Th calibration source.

Temperature (mK)	Sensitivity (nV/keV)	η (MeV^{-1})	τ_r (ms)	τ_d (ms)	FWHM$_{bsln}$ (keV)	FWHM$_{bsln}$ (nV)
22	55	1.7×10^{-3}	6.3	54	1.6	88

Table 4.17 – The sensitivity, η, rise-time (at 2.6 MeV), decay-time (at 2.6 MeV), baseline resolution in keV and nV for small TeO_2 with 10 μm-Al-film-coating on one side.

The energy spectrum of small TeO_2 at 22 mK is shown in Fig. 4.29. The energy resolution FWHM at the ^{212}Bi 609 keV is around 3.8 keV. The sensitivity of the crystal was not affected by the addition of Al film (55 nV/keV). In addition, the bolometric performance in terms of the reduced sensitivity is the same as in CROSS1. Table 4.17 shows the bolometric parameters.

Al film coating on TeO_2 showed to be effective, as one can appreciate in Fig. 4.30, where the surface α's from the uranium source are clearly separated from the bulk. The surface α's from the polonium source are in the bulk region, as expected. The surface events are faster than the bulk events also for TeO_2. The interpretation of distribution of the uranium surface α's in the figure is describe on page 70 (CROSS3). The Po α line is at its nominal energy (5.3 MeV) because the QF of α is close to unity for TeO_2 [112]. On the other hand, the U α's are at a higher energy because the thermalization efficiency of close-to-film events is higher than bulk events and is maximum for full absorption in the film.

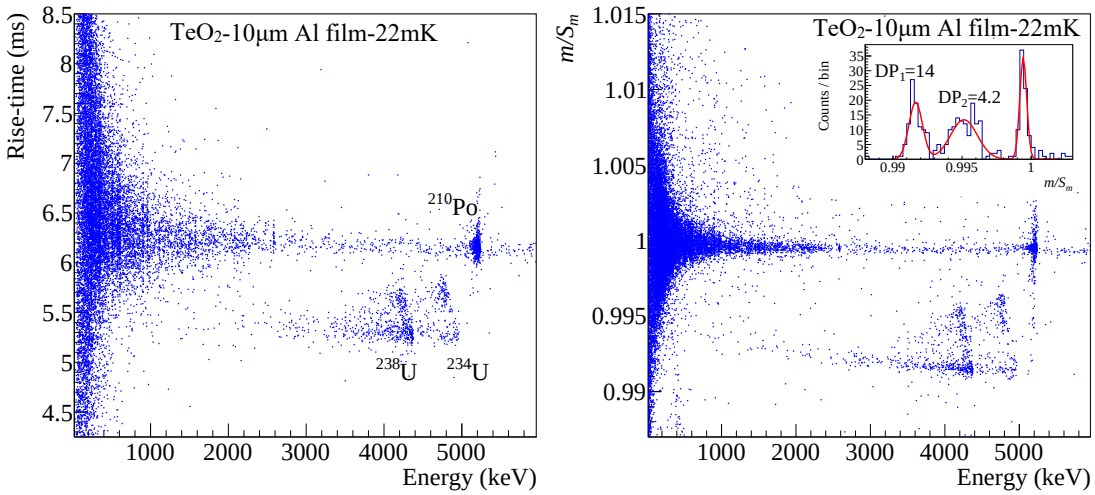

Figure 4.30 – *Left*: The rise-time vs the energy . *Right*: The fitted-amplitude vs the energy for small TeO_2 with 10 μm-Al-film-coating on one side.

4.5.3.3 *One surface 1 μm Al film coating (CROSS3)*

It is interesting to see the effect of Al film thickness on discrimination between surface and bulk events. For this test, a 1 μm Al film was evaporated on one surface of TeO_2. The working point was chosen to be as close as possible to the previous tests (Table 4.18). The temperature of the thermistor is a little bit higher than the previous test, but this should not affect the discrimination or the bolometric performance significantly. The bolometric performance in terms of sensitivity and the reduced sensitivity are preserved. The measurement bolometric parameters are given in Table 4.19. The energy spectrum, shown in Fig. 4.31, shows clearly the peaks of the γ calibration source (^{232}Th). The resolution of the peaks is mostly affected by the instability of the baseline.

Temperature	Current [nA]	V_{bol} [mV]	R_{bol} [MΩ]	Thermistor temperature [mK]
22 mK	5.0	3.6	0.72	23.2

Table 4.18 – The bias current, voltage, the resistance and the temperature of the thermistor of small TeO_2 with 1 μm Al film coating on one side.

Temperature (mK)	Sensitivity (nV/keV)	η (MeV^{-1})	τ_r (ms)	τ_d (ms)	FWHM$_{bsln}$ (keV)	FWHM$_{bsln}$ (nV)
22	43	1.8×10^{-3}	7	63	2.0	86

Table 4.19 – The sensitivity, η, rise-time (at 2.6 MeV), decay-time (at 2.6 MeV), baseline resolution in keV and nV for small TeO_2 with 1 μm Al film coating on one side.

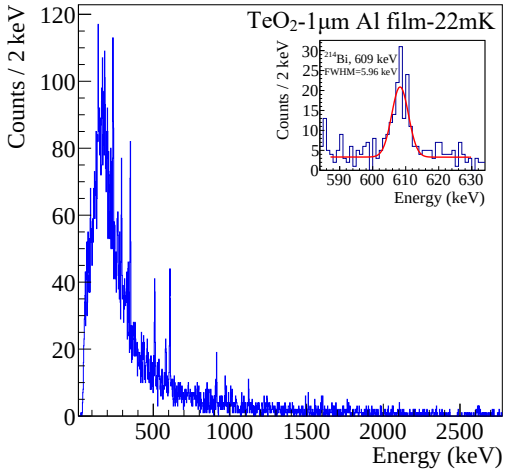

Figure 4.31 – The γ spectrum for small TeO_2 with 1 μm-thick Al film coating on one side. The peaks are generated by the environmental radioactivity and by the ^{232}Th calibration source.

The crucial issue is the discrimination capability. In Fig. 4.32, the rise-time pulse shape parameter shows some discrimination between bulk and surface events, not sufficient though for the full rejection of surface events. On the other hand, the fitted-amplitude parameter shows almost a full separation between surface α's and the bulk. Enough to reject 99.9% of the surface α's. The ability of having discrimination with a thinner film is important, as the evaporation process is easier and less time consuming, and the film adhesion better.

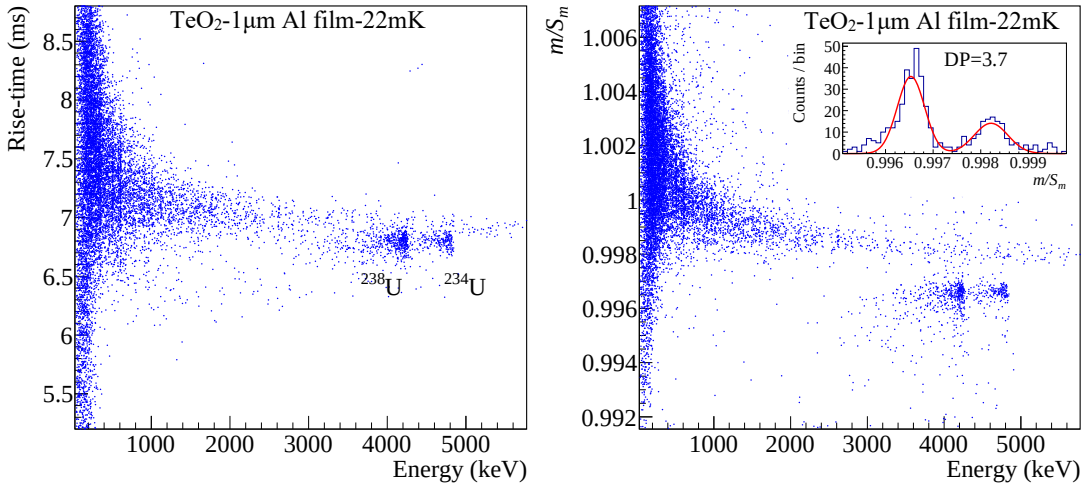

Figure 4.32 – *Left*: The rise-time vs the energy. *Right*: The fitted-amplitude vs the energy. The detector is small TeO_2 with 1 μm Al film coating on one side.

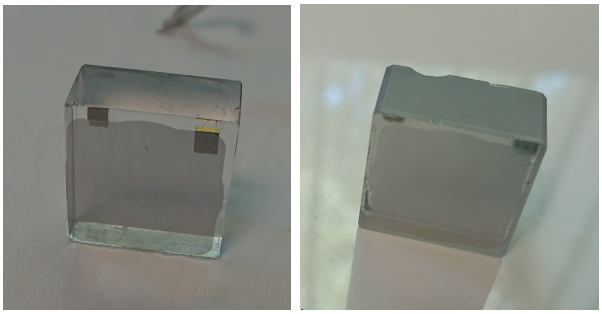

Figure 4.33 – *Left*: Small LMO with 10 nm Pd film. *Right*: Small TeO_2 with 10 nm Pd film.

4.5.4 Small Li_2MoO_4 with Pd film coating

The results achieved with Al film coating show lights and shadows. In general, surface α's separation works when one surface is coated. Problems arise when the coating is extended to a significant fraction of the crystal, as was shown in section 4.5.2. However, it is clear that Al coating has missed one of the main CROSS goals, also when it works for α's: the separation of surface β events. For this reason, we decided to move to other options for the coating material.

According to the results achieved using Al film, the mechanism of discrimination between surface and bulk events rely on thermalizing faster the surface events (see section 3.4.1). This is the opposite of the initial CROSS principle. A superconductor is not an ideal material to accelerate thermalization, as it can trap energy in form of quasiparticles for a long time with respect to the phonon pulse evolution. It makes sense then to try another coating material, a normal metal, with the hope to improve further the thermalization for surface events and open the possibility to discriminate also surface β's. One drawback of normal metals is their high heat capacity (due to the Fermi gas term proportional to the temperature at low temperatures), which will affect the sensitivity of the bolometer (see Eq. 3.4 and related discussion in Section 3.1.1). It is crucial to reduce the heat capacity by moving from μm scale to nm scale thickness.

Palladium films were chosen to coat small LMO and TeO_2. Palladium can give continuous very thin films by standard deposition by evaporation (down to 2.5 nm if needed). It has a good adhesion without under-layers (like SiO for example). It does not react with the atmosphere. Its high heat capacity (the so called Sommerfeld coefficient for the specific heat is quite high for palladium, see Section 3.1.1) can be compensated by the ability of depositing very thin films. Small LMO and TeO_2 with a 10 nm Pd film is shown in Fig. 4.33. The film is so thin that it is practically transparent and one can see the Ge-NTD glued on the opposite surface in the case of polished small LMO.

4.5.4.1 *One surface 10 nm Pd film coating (CROSS7)*

A pulse shape discrimination test on small LMO with Pd was performed. A 10 nm thick Pd film was evaporated on one face of small LMO. The film was faced by an uranium α source. The applied bias and the resistance of the thermistor is shown in Table 4.20. The temperature of the crystal is 26 mK for a floating plate temperature of 22 mK. The calibration of this crystal was not trivial, the γ peaks from the ^{232}Th calibration were not clear. The energy resolution of the spectra is not good even after stabilization (Fig. 4.34). The sensitivity of the LMO crystal has dropped to 23 nV/keV, two times

Temperature	Current [nA]	V_{bol} [mV]	R_{bol} [MΩ]	Thermistor temperature [mK]
22 mK	6.0	3.1	0.52	26.2

Table 4.20 – The bias current, voltage, the resistance and the temperature of the thermistor of small LMO with 10-nm-thick Pd-film coating.

lower than the sensitivity of the same crystal with Al film coating. The same decrease is appreciable on the reduced sensitivity η. This is because of the higher heat capacity of Pd with respect to Al, which starts to compete with that of the whole LMO crystal. The bolometric performance parameters are shown in Table 4.21.

The effect of Pd film coating on pulse shape discrimination is shown in Figures 4.35. Using the rise-time parameter, we see discrimination between surface α events and the bulk events. In addition, there are hints for discrimination also for lower energy events (between 0 and 2 MeV). These events appear clearly using the fitted-amplitude parameter. There are clearly two separated populations at an energy lower than the α's energy. The events are interpreted to be surface β's from the uranium source. All the surface events were selected (events in red in Fig. 4.36 (*left*)) roughly manually. A quantitative selection method has been implemented and will be used for another test in section 4.5.8. The light yield (Fig. 4.36 (*right*)) shows that surface α's have a much lower light compared to the β/γ, whereas the other surface events at lower energy lay in the β/γ band, which means that they can be consistently interpreted as β's from the uranium source. The bad energy resolution can be due to the fact that β surface sensitivity was achieved in small crystals, where position effects can show up due to the large fraction of the crystal that behaves as surface. The detector response is not presumably the same in the bulk and at the surface. The result of achieving discrimination for surface β is of great importance and can be considered a breakthrough, as the goal of discriminating both surface α's and β's is achieved for the first time with a bolometer.

Temperature (mK)	Sensitivity (nV/keV)	η (MeV^{-1})	τ_r (ms)	τ_d (ms)	$FWHM_{bsln}$ (keV)	$FWHM_{bsln}$ (nV)
22	23	1.2×10^{-3}	7	92	3.6	83

Table 4.21 – The sensitivity, η, rise-time (at 2.6 MeV), decay-time (at 2.6 MeV), baseline resolution in keV and nV for small LMO with 10-nm-thick Pd-film coating on one side.

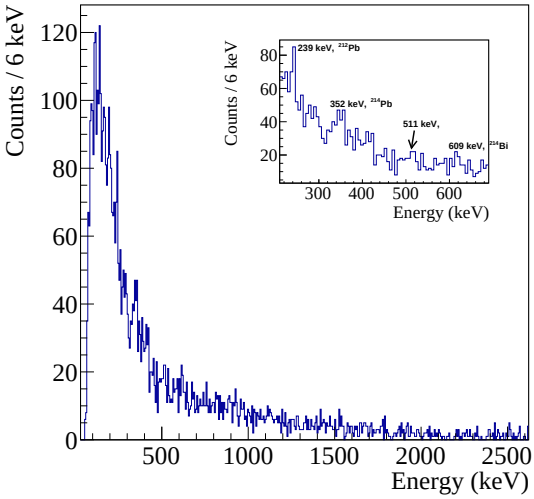

Figure 4.34 – The energy spectrum for small LMO with 10-nm-thick Pd-film coating at 22 mK.

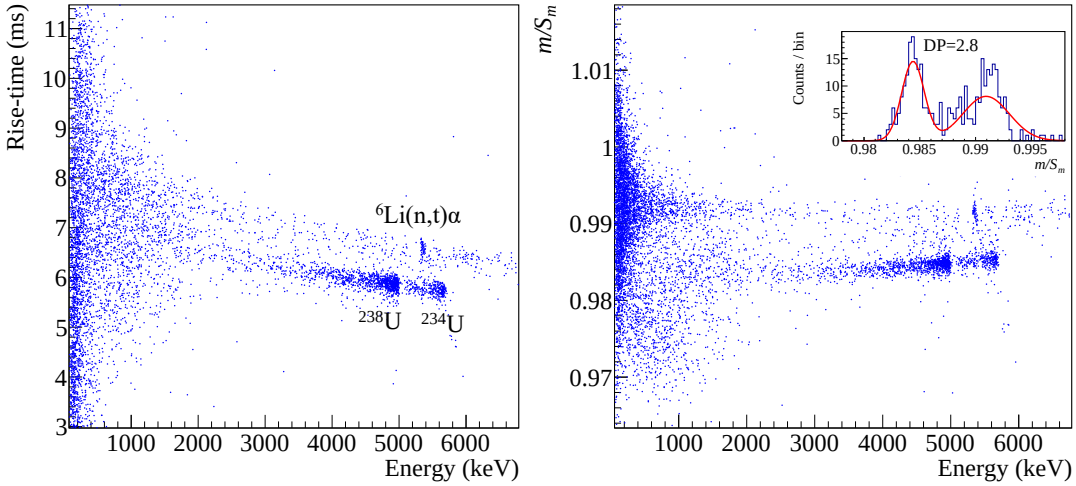

Figure 4.35 – *Left*: The rise-time vs the energy. *Right*: The fitted-amplitude vs the energy — Small LMO with 10-nm-thick Pd-film coating on one side.

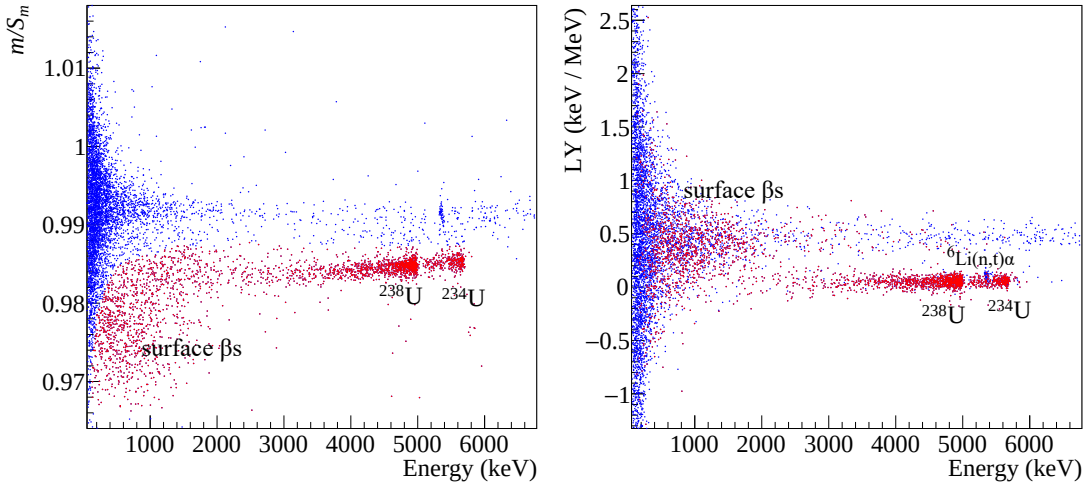

Figure 4.36 – *Left*:The fitted-amplitude vs the energy for small LMO with 10nm-Pd-film-coating on one side. The events that are highlighted in red are the surface events. *Right*: The light yield versus the energy, where it is clear that the surface β's have a higher light yield with respect to surface α. This strengthens the hypothesis that these events are β's.

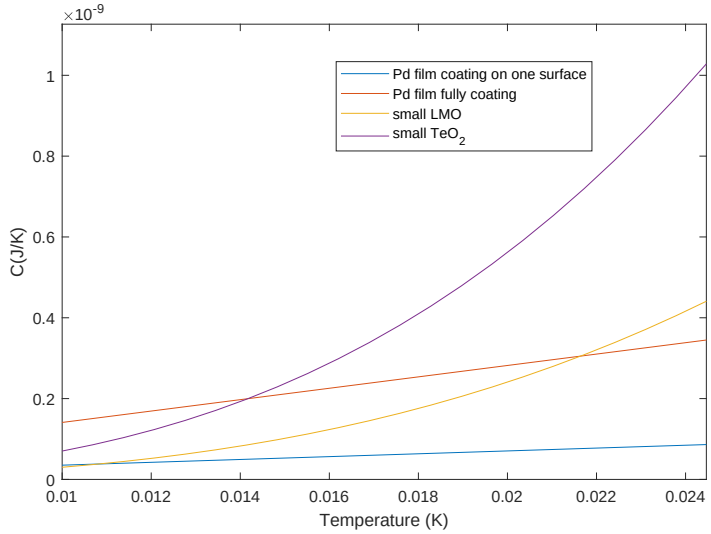

Figure 4.37 – A comparison between the heat capacities of small LMO and small TeO_2 without Pd coating, with one side coating, fully coated.

The next step was to fully cover small LMO with 10 nm Pd film. Unfortunately the sensitivity of the crystal was destroyed because of the high contribution of the Pd film on the heat capacity. In fact, the specific heat of the Pd film is given by Eq. 3.4 where γ_N is equal to 9.6×10^{-3} (J/K/mol) [113] (page 583), and therefore the film heat capacity is:

$$C = \gamma_N \frac{V \cdot \rho}{A} T \ (J/K) \tag{4.3}$$

where V, ρ and A are the volume, density and atomic mass of the film. This implies that the heat capacity of a $1.8\times1.8\times1$ cm^3 Pd film is 3.5×10^{-9}T J/K. The heat capacity of

small LMO (from Table 3.1), Pd film one side coverage and the Pd film full coverage is shown in Fig. 4.37.

4.5.5 Small TeO_2 with Pd film coating

4.5.5.1 *One surface Pd film coating (CROSS7)*

Pulse shape discrimination was also tested on TeO_2 with 10 nm Pd film coating on one surface. The film was faced by an uranium α source. The working point is shown in Table 4.22. The temperature of the thermistor is 23 mK with 22 mK floating plate temperature. The sensitivity of the crystal has also dropped compared to having Al film coating because of the higher heat capacity of Pd. The bolometric properties of the crystal are shown in Table 4.23. The energy resolution of the crystal is worse compared to having Al film (Fig. 4.38).

The discrimination capability between the surface and bulk events of the crystals is negligible (Fig. 4.39). So the Pd film showed its feasibility only for LMO. The reasons for the difference between LMO and TeO_2 are not clear. Also as for LMO, a fully coated TeO_2 crystal with Pd film experienced a dramatic reduction of the sensitivity.

Temperature	Current [nA]	V_{bol} [mV]	R_{bol} [MΩ]	Thermistor temperature [mK]
22 mK	3.4	2.56	0.754	23

Table 4.22 – The bias current, voltage, the resistance and the temperature of the thermistor of small TeO_2 with 10-nm-thick Pd-film coating.

Temperature (mK)	Sensitivity (nV/keV)	η (MeV^{-1})	τ_r (ms)	τ_d (ms)	$FWHM_{bsln}$ (keV)	$FWHM_{bsln}$ (nV)
22	30	1.8×10^{-3}	9	138	2.8	83

Table 4.23 – The sensitivity, η, rise-time (at 2.6 MeV), decay-time (at 2.6 MeV), baseline resolution in keV and nV for small TeO_2 with 10-nm-thick Pd-film coating.

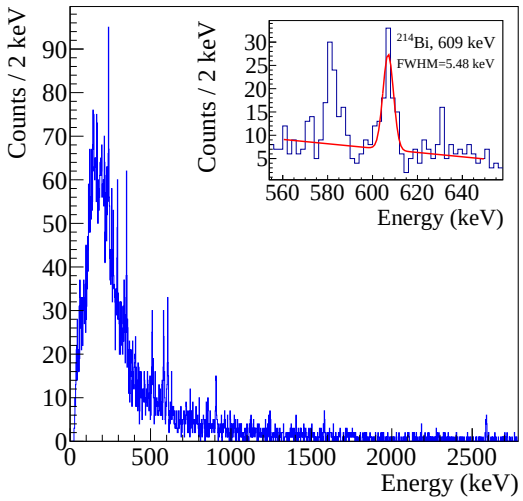

Figure 4.38 – The energy spectrum for small TeO_2 10 nm Pd film coating at 22 mK. The peaks are generated by the environmental radioactivity and by the ^{232}Th calibration source.

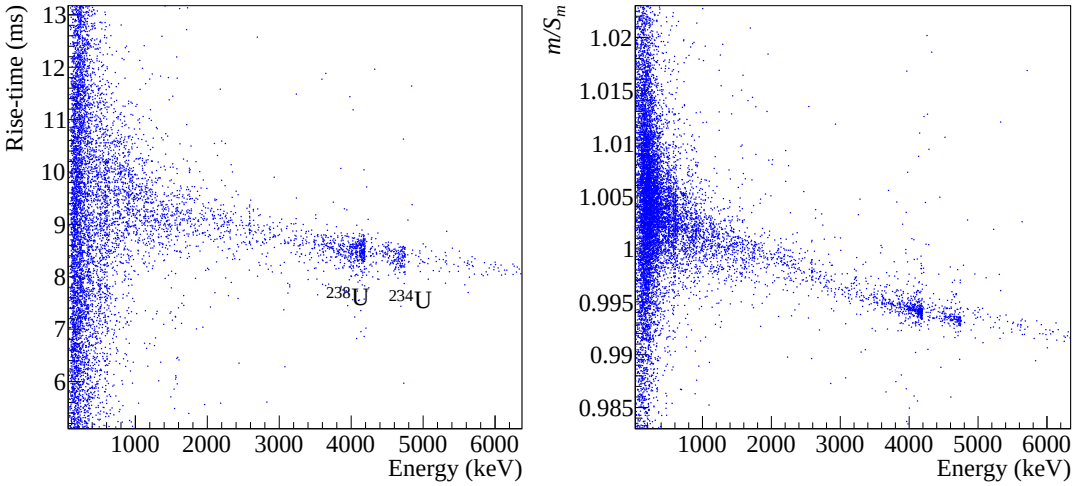

Figure 4.39 – *Left*: The rise-time vs the energy. *Right*: The fitted-amplitude vs the energy for small TeO_2 with 10-nm-thick Pd-film coating on one side

4.5.6 Small Li_2MoO_4 with Pd-Al bi-layer film coating (CROSS12-13-14)

Giving up Pd because of its high heat capacity was not our choice because it showed that we are able to discriminate also surface β's. The choice was to search for a way to decrease the heat capacity of Pd. The idea was to introduce superconductivity in Pd using Al film.

Al is a superconductor at the temperature we work at ($\sim$ 20 mK), having T_c=1.2 K. Because of the proximity effect, the Al film will introduce superconductivity in the Pd film. The bi-layer Pd-Al film was studied to measure the T_c of the film. Pd film was

already decided to have a thickness of 10 nm because it was working well in terms of pulse shape discrimination for LMO. The T_c of the bi-layer film depends on the thickness of Al film. Different Al film thicknesses were tested to get a suitable T_c. T_c should not be too low to insure that the film has dropped sufficiently in heat capacity as the temperature decreases. In addition, not a high T_c because this means we need a thicker Al film which makes evaporation takes more time. The Al film thickness that was chosen is 100 nm, giving a T_c around 650 mK.

It may be noticed that this procedure may appear inconsistent. If superconductivity by itself does not help discrimination when aiming at a faster thermalization because of energy trapping in quasiparticles, this issue should persist with the bi-layer. However, the quasiparticle lifetime depends strongly on the type of superconductor and on T_c, so we decided to perform this test.

A 10 nm Pd and 100 nm Al films were deposited on one surface of small LMO. The first layer evaporated is Pd and then Al was evaporated on it. A uranium α source was placed facing the film. The working point chosen was similar to the one of small LMO with just one surface Pd coating (Table 4.24). The floating plate temperature was chosen to be at 21.5 mK to recover the same resistance of the thermistor. The sensitivity of the bolometer is doubled compared to having only Pd film coating (Table 4.25). This proves that Al film is extending superconductivity to Pd film. The reduced sensitivity is also comparable to CROSS1.

Temperature	Current [nA]	V_{bol} [mV]	R_{bol} [MΩ]	Thermistor temperature [mK]
21.5 mK	6.0	3.1	0.52	23.4

Table 4.24 – The bias current, voltage, the resistance and the temperature of the thermistor of small LMO with 10 nm-Pd-100 nm-Al-films coating.

Temperature (mK)	Sensitivity (nV/keV)	η (MeV^{-1})	τ_r (ms)	τ_d (ms)	$FWHM_{bsln}$ (keV)	$FWHM_{bsln}$ (nV)
21.5	43	2.1×10^{-3}	7.5	58	2.4	103

Table 4.25 – The sensitivity, η, rise-time (at 2.6 MeV), decay-time (at 2.6 MeV), baseline resolution in keV and nV for small LMO with 10 nm-Pd-100 nm-Al-films coating.

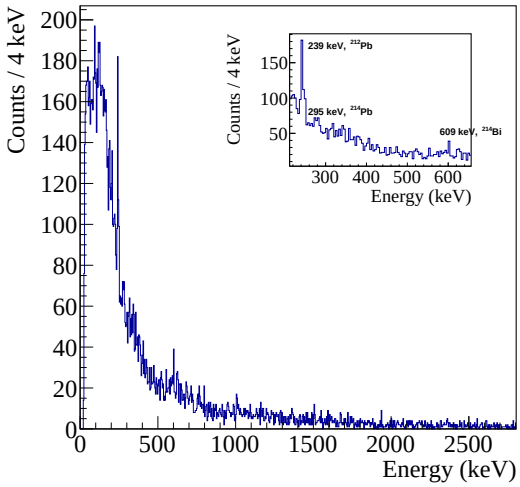

Figure 4.40 – The energy spectrum for small LMO with 10 nm Pd-100 nm Al bi-layer film coating on one surface at 22 mK.

The energy spectrum, shown in Fig. 4.40 shows that the detector has no good energy resolution. The pulse shape discrimination parameters (the rise-time and the fitted amplitude) shows that surface α's are separated from the bulk events. (Fig. 4.41). In addition, surface β discrimination is also apparent (from 0 till $\sim$ 2 MeV). These events were selected (in red Fig. 4.42 (*left*)) and plotted in a light vs heat scatter plot, where they populate the region with high light output, confirming that they are β's.

Another test was performed having this time a Po α source facing the Pd-Al bi-layer. As with the uranium source, surface α's and surface β's are separated from the bulk (Fig. 4.43). Some of the neutron capture events are even more discriminated than surface α's, as shown in Fig. 4.43 (*right*). This phenomenon is not well understood yet.

The same detector was operated after removing the α/β source with the purpose to confirm that β's from the sources were actually discriminated. The plot in Fig. 4.44 shows the pulse shape parameter (fitted amplitude) as a function of the energy. There is a clear difference in the events below 2 MeV between this measurement and the measurement with the β sources. No big cluster of events appear in the surface event region as in Figures 4.41 and 4.43. This confirms that what we saw in the previous runs were definitely β's from the source.

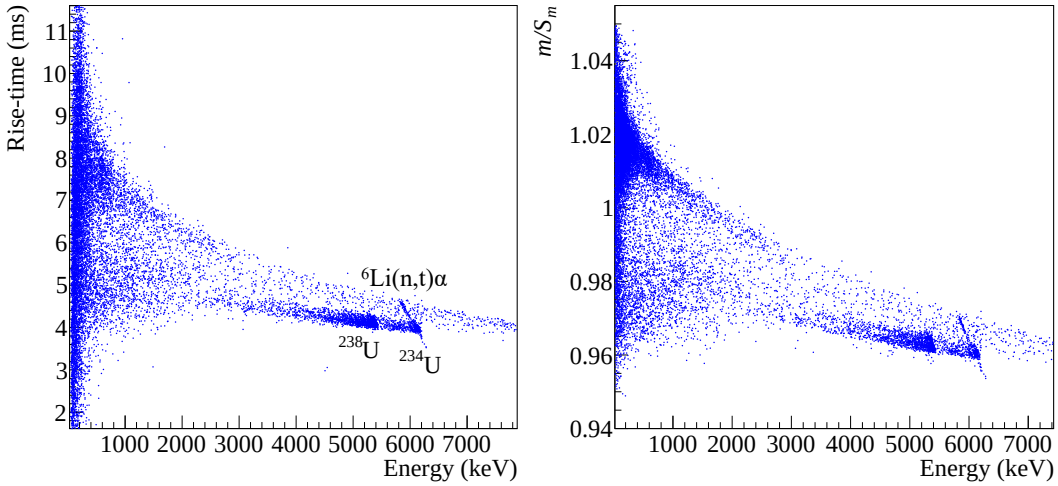

Figure 4.41 – *(Left)*: The rise-time vs the energy. *(Right)*: The fitted-amplitude vs the energy for small LMO with 10nm Pd-100nm Al film coating on one side. A clear separation for surface α's and β's emitted from the U source.

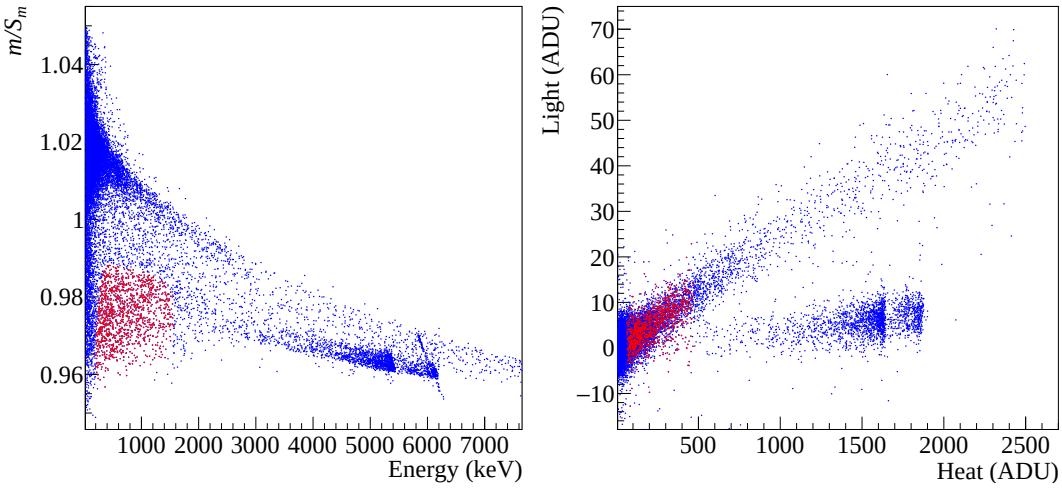

Figure 4.42 – *Left*: Fitted-amplitude vs energy for small LMO with 10 nm Pd-100 nm Al films coating on one side. The events that are highlighted in red are the surface β events. *Right*: Light yield energy, where it is clear that the surface β's have, as expected, a higher light yield with respect to the α's.

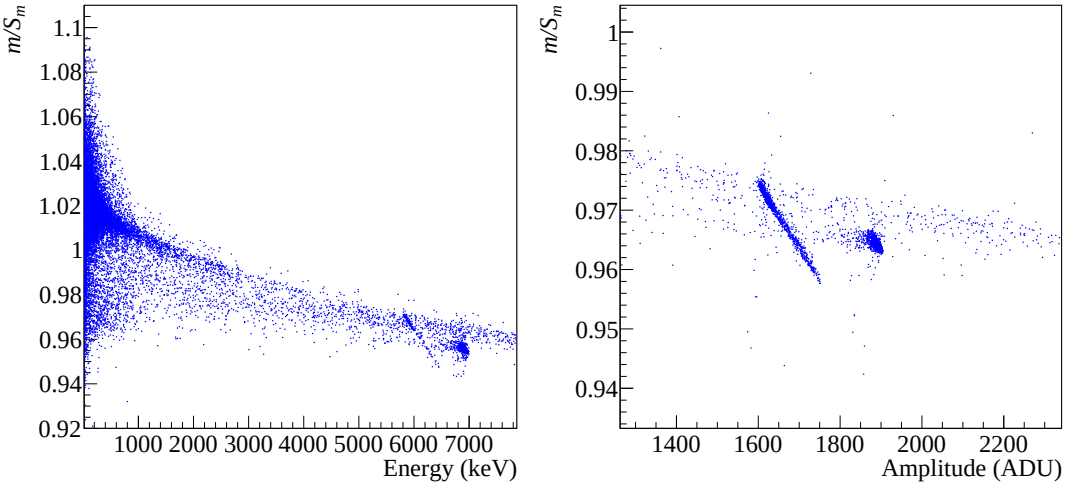

Figure 4.43 – *Left*: Fitted-amplitude vs energy. *Right*: Zoom on neutron capture events and Po sources α's. The detector is small LMO with 10 nm Pd and 100 nm Al bi-layer films coating on one side. A clear separation for surface α's and β's emitted from the Po source is appreciable.

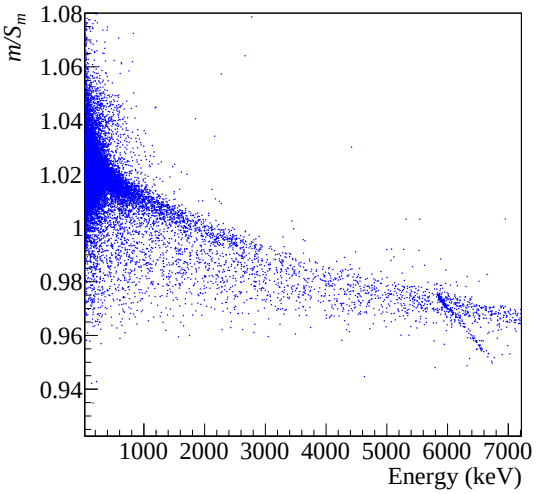

Figure 4.44 – Fitted-amplitude vs Energy for small LMO with 10 nm Pd and 100 nm Al bi-layer films coating on one side with no source.

4.5.7 Small TeO_2 with Pd-Al bi-layer film coating (CROSS12-13-14)

Small TeO_2 with 10 nm Pd and 100 nm Al bi-layer coating on one surface was also studied. A uranium α source was used. The working point chosen was similar to the one of small TeO_2 with just Pd film (Table. 4.26). The energy spectrum is shown in Fig. 4.45. The sensitivity has not been improved (Table. 4.27) compared to having just Pd film coating. However, the pulse shape discrimination has been improved after the addition of Al film. Surface α's are well separated from the bulk as can been from Fig. 4.46. In addition, there are lower energy events that are shifted from the bulk towards the surface events. These events, as for small LMO, are said to be surface β's. Checking the light

output of these events is not helpful (Fig. 4.47), as TeO_2 is a very poor scintillator and working with a Neganov-Luke light detector is not sufficient to check low energy events.

An additional confirmation that the lower energy events are surface β's was even here obtained by removing the α/β sources. Fig. 4.48 shows the result, no discriminated events are apparent between 0 MeV and 2 MeV. What we saw before are definitely surface β's. But it is still not understood why surface β's in small LMO are better discriminated from the bulk with respect to TeO_2.

Temperature	Current [nA]	V_{bol} [mV]	R_{bol} [MΩ]	Thermistor temperature [mK]
22.5 mK	3.4	2.6	0.76	23.1

Table 4.26 – The bias current, voltage, the resistance and the temperature of the thermistor of small TeO_2 with 10nm-Pd-100nm-Al-films coating.

Temperature (mK)	Sensitivity (nV/keV)	η (MeV^{-1})	τ_r (ms)	τ_d (ms)	$FWHM_{bsln}$ (keV)	$FWHM_{bsln}$ (nV)
22.5	26	1.5×10^{-3}	13	110	5.8	150

Table 4.27 – The sensitivity, η, rise-time (at 2.6 MeV), decay-time (at 2.6 MeV), baseline resolution in keV and nV for small TeO_2 with 10nm-Pd-100nm-Al-films coating.

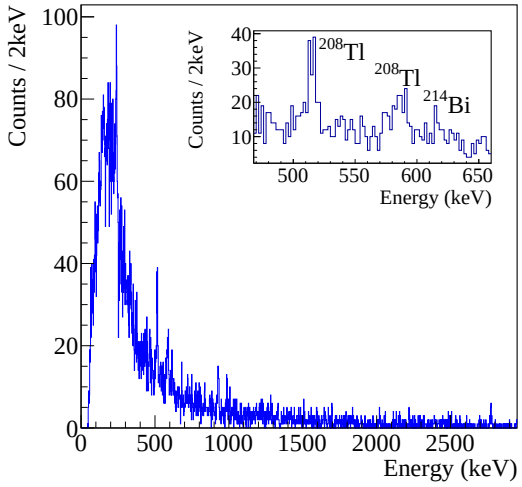

Figure 4.45 – The energy spectrum for small TeO_2 with 10 nm Pd-100 nm Al bi-layer film coating on one surface at 22 mK.

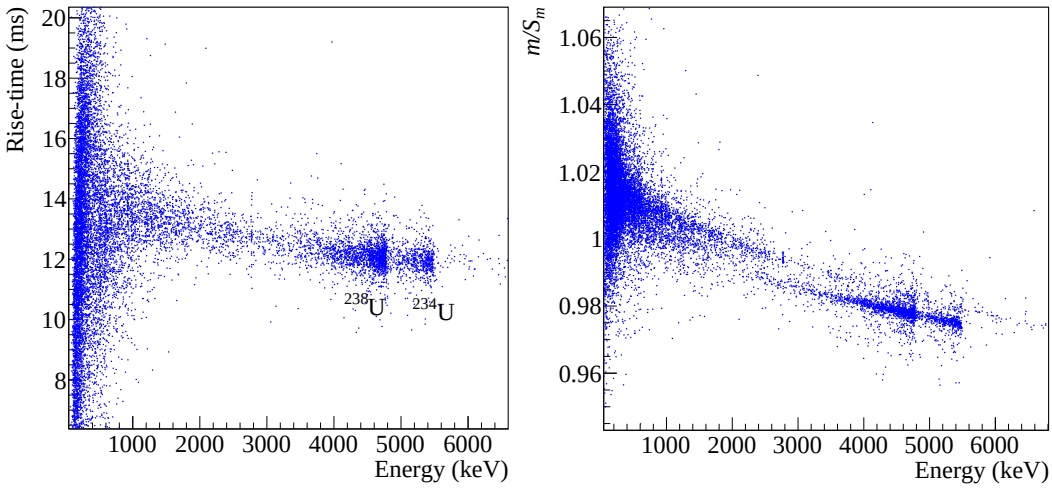

Figure 4.46 – *Left*: The rise-time vs the energy. *Right*: The fitted-amplitude vs the energy. The detector is a small TeO_2 with 10 nm Pd-100 nm Al film coating on one side.

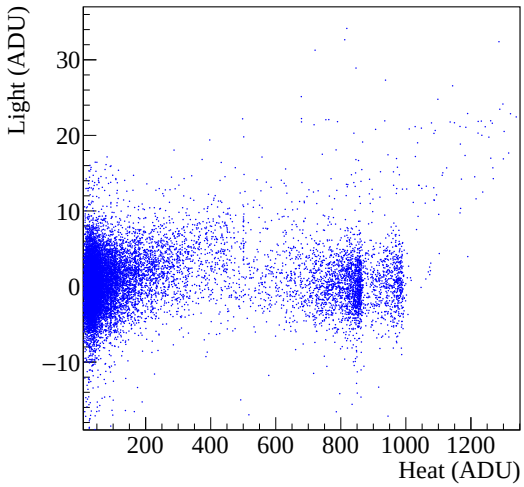

Figure 4.47 – The heat vs light for small TeO_2 with 10 nm Pd-100 nm Al film coating on one side.

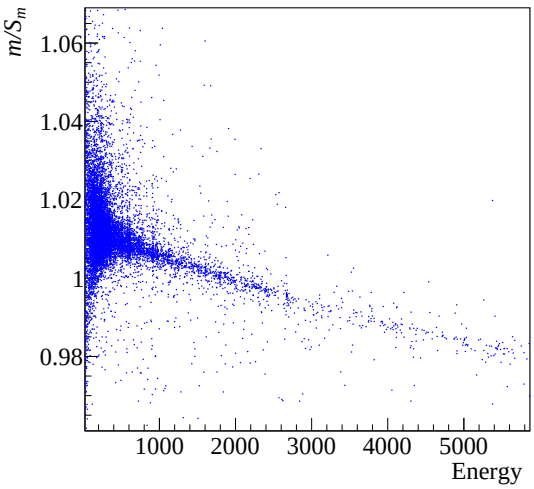

Figure 4.48 – The fitted-amplitude vs the energy for small TeO_2 with 10 nm Pd-100 nm Al film coating on one side with no source.

4.5.8 Surface β spectrum fit with MC model for small LMO

After proving that Pd+Al bi-layer film provides surface β separation in Li_2MoO_4 (lower fitted-amplitude PSD events in Fig. 4.49 that extend up to $\sim$ 2 MeV), it was very instructive to fit the β spectrum with a Monte Carlo model. Two β spectra were fitted, from ^{234m}Pa and ^{210}Bi β decays. The surface β events were selected according to the following procedure. (I will describe only the one performed for ^{234m}Pa, the selection of ^{210}Bi β's are done in a similar way.)

First the events in Fig. 4.49 are stabilized along the fitted-amplitude PSD parameter axis, as shown in Fig. 4.50. This will make the next step easier and more accurate. Next, the events were divided into intervals of 50 keV at low energy and larger intervals (up to 300 keV) at higher energy (up to 3000 keV). A double Gaussian fit was performed on each interval for the bulk and surface events (Fig. 4.51). This allows us to extract the standard deviation of the bulk events for each interval, used to set a discrimination threshold between bulk and surface events. The black points in Fig. 4.50 represent 3σ from the mean value of the bulk events, this will include more than 99% of the bulk events. The black points (3σ) are fitted with a power law ($a.x^b+c$) curve (Fig. 4.52), so that the events that are under the curve can be considered as surface events. The events that have been selected are not only β's from the source, there are also background events. To select the background, the measurement without the source was used. The same treatment was applied to the measurement with just the background to select the events in the same region (Fig. 4.53). A Monte Carlo simulation was performed to simulate both β sources. The uranium source was simulated as a source with a depth of 150 nm, as we know from the plots that some α's are energy degraded. The chosen depth reproduce well the low energy tail of the α population. On the other hand, the Po source doesn't show hints of degradation of particles energies, so it is considered to be directly on the surface of the copper tape. This is consistent with the two different methods of fabricating the sources. Fig. 4.54 and 4.55 show the fitted β spectrum of ^{214}Bi and ^{234m}Pa. The green line represents the Monte Carlo simulated β spectra of ^{210}Bi and ^{234m}Pa respectively. The red line represents the selected β's from our data and

the blue line the selected background. As mentioned before, selected β events contains also background, so the β spectrum was fitted with a model that contains a combination of the MC simulation and the background. The fit is plotted in black, as can be seen from the figures 4.54 and 4.55.

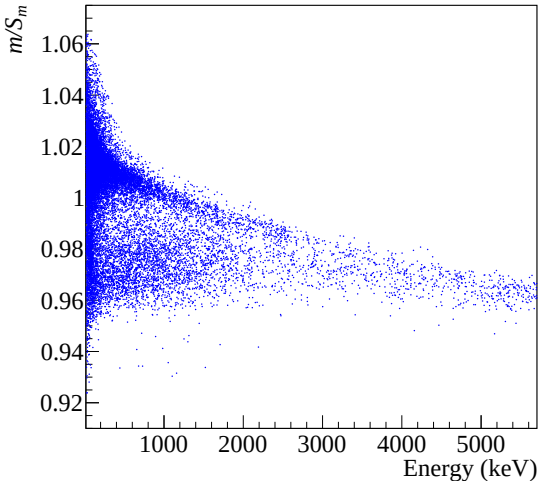

Figure 4.49 – The unstabilized fitted-amplitude vs the energy for small LMO with 10 nm Pd-100 nm Al film coating on one side with U source.

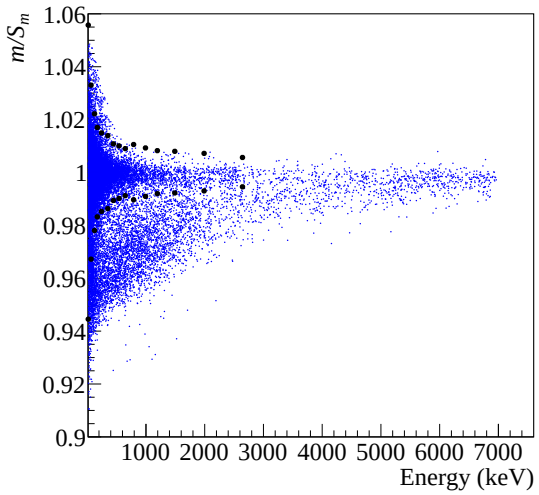

Figure 4.50 – The stabilized fitted-amplitude vs the energy for small LMO with 10 nm Pd-100 nm Al film coating on one side with U source. The black points are 3σ away from the center of the bulk event distribution (see Fig. 4.51).

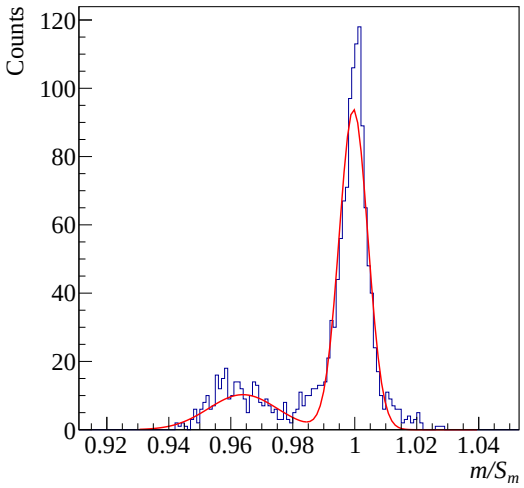

Figure 4.51 – Double Gaussian fit for a selected 50 keV range. The distributions are related to the bulk and surface β's.

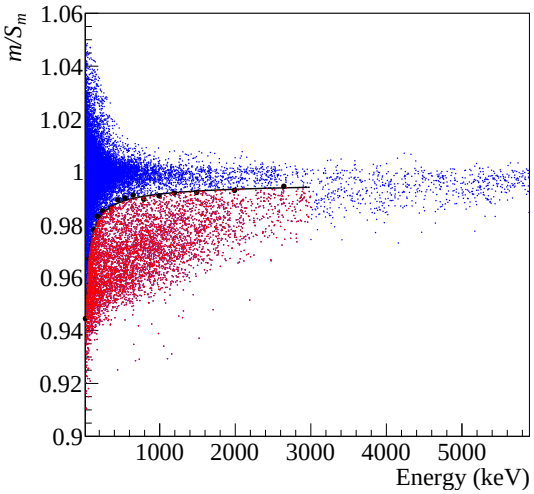

Figure 4.52 – U source measurement: Fitting the 3σ points with a.x^b+c to select the events under this curve as surface β's plus background.

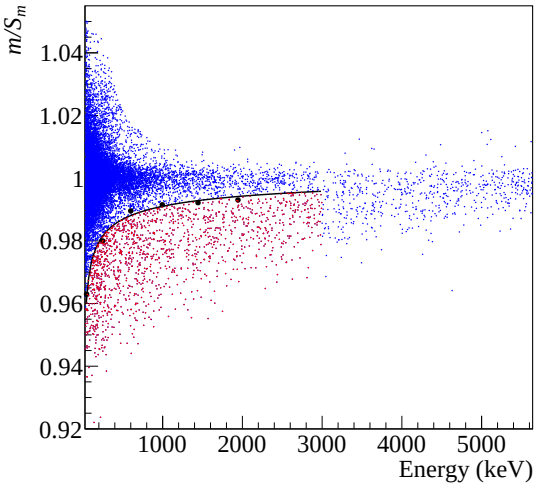

Figure 4.53 – No source measurement: Fitting the 3σ points with a/x^b+c to select the events under this curve as surface background.

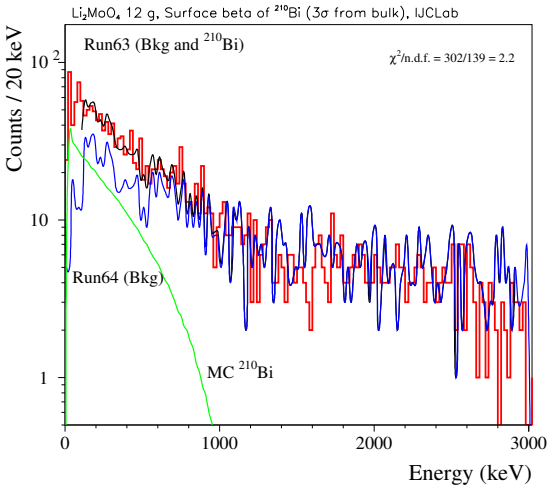

Figure 4.54 – Fitting the β's from ^{214}Bi plus the background from our experiment with a Monte Carlo model plus the background. The green spectrum is the ^{210}Bi β's simulated by MC. The blue spectrum is the estimated background from the source free measurement. The red spectrum is the selected source surface β plus the background. The black line is the MC model fit applied to red spectrum.

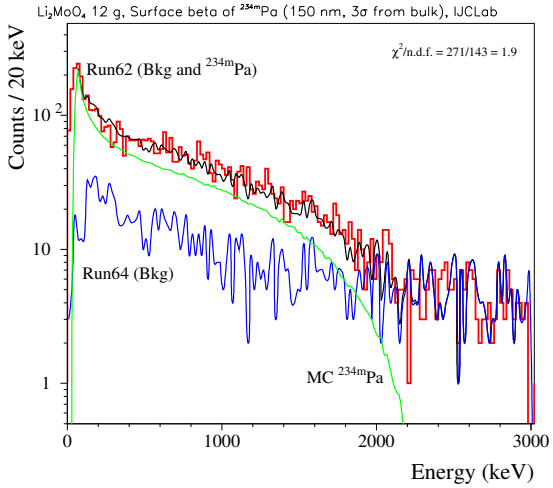

Figure 4.55 – Fitting the β's from ^{234m}Pa plus the background from our experiment with a Monte Carlo model plus the background. The green spectrum is the ^{234m}Pa β's simulated by MC. The blue spectrum is the estimated background from the source free measurement. The red spectrum is the selected source surface β plus the background. The black line is the MC model fit applied to red spectrum.

From Fig. 4.52, it can be noticed that surface β's are more separated from the bulk at lower energy and tends to be closer to the bulk at energy around 2 MeV. It was interesting to estimate the range of β's in LMO [114]. It was found that a β with an energy of 1 MeV has a maximum range about 2 mm and a β with an energy of 2 MeV has a maximum range of about 4 mm (Fig. 4.56). The shape of the β population goes with our expectations: the lower range β's (low energy) are more separated from the bulk compared to the higher range β's because of higher fraction of energy deposited near the surface.

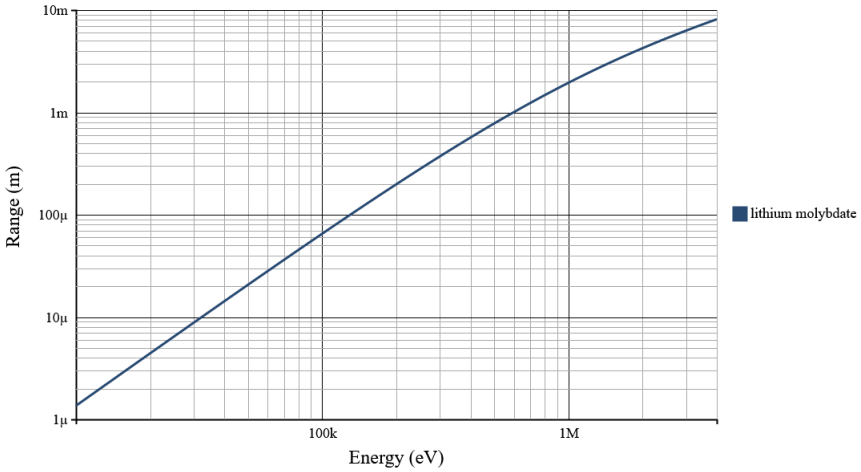

Figure 4.56 – The β range as a function of its energy calculated according to the computational tool described in [114]

It is important to compare the number of surface α's to surface β's for the two sources, uranium and polonium. It is expected that for each α decay there is a β decay,

so the counts should be equal. Starting with the less complicated source, Po, that does not show a degraded α's in the scatter plots (Fig. 4.43) except a negligible amount. This means that there is no risk of having a significant amount of alphas being absorbed in the source. The surface β's were extracted from the scatter plot similar to Fig. 4.52, but for the Po source measurement, and selecting the events under the fit curve. Of course these events are not pure surface β's, there are also background (beta+bkg). The backgrounds were extracted from Fig. 4.53 by selecting the events under the fit curve (bkg). Subtracting the beta+bkg from the bkg will give as the pure surface β counts. The surface α's selection is rather easy by using the light output. The number of counts for the surface events was found to be rather close: 844 counts for β's and 754 counts for α's. Studying the counts in the U source is more complicated since we already see a high portion of alphas being energy-degraded. This means that there is an unknown fraction of alphas not escaping the copper foil of the source in contrast to β's that will just escape without any problem. The same evaluation technique was used for U source measurement and it was found that surface β counts is 3875 and the surface α counts is found to be 2460. α's are much lower as expected.

4.5.9 Small LMO with Pd-Al bi-layer grids coating (CROSS15)

As will be discussed in Section 4.7, PSD capability is shown to occur down to 1-2 mm away from the film. So it is not necessary for the particles to pass and deposit energy in the film, it is enough to deposit the energy in the vicinity of the film. For this reason, it was reasonable to use a Pd-Al grid (in accordance with our qualitative model of surface sensitivity, based on the initial formation of a high-energy phonon blob of 1 mm scale). The idea for using Pd-Al grid came to avoid having a complete covering of the crystal with the film. As shown from the results of CROSS9, the addition of coating material led to losing the good discrimination between the bulk and surface events. This should also lead to a lower heat capacity contribution of the coated grid compared to when having a film.

Small LMO with Pd-Al grid on one surface of the crystal is shown in Fig. 4.57. A 10 nm Pd and 100 nm Al bi-layer grids were deposited on one surface of small LMO. The thickness of the grid lines is 70 μm and the spacing between the lines is 700 μm. A U source was shining the coated surface. The measurement was performed at 18 mK to get a similar working point as when having Pd-Al film. The working point is shown in Table 4.28. The sensitivity has been increased, possibly because of the lower heat capacity of the grid compared to when having a film (Table. 4.29). The reduced sensitivity is comparable to CROSS1 (bare crystal case). Fig. 4.58 shows the energy spectrum which shows peaks with bad resolution.

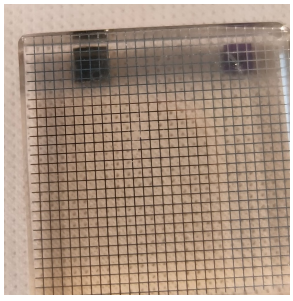

Figure 4.57 – Small LMO with Pd-Al grid.

Temperature	Current [nA]	V_{bol} [mV]	R_{bol} [MΩ]	Thermistor temperature [mK]
18 mK	6.0	3.3	0.56	22.4

Table 4.28 – The bias current, voltage, the resistance and the temperature of the thermistor of small LMO with 10nm-Pd-100nm-Al-grids coating.

Temperature (mK)	Sensitivity (nV/keV)	η (MeV^{-1})	τ_r (ms)	τ_d (ms)	$FWHM_{bsln}$ (keV)	$FWHM_{bsln}$ (nV)
18	51	2.5×10^{-3}	13	65	2.8	143

Table 4.29 – The sensitivity, η, rise-time (at 2.6 MeV), decay-time (at 2.6 MeV), baseline resolution in keV and nV for small LMO with 10nm-Pd-100nm-Al-grids coating.

Fig. 4.59 shows that rise-time and the fitted amplitude pulse shape parameters. The separation of surface α's and β's from the bulk is now even better and much more appreciated than when having a Pd-Al film. This result is very encouraging as it may open the door for a fully grids coated crystal avoiding the high fraction of coated surface. The surface betas were selected, following the steps described in the previous section, and they are plotted in red in Fig. 4.60.

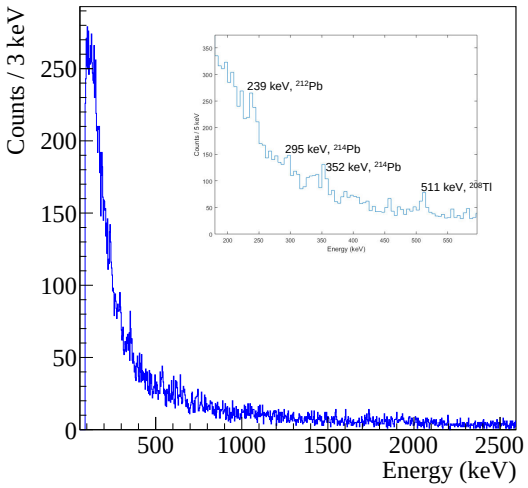

Figure 4.58 – The calibrated energy spectrum of small LMO with 10 nm Pd and 100 nm Al bi-layer grid coating.

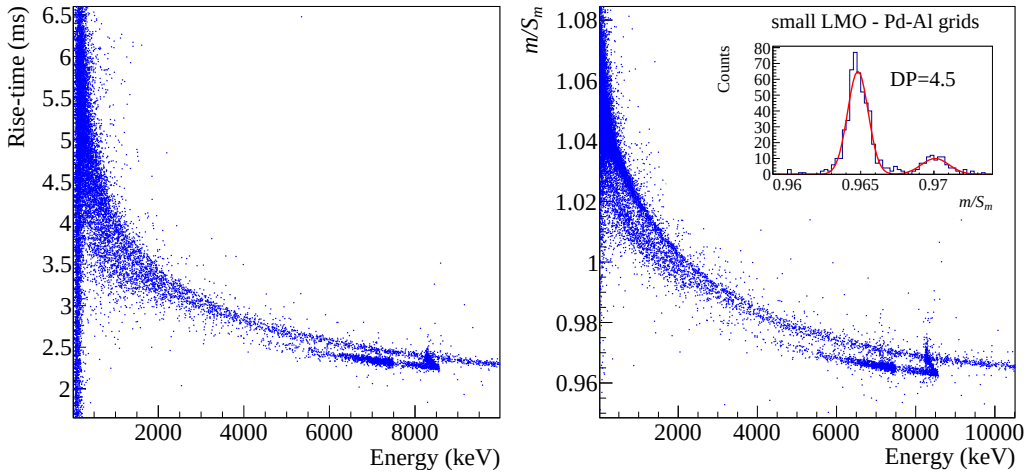

Figure 4.59 – *(Left)*: Rise-time vs energy. *(Right)*: Fitted-amplitude energy. The detector is small LMO with 10 nm Pd-100 nm Al grids coating on one side. A clear separation for surface α's and β's emitted from the U source is appreciable.

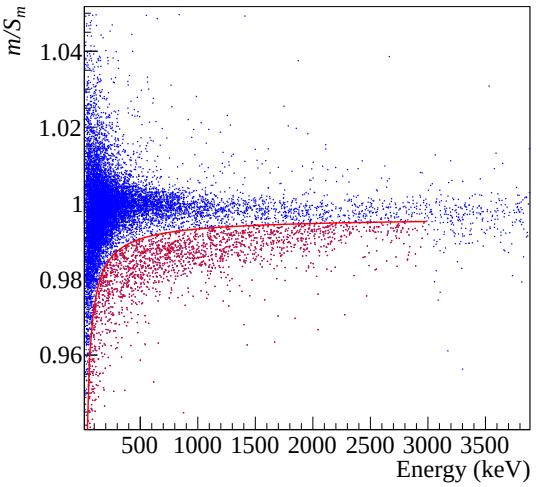

Figure 4.60 – The selection of surface betas based on the same steps described in section 4.5.8.

4.6 TeO_2 with NbSi and Ge-NTD sensors

In all the tests done with Ge-NTD sensor, the surface events have a faster rise-time with respect to the bulk events. The use of an athermal-phonon sensitive sensor showed a different result. A $20 \times 20 \times 5$mm TeO_2 crystal equipped simultaneously a Ge-NTD and an NbSi sensor (Fig. 4.62) was measured to understand how a thermal-phonon sensitive sensor and an athermal-phonon sensitive sensor behave with respect to surface events close to Al film. The Ge-NTD thermistor is sensitive mainly to the thermal component of the signal due to its slowness and the glue interface, while the NbSi is deposited directly on a large area of the crystal (14×14mm^2). This makes these sensors highly sensitive to the prompt athermal component of the phonon population produced by the

impinging particle. The Nb fraction in the 0.65 nm thick film is 8.65%. With these parameters, the NbSi film behaves likes the Ge-NTD sensor, featuring an exponential increase of the resistance as the temperature decreases. The film can be read out by the same electronics used for the NTD Ge thermistors, but the optimal resistances (several MΩ's) are achieved in the 30-40 mK temperature range, because of the extremely high impedance of the sensor. The NTD Ge thermistor, glued on a 20×20 mm surface in the part not covered by the film, was selected in order to have resistances similar to that of the film in the same temperature range. A description of the NbSi-film-production procedure is described in Ref. [89].

A 10 μm Al film was evaporated on the 20×5mm side of the crystal. A uranium α source was placed facing the coated surface in order to generate the surface events to be discriminated. A similar source was deposited directly on the opposite uncoated surface surface, providing bulk-like events. The detector was operated at ∼30 mK with the two sensor, Ge-NTD and NbSi, working simultaneously. Fig. 4.61 shows a comparison of the pulse shapes related to the same bulk event detected by the two sensors. The NbSi pulse is faster because of the important athermal-phonon component.

The amplitude vs the rise-time for NbSi and Ge-NTD is shown in Fig. 4.63, right and left panels simultaneously. The inset of the figures shows the difference in pulse shape between the bulk and surface events of the same deposited energy. The rise-time behaviour is opposite for the two sensors. It has been confirmed that the surface events are faster than the bulk events for Ge-NTD sensors as already discussed in the results above. On the contrary, surface events are slower than bulk events when read by NbSi sensor according to the argument exposed in section 3.4.1.

Although NbSi sensor works well in terms of providing the required discrimination between surface and bulk events as when using a Ge-NTD, it was not considered in CROSS prototypes because of the more complicated procedure to deposit on the crystal compared to NTD that needs only to be glued. In addition, Ge-NTD showed a better energy resolution.

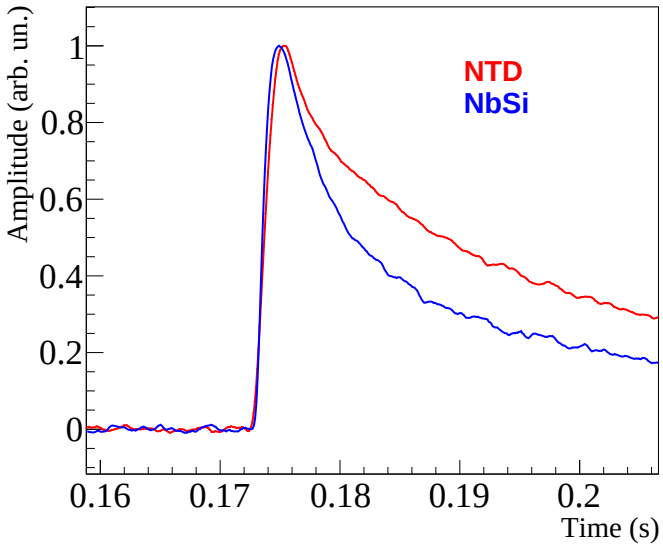

Figure 4.61 – Comparison between normalized pulses provided by the NbSi sensor and by the Ge-NTD thermistor for the same bulk event.

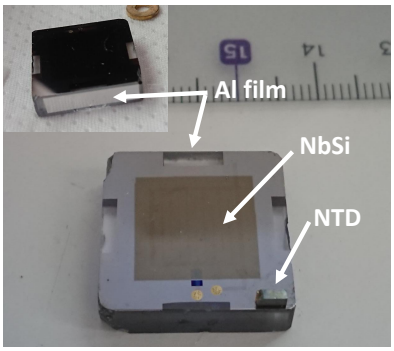

Figure 4.62 – 20×20×5 mm^3 TeO_2 with NbSi sensor and Ge-NTD sensor. A 10 μm Al film is evaporated on one 20×5 mm side. The film is faced by a U source to mimic surface events and another drop of U source is put on the opposite side without coating to mimic bulk events.

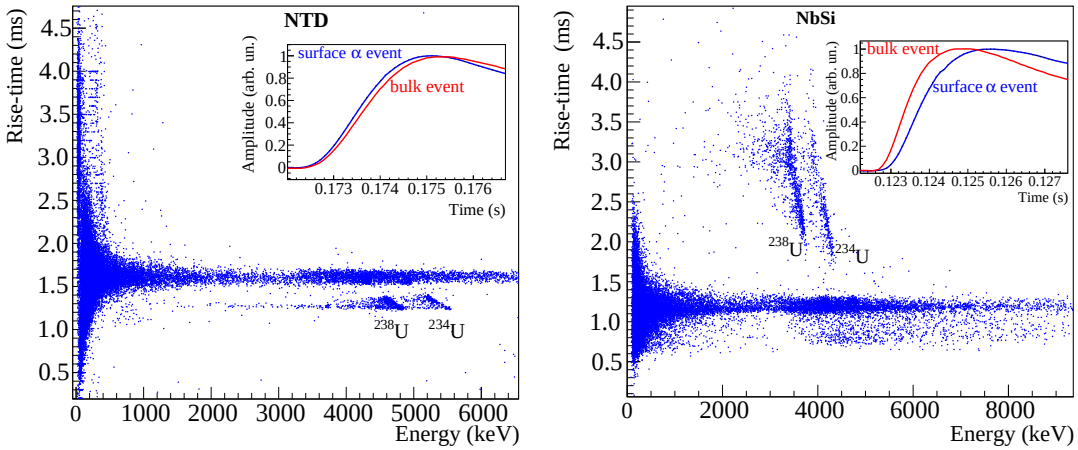

Figure 4.63 – The same set of events acquired by TeO_2 represented with rise-time vs. pulse-amplitude plots for Ge-NTD signals (*left*) and NbSi-film signals (*right*). The inverted behaviour of the two sensors in terms of rise-time of surface events is apparent. In the insets, a direct comparison of signal rise-times for bulk and surface events is shown.

4.7 Depth-dependence of discrimination

From Fig. 4.16, the neutron capture on ^{6}Li (events in region 4) can provide valuable information about the dependence of discrimination capability on the depth of the interaction from the coated surface. The neutron capture events in the figure show that the related distribution does not lie entirely in the bulk event band. There is a tail that tends towards the surface event region. This happens in spite that the neutrons have a long neutron absorption length compared to the thickness of the film.

The isotope ^{6}Li has a 7.8% natural abundance [115] and a very high cross-section for thermal neutron capture (940 barns) [116]. The thermal-neutron capture on ^{6}Li releases a total kinetic energy of 4.78 MeV from the emission of a 2.05 MeV α particle and a 2.73 MeV triton. The ranges of the α particle and the triton in Li_2MoO_4 are 17 μm and 40 μm respectively. The thermal neutrons has an absorption length of 6.6mm in

Li_2MoO_4. This means that the neutron capture events can penetrate deeply in the crystal ($20\times20\times10$ mm^3) with a significant fraction of the events occurring close to the film. The energy deposition for each event can be assumed as point-like (the total energy release is confined within $\sim$ 50 μm around the neutron capture events) with a total energy of 4.78 MeV. A Monte Carlo simulation (GEANT4) for a 25 meV neutrons with an isotropic flux was performed to evaluate the distribution of the neutron capture events in small LMO along the axis perpendicular to the surface with Al coating. The simulation of a 1M isotropic thermal neutrons shows that 12.5% are captured in the crystal. The distribution of the neutron capture events along the 10mm width of the crystal (perpendicular to the coated side) is shown in Fig. 4.64. An important contribution to the distribution of the neutron capture events near the coated surface come from neutrons that reached the detector from the sides that are not coated.

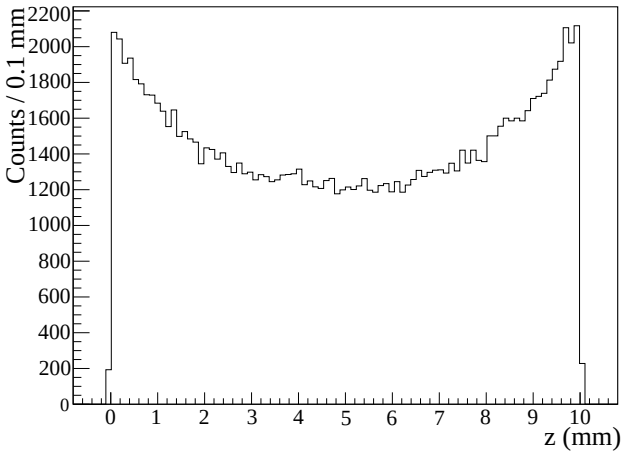

Figure 4.64 – Distribution of the distances of the neutron-capture events from the surface with Al film (at z=0) evaluated by a Monte Carlo simulation in a $20\times20\times10$ mm Li_2MoO_4 detector (10^6 generated neutrons, 125468 neutron captures).

From Fig. 4.64, we can obtain the ratio between neutron-capture events occurring up to a distance z from the Al film and the total number of neutron-capture events S_z:

$$R_C(z) = \frac{\int_0^z C(z')dz'}{S_z} \tag{4.4}$$

This will allow us to establish a relationship between R_C and the depth z, shown in Fig. 4.65. The curve is fit with a 4th order polynomial (z=$c_4R_C^4$ + ...).

From our data (Fig. 4.16) we can extract a relationship between the rise-time and the ratio of neutron-capture events and the total neutron-capture events, as discussed below in detail. The bulk events in Fig. 4.16 were used to stabilize all the events along the rise-time. This will prevent any overestimation of the rise-time distribution width when a large energy range is chosen. The neutron capture events can be isolated completely from the rest of the bulk events (mainly cosmic-ray events) using the light channel. In fact, the neutron-capture events have a lower light yield compared to the β/γ (Fig. 4.66). (The light yield of the neutron-capture events and the surface α's in Fig. 4.66 appears negative because there was a problem of cross-talk between electronic modules which

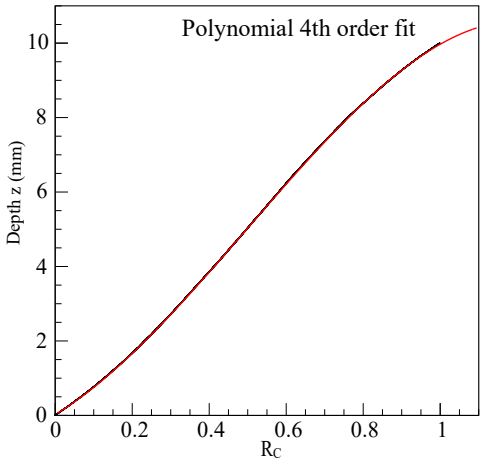

Figure 4.65 – The cumulative ratio of neutron capture events along the z-axis (distance from the Al film) obtained from the Monte Carlo distribution in Fig. 4.64.

brought to evaluate the amplitude incorrectly, but this does not spoil the discrimination power.) Note that the surface α's can be easily discriminated from the rest of the events using the rise-time.

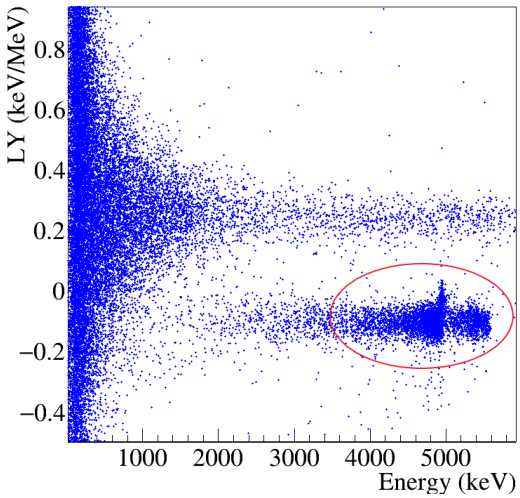

Figure 4.66 – The separation of neutron capture events from the bulk using the light yield.

Fig. 4.67 shows the distribution of the neutron capture events over the rise-time, which lies between 5.9 and 6.4 ms. The peak of the distribution corresponds to the neutron events sitting in the bulk event region. The tail of the distribution on the left of the peak (shorter rise-time), corresponds to surface events. The whole distribution is fitted with a Crystal ball function (red fit in Fig. 4.67). The right part of the distribution is fitted with a half Gaussian and then it is prolonged to a full Gaussian fit (green fit in Fig. 4.67). The Gaussian part of the distribution is assumed to be the bulk neutron capture events. Subtracting the full distribution from the Gaussian distribution will leave

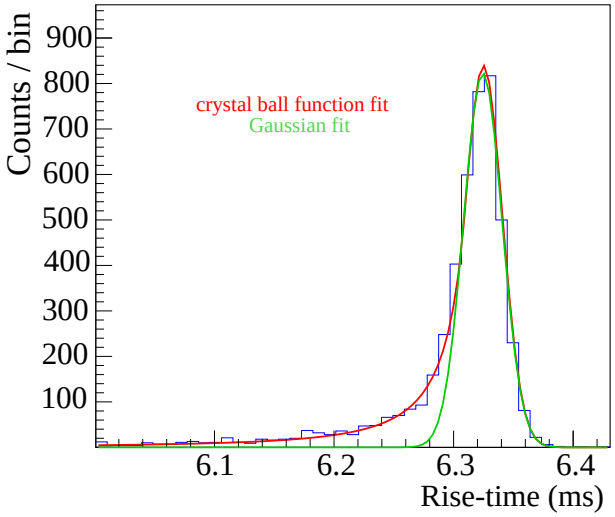

Figure 4.67 – Rise-time distribution for neutron-capture events for small LMO. The slower rise-time part on the right is fitted with a half-Gaussian fit and then extended to a full Gaussian. The Gaussian peak contains the bulk events. The whole distribution is fitted with a Crystal Ball function. The tail at faster rise-time values contains close-to-Al-film events, i.e. surface events.

us with only the surface neutron capture events $S(t_R)$ (the tail component of the neutron capture events distribution). A ratio S_R between the surface events up to a rise-time t_R (maximum value is taken 6.3 ms, corresponding to the end of surface neutron capture events) and the total number of neutron events (the surface and bulk) is constructed by integration:

$$R_R(t_R) = \frac{\int_{t_{R_{min}}}^{t_R} S(t'_R)dt'_R}{S_R} \tag{4.5}$$

Fig. 4.68 shows the R_R as a function of the rise-time. Using the polynomial fit in Fig. 4.65, we can obtain a relationship between the rise-time and the depth z for our data by substituting the ratio R_R. Fig. 4.69 shows the relationship between the rise-time and the depth z from the Al-film. Events that are within 1.4mm from the Al-film can be discriminated. Above this distance it will be hard to discriminate the surface events from the bulk events. The inset of Fig. 4.69 shows the relationship between rise-time and z in logarithmic scale, which is approximately linear.

No phonon-physics model has been developed to explain this behavior yet. However, these data are very useful to test future first-principle description of the observed mechanism.

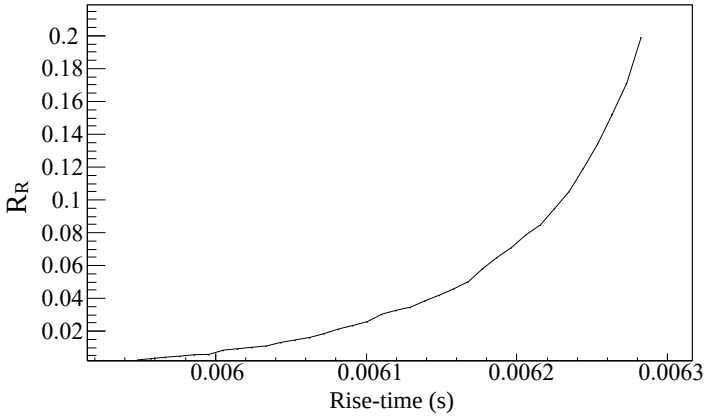

Figure 4.68 – The ratio of neutron capture events near the surface as a function of the rise-time. This has been extracted from data in Fig. 4.67.

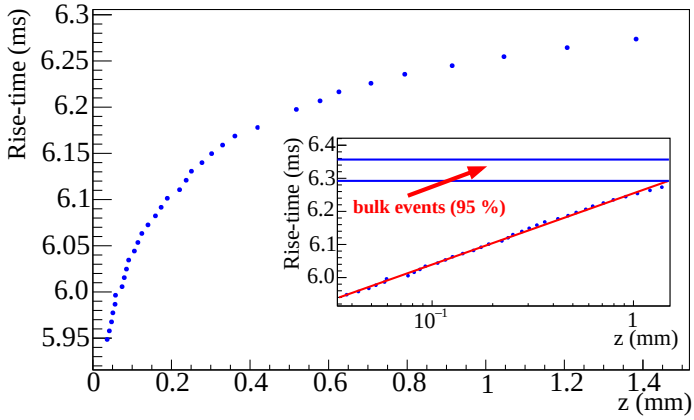

Figure 4.69 – Pulse rise-time as a function of the depth of the neutron impact point for small LMO. In the inset, the same relationship in semi-log scale. The band shown in blue represents the bulk events. The surface events are proven to be affected by the Al film when the impact point is within 1.4 mm, beyond this distance the events will lay in the bulk events.

4.8 Summary

In this chapter, we have presented a new bolometric technology capable of rejecting surface events. This will set the ground for future large experiments searching for $0\nu\beta\beta$ with a background level of only 0.5 counts/(ton yr) (using Eq.2.8 where: $BI \sim 10^{-5}$ counts/(keV kg yr), M=1 ton, T= 10 yr and ΔE=5 keV) and compatible with ton-scale setups. We remind that the key idea in CROSS is to be able to reject the surface events, α's and β's, by pulse shape discrimination. We summarise below in a few points the achieved conclusions:

1. Al films with thickness $\geq$ 1 μm lead to pulse shape discrimination on surface α events if just one face is covered. This result is achieved in small ($20 \times 20 \times 10$ mm)

Li_2MoO_4 and TeO_2 crystals and in a large ($\varnothing 40 \times 20$ mm) Li_2MoO_4 crystal. Apart from some ambiguous hints, there is no evidence of surface β separation. (CROSS2 and CROSS3)

2. The sensitivity to surface events in one-face Al-film-covered Li_2MoO_4 crystals extends down to about 1.4 mm from the film if the energy deposition is point-like (within 50 μm scale) as observed in neutron capture events (section 4.7). In spite of that, apart from some ambiguous hints, there is no evidence of separation for surface millimetre-range β's.

3. The mechanism responsible for separation using Ge-NTD sensors is confirmed as an enhanced thermalization of surface events, as shown by their faster response with respect to the bulk. This mechanism was clearly confirmed with a double readout TeO_2 crystal featuring both a thermal and an athermal phonon sensor (section 4.6).

4. To improve separation for surface β's, a normal-metal 10-nm-thick Pd film was deposited on a face of small $20 \times 20 \times 10$ mm crystals. Surface β separation was obtained in case of Li_2MoO_4 (even with 2 MeV β's that have a maximum range of about 4 mm), but at the price of an (expected) reduction of the sensitivity due to the film heat capacity. The surface α's were still discriminated from the bulk, but with a lower DP compared to having an Al film. (section 4.5.4 and section 4.5.5)

5. Surface β separation was kept and sensitivity was recovered by using a Pd-Al bi-layer (10 nm/100 nm) film, that exhibits a superconductive behaviour because of the proximity effect. The separation was satisfactory in Li_2MoO_4 but less evident in TeO_2 (section 4.5.6 and section 4.5.7 respectively)

6. In general, energy resolution is worsened when the detectors have β surface sensitivity, but remains as good as in crystals with Al films (α separation only). This may be due to the fact that β surface sensitivity was achieved in small crystals, where position effects can show up due to the large fraction of the crystal that behaves as surface. The detector response is not presumably the same in the bulk and at the surface. In addition, we have low statistics measurements that gives big uncertainty in estimating the energy resolution.

7. Increasing the covered-surface/volume ratio tends to deteriorate the surface event rejection, at least with Al film where this was tested (CROSS9).

8. In general, results are more ambiguous and less reproducible in TeO_2 than in Li_2MoO_4. This may be due to the fact that TeO_2 faces have not been polished as in Li_2MoO_4. The surface roughness can induce a thermalizing effect that competes with that of the films.

9. The effect of films on the sensitivity is in general negligible for superconductive films, but normal-metal films spoil detector performance by decreasing the pulse amplitude. In Fig. 4.70, the reduced sensitivity η is plotted as a function of the sensitivity. The negative effect of normal Pd coating is appreciable, while in the other cases the detector behaviour is similar to that obtained with a bare crystal.

10. Pd-Al bi-layer grids were tested on small Li_2MoO_4. It showed to work perfectly in discriminating surface β and α events (section 4.5.9). This result is of great

importance as the grids help in achieving a reduction in the covered-surface/volume ratio when considering fully coating the crystal thus avoiding the problem described in the 7^{th} point.

For the future actions, we will consider as established the protocol of using Pd-Al bi-layers grids. The main problem of keeping the sensitivity to surface events even when covering a large fraction of the crystal should be solved with grids coating. Fully Pd-Al bi-layer grids coating will be tested first on small crystals and then on large ones. Another advantage of the grids is that they will allow us to use light detectors even for fully covered crystals.

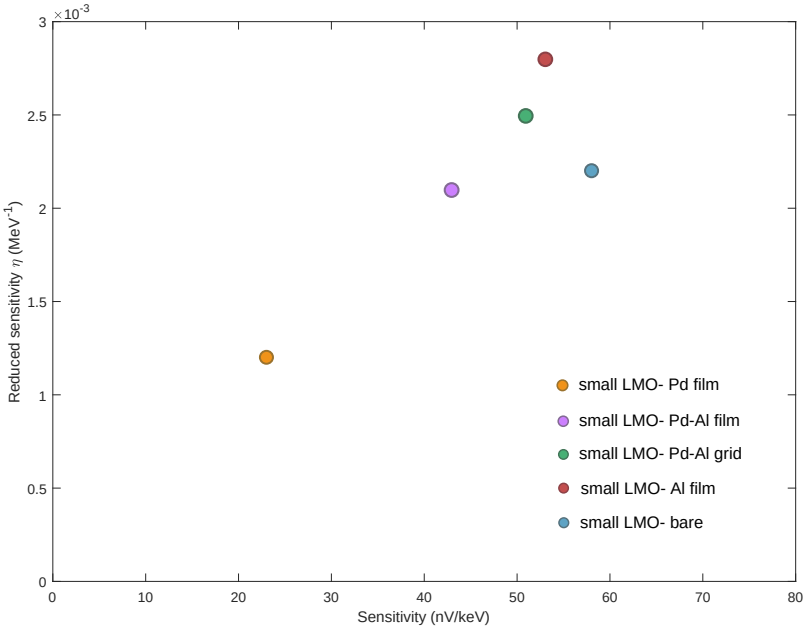

Figure 4.70 – The reduced sensitivity versus the sensitivity for the different CROSS runs on small LMO.

Chapter 5

CUPID-Mo

CUPID-Mo is a neutrinoless double-beta decay bolometric experiment based on the isotope ^{100}Mo. In spite of being considered a small scale experiment, CUPID-Mo showed to be among the most leading ones in the field, with a new world leading limit on $0\nu\beta\beta$ half-life of ^{100}Mo $T^{0\nu}_{1/2} > 1.5{\cdot}10^{24}$ yr.

5.1 Introduction

The CUPID experiment (CUORE Upgrade with Particle IDentification) is the future proposed follow-up of CUORE (Cryogenic Underground Observatory for Rare Events), to be installed at the CUORE cryogenic infrastructure at LNGS. The aim of CUPID is to decrease the background (mainly α particles from the contamination of the crystals or the nearby materials [63]) in the ROI and to increase the mass of the $0\nu\beta\beta$ isotope chosen. The suppression of the α particles can be achieved by having a dual heat-light readout system [80]. For this, a Ge optical bolometer (light detector (LD)) is used to collect the light emitted from the scintillating bolometer after a particle interacts in it. Rejecting the α particles is possible with this technology thanks to the different light yield of β and α particles at an equal deposited energy. To test this technology of dual readout, two CUPID demonstrators were developed and operated: CUPID-0 and CUPID-Mo. CUPID-0 studied 26 enriched Zn^{82}Se crystals since 2017 and it is located at LNGS. It has proved the feasibility of the complete rejection of the α background reaching the lowest background achieved by a cryogenic experiment ($3.5^{+1.0}_{-0.9} \cdot 10^{-3}$ counts/(keV kg yr) [117]) in the ROI. However, the obtained FWHM energy resolution at the Q-value of ^{82}Se (20.05 $\pm$ 0.34 keV [79]) and the radiopurity of the crystals [118] does not fulfil the requirements of CUPID. The promising demonstrator CUPID-Mo is based on a technology developed by the LUMINEU project that studied Li_2MoO_4 [57, 66] and that has shown to have excellent radiopurity and FWHM energy resolution at the $Q_{\beta\beta}$ of ^{100}Mo. CUPID-Mo aims to show the applicability of the LUMINEU technology to a larger scale preserving the good energy resolution and the high crystal radiopurity, and efficiently rejecting the α's to have zero background in ROI. This allows CUPID-Mo to be in the group of leading $0\nu\beta\beta$ experiments.

Table 5.4 summarizes approximately all the stages of CUPID-Mo experiment. The assembly of the detectors started in fall 2017 and then they have been installed at LSM underground laboratory (Laboratoire Souterrain de Modane) in the EDELWEISS cryostat at the beginning of 2018. The experiment faced some cryogenic problems in spring 2018 that led to delay the Commissioning I to summer 2018. Shortly afterwards

	Accomplishment
Fall 2017	Assemble the detectors at CSNSM and LAL (IJCLab)
January 2018	Install the detectors at LSM in EDELWEISS-III
Spring 2018	Cryogenic problems lead to some delay
Summer 2018	Commissioning I at 20.5-22.0 mK
August 2018	Serious cryostat failure that took long time to fix Assembly Upgrade: change some LD's Ge-NTD, fix the contacts & add reflecting foils
Winter 2018/2019	Commissioning II at 19.25-22.0 mK
Since Mar. / Nov. 2019	Physics data taking at 20.7 / 22.0 mK Notable interruption: LHe refill and Th/U calibration (every $\sim$ 10 days) Neutron irradiation (Apr., Jun. 2019) Partial warm-up (Mar., Oct., Dec. 2019) calibration with two ^{56}Co γ sources (June-July 2020)
Jun. 2019 / Jun. 2020	Data blinding / unblinding

Table 5.1 – A brief history for the stages of the CUPID-Mo experiment.

a serious cryostat failure occurred that leads to heat up the cryostat and makes some upgrades to the assembly while fixing the cryogenic problem. Commissioning II started in winter 2018/2019. The physics data taking started in March 2019 at 20.7 mK and then at 22.0 mK from November 2019 till June 2020. During this period, different calibration sources are used (see the table). The analysis was performed by blinding the ROI. The unblinding was done at the end of the experiment in June 2020.

5.2 Experimental setup

5.2.1 The bolometers: Li_2 $^{100}MoO_4$ crystals and Ge wafers

CUPID-Mo consists of 20 enriched Li_2 $^{100}MoO_4$ scintillating bolometers (enrLMO). Each crystal weighs 0.2 kg (4.158 kg total weight of the 20 crystals), with enrichment to $\sim$ 97% in ^{100}Mo, giving a total of 2.264 kg of ^{100}Mo ($1.36 \cdot 10^{25}$ nuclei). The crystals are of a cylindrical shape with a size of $\varnothing 44 \times 45$ mm. Four of these crystals has been tested before under the LUMINEU project [57]. The Nikolaev Institute of Inorganic Chemistry (NIIC, Novosibirsk, Russia) produced these crystals by a double-crystallization crystal growth using the low-thermal-gradient Czochralski technique [39]. It is crucial to have high purification level of the materials used for crystal growth: ^{100}Mo, ^{100}Mo oxide and lithium carbonate. A double-crystallization is carried out to have a higher crystal perfection and a lower level of impurities. After slicing the boules into the required crystal shape, the surface of the crystal is polished using radiopure silicon oxide abrasive powder and vacuum oil. Fig. 5.1 shows some of the produced Li_2 $^{100}MoO_4$ crystals. The crystals were then stored at LSM under nitrogen flux to avoid contaminating them with radon and cosmogenic activation before their assembly.

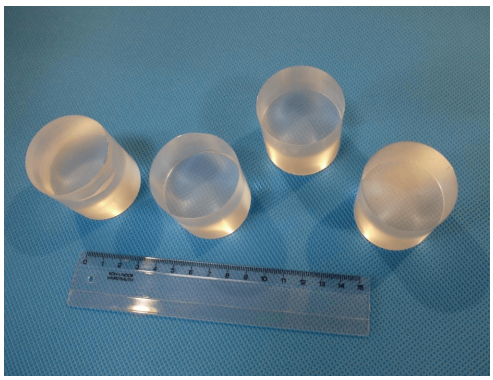

Figure 5.1 – $Li_2\,^{100}MoO_4$ crystal produced for the CUPID-Mo experiment.

A high-purity Ge wafer is complementing each scintillating $Li_2\,^{100}MoO_4$ crystal to read out the scintillation light, and it is placed facing the bottom of each crystal. It has a diameter of 44.5 mm and a thickness of 175 μm. In order to increase the light collection, the Ge wafer is coated with a ∼70 nm silicon oxide (SiO) layer on both sides, leaving a small part exposed to glue the sensor on it. This increases the light collection by ∼35% [119].

5.2.2 Thermistors

Ge-NTD sensors are used as thermal [120] sensors for enrLMO and Ge wafers. The ones glued on the crystals have size of 3×3×1 mm^3, while the sensors glued on the light detectors have a smaller size to reduce their heat capacity contribution, thus increasing the sensitivity. The Ge-NTD on the LDs has been cut from the 3×3×1 mm^3 NTD once horizontally and twice vertically to get 6 NTDs with a size of 3×0.8×0.4 mm^3. Only two LDs were equipped with 1/3 Ge-NTD (Ge-NTD cut into 3 pieces). The NTDs are glued on the crystals with a dedicated tool using a two-component epoxy resin (Araldite® Rapid). The NTD is kept 50 μm away from the enrLMO using a Mylar mask, this will allow to have separated gluing spots. The NTD of enrLMO are glued with 6 or 9 tiny spot matrix. Because of the smaller size of the NTDs of LDs, they were glued on the LD with a uniform veil of glue. Separate spots help in reducing the effects of different thermal contractions between enrLMO and the Ge-NTD. This effect is less harmful for the Ge-glue-Ge interface of the LD.

During Commissioning I, all the LDs with a size of 1/6 NTDs exhibited a high noise with a strong 1/f component. The exception was just for one LD with a 1/3 Ge-NTD (the other LD with 1/3 NTD had lost contacts). This may be related to the size or to the cutting technique. Fig. 5.2 shows an example of 4 LDs, the 3 LDs equipped with 1/6 NTD show a worse noise condition compared to the one with 1/3 NTD. Turning off the GM cryocooler improves a bit the noise level but does not remove the 1/f noise in LDs (Fig. 5.3). Even when the NTDs were strongly biased, the issue of bad noise was not solved (Fig. 5.4). After a serious cryogenic failure and heating up the cryostat, it was necessary to work on the LDs to improve their performance. The detectors were disassembled to perform a run on some of the LDs at the CSNSM (Orsay) aboveground cryostat (Ulysse) to investigate this issue. The 1/f noise issue of the LDs, observed at LSM with AC electronics, is prominent also for DC electronics in Ulysse, and therefore, it is related to the reduced NTD size and not to some features of the readout. Fig. 5.5 shows a LD with 1/6 NTD tested again in Ulysse where a clear 1/f noise is dominant even

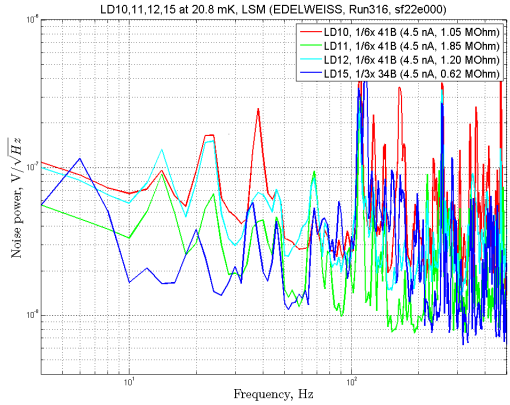

Figure 5.2 – Noise power spectrum for three LD with 1/6 NTD and one LD with 1/3 NTD. The LD with 1/6 NTD shows a prominent 1/f noise.

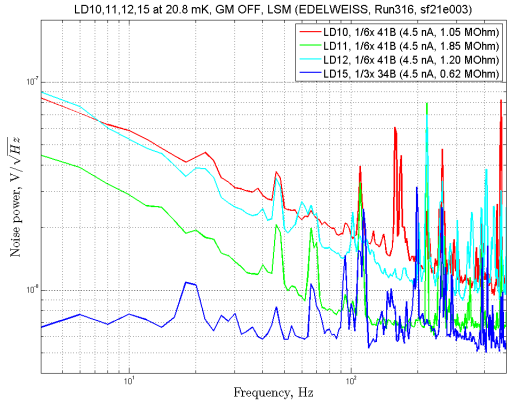

Figure 5.3 – Noise power spectrum for three LDs with 1/6 NTD and one LD with 1/3 NTD with the GM cryocooler off. The result is a lower noise, but the 1/f noise still persists.

with over biasing the NTD (up to 50 nA). A 1/3 Ge-NTD was glued on two CUPID-Mo LDs and was tested in addition to new LDs with also 1/3 NTD. The result is shown in Fig. 5.6. The issue of 1/f noise was therefore clarified, and 1/3 NTDs were used to replace all the existing 1/6 NTDs on LDs, leaving just one LD with 1/6 Ge-NTD due to lack of NTDs.

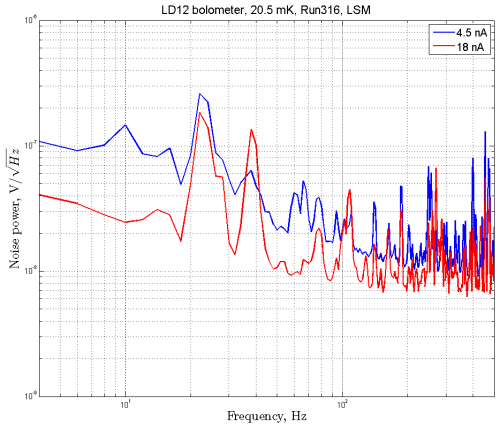

Figure 5.4 – The noise power spectrum of one LD with 4.5 nA and an over bias of 18 nA. Over biasing does not remove the 1/f component in the noise.

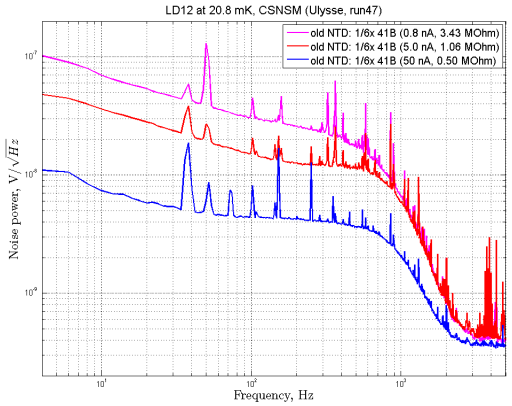

Figure 5.5 – A LD from the CUPID-Mo detectors was tested in another cryostat with DC electronics. The 1/f is still there, implying that it is related to the Ge-NTD size. Over biasing does not remove the 1/f noise although it does reduce the noise level in general.

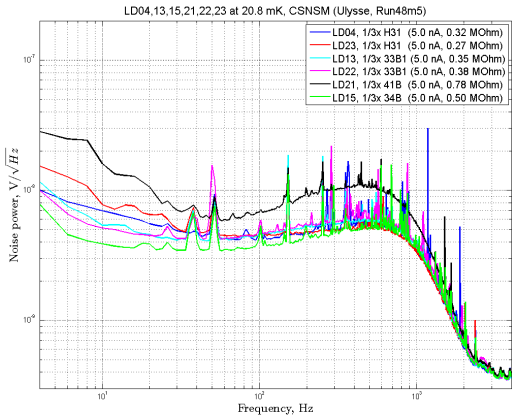

Figure 5.6 – The 1/6 NTDs on LDs were replaced by 1/3 NTDs. A significantly better noise is achieved.

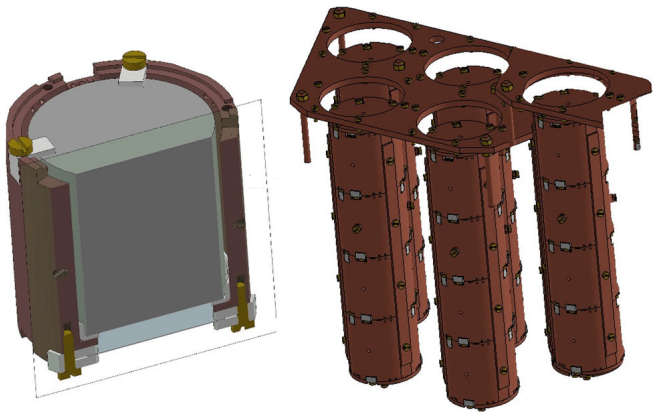

Figure 5.7 – The design of a single detector module (*left*) which contains a ∅44 × 45 mm enrLMO and a ∅44 × 0.175 mm Ge wafer LD on the bottom. The full 20 enrLMO and 20 Ge LD are assembled in 5 towers, each tower containing four detector modules (*right*) [98].

The enrLMOs are also instrumented with a heater. The heater is made out of a silicon substrate (about 2.5×2.5×0.5 mm) with a heavily doped meander that works as a weakly temperature dependent thermistor, and it is used to inject periodically a constant Joule power through a pulser system to stabilize the response of the bolometer (affected by temperature drifts) in the offline analysis.

5.2.3 Detector structure and assembly

The complete detector structure consists of 20 modules, each one being a single piece copper holder housing an enrLMO and a Ge LD. The detector modules are arranged in five towers, each tower containing four modules as shown in Fig. 5.7. This design is compact, allowing to house 40 bolometers in a restricted experimental space. All the elements used in a single detector module are shown in Fig. 5.8. Before starting assembling the detector, all the materials were well cleaned to minimize the contamination. The copper holders were etched with citric acid, and the PTFE pieces were cleaned with ethanol in an ultrasonic bath. The 3 small L-shape PTFE are placed at the bottom of the copper holder to support the enrLMO and decouple them from the thermal bath (copper holder). The 3 larger L-shaped PTFE are used to press the crystals from the top and fix them by copper screws, as can be seen clearly in Fig. 5.9 (*left*). The LD is clamped with 3 PTFE pieces and fixed with copper screws facing the bottom of the crystal (the side without an NTD and heater). Fig. 5.9 (*right*) shows the Ge-wafer clamped between three PTFE pieces and fixed.

Kapton with gold pads were glued on the copper holder and the Ge-NTDs were bonded with a 25 μm gold wire to these pads to provide the electrical readout in addition to the thermal link to the copper holder.

In Commissioning I, reflective foils were not used to surround the enrLMO to increase the light collection in LDs. It was demonstrated previously from the results of LUMINEU R&D on enrLMO that the $\alpha/\gamma(\beta)$ separation is sufficient to reject all the α's without a reflective foil. Fig. 5.10 shows the light yield scatter plots for enrLMO without (*top*) and with (*bottom*) a reflective foil. An additional argument to reject the use of a reflective foil in CUPID-Mo was to avoid a source of background due to what is called "bright alphas" [66] (Fig. 5.11). The reflective foil has some scintillation properties, so when

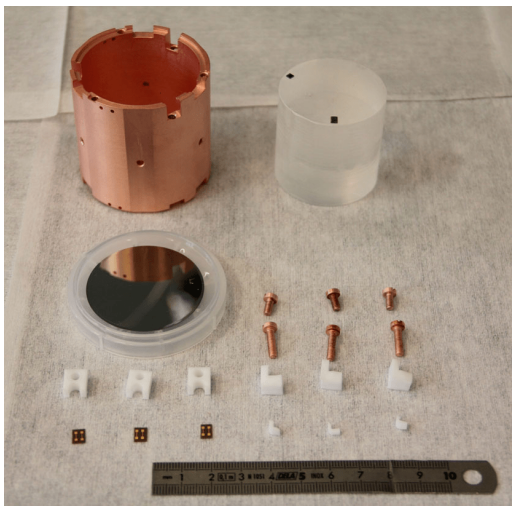

Figure 5.8 – All components used to assemble a detector module: a copper holder, a $Li_2\ ^{100}MoO_4$ crystal with glued NTD and heater, a Ge LD with NTD, the copper screws, the PTFE spacers and fixing elements, the Kapton with golden pads. Note that the reflecting foil is not shown here [98].

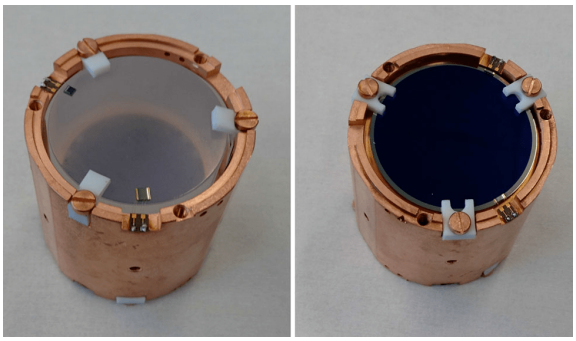

Figure 5.9 – A detector module with a top (*left*) and a bottom (*bottom*) view. On the bottom, the Ge NTD is placed [98].

an α particle from a surface-originated decay deposit energy in the reflecting film it scintillates. This scintillation adds up to the scintillating light produced from the α energy deposition in the crystal. It may then happen that energy-degraded α's have an enhanced light amplitude with respect to the expected value for α particles, and they can even leak into the ROI of ^{100}Mo in the heat-light scatter plot. Because of the bad performance of the LD during Commissioning I, in addition to replacing the NTDs as mentioned before, a reflective foil (3M Vikuiti^{TM}) was added in Commissioning II to avoid the risk of having a bad $\alpha/\gamma(\beta)$ separation.

A single module assembly, with a top and bottom view, is shown in Fig. 5.9. Four single detector modules are affixed together with three long copper bars, as shown in Fig. 5.12. The modules in a single tower are open to each other with the LD being on the bottom of each module. Therefore, each of the lower three crystals is seen by two light detectors and the top crystal is seen by just one.

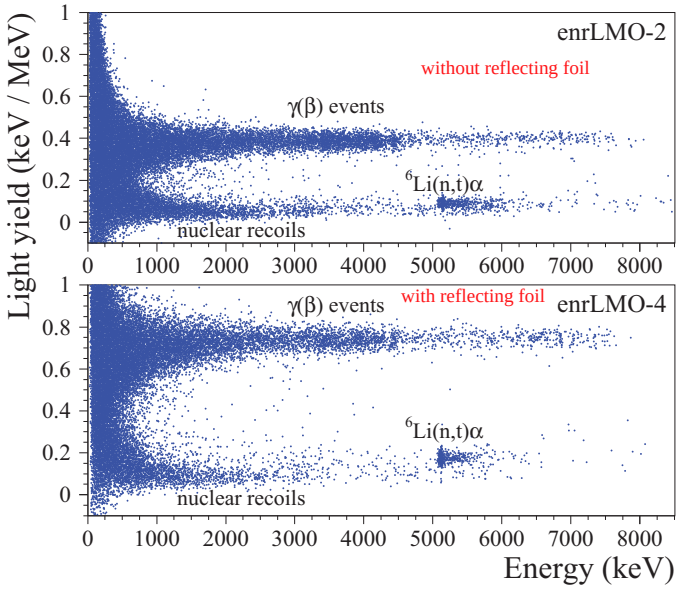

Figure 5.10 – The scatter-plots of light yield vs. heat energy of the AmBe data enrLMO without a reflecting foil (*top*) and another enrLMO with a reflecting foil operated at LSM. The light yield without a reflecting foil is good and sufficient, however, it is higher when using a reflecting foil as expected [57].

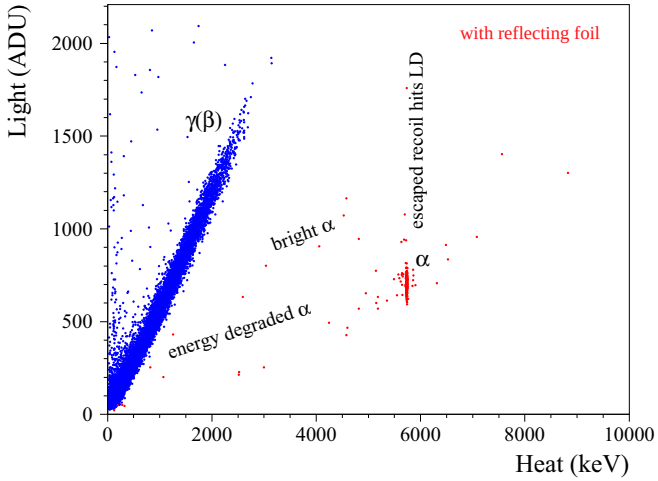

Figure 5.11 – Light vs heat for enrLMO with a reflective foil of the LUMINEU project. α particles are discriminated, but some α's are characterized by a higher light yield ("bright α's") due to the reflective foil [65]. See text.

5.2.4 Wiring

Silk-covered constantan twisted wires were soldered on the other side of the Kapton pad that is bonded to the NTD. A Kapton pad was also glued on the top of each tower to arrange the wires conveniently (Fig. 5.13 (*left*)). The constantan wiring of the NTDs and the heater (the heaters on each tower are connected in parallel) are soldered to one side

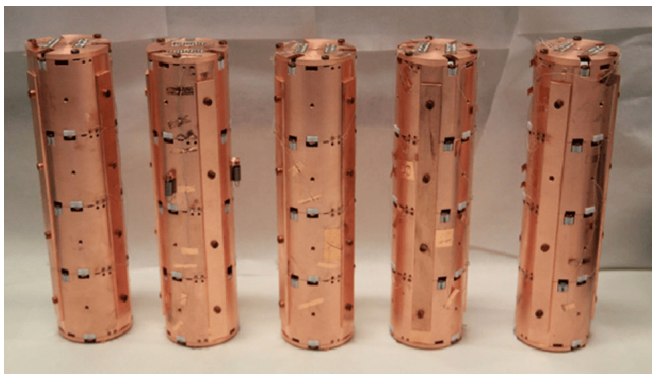

Figure 5.12 – The 5 assembled towers.

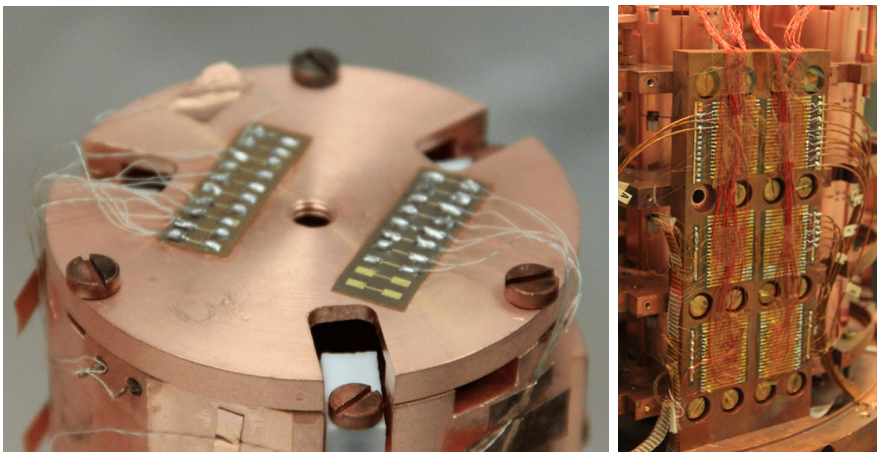

Figure 5.13 – The connections of the all the Ge-NTDs and heaters in a tower, silk constantan twisted wires, are soldered on the top of the tower on a Kapton golden pad (*left*). Copper wires are soldered from the Kapton pad on the top of the tower to a copper plate placed inside the cryostat.

of the Kapton pad on the top of the tower and copper wires were soldered on the facing pads going to the copper plate placed inside the cryostat (Fig. 5.13 (*right*)). The copper plate provides the link to Si-JFET (junction gate field-effect transistor) pre-amplifiers at 100 mK.

5.2.5 Suspending the towers

Each tower is suspended with three stainless steel springs to mitigate the vibrations from thermal machines that can introduce noise, especially in the light detectors. Fig. 5.14 (*left*) shows a tower suspended by three springs, where two springs are visible in the picture. The springs have a diameter of 0.5 mm and 10 N load. Fig. 5.14 (*right*) shows the five towers installed in the EDELWEISS cryostat.

5.2.6 The cryogenic facility

CUPID-Mo is installed in the EDELWEISS-III cryostat [66, 121], which is a wet cryostat (see Appendix A). The EDELWEISS infrastructure is located underground in one amongst the deepest laboratories in the world with a depth of 1700 m to reduce the

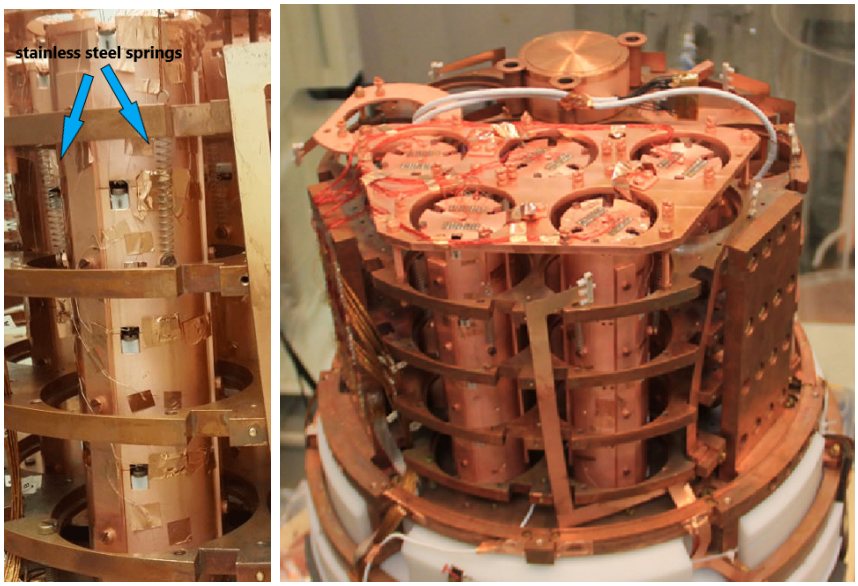

Figure 5.14 – (*left*): One CUPID-Mo tower is suspended by means of three stainless steel springs. (*right*): The five towers are suspended in the cryostat [98].

cosmic muon flux to 5 muon/m^2/day [122]. The cryostat is contained within an active and passive shielding. A layer of 20 cm of lead and 55 cm of polyethylene shield against environmental radiation. A layer of 2 cm in the inner part of the lead shield is made of Roman lead, which has low ^{210}Pb radioactivity, < 0.12 Bq/kg. It is crucial also to protect the detectors from any radioactivity coming from any nearby materials. For that, a 14 cm layer of Roman lead and 10 cm of polyethylene is used at the 1K-plate. The cryostat is surrounded by 100 m^2 plastic scintillator muon-veto system allowing to detect 97.7% of muons passing through a central with 1 m radius. The atmosphere between the lead and the cryostat copper screens is radon free ($\sim$ 30 mBq/m^3 of ^{222}Rn). The whole set-up is placed in a class 10000 clean room. The cryostat contains twelve slots, five of which are used by CUPID-Mo to read out the five towers (Fig. 5.14 (*right*)).

5.2.7 CUPID-Mo calibration sources

A significant amount of the time for data taking is dedicated to calibrating the detectors. For enrLMO calibration, mixed U/Th, AmBe and ^{56}Co sources were used depending on the aim. The mixed U/Th source has a $\sim$ 50 Bq of ^{232}Th, $\sim$ 100 Bq of ^{238}U and few Bq of ^{235}U. It has a prominent γ line 2615 keV, which is the closest peak from this source to the ^{100}Mo $Q_{\beta\beta}$. The AmBe is a neutron and a γ source which emits around 21 neutrons/s. The neutrons are generated by the following nuclear reaction:

$$^{9}Be + \alpha \rightarrow n +^{12} C^{*} + Q(5.704MeV) \tag{5.1}$$

the α comes from the decay of ^{241}Am. The excited $^{12}C^{*}$ emits 4.44 MeV γ-rays. The ^{56}Co calibration has a prominent γ line at 3253 keV, very close to the $Q_{\beta\beta}$ thus allowing to compute the energy resolution in the ROI more precisely.

For the light detectors calibration, high activity ^{60}Co γ source is used during LHe refill (every 10 days). When the crystals and the setup are exposed to the ^{60}Co γ source,

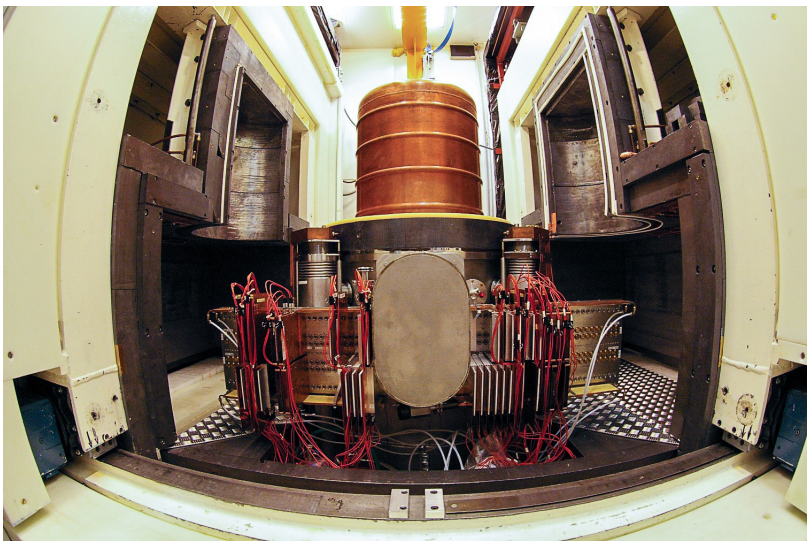

Figure 5.15 – The EDELWEISS cryostat.

X-ray fluorescence from Mo and Cu are emitted. The X-rays peak from Mo and Cu are shown in Table 5.2.

Material	From $K_{\alpha 1}$ Energy [Internsity I]	From $K_{\alpha 2}$	From $K_{\beta 1}$
Mo	17.48 keV [100%]	17.37 keV [52%]	19.61 keV [15%]
Cu	8.05 keV [100%]	8.03 keV [51%]	8.91 keV [17%]

Table 5.2 – The X-rays emitted from Mo and Cu after γ irradiation from ^{60}Co.

5.3 General CUPID-Mo detectors performances

The performance of enrLMO showed a good uniformity, suitable for larger arrays. Operated at 20.7 mK, enrLMO showed a good sensitivity with a median value around 17 nV/keV, which is typical for crystals with such a size and operation temperature [79]. The obtained median values for the rise-time and the decay-time are around 24 ms and 299 ms respectively. These values are consistent with the values from the LUMINEU project [57]. The data were calibrated with a mixed Th/U γ source using the prominent peak of ^{208}Tl at 2615 keV. This peak was used to stabilize the detector response correcting the signal gain due to temperature drifts. This means that there is a bias on the energy resolution of this peak, especially when the statistics is low (2.2 days). To calibrate, a first-order polynomial fit with zero intercept was performed on the 2615 keV peak. This of course means that the detector non-linearity is neglected. The energy spectrum is shown in Fig. 5.16 and the fit on the 2615 keV peak is shown in its inset, where the FWHM is 5.3 keV. The fit is performed with a model that includes a Gaussian function, a smeared step function for multi-Compton events and a flat background around the peak. Table 5.3 shows the performances of all of the enrLMO crystals at 20.7 mK. It shows the resistance of the thermistor, the rise-time, the decay-time, the sensitivity and the

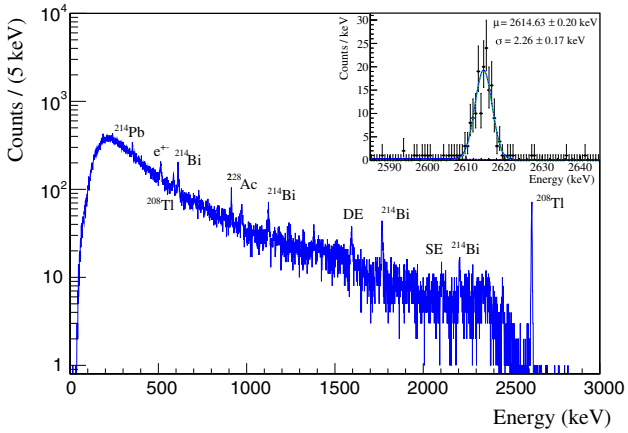

Figure 5.16 – The energy spectrum of 19/20 enrLMO with clear γ peaks from Th/U. The inset shows a fit on the 2614.5 keV ^{208}Tl peak.

baseline resolution, which is estimated using a random trigger injected every 101 s. The estimated median baseline resolution for enrLMO is 1.97 keV. There is just one detector that shows a bad performance and it was excluded from the analysis (enrLMO 2) [98]. These data were analysed using DIANA analysis tool (a software package for bolometers developed by the CUORE collaboration) by the analysis group of CUPID-Mo based on optimum filter.

5.3.1 AmBe data

The light yield was studied using the AmBe calibration data which, thanks to the γ lines above 2615 keV and the neutron capture events at 4784 keV, allows us to estimate the bolometric performances more precisely with respect to the U/Th calibration [79], specifically the light yield and the DP. The data were acquired at 20.7 mK. The presented data were processed with the CSNSM tool described in Section 4.4 and used for all the CROSS detectors. The stabilization of the data was performed using the α+t events from the neutron capture on ^{6}Li. The calibration of enrLMO and the LD were done using the 511 keV γ-rays and the 17.5 keV X-rays induced by ^{60}Co respectively. Fig. 5.17 shows on the *left* the energy spectrum in the α region with the resolution of the peaks. The associated ^{60}Co calibration of the light detectors had a very low statistics, preventing from performing a fit on the X-ray peaks. The *right* figure shows the light yield of one enrLMO, which is around 0.85 keV/MeV providing the capability of rejecting 99.9% of the α particle with 99.9% acceptance of $\gamma(\beta)$. Table 5.4 contains the values of the light yield, quenching factor, the baseline resolution and the sensitivity of all the light detectors. The crystals that are faced by just a one LD on the bottom and a Cu cap from the top show the highest light yield. That is due to the fact that the Cu cap is reflecting some of scintillation light to be collected by the bottom LD. In addition, the light yield of the top LD is higher than that of the bottom LD. This is due to the fact that the bottom protrusion that acts as a support for the crystal makes the bottom aperture a bit smaller than the top one. Note that the α spectrum in Fig. 5.17 (*left*) are at their right energy position because they were calibrated by an α peak. Usually, the whole energy spectrum is calibrated with γ's: this leads to observing the α's at a $\sim$7% higher energy due to a so-called thermal quenching. The scintillation light quenching factor (QF) for the α+t with respect to γ/β is $\sim$23.5%, higher than the QF of α particle

enrLMO	R_{work} (MΩ)	τ_r (ms)	τ_d (ms)	A_{signal} (nV/keV)	$FWHM_{bsln}$ (keV)
1	1.37	31	476	10	2.01
2	1.04	48	1093	1.2	30.6
3	0.75	33	302	14	2.56
4	1.07	29	264	25	2.23
5	1.77	19	584	21	1.52
6	1.69	23	384	25	3.62
7	0.85	24	357	21	1.15
8	1.53	29	406	24	1.04
9	0.69	28	464	13	4.48
10	1.94	32	341	28	0.98
11	2.99	18	173	23	1.7
12	3.76	21	213	15	1.85
13	1.37	25	445	15	4.62
14	1.16	15	95	15	3.77
15	1.24	28	195	6	4.98
16	1.38	21	228	20	1.47
17	1.51	24	292	23	1.94
18	2.22	18	192	17	2.09
19	1.36	20	173	18	1.38
20	2.48	14	97	17	1.89
Median	1.37	24	297	17	1.97

Table 5.3 – The performance of enrLMO crystals operated at 20.7 mK: the Ge-NTD resistance, rise-time, decay-time, sensitivity and the baseline resolution.

of ^{210}Po which is ∼19.7%. Exploiting the combined light from the two LD facing an enrLMO can further improve the discrimination power (section 5.4.2).

enrLMO	LY_b (keV/MeV)	LY_t (keV/MeV)	QF_b	QF_t	$FWHM_b$ (eV)	LD $signal_b$ (μV/keV)
1	0.66	0.69	0.235	0.233	0.19	0.51
2	0.91	- (Cu cap)	0.233	-	0.08	1.16
3	0.39	0.81	0.275	0.236	0.80	0.4
4	0.60	0.57	0.234	0.254	0.12	1.63
5	0.85	- (Cu cap)	0.231	-	0.07	1.05
6	0.62	0.69	0.230	0.232	0.15	0.92
7	- (lost)	0.73	-	0.234	-	-
8	0.60	- (lost)	0.236	-	0.31	0.65
9	0.92	- (Cu cap)	0.234	-	0.13	0.96
10	0.62	0.76	0.231	0.232	0.15	1.12
11	0.61	0.71	0.233	0.238	0.15	2.33
12	0.65	0.74	0.230	0.230	0.07	0.97
13	0.87	- (Cu cap)	0.236	-	0.11	1.2
14	0.57	0.62	0.234	0.237	0.12	1.13
15	0.60	0.69	0.239	0.238	0.09	1.21
16	0.57	0.69	0.235	0.233	0.22	0.75
17	0.84	- (Cu cap)	0.233	-	0.17	1.18
18	0.63	0.74	0.230	0.233	0.11	1.15
19	0.67	0.74	0.228	0.230	0.16	1.21
20	0.65	0.74	0.237	0.234	0.16	0.56
Median	0.68	0.71	0.235	0.235	0.18	1.00

Table 5.4 – The performance of the Ge LDs: the light yield and the quenching factor (QF) for the top (t) and bottom (b) LD, the baseline resolution and the sensitivity of the bottom LD.

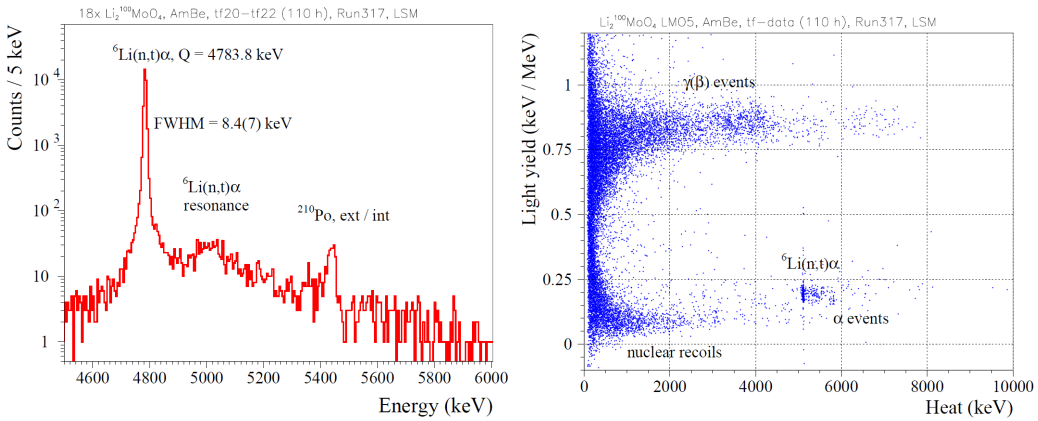

Figure 5.17 – (*left*): the energy spectrum in the α region (calibrated by α's). Two peaks are apparent, the neutron capture events and the α's from ^{210}Po. (*right*): The light yield vs the energy (keV) scatter plot (calibrated with γ lines).

γ peak	Intensity (%)
511	38.0
847	99.9
1038	14.2
1238	66.9
1771	2.3
2035	7.9
2599	17.3
3254	8.1
3451	1.0

Table 5.5 – Some of the γ peaks of ^{56}Co.

5.3.2 ^{56}Co

A ^{56}Co source calibration was performed in order to have a precise measurement on the energy resolution in the ROI of enrLMO, since the source provides γ peaks around $Q_{\beta\beta}$. The source consists of an irradiated ⌀0.25×10 cm ^{56}Fe wire with a ^{56}Co activity of ∼60 Bq. The length of the wire was tuned to prevent a high rate of γ peaks that can lead to pile up events. The source is shown in Fig. 5.18 (*left*). ^{56}Co is produced via ^{56}Fe(p,n)^{56}Co reaction. ^{56}Co decay provides many prominent γ peaks, thus allowing us to calibrate and correct the non-linearity in the detector. Table 5.5 shows the most prominent peaks. Two ^{56}Co sources were placed in the position shown in Fig. 5.18 (*right*). The total activity of the sources is ∼118 Bq.

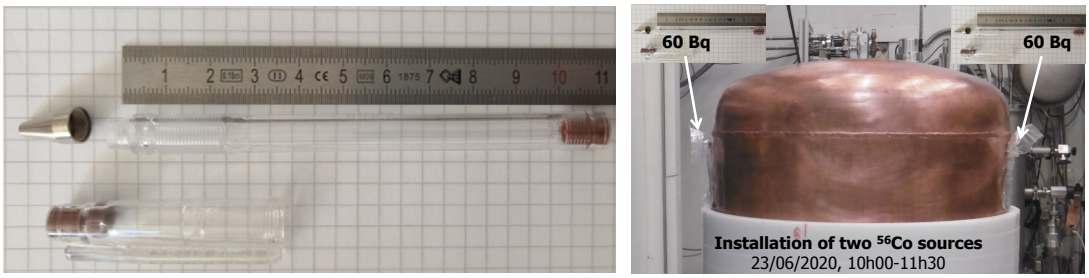

Figure 5.18 – (*left*): ^{56}Co source that consists of a ^{56}Fe wire. (*right*): the position of two ^{56}Co source outside the cryostat.

The bolometric response is stabilized using the 1238 keV events distribution vs baseline offset. An energy spectrum was roughly calibrated by the 1238 keV peaks (Table 5.3). The analysis of this calibration will be improved soon using other γ peaks observed. This calibration was done at the last stage of the CUPID-Mo experiment, so it was necessary to perform a fast analysis to check that the activity of the source in each crystal is not high. Otherwise, the position of the source has to be changed. Fig. 5.19 shows the γ spectrum of the ^{56}Co calibration data, where many γ peaks are apparent. The closest peak to the $Q_{\beta\beta}$, 3253 keV, is prominent with 57 counts/d for the 19 enrLMO in the range 3230-3270 keV. The rate for each tower is plotted in Fig. 5.20. The rate on each detector doesn't exceed the requirement of being below 1/6 Hz.

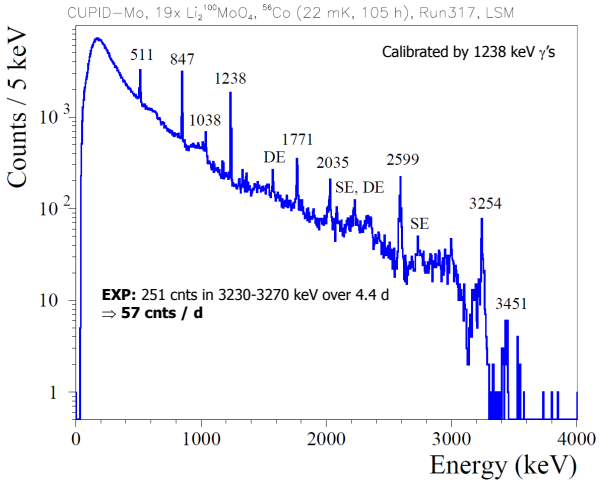

Figure 5.19 – The summed energy spectrum of ^{56}Co source for 19/20 enrLMOs.

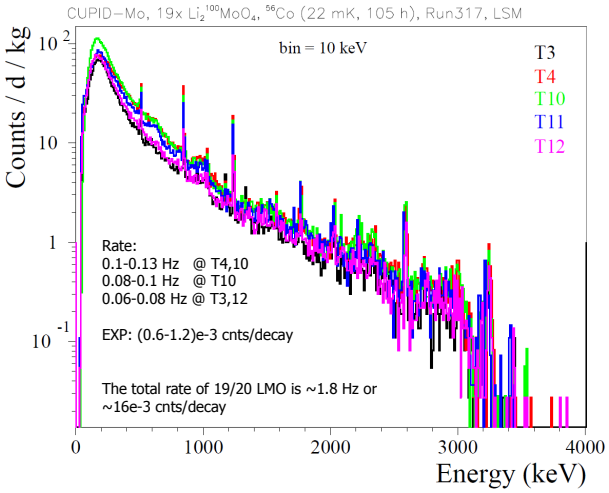

Figure 5.20 – The summed energy spectrum on each tower that shows the rate for each one.

5.4 Triple readout: two LD facing a Li_2 $^{100}MoO_4$ crystal

5.4.1 Escaped surface-event rejection

Events happening on the surface of the crystal can be a challenging source of background in the ROI. While most of the α's can be rejected with dual heat-light readout using the LY, some surface α events can exhibit a more enhanced light signal, thus leaking in the $\gamma(\beta)$ region. These surface events can originate from an escape of some particles from the surface of the crystal to hit directly the light detector. It can be an escape of a nuclear recoil, an α particle or tritium produced from the thermal neutron capture on ^{6}Li (the last case is relevant only in case of neutron calibration). CUPID-Mo setup has the advantage of having 13 crystals facing two light detectors (they should be 15, but one light detector is lost). This feature of triple readout allows us to tag the surface

events on the crystal. On one light detector the escaped event will provide a high fake light signal, but on the other facing light detector these escaped events will have zero or very low light output. Fig. 5.21 shows an example of such a triple readout for an AmBe measurement of enrLMO6 faced by two light detector, LD5 and LD6. The α and neutron capture events in LD5 are selected (red events in the *top-left* figure) and the same events are selected in LD6 (*top-right*). It appears that two events in LD6 are in the $\gamma(\beta)$ band in the ROI and some other events have a more enhanced light with respect to the neutron capture events (probably α or tritium escapes after capture events). Therefore, if we apply the usual cuts using LD6 only and inspect the selected events, we will observe some events in the $\gamma(\beta)$ band that are escaped events in LD6 and can be discriminated only with the help of the LD5 light output. Thanks to this triple readout one can reject these backgrounds.

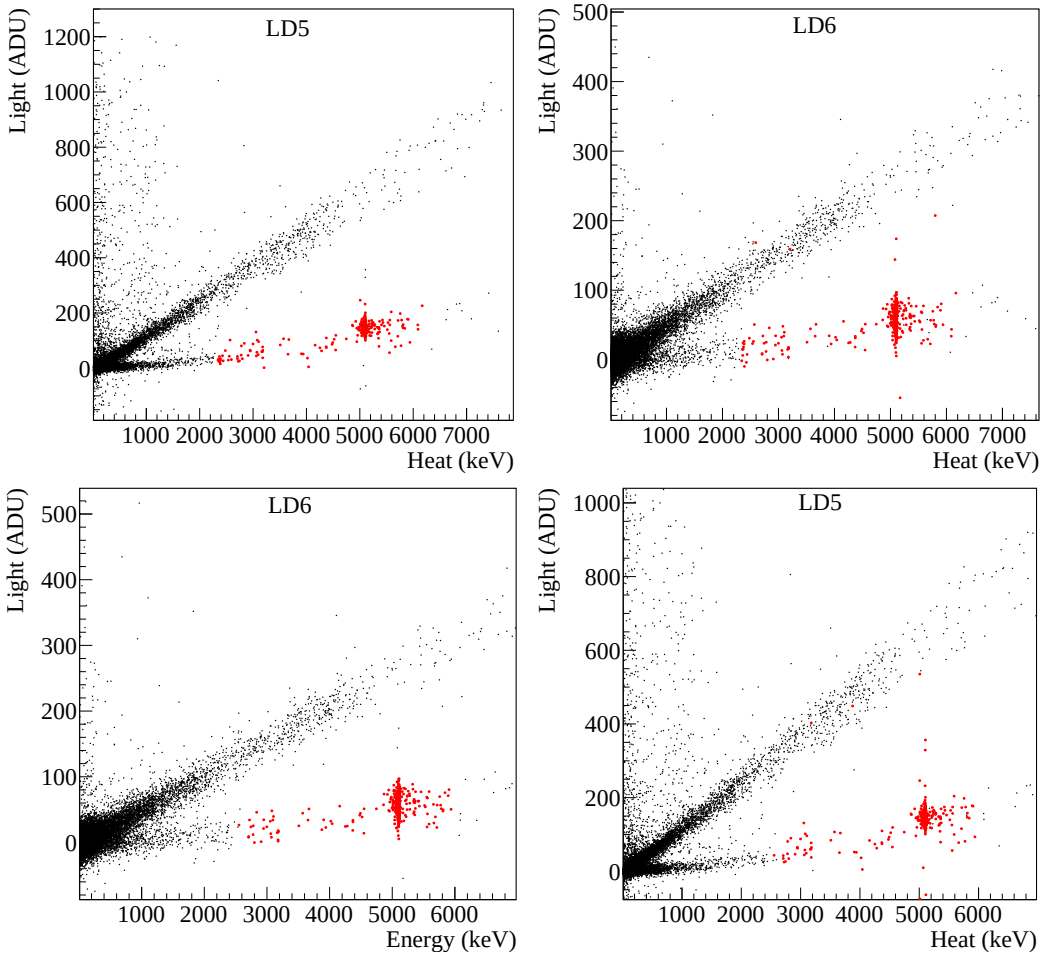

Figure 5.21 – (*top left*): light vs heat of LD5, the α events are selected on this detector (red). *top right*): light vs heat of LD6, the α events that were selected in LD5 are plotted (red). We see some events appear in the γ/β band. These are surface events in the crystal that escaped, depositing energy directly in LD6 (see text). (*bottom left* and *bottom right*): symmetrically, surface events appear in LD5 after selecting α particles in LD6 according to the same argument as in the top figure.

5.4.2 Discrimination power improvement

Another advantage of having a triple readout is the improvement of the discrimination between α and $\gamma(\beta)$ using the light yield. This can be achieved by combining either the raw binary files of the two light detectors before data processing or the output files after data processing (ntp file). Before data processing, the two binary files of the two light detector can be either summed point by point in the window (bit by bit) or by applying a weighted average according to the following equation:

$$\frac{\mathrm{BIN}_{\mathrm{LD1}} \cdot \sigma^2_{\text{baseline LD2}} + \mathrm{BIN}_{\mathrm{LD2}} \cdot \sigma^2_{\text{baseline LD1}}}{\sigma^2_{\text{baseline LD1}} + \sigma^2_{\text{baseline LD2}}} \tag{5.2}$$

where BIN is the binary files and σs are the standard deviation of the baseline distribution in keV, so they represent the signal to noise ratio. This equation allows us to weigh more the output of the LD with better noise.

The LY and the DP are shown in Fig. 5.22 *middle-right* and *bottom* for summed binary files and weighted average binary files respectively. The DP is bit better for the BIN weighted average method, however, in some cases the summed BIN show a better DP as shown in Table 5.6.

Another method for combining the outcome of the two light detectors is to do a weighted average on the light amplitude following Eq 5.2 and by replacing the BIN by the light amplitude of each light detector. Figure 5.22 *bottom-left* shows the LY and the DP following the later described method. The DP is better than the individual DP for each LD. Table 5.6 shows all the triple readout detectors with their corresponding DP. From the results of the DP it was shown that merging the filtered amplitudes of each LD according to a weighted average results in the best α and $\gamma(\beta)$ separation.

This method is specifically useful when one of the two light detector shows a bad performance in terms of discrimination, in which combining the outputs of the two light detectors will lead to improvement.

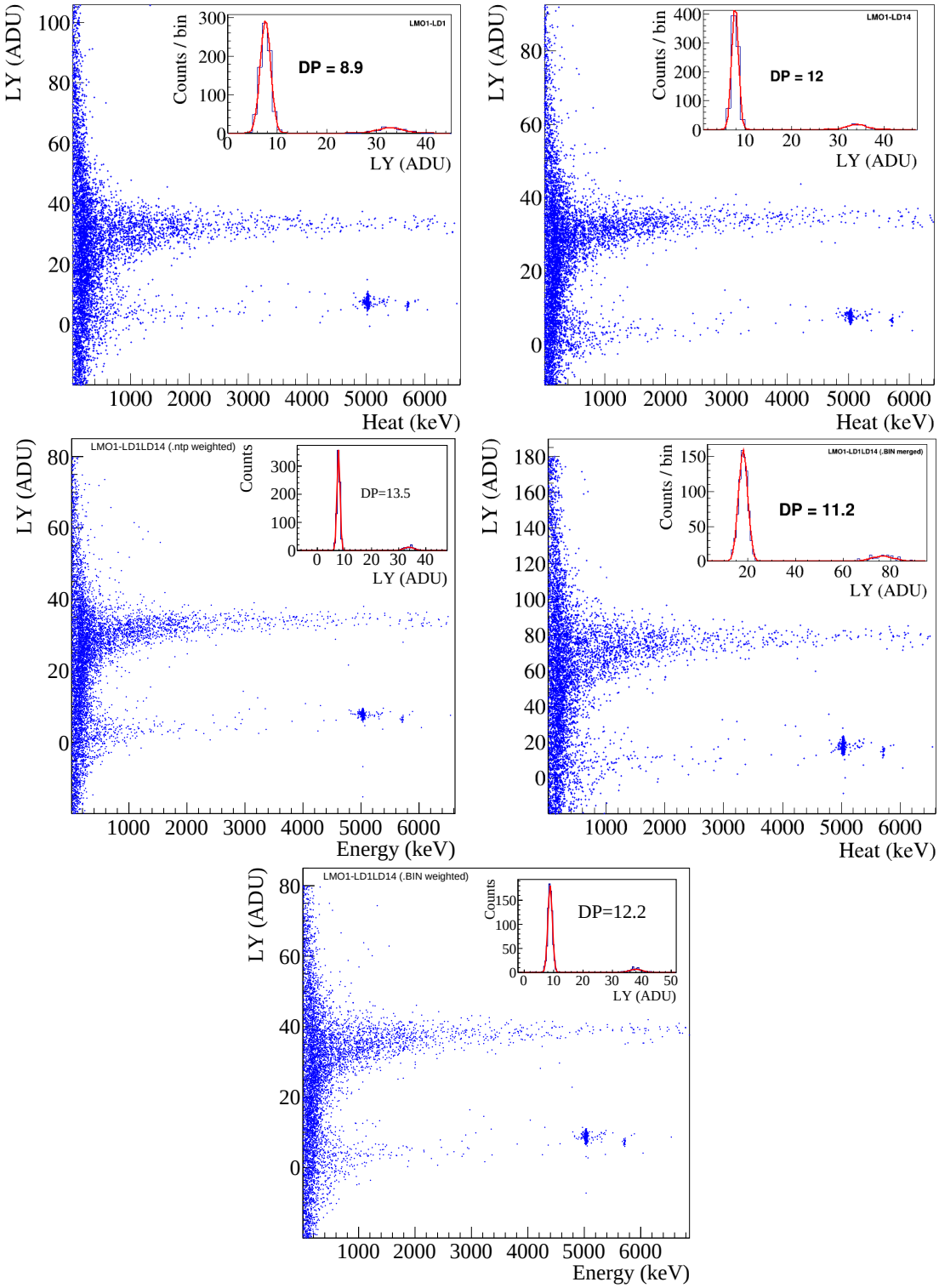

Figure 5.22 – LMO1 faced by two LDs.(*top left*): the LY of LD1 with the DP. (*top right*): the LY if LD14. (*middle left*): the LY and DP of the ntp weighted average combination of the two LDs. (*middle right*): the LY and DP of the binary file (BIN) summed combination of the two LDs. (*bottom*): the LY and DP of the BIN weighted average combination of the two LDs.

enrLMO	DP_b	DP_t	$DP_{\text{ntp weighted}}$	$DP_{\text{BIN summed}}$	$DP_{\text{BIN weighted}}$
1	8.9	12	13.5	11.2	12.2
2	14.2	- (Cu cap)	-	-	-
3	2.3	11.2	11.4	10.2	13.5
4	8.9	2.7	9.3	10.0	9.5
5	13.3	- (Cu cap)	-	-	-
6	7.9	7.8	9.6	5.8	10.1
7	- (lost)	10.3	-	-	-
8	6.5	- (lost)	-	-	-
9	11.6	- (Cu cap)	-	-	-
10	11.0	11.0	13.3	13.2	6.2
11	10.3	8.5	15.2	7.7	14.7
12	12	9.8	14.6	15.7	10.8
13	13.1	- (Cu cap)	-	-	-
14	8.5	8.6	12.9	12.9	12.4
15	13.9	7	14.5	9.8	8.8
16	8	9.9	9.3	9	15.3
17	11.7	- (Cu cap)	-	-	-
18	13.4	9	14.4	18.7	13
19	10.2	11.7	13.7	9.9	14.4
20	10.8	10	13.4	12.4	10.8

Table 5.6 – The table shows that discrimination power (DP) achieved by the top (t) and bottom (b) light detectors, the combined light output of the two LD by weighted average (Eq. 5.2) of the filtered amplitude (ntp weighted), the summed binary files before data processing of the two data processing and the combined binary files of the two LD by weighted average (Eq. 5.2).

5.5 A new limit on $0\nu\beta\beta$-decay of ^{100}Mo

The analysis group of CUPID-Mo have a made big efforts to achieve the final results. They have analysed a total of 240 days of physics data and 73 days of calibration data. Not all the physics data were considered for the Neutrino 2020 conference (where the results were presented for the first time), as only 224 out of the 240 days have a high statistics calibration data that allowed us to calibrate the energy scale precisely. The data are split into 7 data-sets according to the operation conditions. One enrLMO was rejected due to bad performance. The periods of temperature instability were also rejected. The continuous streamed data are processed with DIANA, a tool developed by CUORE [123] and CUPID-0 [124]. The DIANA tool is based on optimum filter (OF) analysis. Triggering offline with the OF decreases energy thresholds for enrLMO and LD, around 9.7 keV and 0.5 keV respectively. The data were blinded from June 2019 till June 2020, and then unblinded in June 2020. The blinded energy spectrum is shown in Fig. 5.23. The total exposure is 2.17 kg$\times$ yr and analysis efficiency η=(90.5$\pm$0.4(stat)$^{+0.9}$ $-$0.2(syst.))%. The energy resolution of the 2615 keV ^{208}Tl peak is around 7.1 keV

FWHM (Fig. 5.24). Fig. 5.25 shows the approximated energy resolution FWHM at the $Q_{\beta\beta}$ is 7.6 keV by a polynomial fit of the γ peaks.

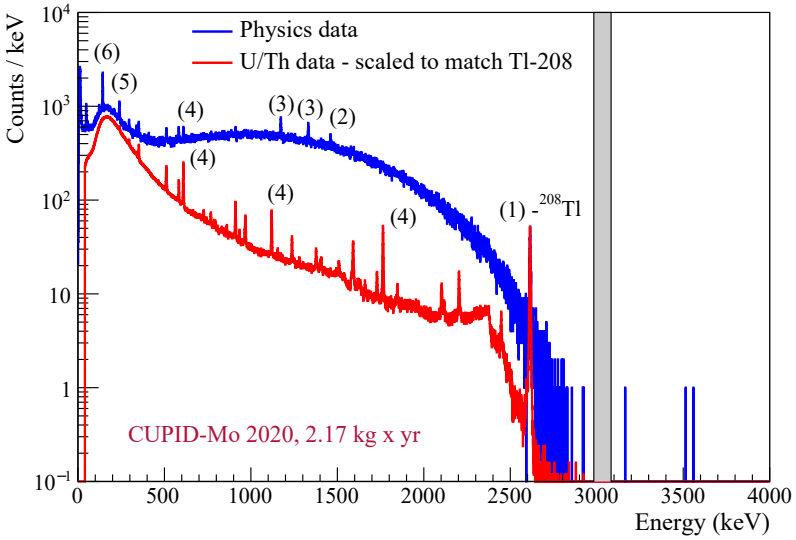

Figure 5.23 – The calibrated energy spectrum for 2.17 kg ×yr.

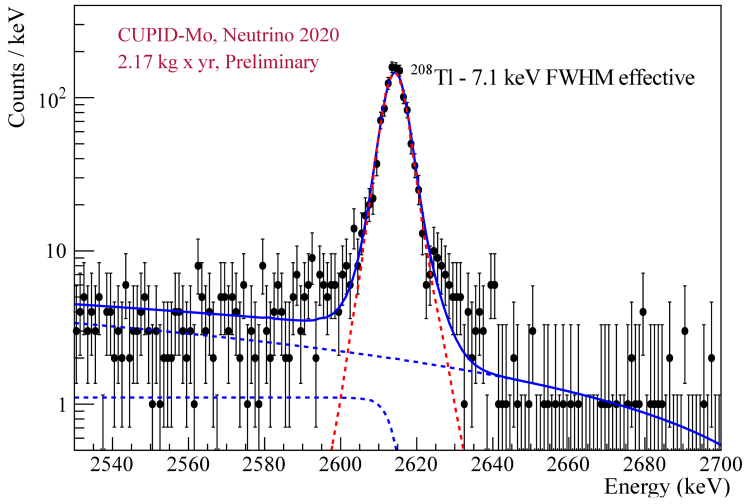

Figure 5.24 – 2615 keV ^{208}Tl peak fit. The energy resolution is 7.1 keV FWHM.

After unblinding the data, it was observed that the ROI contains zero events ($\pm$ 50 keV around the $Q_{\beta\beta}$), as shown in Fig. 5.26. There is just one event in the side-band. (This event resulted to be generated by an internal decay of ^{208}Tl and was eliminated in a subsequent analysis thanks to a delayed α-β coincidence.) With these results on the background, CUPID-Mo achieved a new world leading limit on $0\nu\beta\beta$ of ^{100}Mo with a half-life $T^{0\nu}_{1/2} > 1.5 \cdot 10^{24}$ yr (90% C.I.) [41]. The limit corresponds to an effective Majorana mass $\langle m_{\beta\beta} \rangle <$ (0.31-0.54) eV depending on the Nuclear Matrix Element in the light Majorana neutrino exchange regime.

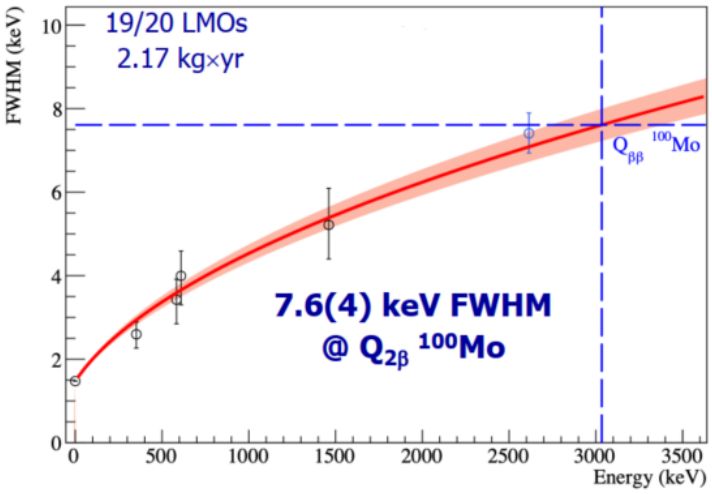

Figure 5.25 – The energy resolution at $Q_{\beta\beta}$ is approximated by a polynomial fit of the gamma peaks.

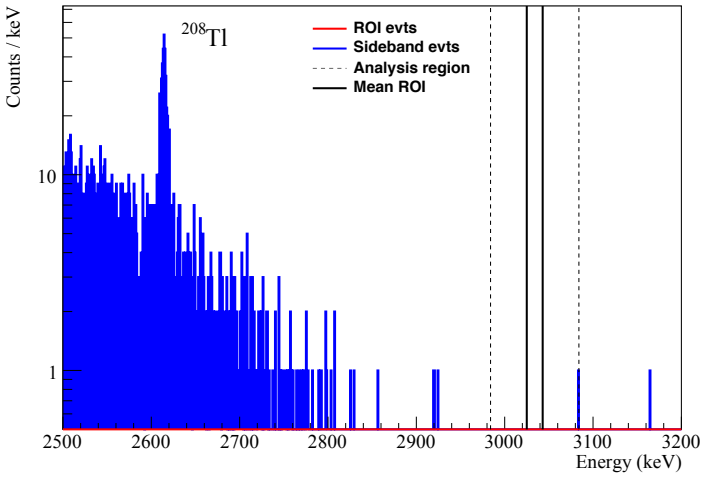

Figure 5.26 – Energy spectrum after unblinding for 2.17 kg ×yr. No event is observed in the ROI [41].

5.6 Conclusion and prospects

CUPID-Mo, demonstrator of CUPID, has validated the reliability of the used technology of dual heat-light readout. With 20 enrLMO and 20 Ge LD, the experiment showed a good uniformity and performance of the detectors. The energy resolution at the Q-value is around 7.7 keV FWHM and the baseline resolution 2 keV FWHM. The preliminary estimation of the background index in the ROI is 3.5×10^{-3} counts/(keV kg yr). A new limit was achieved on the half-life of the $0\nu\beta\beta$ decay of 100-Mo $T^{0\nu}_{1/2} > 1.5 \cdot 10^{24}$ yr (90% C.I.). The results of CUPID-Mo are very encouraging for the CUPID experiment, which will consist of ∼1500 Li_2 $^{100}MoO_4$ scintillation crystals (∼250 kg of ^{100}Mo) installed in the existing CUORE cryostat. It is foreseen to reach a background index of 10^{-4} counts / (keV · kg · yr), evaluated using the background model for the CUORE cryostat and the infor-

mation on crystal and other-element radiopurity coming from CUPID-Mo and CUPID-0 results. This will provide a limit on the half-life of $T_{1/2}^{0\nu} > 1.1 \cdot 10^{27}$ yr in 10 yr data taking, which corresponds to a sensitivity to the effective Majorana mass $m_{\beta\beta}$ of 12-20 meV. CUPID will be therefore one of the most promising neutrinoless double-beta decay experiments of the next generation, with remarkable advantages with respect to the competitors: an existing tested infrastructure, a fully-developed mature detector technology and a reliable background model.

Chapter 6

Conclusions and perspectives

The CROSS prototype tests have demonstrated the viability of a new bolometric technology capable of setting the grounds for future $0\nu\beta\beta$ experiments with a very low background level. It has been shown that Al-Pd bi-layer film coating fulfils our desired pulse shape discrimination capability of surface β and α events when coating on one surface. In addition, Pd-Al grids showed to have a better discrimination power between surface events (β and α) and bulk events. The separation achieved by Pd-Al coating was satisfactory in Li_2MoO_4 but less evident in TeO_2. The coating works as pulse shape modifiers for surface events by accelerating the thermalisation of the surface events compared to the bulk events. Few μm Al film coating on one surface of a small cubic crystals have shown that we can discriminate only surface α events on both Li_2MoO_4 and TeO_2. Increasing the fraction of film-coated surface in the crystal somehow affects badly the discrimination power between surface and bulk events. The physical interpretation is still not in our hands, but an explanation could be that the bulk events also get affected by the increased amount of coating material, which leads also to their faster thermalization. So, Pd-Al bi-layer grids will be implemented on crystals for the future CROSS demonstrator.

6.1 The CROSS demonstrator in the Canfranc underground laboratory

The next step in the CROSS prototype experiments (CROSS16) is to test Pd-Al grids coating on a large crystals at IJCLab, Orsay, with two possible configurations: lateral sides coating and full crystal coating. If full crystal coating will be successful in giving sensitivity to surface α's and β's with the required discrimination power (at least 90% rejection for surface β's and 99.9% rejection for surface α's - corresponding to DP$\geq$ 3.5), this option will be adopted for the CROSS demonstrator (see Fig. 6.1, center). Notice that full coating by grids is compatible with light collection. Therefore, if the surface α DP achieved by coating is not or only marginally sufficient, light detectors can be added (see Fig. 6.1, left).

If good results on discrimination were only achieved when having less fraction of coated surface (only four coated lateral sides), this will be considered as the protocol. In this case, we will keep light detectors between the Li_2MoO_4 cubes facing the non-coated surface. The light detectors will help in α separation and will reject surface β's from the non-coated top and bottom sides by coincidence analysis (see Fig. 6.1, right).

The future medium-scale CROSS demonstrator will run at the existing CROSS fa-

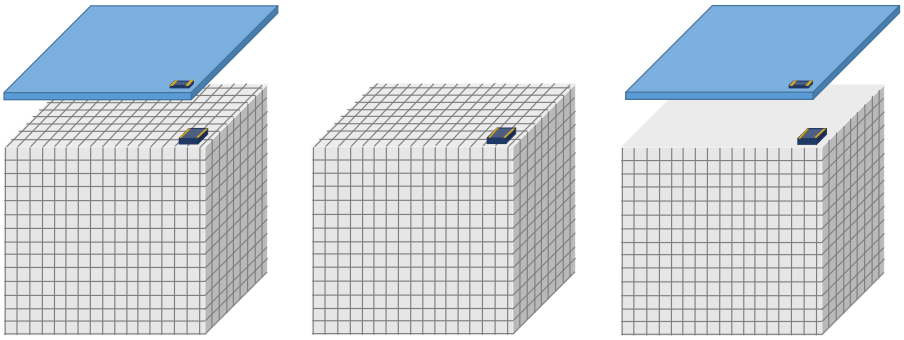

Figure 6.1 – A scheme of the three possible detector modules for the CROSS demonstrator to be confirmed with the CROSS16 experiment. (See text.)

cility at LSC underground laboratory (Laboratorio Subterráneo de Canfranc). The Li_2MoO_4 crystals already exist, in addition to all the requirements for a bolometric experiment (cryostat, electronics...etc). So basically it can start as soon as possible, but, as mentioned in the previous paragraph, the final protocol will be chosen after the CROSS16 experiment (Fig. 6.1).

The medium-scale demonstrator experiment will consist of at least 32 existing enriched $Li_2\ ^{100}MoO_4$ crystals (there are additionally 20 CUPID-Mo crystals and 18 cubic crystals to be received soon, but here we will conservatively discuss the option with existing material) with a total of 4.7 kg of ^{100}Mo (enriched in ^{100}Mo at $> 95\%$). The crystals are of cubic shape with 45mm side and a mass of 0.28 kg. The crystals were produced in a similar way as the LUMINEU experiment, which ensures high radio-purity and excellent bolometric performance [57, 66, 125]. Some of these crystals have already been successfully tested as scintillating bolometers in the CROSS facility [126].

The 32 crystals will be arranged in a tower of eight floors with four crystals each, according to one of the schemes shown in Fig. 6.1. The floors are open to each other so as to provide us with background rejection through anti-coincidences. The experiment has two purposes: one is to confirm the CROSS technology on large detector arrays and to check the reproducibility of the experiment in terms of surface event rejection; the other purpose is to provide a competitive limit on $0\nu\beta\beta$ of ^{100}Mo. The background index in the CROSS facility is assumed to reach 10^{-2}-10^{-3} counts/(keV kg yr), a reasonable value considering that the system, despite the cryostat has been fabricated with radiopure materials and that shielding works effectively, is not optimized for extreme low radioactivity yet. (A veto system to mitigate cosmic ray background will be installed in the future.) This BI value is within the reach of middle scale bolometric demonstrators, as shown by the results of CUPID-0 [79] and CUPID-Mo [41]. Note that the surface β rejection is not a requirement to reach such a BI, but it is crucial for future large-scale searches beyond the current baseline of CUPID. That's why it is very important to validate the CROSS technology with the foreseen middle-scale demonstrator.

The expected sensitivity to $0\nu\beta\beta$ is shown in Table 6.1, considering a set of recent matrix element calculations for ^{100}Mo. A 2-year sensitivity is competitive with all the present searches except the KamLAND-Zen experiment [48] and GERDA [52]. A 5-year

Background level counts/(keV kg yr))	Live time (yr)	Half-life limit (yr) at 90%	$m_{\beta\beta}$ (meV) at 90%
10^{-2}	2	8.5×10^{24}	124-222
10^{-3}	2	1.2×10^{25}	103-185
10^{-2}	5	1.7×10^{25}	88-159
10^{-3}	5	2.8×10^{25}	68-122

Table 6.1 – Sensitivity of the CROSS demonstrator to be operrated in the cryogenics facility of the Canfranc underground laboratory, with the assumption of two background levels.

live-time with a background level of the order of 10^{-3} counts/(keV kg yr) is practically equivalent to the KamLAND-Zen current limit. In all cases, the current worldwide best limit on ^{100}Mo (see Section 5.5 and Ref. [41]) will be largely improved. This shows the potential of the CROSS technology even if the experiment can be considered as a small size demonstrator.

TeO_2 crystals for the CROSS demonstrator are an open option at a very small scale (four or eight crystals in total to be added to the Li_2MoO_4 tower discussed above). The CROSS collaboration is developing a protocol for the production of radio-pure TeO_2 crystals, improving that available now [127]. The purpose is to validate the CROSS technology also on TeO_2. This goal is very important for long term prospects, where the use of TeO_2 on large scale could provide competitive experiments also without enrichment due to the high natural isotopic abundance of the candidate ^{130}Te.

6.2 Impact of the CROSS technology on future bolometric searches for $0\nu\beta\beta$

The results achieved by the ton-scale cryogenic experiment CUORE and its related background model showed that an experiment capable of rejecting the α surface background is compatible with a background level of the order of 10^{-4} counts/(keV kg yr) at the ROI (~3 MeV). CUPID-Mo has demonstrated the technology of rejecting α particles by the use of dual heat-light readout. The future large scale experiment CUPID will adopt this dual readout technology. It is foreseen to reach a background index of the order of 10^{-4} counts/(keV kg yr) by rejecting the dominate surface α background (see Fig. 6.2).

The CROSS technology can provide additionally a rejection for surface β background, with the ability of reaching a background index of the order of 10^{-5} counts/(keV kg yr). Several background components must be reduced to reach this level (see Fig. 6.2), but this goal is impossible without mitigating the surface β background, which contributes substantially to the bars “Detector Holder" and “LMO" shown in Fig. 6.2. The left dominant background contribution to CUPID-like-experiments with CROSS technology is the random coincidence of $2\nu\beta\beta$ which needs additional R&D to be reduced.

The CROSS technology applied for example to a possible expansion of CUPID, dubbed CUPID-1T (ton scale experiment), has the potential to explore fully the inverted-ordering region and to cover some part of the normal ordering region, even in case of vanishing lightest neutrino mass. Fig. 6.3 shows the sensitivity to the effective Majorana

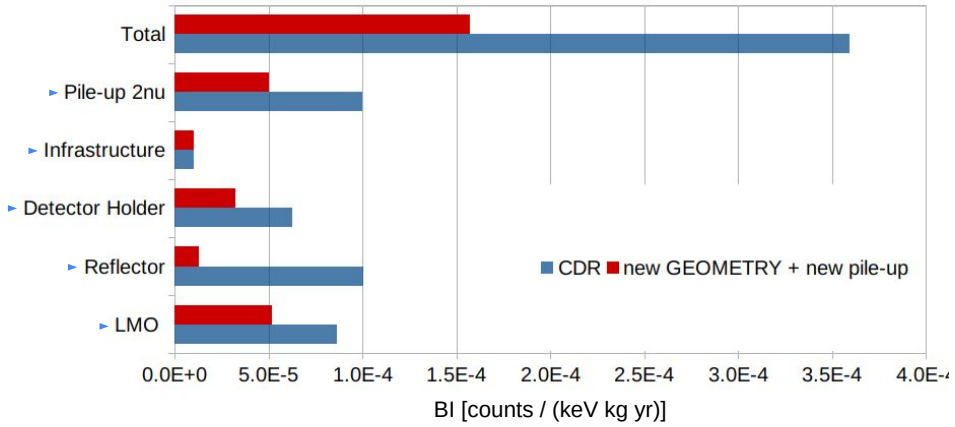

Figure 6.2 – CUPID background budget. Contributions from different components. In blue, the background estimation in CUPID CDR [39]; In red, the current estimation with an upgraded detector geometry.

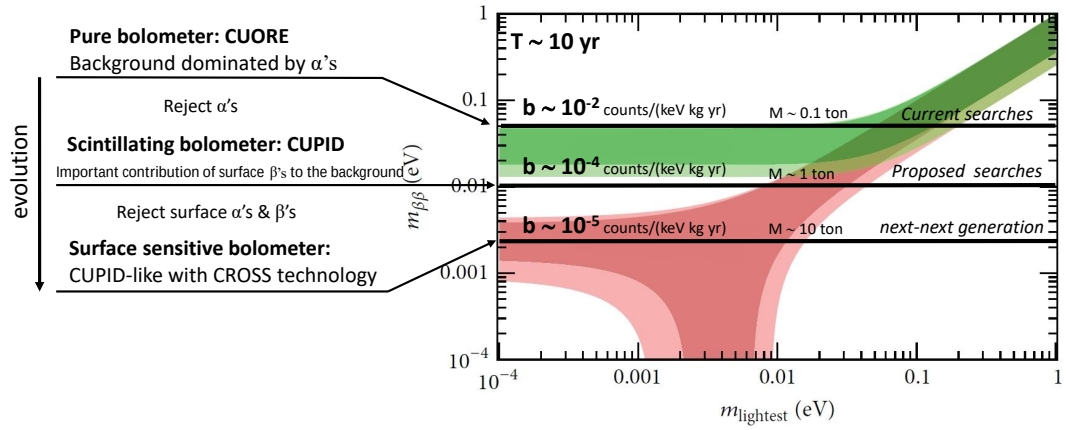

Figure 6.3 – The sensitivity on the effective Majorana mass of the current, next generation (proposed searches) and next-next generation experiments.

mass of CUORE, CUPID with dual-readout, and CUPID-1T with the application of the CROSS technology.

Appendix A

The cryostat

The cryostat is a system that houses the dilution refrigerator and contains the bolometers. The dilution refrigerator is a cooling unit that brings the bolometers to the very low temperatures (∼10-20 mK) required for the heat capacity of the detectors to be low enough. Two different cryostats are described: the wet cryostat that uses cryogenics liquids to cool down (as EDELWEISS cryostat, housing CUPID-Mo) and dry cryostat that does not (as Ulysse, housing CROSS prototypes).

The cryostat consists of several cylindrical copper screens one inside the other, each one at a certain temperature stage. The Outer Vacuum Chamber (OVC) is the outer screen that houses inside all the others. This screen is at room temperature (300 K) and the chamber inside is pumped to high vacuum to isolate the inside screens and preventing heat conduction and convection from the outside. Vacuum however does not protect the inner part of the cryostat against the 300 K blackbody radiation. Reflecting materials covering the screen are capable of reducing the effects of this radiation to a manageable level.

Inside the OVC, one can find first a 80 K screen and, more internally, the IVC (Inner Vacuum Chamber). The screen of the IVC is at 4 K. This temperature can be reached by using a special thermal machine named Pulse Tube in a dry cryostat or a helium bath (boiling temperature at 4.2 K) in a wet cryostat. A thermal machine can be additionally used to slow down helium evaporation in a wet cryostat. The Pulse Tube and thermal machines in general introduce vibrations in the cryostat, generating noise in the bolometers, especially the light ones made of thin wafers, as the light detectors. So it is necessary to mechanically decouple the detectors using spring-based suspensions.

The IVC houses the dilution unit circuit that consists of several parts, including other screens at 1 K, 50 mK and base temperature. The coldest part of the dilution unit is the mixing chamber, to which the detectors are thermally connected.

The key point of the dilution refrigerator is the use of a ^{3}He-^{4}He mixture. At very low temperatures, the mixture separates into two phases: almost pure ^{3}He — concentrate phase — floats on the top (being the lighter phase), while at the bottom we find the other phase — dilute phase — consisting of ^{4}He with a few percentage of ^{3}He.

Fig. A.1 shows the phase diagram depending on the temperature and the ^{3}He concentration in the dilute phase. The reason why some ^{3}He atoms dilute themselves in the ^{4}He phase is due to the Van der Waals force. In fact, ^{3}He and ^{4}He can be closer in distance than ^{3}He-^{3}He, thus the Van der Waals force is larger in the former case that will lead to ^{3}He atoms jumping to the ^{4}He dilute phase. If we can remove ^{3}He atoms from the diluted phase, ^{3}He atoms from the concentrated phase will cross the phase boundary to

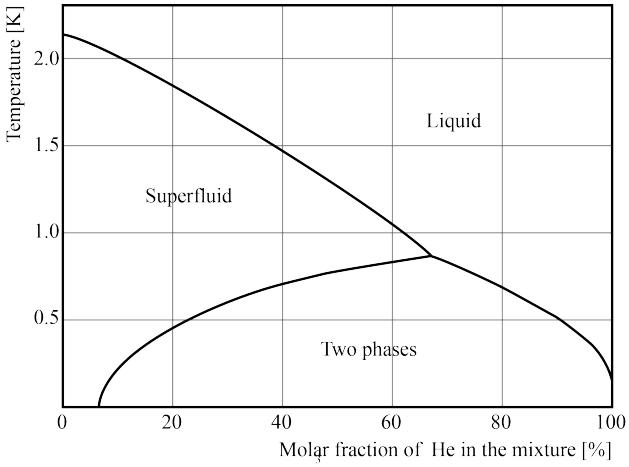

Figure A.1 – Phase diagram of He^3He-^{4} mixtures.

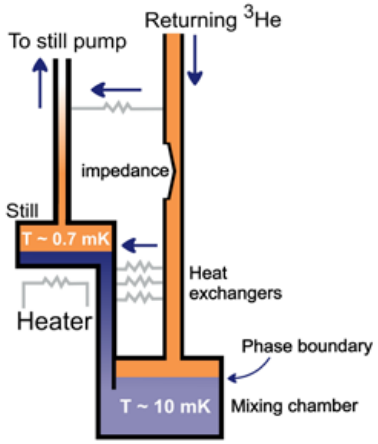

Figure A.2 – Mixture circuit in a dilution unit.

occupy the vacant energy states. This produces cooling power at very low temperatures. The cooling power is given by the enthalpy difference ΔH between ^{3}He in diluted phase and pure ^{3}He, where the enthalpy of ^{3}He in the dilute phase is higher than for pure ^{3}He.

The mixing chamber contains around 6.4% and the still contains around 1% of ^{3}He in the dilute phase. The dilute phase in the mixing chamber is connected to the dilute phase in the still by a pipe (Fig. A.2). The difference in ^{3}He concentration between the still and the mixing chamber results in an osmotic pressure gradient along the connecting pipe that attract ^{3}He in the dilute phase from the mixing chamber to the still. The ^{3}He with the lower vapour pressure in the still is then pumped out the cryostat. It then enters the cryostat passing in strong thermal contact with the Pulse Tube or the helium bath that cools it down to 4 K. Then the temperature of ^{3}He gets lower (down to 1 K) after passing through a Joule-Thomson flow impedance (dry cryostat) or through a pumped secondary liquid helium bath — 1 K pot — (wet cryostat). ^{3}He on its way to the mixing chamber is further thermalised when set in contact with the ^{3}He going from the mixing chamber to the still by means of heat exchangers.

Bibliography

[1] W. Pauli. Letter to L. Meitner and her colleagues (letter open to the participants of the conference in tubingen). 1930.

[2] E. Fermi. Tentativo di una teoria dei raggi b. *Il Nuovo Cimento (1924-1942)*, 11:1, 1934. doi:10.1007/BF02959820.

[3] F. Reines and C. L. Cowan. Detection of the free neutrino. *Phys. Rev.*, 92:830, 1953. doi:10.1103/PhysRev.92.830.

[4] G. Danby et al. Observation of high-energy neutrino reactions and the existence of two kinds of neutrinos. *Phys. Rev. Lett.*, 9:36, 1962. doi:10.1103/PhysRevLett.9.36.

[5] K. Kodama et al. Observation of tau neutrino interactions. *Phys. Lett. B*, 504:218, 2001. doi:10.1016/S0370-2693(01)00307-0.

[6] R. Davis. Attempt to detect the antineutrinos from a nuclear reactor by the $Cl^{37}(\overline{\nu}, e^{-})A^{37}$ reaction. *Phys. Rev.*, 97:766, 1955. doi:10.1103/PhysRev.97.766.

[7] J. Bahcall and R. Ulrich. Solar models, neutrino experiments, and helioseismology. *Rev. Mod. Phys.*, 60:297, 1988. doi:10.1103/RevModPhys.60.297.

[8] V. Gribov and B. Pontecorvo. Neutrino astronomy and lepton charge. *Phys. Lett. B*, 28:493, 1969. doi:10.1016/0370-2693(69)90525-5.

[9] Y. Fukuda et al. Evidence for oscillation of atmospheric neutrinos. *Phys. Rev. Lett.*, 81:1562, 1998. doi:10.1103/PhysRevLett.81.1562.

[10] Q. R. Ahmad et al. Measurement of the rate of $\nu_e + d \rightarrow p + p + e^{-}$ interactions produced by ^{8}b solar neutrinos at the sudbury neutrino observatory. *Phys. Rev. Lett.*, 87:071301, 2001. doi:10.1103/PhysRevLett.87.071301.

[11] E. Majorana. Teoria simmetrica dell'elettrone e del positrone. *Nuovo Cim.*, 14:171, 1937. doi:10.1007/BF02961314.

[12] A. B. Balantekin and B. Kayser. On the properties of neutrinos. *Annu. Rev. Nucl. Part. S*, 68:313, 2018. doi:10.1146/annurev-nucl-101916-123044.

[13] K. Eguchie et al. First results from kamland: Evidence for reactor antineutrino disappearance. *Phys. Rev. Lett.*, 90:021802, 2003. doi:10.1103/PhysRevLett.90.021802.

[14] M. H. Ahn et al. Measurement of neutrino oscillation by the k2k experiment. *Phys. Rev. D*, 74:072003, 2006. doi:10.1103/PhysRevD.74.072003.

[15] F. Capozzi et al. Addendum to "global constraints on absolute neutrino masses and their ordering". *Phys. Rev. D*, 101:116013, 2020. doi:10.1103/PhysRevD.101.116013.

[16] KATRIN Collaboration and KATRIN Collaboration. Katrin design report 2004. Technical report, Forschungszentrum Jülich, 2005. 51.54.01; LK 01.

[17] M. Aker et al. Improved upper limit on the neutrino mass from a direct kinematic method by katrin. *Phys. Rev. Lett.*, 123:221802, 2019. doi:10.1103/PhysRevLett.123.221802.

[18] Ch. Kraus et al. Final results from phase ii of the mainz neutrino mass searchin tritium β-decay. *Eur. Phys. J. C*, 40:447, 2005. doi:10.1140/epjc/s2005-02139-7.

[19] V. N. Aseev et al. Upper limit on the electron antineutrino mass from the troitsk experiment. *Phys. Rev. D*, 84:112003, 2011. doi:10.1103/PhysRevD.84.112003.

[20] Planck Collaboration. Planck 2018 results - vi. cosmological parameters. *A&A*, 641:A6, 2020. doi:10.1051/0004-6361/201833910.

[21] M. Goeppert-Mayer. Double beta-disintegration. *Phys. Rev.*, 48:512, 1935. doi:10.1103/PhysRev.48.512.

[22] W. H. Furry. On transition probabilities in double beta-disintegration. *Phys. Rev.*, 56:1184, 1939. doi:10.1103/PhysRev.56.1184.

[23] A. Giuliani and A. Poves. Neutrinoless Double-Beta Decay. *Adv. High Energy Phys.*, 2012:857016, 2012. doi:10.1155/2012/857016.

[24] H. Päs and W. Rodejohann. Neutrinoless Double Beta Decay. *New J. Phys.*, 17:115010, 2015. doi:10.1088/1367-2630/17/11/115010.

[25] S. Dell'Oro et al. Neutrinoless double beta decay: 2015 review. *Adv. High Energy Phys.*, 2016:2162659, 2016. doi:10.1155/2016/2162659.

[26] J.D. Vergados et al. Neutrinoless double beta decay and neutrino mass. *Int. J. Mod. Phys. E*, 25:1630007, 2016. doi:10.1142/S0218301316300071.

[27] Alexander Barabash. Precise half-life values for two-neutrino double-β decay: 2020 review, 2020.

[28] O. Cremonesi and M. Pavan. Challenges in Double Beta Decay. *Adv. High Energy Phys.*, 2014:951432, 2014. doi:10.1155/2014/951432.

[29] A. Giuliani et al. Double Beta Decay APPEC Committee Report. 2019. arXiv:1910.04688.

[30] F. Šimkovic. $0\nu\beta\beta$ and $2\nu\beta\beta$ nuclear matrix elements, quasiparticle random-phase approximation, and isospin symmetry restoration. *Phys. Rev. C*, 87:045501, 2013. doi:10.1103/PhysRevC.87.045501.

[31] J. Menéndez et al. Disassembling the nuclear matrix elements of the neutrinoless $\beta\beta$ decay. *Nuclear Physics A*, 818:139, 2009. doi:10.1016/j.nuclphysa.2008.12.005.

[32] J. Barea et al. $0\nu\beta\beta$ and $2\nu\beta\beta$ nuclear matrix elements in the interacting boson model with isospin restoration. *Phys. Rev. C*, 91:034304, 2015. doi:10.1103/PhysRevC.91.034304.

[33] J.J Gómez-Cadenas et al. Sense and sensitivity of double beta decay experiments. *Journal of Cosmology and Astroparticle Physics*, 2011:007, 2011. doi:10.1088/1475-7516/2011/06/007.

[34] M. Agostini et al. Probing majorana neutrinos with double-β decay. *Science*, 365:1445, 2019. doi:10.1126/science.aav8613.

[35] S. I. Alvis. Search for neutrinoless double-β decay in ^{76}Ge with 26 kg yr of exposure from the majorana demonstrator. *Phys. Rev. C*, 100:025501, 2019. doi:10.1103/PhysRevC.100.025501.

[36] N. Abgrall et al. The large enriched germanium experiment for neutrinoless double beta decay (legend). *AIP Conf. Proc*, 1894:020027, 2017. doi:10.1063/1.5007652.

[37] Alessio Caminata et al. Results from the Cuore Experiment. *Universe*, 5:10, 2019. doi:10.3390/universe5010010.

[38] D. Q. Adams et al. Improved limit on neutrinoless double-beta decay in ^{130}Te with cuore. *Phys. Rev. Lett.*, 124:122501, 2020. doi:10.1103/PhysRevLett.124.122501.

[39] W.R. Armstrong et al. CUPID pre-CDR. 2019. arXiv:1907.09376.

[40] O. Azzolini et al. Final result of cupid-0 phase-i in the search for the ^{82}Se neutrinoless double-β decay. *Phys. Rev. Lett.*, 123:032501, 2019. doi:10.1103/PhysRevLett.123.032501.

[41] E. Armengaud et al. A new limit for neutrinoless double-beta decay of ^{100}Mo from the CUPID-Mo experiment. 2020. arXiv:2011.13243.

[42] V. Alenkov et al. First results from the amore-pilot neutrinoless double beta decay experiment. *Eur. Phys. J. C*, 79:791, 2019. doi:10.1140/epjc/s10052-019-7279-1.

[43] G. Anton et al. Search for neutrinoless double-β decay with the complete exo-200 dataset. *Phys. Rev. Lett.*, 123:161802, 2019. doi:10.1103/PhysRevLett.123.161802.

[44] J. B. Albert et al. Sensitivity and discovery potential of the proposed nexo experiment to neutrinoless double-β decay. *Phys. Rev. C*, 97:065503, 2018. doi:10.1103/PhysRevC.97.065503.

[45] J. Martín-Albo et al. Sensitivity of next-100 to neutrinoless double beta decay. *J. High Energy Phys.*, 2016:159, 2016. doi:10.1007/JHEP05(2016)159.

[46] A. Giuliani. The Mid and Long Term Future of Neutrinoless Double Beta Decay, June 2018. doi:10.5281/zenodo.1286915.

[47] C. Adams et al. Sensitivity of a tonne-scale next detector for neutrinoless double beta decay searches, 2020. arXiv:2005.06467.

[48] A. Gando et al. Search for majorana neutrinos near the inverted mass hierarchy region with kamland-zen. *Phys. Rev. Lett.*, 117:082503, 2016. doi:10.1103/PhysRevLett.117.082503.

[49] Y. Gando (for the KamLAND-Zen Collaboration). Neutrinoless double beta decay search with liquid scintillator experiments. In *Proceedings, Prospects in Neutrino Physics (NuPhys2018): London, UK, December 19-21, 2018*, 2019. arXiv:1904.06655.

[50] A. Minotti. Status of the supernemo experiment. 2020.

[51] R. Arnold et al. Measurement of the double-beta decay half-life and search for the neutrinoless double-beta decay of ^{48}Ca with the nemo-3 detector. *Phys. Rev. D*, 93:112008, 2016. doi:10.1103/PhysRevD.93.112008.

[52] M. Agostini et al. Final results of gerda on the search for neutrinoless double-β decay. *Phys. Rev. Lett.*, 125:252502, 2020. doi:10.1103/PhysRevLett.125.252502.

[53] R. Arnold et al. Final results on ^{82}Se double beta decay to the ground state of ^{82}Kr from the nemo-3 experiment. *Eur. Phys. J. C*, 78:821, 2018. doi:10.1140/epjc/s10052-018-6295-x.

[54] A. Jeremie. The SuperNEMO demonstrator double beta experiment. *Nucl. Instrum. Methods Phys. Res. A*, 958:162115, 2019. doi:10.1016/j.nima.2019.04.069.

[55] J. Argyriades et al. Measurement of the two neutrino double beta decay half-life of Zr-96 with the NEMO-3 detector. *Nucl. Phys. A*, 847:168, 2010. doi:10.1016/j.nuclphysa.2010.07.009.

[56] R. Arnold et al. Results of the search for neutrinoless double-β decay in ^{100}Mo with the nemo-3 experiment. *Phys. Rev. D*, 92:072011, 2015. doi:10.1103/PhysRevD.92.072011.

[57] D. V. Poda. 100mo-enriched li2moo4 scintillating bolometers for $0\nu2\beta$ decay search: From lumineu to cupid-0/mo projects. *AIP Conf. Proc*, 1894:020017, 2017. doi:10.1063/1.5007642.

[58] A. S. Barabash et al. Final results of the aurora experiment to study 2β decay of ^{116}Cd with enriched $^{116}Cdwo_4$ crystal scintillators. *Phys. Rev. D*, 98:092007, 2018. doi:10.1103/PhysRevD.98.092007.

[59] R. Arnold et al. Measurement of the 2ν β β decay half-life and search for the 0ν β β decay of 116Cd with the NEMO-3 detector. *Phys. Rev. D*, 95:012007, 2017. doi:10.1103/PhysRevD.95.012007.

[60] R. Arnold et al. Measurement of the $2\nu\beta\beta$ decay half-life of ^{150}Nd and a search for $0\nu\beta\beta$ decay processes with the full exposure from the nemo-3 detector. *Phys. Rev. D*, 94:072003, 2016. doi:10.1103/PhysRevD.94.072003.

[61] E. Caden. Status of the sno+ experiment. *J. Phys. Conf. Ser*, 1342:012022, 2020. doi:10.1088/1742-6596/1342/1/012022.

[62] D. Poda and A. Giuliani. Low background techniques in bolometers for double-beta decay search. *Int. J. Mod. Phys. A*, 32:1743012, 2017. doi:10.1142/S0217751X17430126.

[63] C. Alduino and K. Alfonso. The projected background for the cuore experiment. *Eur. Phys. J. C*, 77:543, 2017. doi:10.1140/epjc/s10052-017-5080-6.

[64] E. Fiorini and T.O. Niinikoski. Low-temperature calorimetry for rare decays. *Nucl. Instrum. Meth.*, 224:83, 1984. doi:https://doi.org/10.1016/0167-5087(84)90449-6.

[65] T.B. Bekker et al. Aboveground test of an advanced Li_2MoO_4 scintillating bolometer to search for neutrinoless double beta decay of ^{100}Mo. *Astropart. Phys.*, 72:38, 2016. doi:10.1016/j.astropartphys.2015.06.002.

[66] E. Armengaud et al. Development of ^{100}Mo-containing scintillating bolometers for a high-sensitivity neutrinoless double-beta decay search. *Eur. Phys. J. C*, 77:785, 2017. doi:10.1140/epjc/s10052-017-5343-2.

[67] A.E. Musikhin et al. The heat capacity of li2moo4 in the temperature range 6–310k. *J. Alloy Compd*, 639:145, 2015. doi:10.1016/j.jallcom.2015.03.159.

[68] M. Barucci. Measurement of low temperature specific heat of crystalline teo2 for the optimization of bolometric detectors. *J. Low Temp. Phys.*, 123:303, 2001. doi:10.1023/A:1017555615150.

[69] E. E. Haller et al. Ntd germanium: A novel material for low temperature bolometers. page 21, 1984. doi:10.1007/978-1-4613-2695-3_2.

[70] L. Dumoulin et al. Nb-si thin films as thermometers for low temperature bolometers. *J. Low Temp. Phys*, 93:301, 1993. doi:10.1007/BF00693437.

[71] O. Crauste et al. Tunable superconducting properties of a-nbsi thin films and application to detection in astrophysics. *J. Low Temp. Phys*, 163:60, 2011. doi:10.1007/s10909-010-0284-2.

[72] B. I. Shklovskii and A. L. Efros. Electronic properties of doped semiconductors. 45, 1984. doi:10.1007/978-3-662-02403-4.

[73] M. Barucci et al. Electrical characteristics of heavily doped ntd ge at very low temperatures. *Physica B Condens. Matter*, 368:139, 2005. doi:10.1016/j.physb.2005.07.008.

[74] E. Haller et al. Neutron transmutation depot (ntd) germanium thermistors for submillimetre bolometer applications. 388, 1996.

[75] M. Pedretti et al. Measurement of thermal properties for modeling and optimization of large mass bolometers. *Physica B: Condens. Matter*, 329-333:1614, 2003. doi:10.1016/S0921-4526(02)02426-2.

[76] D. Yvon et al. Evidence for signal enhancement due to ballistic phonon conversion in nbsi thin films bolometers. *Nucl. Instrum. Meth. A*, 370:200, 1996. doi:10.1016/0168-9002(95)01097-1.

[77] S. H. Moseley et al. Thermal detectors as x-ray spectrometers. *J. Appl. Phys*, 56:1257, 1984. doi:10.1063/1.334129.

[78] C. Alduino and F. Alessandria. First results from cuore: A search for lepton number violation via $0\nu\beta\beta$ decay of ^{130}Te. *Phys. Rev. Lett.*, 120:132501, 2018. doi:10.1103/PhysRevLett.120.132501.

[79] L. Cardani. Final results of the cupid-0 phase i experiment. *J Low. Temp. Phys.*, 199:425, 2020. doi:10.1007/s10909-020-02382-w.

[80] S. Pirro et al. Scintillating double beta decay bolometers. *Phys. Atom. Nucl.*, 69:2109, 2006. doi:10.1134/S1063778806120155.

[81] N. Coron et al. Scintillating and particle discrimination properties of selected crystals for low-temperature bolometers: From LiF to BGO. *Nucl. Instrum. Meth. A*, 520:159, 2004. doi:10.1016/j.nima.2003.11.282.

[82] L. Berge et al. Complete event-by-event $\alpha/\gamma(\beta)$ separation in a full-size TeO_2 CUORE bolometer by Neganov-Luke-magnified light detection. *Phys. Rev. C*, 97:032501, 2018. doi:10.1103/PhysRevC.97.032501.

[83] T. Tabarelli de Fatis. Cerenkov emission as a positive tag of double beta decays in bolometric experiments. *Eur. Phys. J. C*, 65:359, 2010. doi:10.1140/epjc/s10052-009-1207-8.

[84] B.S. Neganov and V.N. Trofimov. Colorimetric method measuring ionizing radiation. *Otkryt. Izobret.*, 146:215, 1985.

[85] P. N. Luke. Voltage-assisted calorimetric ionization detector. *J. Appl. Phys*, 64:6858, 1988. doi:10.1063/1.341976.

[86] D. V. Kazakovtsev and Y. B. Levinson. Phonon diffusion with frequency down-conversion. page 162, 1996. doi:10.1142/9789814317344_0023.

[87] T. I. Galkina. Generation and propagation of phonons in crystalline and amorphous silicon under optical excitation. page 410, 1987.

[88] The CROSS collaboration. The $0\nu2\beta$-decay cross experiment: preliminary results and prospects. *JHEP*, 2020:18, 2020. doi:10.1007/JHEP01(2020)018.

[89] C. Nones. Superconducting aluminum layers as pulse shape modifiers: An innovative solution to fight against surface background in neutrinoless double beta decay experiments. *J. Low Temp. Phys*, 167:1029, 2012. doi:10.1007/s10909-012-0558-y.

[90] John F. Cochran and D. E. Mapother. Superconducting transition in aluminum. *Phys. Rev.*, 111:132, 1958. doi:10.1103/PhysRev.111.132.

[91] S. Tamura. Numerical evidence for the bottleneck frequency of quasidiffusive acoustic phonons. *Phys. Rev. B*, 56:13630, 1997. doi:10.1103/PhysRevB.56.13630.

[92] R. Orbach and L. A. Vredevoe. The attenuation of high frequency phonons at low temperatures. *Phys. Phys. Fiz*, 1:91, 1964. doi:10.1103/PhysicsPhysiqueFizika.1.91.

[93] J. Schnagl et al. First tests on phonon threshold spectroscopy. *Nuclear Instruments and Methods in Physics Research Section A: Accelerators, Spectrometers, Detectors and Associated Equipment*, 444:245, 2000. doi:10.1016/S0168-9002(99)01378-9.

[94] E. Gatti and P.F. Manfredi. Processing the Signals From Solid State Detectors in Elementary Particle Physics. *Riv. Nuovo Cim.*, 9N1:1, 1986. doi:10.1007/BF02822156.

[95] C. Arnaboldi et al. A Calorimetric search on double beta decay of Te-130. *Phys. Lett. B*, 557:167, 2003. doi:10.1016/S0370-2693(03)00212-0.

[96] C. Arnaboldi et al. Results from a search for the 0 neutrino beta beta-decay of Te-130. *Phys. Rev. C*, 78:035502, 2008. doi:10.1103/PhysRevC.78.035502.

[97] N. Moggi and C. Alduino. Results from cuore and cuore-0. *AIP Conf. Proc*, 1894:020016, 2017. doi:10.1063/1.5007641.

[98] E. Armengaud et al. The cupid-mo experiment for neutrinoless double-beta decay: performance and prospects. *Eur. Phys. J. C*, 80:44, 2020. doi:10.1140/epjc/s10052-019-7578-6.

[99] F. Alessandria et al. CUORE crystal validation runs: results on radioactive contamination and extrapolation to CUORE background. *Astropart. Phys.*, 35:839, 2012. doi:10.1016/j.astropartphys.2012.02.008.

[100] V.D. Grigorieva et al. Li2moo4 crystals grown by low thermal gradient czochralski technique. *J. Mat. Sci. Eng. B*, 7:63, 2017. doi:10.17265/2161-6221/2017.3-4.002.

[101] A.S. Barabash et al. Average and recommended half-life values for two-neutrino double beta decay. *Nucl. Phys. A*, 935:52, 2015. doi:10.1016/j.nuclphysa.2015.01.001.

[102] D.M. Chernyak et al. Random coincidence of $2\nu2\beta$ decay events as a background source in bolometric $0\nu2\beta$ decay experiments. *Eur. Phys. J. C*, 72:1989, 2012. doi:10.1140/epjc/s10052-012-1989-y.

[103] A. Giuliani et al. A multi-isotope $0\nu2\beta$ bolometric experiment. *Eur. Phys. J. C*, 78:272, 2018. doi:10.1140/epjc/s10052-018-5750-z.

[104] F. Alessandria et al. CUORE crystal validation runs: results on radioactive contamination and extrapolation to CUORE background. *Astropart. Phys.*, 35:839, 2012. doi:10.1016/j.astropartphys.2012.02.008.

[105] V. Novati et al. Charge-to-heat transducers exploiting the Neganov-Trofimov-Luke effect for light detection in rare-event searches. *Nucl. Instrum. Meth. A*, 940:320, 2019. doi:10.1016/j.nima.2019.06.044.

[106] A. Alessandrello et al. Methods for response stabilization in bolometers for rare decays. *Nucl. Instrum. Meth. A*, 412:454, 1998. doi:10.1016/S0168-9002(98)00458-6.

[107] M. Mancuso et al. An Aboveground Pulse-Tube-Based Bolometric Test Facility for the Validation of the LUMINEU $ZnMoO_4$ Crystals. *J. Low Temp. Phys.*, 176:571, 2014. doi:10.1007/s10909-013-1044-x.

[108] C. Arnaboldi et al. The programmable front-end system for cuoricino, an array of large-mass bolometers. *IEEE Trans. Nucl. Sci.*, 49:2440, 2002. doi:10.1109/TNS.2002.803886.

[109] C. Arnaboldi et al. A novel technique of particle identification with bolometric detectors. *Astropart. Phys*, 34:797, 2011. doi:10.1016/j.astropartphys.2011.02.006.

[110] S. Agostinelli et al. GEANT4–a simulation toolkit. *Nucl. Instrum. Meth. A*, 506:250, 2003. doi:10.1016/S0168-9002(03)01368-8.

[111] J. Allison. Geant4 developments and applications. *IEEE Trans. Nucl. Sci.*, 53:270, 2006. doi:10.1109/TNS.2006.869826.

[112] F. Bellini et al. Response of a TeO_2 bolometer to alpha particles. *JINST*, 5:P12005, 2010. doi:10.1088/1748-0221/5/12/P12005.

[113] L.H. Bennett. *Electronic Density of States*. NBS special publication. Government Press, 1971.

[114] G. Wilson et al. Electron range computational tool for arbitrary materials over a wide energy range. 2018. poster. paper 89.

[115] J. Meija et al. Isotopic compositions of the elements 2013 (iupac technical report). *Pure and Applied Chemistry*, 88:293, 2016. doi:https://doi.org/10.1515/pac-2015-0503.

[116] M.B. Chadwick et al. Endf/b-vii.1 nuclear data for science and technology: Cross sections, covariances, fission product yields and decay data. *Nuclear Data Sheets*, 112:2887, 2011. doi:10.1016/j.nds.2011.11.002.

[117] O. Azzolini et al. Search for neutrinoless double beta decay of ^{64}zn and ^{70}zn with cupid-0. *Eur. Phys. J. C*, 80:702, 2020. doi:10.1140/epjc/s10052-020-8280-4.

[118] O. Azzolini et al. Background Model of the CUPID-0 Experiment. *Eur. Phys. J. C*, 79:583, 2019. doi:10.1140/epjc/s10052-019-7078-8.

[119] M. Mancuso et al. An experimental study of antireflective coatings in ge light detectors for scintillating bolometers. *EPJ Web of Conferences*, 65:04003, 2014. doi:10.1051/epjconf/20136504003.

[120] E.E. Haller. Advanced far-infrared detectors. *Infrared Phys. Technol.*, 35:127, 1994. doi:10.1016/1350-4495(94)90074-4.

[121] E. Armengaud et al. Performance of the edelweiss-iii experiment for direct dark matter searches. *JINST*, 12:P08010, 2017. doi:10.1088/1748-0221/12/08/P08010.

[122] B. Schmidt et al. Muon-induced background in the edelweiss dark matter search. *Astropart. Phys*, 44:28, 2013. doi:10.1016/j.astropartphys.2013.01.014.

[123] C. Alduino et al. Analysis techniques for the evaluation of the neutrinoless double-β decay lifetime in ^{130}Te with the cuore-0 detector. *Phys. Rev. C*, 93:045503, 2016. doi:10.1103/PhysRevC.93.045503.

[124] O. Azzolini et al. Search of the neutrino-less double beta decay of ^{82}se into the excited states of ^{82}kr with cupid-0. *Eur. Phys. J. C*, 78:888, 2018. doi:10.1140/epjc/s10052-018-6340-9.

[125] L. Berge et al. Purification of molybdenum, growth and characterization of medium volume ZnMoO(4) crystals for the LUMINEU program. *JINST*, 9:P06004, 2014. doi:10.1088/1748-0221/9/06/P06004.

[126] A. Armatol et al. A CUPID Li_2 $^{100}MoO_4$ scintillating bolometer tested in the CROSS underground facility. 2020. arXiv:2011.13806.

[127] D.R. Artusa et al. Enriched TeO_2 bolometers with active particle discrimination: towards the CUPID experiment. *Phys. Lett. B*, 767:321, 2017. doi:10.1016/j.physletb.2017.02.011.

université PARIS-SACLAY

ÉCOLE DOCTORALE
Particules, hadrons, énergie et noyau: instrumentation, imagerie, cosmos et simulation (PHENIICS)

Titre: CROSS et CUPID-Mo: stratégies futures et nouveaux résultats dans la quête bolométrique du $0\nu\beta\beta$

Mots clés: Détecteurs à basse température, Double désintégration beta , Sensibilité de surface, Bolomètres

Résumé: La désintégration double-beta sans émission de neutrino est une transition nucléaire hypothétique et rare ($T_{1/2}>10^{26}$ ans). Son observation fournirait de précieuses informations sur la nature des neutrinos. En particulier, cela démontrerait que ceux-ci sont des particules de Majorana et qu'il n'y a pas conservation du nombre de lepton. Cette désintégration peut être étudiée avec des bolomètres dont l'absorbeur contient l'isotope susceptible de se désintégrer, mais la possibilité d'analyser ce processus rare dépend crucialement du niveau de bruit de fond dans la région d'intérêt. Une nouvelle R&D a récemment débuté au sein du projet CROSS (Cryogenic Rare-event Observatory with Surface Sensitivity) visant au développement de bolomètres cryogéniques incluant les isotopes prometteurs ^{100}Mo and ^{130}Te. Ces bolomètres sont capables de discriminer les interactions α et β de surface via l'exploitation des propriétés d'un matériau supraconducteur (film d'Al) ou d'un métal normal (film de Pd) déposé sur les faces du cristal (Li_2MoO_4 and TeO_2). Ces films jouent le rôle de modificateurs de forme pour les impulsions. Les résultats des tests sur des prototypes fabriqués et testés au CSNSM (Orsay, France) ont montré la capacité de films d'Al (de Pd) de quelques μm (nm) d'épaisseur déposés à la surface du cristal de discriminer les événements de surface des événements bulk, avec un niveau de réjection compatible avec celui exigé par les expériences finales. Alors que le film d'Al ne peut identifier que les particules α de surface, avec des films métalliques normaux, nous avons été capables de séparer également les composantes β de surface. Ceci constitue une avancée importante dans la technologie bolométrique pour la décroissance double beta qui pourrait atteindre, avec cette technologie, un indice de bruit de fond de l'ordre de 10^{-5} événements/(keV kg an). De plus, la présente thèse expose les résultats de l'expérience CUPID-Mo, un démonstrateur de CUPID, une expérience d'une tonne de prochaine génération pour la détection du $0\nu\beta\beta$. CUPID-Mo utilise des bolomètres scintillants en Li_2MoO_4 qui discriminent entre les α et les β/γ, permettant ainsi de rejeter la contribution dominante au bruit de fond (particules α). L'expérience a permis d'atteindre une nouvelle limite sur le temps de demi-vie de la désintégration $0\nu\beta\beta$ dans le ^{100}Mo : $T_{1/2} > 1.5 \cdot 10^{24}$ ans à 90% C.I..

Title: CROSS and CUPID-Mo: future strategies and new results in bolometric search for $0\nu\beta\beta$

Keywords: Low-temperature detectors, Double-beta decay, Surface sensitivity, Bolometers

Abstract: Neutrinoless double-beta decay is a hypothetical rare nuclear transition ($T_{1/2}>10^{26}$ yr). Its observation would provide an important insight about the nature of neutrinos ascertaining that they are Majorana particles and demonstrating that the lepton number is not conserved. This decay can be investigated with bolometers embedding the double beta decay isotope, the possibility to investigate this rare process is strongly influenced by the background level in the region of interest. A new R&D has recently begun within the CROSS project (Cryogenic Rare-event Observatory with Surface Sensitivity) aiming at the development of bolometric detectors, embedding the promising isotopes ^{100}Mo and ^{130}Te, capable of discriminating surface α and β interactions by exploiting the properties of superconducting material (Al film) or normal metal (Pd film) deposited on the crystal faces (Li_2MoO_4 and TeO_2). These films work as pulse-shape modifiers. The results of the tests on prototypes performed at CSNSM (Orsay, France) showed the capability of a few-μm (nm)-thick Al (Pd) film deposited on the crystal surface to discriminate surface from bulk events, with the required rejection level of the surface background. While Al film can only identify surface α particles, with normal-metal films we were able to separate also the β surface component. This is a breakthrough in bolometric technology for double beta decay that could lead to reach a background index in the range 10^{-5} counts/(keV kg yr). In addition, the thesis covers the CUPID-Mo experiment, a demonstrator of CUPID, the next-generation ton-scale cryogenic $0\nu\beta\beta$ experiment. CUPID-Mo employs Li_2MoO_4 scintillating bolometers that allows to discriminate between α and β/γ, thus rejecting the dominant contribution on the background that consists in α particle interactions. The experiment achieved a new limit on the half-life of $0\nu\beta\beta$ decay in ^{100}Mo of $T_{1/2} > 1.5 \cdot 10^{24}$ yr at 90% C.I., the best ever obtained worldwide on this isotope.

Université Paris-Saclay
Espace Technologique / Immeuble Discovery
Route de l'Orme aux Merisiers RD 128 / 91190 Saint-Aubin, France